Πανεπιστήμιο Κύπρου
University of Cyprus

DEPARTMENT OF MECHANICAL AND MANUFACTURING ENGINEERING

P-type half-Heusler and Bismuth-Telluride thermoelectric materials

DOCTOR OF PHILOSOPHY DISSERTATION

IOANNA IOANNOU

[2022]

Πανεπιστήμιο Κύπρου
University of Cyprus

DEPARTMENT OF MECHANICAL AND MANUFACTURING ENGINEERING

P-type half-Heusler and Bismuth-Telluride thermoelectric materials

DOCTOR OF PHILOSOPHY DISSERTATION

IOANNA IOANNOU

A Dissertation Submitted to the University of Cyprus in Partial Fulfillment of the Requirements for the Degree of Doctor of Philosophy

[2022]

VALIDATION PAGE

Doctoral Candidate: Ioanna Ioannou

Doctoral Thesis Title: P-type Half-Heusler and Bismuth-Telluride thermoelectric materials

The present Doctoral Dissertation was submitted in partial fulfillment of the requirements for the Degree of Doctor of Philosophy at the Department of Mechanical and Manufacturing Engineering and was approved in the 28/04/2022 by the members of examination Committee.

Examination Committee:

Research Supervisors: Professor Theodora Kyratsi

Professor Ioannis Giapintzakis

Committee Members: Professor Loucas Louca

Professor Marisol Martin-Gonzalez

Professor Pierre Ferdinand P. Poudeu

DECLARATION OF DOCTORAL

The present doctoral dissertation was submitted in partial fulfillment of the requirements for the degree of Doctor of Philosophy of the University of Cyprus. It is a product of original work of my own, unless otherwise mentioned through references, notes, or any other statements.

Ioanna Ioannou

……

Περίληψη

Την τελευταία δεκαετία τα θερμοηλεκτρικά υλικά τύπου half-Heusler of (MCoSb και MNiSn (M = Ti, Zr, Hf)) έχουν κινήσει το επιστημονικό ενδιαφέρον για εφαρμογές μεσαίων και υψηλών θερμοκρασιών λόγω των υποσχόμενων θερμοηλεκτρικών τους ιδιοτήτων. Παρ' όλα αυτά η σχετικά υψηλή θερμική αγωγιμότητα, τα μειονεκτήματα της κοινώς εφαρμοζόμενης μεθόδου για την σύνθεσή τους (arc-melting) καθώς και το υψηλό κόστος αφνίου (Hf) αποτελούν τροχοπέδη για την ευρεία εφαρμογή τους. Όσον αφορά τις εφαρμογές κοντά στην θερμοκρασία δωματίου, τα θερμοηλεκτρικά υλικά Bismuth-Telluride θεωρούνται μέχρι στιγμής τα αποδοτικότερα. Προσφάτως, εξαιρετικά υψηλά ZT έχουν καταγραφεί για νανοσύνθετα υλικά, υπογραμμίζοντας ότι η περεταίρω μελέτη τους θα μπορούσε να οδηγήσει σε ακόμα καλύτερες θερμοηλεκτρικές ιδιότητες.

Η παρούσα διδακτορική διατριβή χωρίζεται σε δύο μέρη. Στόχο του πρώτου μέρους αποτέλεσε η σύνθεση και ο χαρακτηρισμός των p-type MCoSb στερεών διαλυμάτων, τα οποία προετοιμάστηκαν με την μέθοδο μηχανικής κραματοποίησης και θερμής συμπίεσης. Εφαρμόστηκαν διαφορετικές μέθοδοι βελτιστοποίησης: ισοηλεκτρονιακή αντικατάσταση και σύνθεση νανοδομημένων υλικών για την μείωση της θερμικής αγωγιμότητας, προσαρμογή της πυκνότητας των φορέων αγωγιμότητας για την βελτίωση του παράγοντα ισχύος και αντικατάσταση του Hf για τη μείωση του κόστους. Οι καλύτερες θερμοηλεκτρικές ιδιότητες ZT (973K) ~1.1 εντοπίστηκαν στο υλικό $Hf_{0.6}Ti_{0.4}CoSb_{0.83}Sn_{0.17}$, για την σύνθεση του οποίου χρειάστηκαν μόλις 4 ώρες άλεσης. Η αντικατάσταση του Hf με το φθηνότερο στοιχείο Zr οδήγησε σε μέγιστο ZT(960K)~0.77 από το υλικό $Hf_{0.4}Zr_{0.2}Ti_{0.4}CoSb_{0.83}Sn_{0.17}$.

Στόχο του δεύτερου μέρους αποτέλεσε η βελτίωση της θερμοηλεκτρικής απόδοσης των $Bi_xSb_{2-x}Te_3$ υλικών των οποίων η σύνθεση πραγματοποιήθηκε με δυο διαφορετικούς τρόπους: τήξη και μηχανική κραματοποίηση. Μελετήθηκε η επίδραση του μεγέθους των κόκκων της αρχικής σκόνης στις θερμοηλεκτρικές ιδιότητες και σε δεύτερο στάδιο νανοσύνθετα υλικά κατασκευάστηκαν αναμιγνύοντας σκόνες από τήξη και σκόνες από μηχανική άλεση. Το υψηλότερο ZT(350K)~1.13 καταγράφηκε για το υλικό $Bi_{0.3}Sb_{1.7}Te_3$ το οποίο κατασκευάστηκε από σκόνη τήξης με κόκκους μικρότερους από 45 μm καθώς επίσης και για το υλικό που συντέθηκε με μηχανική κραματοποίηση.

Abstract

Half-Heusler (HH) compounds were recently identified as promising thermoelectric materials for medium-high temperature range applications *(ZT_{max}(1200K)~1.5 for the p-type FeNbSb, ZT_{max}(700K)~1.5 for the n-type (Ti,Zr,Hf)NiSn and ZT_{max}(900K)~1.2 for the p-type (Hf,Ti)CoSb)* . Despite the excellent mechanical and electronic properties of MCoSb and MNiSn (M = Ti, Zr, Hf) alloys, their relatively high thermal conductivity, the disadvantages of arc-melting method that is commonly used for the fabrication of this family of compounds and the high cost of Hf remain barriers for their applicability in commercial thermoelectric devices. On the other hand, the best commercial thermoelectric materials for applications near room temperature are still bismuth telluride-based alloys *(ZT_{max}(320K)~1.86 in p-type $(Bi,Sb)_2Te_3$ alloy)* . Impressively high ZTs were achieved in nanocomposite materials, underlining that the effective scattering of phonons and a moderately good power factor play an important role in achieving a good thermoelectric performance.

This work is divided in two parts. The objective of the first part was the synthesis and characterization of p-type half-Heusler MCoSb (M=Ti, Hf, Zr) thermoelectric solid solutions prepared via mechanical alloying followed by hot-press sintering. Different optimization strategies have been applied: isoelectronic substitution and nanostructuring for the lattice thermal conductivity reduction, doping adjustment for the power factor optimization and Hf replacement for the cost reduction. The adjustment of Ti/Hf and Hf/Zr ratio as well as the carrier concentration optimization by the substitution of Sb with Sn were examined. The best thermoelectric properties were achieved in $Hf_{0.6}Ti_{0.4}CoSb_{0.83}Sn_{0.17}$ composition, prepared by 4 hours ball-milling which reached an impressive ZT (973K) ~1.1. The effect of annealing on the microstructure and thermoelectric properties of this compound as well as the Sb replacement with Bi were also investigated. The Hf substitution with its lighter and cheaper homologue Zr led to a ZT(960K)~0.77 by $Hf_{0.4}Zr_{0.2}Ti_{0.4}CoSb_{0.83}Sn_{0.17}$ prepared by six hours milling. The aim of the second part of this work, was the improvement of the thermoelectric efficiency of bismuth telluride-based materials by tuning both the microstructure and the carrier concentration. P-type hot-pressed $Bi_xSb_{2-x}Te_3$ bulk materials were prepared using different methods: melting and mechanical alloying. The experimental results indicate that the presence of high-density grain boundaries and interfaces in materials prepared using nano-powders and powders consisting of small

micro-sized particles (≤45μm) significantly reduced the lattice thermal conductivity while the formation of antisite defects, caused by hand-grinding and ball milling, resulted in lower carrier concentrations and therefore in higher Seebeck coefficient values. As a consequence, a high ZT(350K) ~ 1.13 was recorded by $Bi_{0.3}Sb_{1.7}Te_3$ composition. In a second step, nano-composite $Bi_{0.3}Sb_{1.7}Te_3$ materials were prepared via mixing nano-powders and micro-sized powders in an attempt to further reduce the lattice thermal conductivity without significantly affect the power factor. However, the unexpected increasing trend of $\kappa_{lattice}$ suggested the presence of high gain boundary electrical resistance which leads to an overestimation of $\kappa_{lattice}$ by using the conventional Wiedemann-Franz law.

Acknowledgements

First and foremost, I would like to thank my supervisors Professor Theodora Kyratsi and Professor Ioannis Giapintzakis for their motivating guidance and support during my PhD studies and for giving me the opportunity to work with them. My sincere thanks to the members of the committee, Professor Loucas Louca, Professor Marisol Martin-Gonzalez and Professor Pierre Ferdinand P. Poudeu for accepting this invitation.

I would also like to thank Dr. Elli Symeou for the training, Dr. Andreas Delimitis for the TEM studies, Dr. Panagiotis Ioannou for the XRD measurements, and our lab-technician Mr. Kypros Stylianou for his help with technical problems.

Moreover, I would like to express my sincere gratitude to the M-Era.Net project "MarTEnergy", funded by the Cyprus Research Promotion Foundation (P2P/KOINA/M-ERA.NET/ 0317/04) and the Ministry of Science Technology and Space of Israel for supporting the half-Heusler research.

Special thanks to all my friends and colleagues for being part of this journey. This experience would not have been the same without you. Thank you for your constant support, understanding and all the funny moments that we shared through our many coffee breaks.

I am also deeply grateful to my family and my partner Marios for always believing in me and encouraging me. Special thanks to my grandparents George and Emilia for their unconditional love, to my sister Elizabeth for keeping me fit and sane during the process of writing this thesis, to my dog Fries for filling my days with smiles and joy, and to all my loved ones for being there for me. Last but not least, I would like to thank my mother Andri for providing me invaluable educational opportunities, for believing in my goals and dreams and making their fulfillment possible through her endless support and love.

Αφιερωμένο στη μητέρα μου,

Που πιστεύει σ' εμένα
ακόμα και όταν εγώ η ίδια
δεν πιστεύω στον εαυτό μου.

List of publications

1. **I. Ioannou, P. S. Ioannou, A. Delimitis, Y. Gelbstein, I. (John) Giapintzakis, and T. Kyratsi, "High thermoelectric performance of p-type half-Heusler (Hf,Ti)Co(Sb,Sn) solid solutions fabricated by mechanical alloying," J. Alloys Compd., vol. 858, pp. 1–11, 2021, doi: 10.1016/j.jallcom.2020.158330. [2021]**

2. Z. Viskadourakis, A. Drymiskianaki, V. M. Papadakis, I. Ioannou, T. Kyratsi, and G. Kenanakis, "Thermoelectric Performance of Mechanically Mixed BixSb2-xTe3—ABS Composites," Materials, vol. 14, no. 7, p. 1706, Mar. 2021. [2021]

3. **I. Ioannou, A. Delimitis, Y. Gelbstein and T. Kyratsi, "Reduction of Hf via Hf/Zr Substitution in Mechanically Alloyed (Hf,Ti)CoSb Half-Heusler Solid Solutions", Inorganics, 10, 51. https:// doi.org/10.3390/inorganics10040051. [2022]**

4. G. Mesaritis, I. Ioannou, A. Delimitis, Y. Gelbstein and T. Kyratsi, "n-type (Zr,Ti)NiSn half Heusler Materials via Mechanical Alloying: Structure, Sb- doping and Thermoelectric Properties", Journal of Physics and Chemistry of Solids [2021]

5. A. Teknetzi, D. Stathokostopoulos, I. Ioannou, E.Tarani,T. Kyratsi and G.Vourlias "Synthesis and Thermoelectric Properties of Cr-Substituted Higher Manganese Silicides Prepared by Pack Cementation", Materials Research Bulletin [2022] (*Submitted*)

6. **I.Ioannou, P. S. Ioannou, T. Kyratsi and I. (John) Giapintzakis "Effect of powder's particle size on the thermoelectric properties of Bi-Sb-Te alloys". (to be submitted) [2022]**

(Publications in bold represent the main findings of this PhD thesis)

List of conference presentations

- XXXIII Panhellenic Conference on Solid State Physics and Materials Science [Nicosia-Cyprus, 17/09/2018 – 19/09/2018]- Poster Presentation: "Effect of grain size on the thermoelectric properties of $Bi_{0.3}Sb_{1.7}Te_3$"

- 2019 Spring Meeting of the European Materials Research Society [Nice-France, 27/05/2019 – 31/05/2019] - Poster Presentation: "Thermoelectric properties of p-type Bismuth-Telluride alloys"

- European Conference on Thermoelectrics 2019 [Limassol-Cyprus, 23/09/2019 – 25/09/2019] - Poster Presentation: "Thermoelectric properties of p-type Half-Heusler TiCoSb Solid Solutions fabricated by Mechanical Alloying and Arc-Melting"

- Virtual Conference on Thermoelectrics 2020 [21/07/2020–23/07/2020] - Oral Presentation: "Enhanced thermoelectric performance of p-type half-Heusler (Hf,Ti)Co(Sb,Sn) solid solutions fabricated by mechanical alloying"

- Virtual Conference on Thermoelectrics 2021 [19/07/2021-22/07/2021] - Oral presentation: "Investigation of the Thermoelectric Properties of p-type Nanostructured half-Heusler (Hf,Zr,Ti)Co(Sb,Sn) Solid Solutions Fabricated by Mechanical Alloying"

- Euromat 2021 [12/09/2021-26/09/2021]- Oral presentation: "Thermoelectric Properties of p-type half-Heusler (Hf,Zr,Ti)Co(Sb,Sn) Solid Solutions Fabricated by Mechanical Alloying"

- Panhellenic Conference on Solid State Physics and Materials Science 2021 [26/09/2021-29/09/2021] - Oral presentation: "Thermoelectric performance optimization of low Hf-concentration p-type (Hf,Zr,Ti)Co(Sb,Sn) half-Heusler solid solutions fabricated via mechanical alloying"

Contents

List of Figures

List of Tables

1. Introduction

Over the last century, the global demand for energy has increased dramatically, as well as the energy-related emissions. The negative consequences of climate change and the exhaustion of fossil fuels have brought to the forefront one major challenge: the energy crisis. Industrial and population growth have led to a huge energy demand in recent years. Billions of people all over the world, and especially in the developing world, are seeking to improve their living standards. According to the energy outlook 2035, the global energy consumption will increase by 41% between 2012 and 2035, while the energy per capita use will increase by 14%[1]. There is no doubt that global energy use will keep increasing in the next decades, therefore a more efficient use of energy is necessary in order to face this problem and avert many others. Countries and governments aim to reduce greenhouse gas emissions, increase the use of renewable energy and achieve energy savings. For instance, the European Union has set itself a long-term goal of reducing greenhouse gas emissions by 80-95%, when compared to 1990 levels, by 2050 [2].

All energy conversion processes are subject to considerable losses. In specific, 72% of the global primary energy consumption is lost after conversion and 63% is lost during combustion and heat transfer processes [3]. Energy use can be more efficient by converting the huge amount of waste heat generated from several industrial and domestic processes into electricity. One possible way is to use thermoelectric devices, which convert heat flux (temperature differences) directly into electrical power (Seebeck phenomenon) and vice versa (Peltier phenomenon).

In 1821, Thomas Seebeck discovered that in a closed circuit consisting of two dissimilar metals, when the junctions are maintained at different temperatures, a potential difference is developed. In recent years, the Seebeck effect has led to the production of thermoelectric power generation devices. Few years later, in 1834, Peltier discovered that when an electric current is passed through a circuit of a thermocouple, heat is evolved at one junction and absorbed at the other junction. This is known as Peltier effect and has led to the creation of thermoelectric refrigeration devices which are used for cooling applications. These devices are environmentally-friendly, with the advantage of small size, no moving parts, no pollutants and high reliability [4][5].

The first functioning devices were developed in the 1950s and 1960s and they are known as the first generation thermoelectrics with a conversion efficiency around 5%. In the 1990's experimental breakthroughs were achieved by using nanoscale precipitates and compositional inhomogeneities which led to the second generation of thermoelectric materials with an expected conversion efficiency around 11-15%. The third generation has been under investigation recently and combines many cutting-edge approaches, like valence band convergence and hierarchical architecturing. The predicted device conversion efficiency of the third generation thermoelectrics rises up to 15–20% [5]. Thermoelectric devices can be used in numerous applications, such as in automobile engines, industrial electronic devices, micro self-powered wireless platforms, health monitoring and tracking systems, aerospace, solar heat utilization systems as well as in temperature control refrigeration etc [6]. Even though the results are encouraging and the efficiency of these devices has increased dramatically, much more work is needed is order to develop highly-efficient, cost-effective and easy-to-prepare thermoelectric materials for large-scale commercial production.

The first chapter of this work, provides a brief introduction to thermoelectricity. Specifically, the thermoelectric effects, the desirable thermoelectric properties of a candidate material, the structure of thermoelectric generators, as well as a variety of applications of thermoelectric devices will be discussed.

1.1 Background

1.1.1 Thermoelectric Effect

The term "thermoelectric effect" encompasses three separately identified effects: the Seebeck effect, Peltier effect, and Thomson effect. The Seebeck and Peltier effects are different manifestations of the same physical process. The Seebeck effect is a phenomenon in which a temperature difference between two dissimilar electrical conductors or semiconductors produces a voltage difference between the two substances. The voltage produced is proportional to the temperature difference between the two junctions. The proportionality constant (S or a) is known as the Seebeck coefficient, and often referred to as "thermopower".

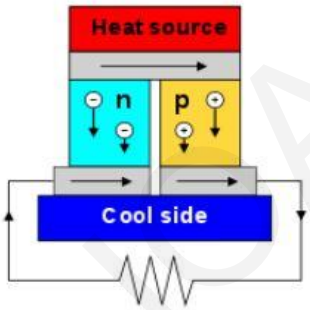

Figure 1.1: A thermoelectric circuit composed of materials of different Seebeck coefficients, configured as a thermoelectric generator.

The Peltier effect is the presence of heating or cooling at an electrified junction of two different conductors and is named after French physicist Jean Charles Peltier, who discovered it in 1834.When a current is made to flow through a junction between two conductors, heat may be generated or removed at the junction.

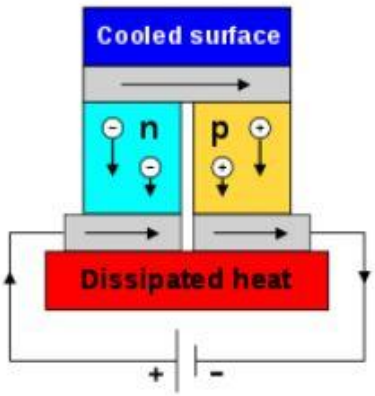

Figure 1.2: The Seebeck circuit configured as a thermoelectric cooler.

In different materials, the Seebeck coefficient is not constant in temperature, and so a spatial gradient in temperature can result in a gradient in the Seebeck coefficient. If a current is driven through this gradient, then a continuous version of the Peltier effect will occur. This Thomson effect was predicted and subsequently observed in 1851 by William Thomson. It describes the heating or cooling of a current-carrying conductor with a temperature gradient.

1.1.2 Thermoelectric Generator

Thermoelectric generators, also called Seebeck generators are solid state devices with no moving parts. The basic building block of a thermoelectric generator is a thermocouple which is made up of one p-type semiconductor and one n-type semiconductor. Thermocouples are sandwiched between two electrically insulating but thermally conducting ceramic plates to form a module (Figure 1.3). If an external load and a temperature gradient is applied, electric energy is generated. Vice versa, if an electric current is passed through the module, heat is absorbed on one side and ejected at the other. In this case, the module can be used for refrigeration (Peltier cooling). The Seebeck effect occurs due to the movement of charge carriers within the semiconductors. The charge carriers at the hot side of the semiconductor have more kinetic energy than the charge carriers at the cold end and move faster towards the cold end. This diffusion leads to a buildup of charge carriers at one side which prevents further movement of high energy carriers at the cold end of the semiconductor. As a result, a voltage potential that is directly proportional to the temperature difference across the semiconductor is created [4][7].

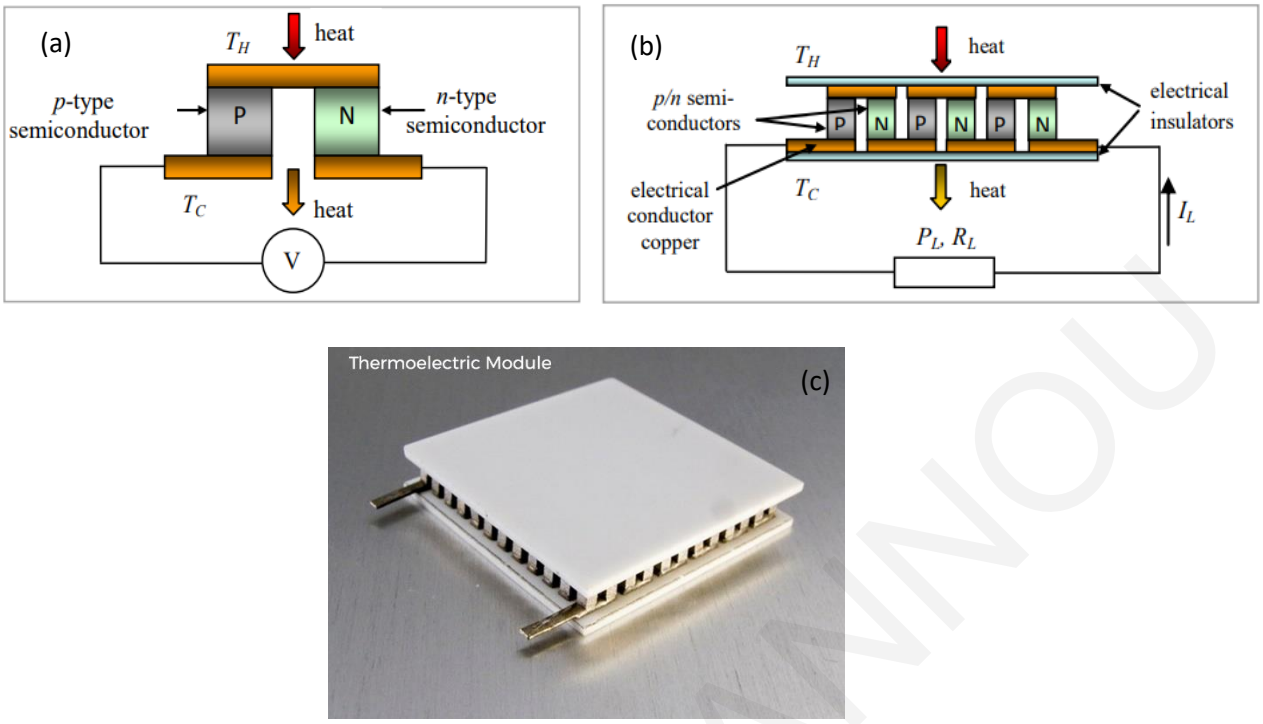

Figure 1.3: The structure of a thermocouple (a) and a schematic drawing of a thermoelectric module (b) [7] and a commercially available TEG fabricated by Ferrotec (c).

1.2.3 Seebeck Coefficient

The Seebeck coefficient of a material is a measure of the magnitude of an induced thermoelectric voltage in response to a temperature difference across that material, as induced by the Seebeck effect. The SI unit of the Seebeck coefficient is volts per kelvin (V/K), although it is more often given in microvolts per kelvin (μV/K). The electronic properties of a solid can be described by the Mott formula, which is obtained from the Boltzman equation by using a single parabolic band approximation[8][9]:

$$S = \frac{\pi^2 {k_B}^2}{3e} T \left(\frac{d[\ln(\sigma(E))]}{dE} \right)_{E=Ef} \quad (1)$$

Where e is the electron charge, and σ(E) the electrical conductivity, that is a function of the energy E, at the fermi level E_F.

The electrical conductivity depends on charge carrier concentration *n* and mobility μ:

$$\sigma = ne\mu \quad (2)$$

Combining those two equations leads to:

$$S = \frac{\pi^2 {k_B}^2}{3e} T \left(\frac{dn(E)}{n dE} + \frac{dn(E)}{\mu dE} \right)_{E=Ef} (3)$$

Increase of Seebeck coefficient can be achieved by the modification of carrier concentration. Metals have a high carrier concentration ($n \geq 10^{22} cm^{-3}$) and $\sigma \geq 10^6 S/m$. Insulators have low n and low σ but high S. In between those two extremes, are semiconductors with n in the range from $10^{18}\ cm^{-3}$ to $10^{21}\ cm^{-3}$ and S in the range 10^{-7} S/m to 10^0 S/m. Degenerate or highly doped semiconductors with a high carrier concentration can be considered to act like a metal. Assuming pure acoustic phonon scattering of carriers, the Seebeck coefficient is given by:

$$S = \frac{8\pi^2 {k_B}^2}{3eh^2} m^* T \left(\frac{\pi}{3n} \right)^{\frac{2}{3}} \quad (4)$$

Where n is the carrier concentration and m* the effective mass.

Seebeck coefficient is negative for n-type materials, positive for p-type materials and for materials which have two carrier types (both electors and holes) is calculated by a weighted average of their electrical conductivity values (σ_e, σ_p):

$$s = \frac{(s_n * \sigma_n + s_p * \sigma_p)}{(\sigma_n + \sigma_p)} \quad (5)$$

Intrinsic semiconductors have both carrier types, as a result the Seebeck coefficient is small. In contrast, doped semiconductors have large Seebeck coefficient because only one type is present. Moreover, the size of the band gap in semiconductors also influences the thermopower. Bipolar conduction plays a role for small band gap materials and at high temperatures. In materials with small band gaps, more minority carriers can be thermally excited from the valence to the conduction band and. This effect cancels out the Seebeck voltage [8][10].

1.2.4 Electrical Conductivity

Electrical conductivity (σ) is the measure of a material's ability to allow the transport of an electric charge. The SI unit of electrical conductivity is siemens per metre (S/m). The reciprocal of σ is the electrical resistivity (ρ). Electrical conductivity and electrical resistivity are related to the carrier concentration (n) through the carrier mobility (μ) (Equation 6). Increase of carrier's concentration and mobility lead to increase of

electrical conductivity. However, mobility decreases when effective mass is large (Equation 7).

$$\frac{1}{\rho} = \sigma = n \cdot e \cdot \mu \qquad (6)$$

$$\frac{1}{\mu} = \frac{e.\tau}{m*} \qquad (7)$$

Where e, the electric charge and τ is the mean scattering time between collisions for the carriers. For semiconductors, σ involves the contributions of both holes and electrons:

$$\sigma = n \cdot e \cdot \mu_e + p \cdot e \cdot \mu_h \qquad (8)$$

Where n, μ_e, p and μ_h are the concentration of electrons, electrons' mobility and hole concentration and mobility, respectively.

1.2.5 Thermal Conductivity

Heat energy in solids can be transported by electrical carriers (holes or electrons), lattice waves (phonons), electromagnetic waves, spin waves, or other excitations. In metals the electrical carriers carry the majority of the heat, while in insulators lattice waves are the dominant heat transporter [11]. In semiconductors, the thermal conductivity (κ) is related to the transfer of heat through a material, either by the electrons or by quantized vibrations of the lattice, called phonons:

$$\kappa = \kappa_e + \kappa_{lattice} \qquad (9)$$

The magnitude of the thermal conductivity as well as its temperature dependence varies drastically depending on the materials properties. Additionally, κ is sensitive to any kind of lattice defects or imperfections, dislocations, anharmonicity of the lattice forces, carrier concentrations, interaction between carriers and phonon and of course the grain size in polycrystalline materials [11].

According to Wiedemann-Franz law, the electronic thermal conductivity κ_e is given by:

$$\kappa_e = L \cdot T \cdot \sigma \qquad (10)$$

Where L is the Lorentz number, T the temperature and σ the electrical conductivity.

For most metals, where charge carriers behave like free-electrons, L can be taken as a constant equal to 2.44×10^{-8} $W\Omega K^{-2}$ (degenerate limit). Although some heavily doped semiconductor thermoelectric materials have an L very close to the degenerate limit,

properly optimized materials often have charge carrier concentrations between the lightly doped (non-degenerate) and heavily doped (degenerate) regions which can result in errors of up to ~40%. A first order correction to the degenerate limit of L can be based on the measured thermopower, |S|, independent of temperature or doping. Kim et al. proposed the following equation [12]:

$$L = \left[1.5 + \exp\left[-\frac{|S|}{116}\right]\right] x10^{-8} \quad (11)$$

Where L is in 10^{-8} $W\Omega K^{-2}$ and S in μV/K.

Equation (11) allows an easy estimation of L from experimental Seebeck coefficient values only, without requiring a numerical solution. For a single parabolic band, L and S are both functions of reduced chemical potential (η) and carrier scattering factor (λ):

$$L = \left(\frac{k_B}{e}\right)^2 \frac{(1+\lambda)(3+\lambda)F_\lambda(\eta)F_{\lambda+2}(\eta) - (2+\lambda)^2 F_{\lambda+1}(\eta)^2}{(1+\lambda)^2 F_\lambda(\eta)^2} \quad (12)$$

$$S = \frac{k_B}{e}\left(\frac{F_{\lambda+1}(\eta)(2+\lambda)}{(1+\lambda)F_\lambda(\eta)} - \eta\right) \quad (13)$$

Where $F_j(\eta)$ represents the Fermi integral,

$$F_j(\eta) = \int_0^\infty \frac{\varepsilon^j d\varepsilon}{1+e^{(\varepsilon-\eta)}} \quad (14)$$

By assuming that the carrier relaxation time is limited by acoustic phonon scattering, equations (12) and (13) can be solved numerically for L and the corresponding S leading to the proposed approximation in equation (11). Equation (11) is accurate within 5% for single parabolic band (SPB) where acoustic phonon scattering is the dominant scattering mechanism and |S|>~10μV/K. For |S|<10μV/K, while the SPB model converges to the degenerate limit, the accuracy of the above equation is reduced and a more complex approximation equation is needed.

In non-metals, lattice thermal transport (phonons) is the main conduction mechanism and also in many semiconductors and alloys it dominates over a wide temperature range. There two types of phonons: optical phonons and acoustic phonons. The acoustic branches of phonons have low frequency and correspond to atoms that are moving in same phase, whereas the optical branches correspond to higher frequencies and atoms moving in opposite phases. In most cases, optical phonons do not affect the heat

transport because of their low group velocity while acoustic phonons are considered as the main heat conductors. However, the interaction between optical and acoustic phonons can significantly influence the thermal transport [11]. Lattice thermal conductivity (κ_l) is expressed by equation 15.

$$\kappa_l = \frac{1}{3}(C_u . u_s . \lambda_{ph}) \qquad (15)$$

Where, C_u is the heat capacity, u_s is the sound velocity and λ_{ph} is the phonon mean free path. As it is interpreted, the crystal structure, impurities, defects, grain boundaries affect the λ_{ph} and therefore the κ_l.

1.2.6 Thermoelectric Figure of Merit

The efficiency of thermoelectric energy converters depends on the transport coefficients of the constituent materials through the figure of merit ZT which includes both the charge and heat transport properties. In other words, ZT depends not only on the electronic structure but also on the crystal structure of a material.

$$ZT = \frac{\sigma S^2 T}{\kappa} = \frac{PF.T}{\kappa} \quad (16)$$

Where σ, S, κ, T and PF are the electrical conductivity, Seebeck coefficient, total thermal conductivity, absolute temperature and power factor, respectively.

ZT is a complex quantity and it depends on both the charge and heat transport properties of a material. The electronic band structure, the lattice characteristics as well as the interaction between phonons and charge carriers influence the thermoelectric figure of merit [4]. Ideally thermoelectric materials should have low thermal conductivity, high electrical conductivity and high Seebeck coefficient. The Power factor (PF) of a material is calculated by its Seebeck coefficient and its electrical conductivity under a given temperature difference. PF is measured in $\frac{W}{K^2 m}$.

$$PF = S^2\sigma \qquad (17)$$

Figure 1.4 illustrates that increasing the carrier concentration (n) leads to an increase of electrical conductivity but also a decrease of Seebeck coefficient while simultaneously increases the electronic thermal conductivity $\kappa_{el.}$ Only the lattice thermal conductivity ($\kappa_{lattice}$) can be manipulated separately, since it does not depend on the electronic

structure. Thus, to achieve high power factors, a compromise has to be found. The maximum of ZT typically occurs at carrier concentrations between 10^{19} and 10^{21} cm^{-3} which is typically found in heavily doped semiconductors.

The maximum thermoelectric efficiency η_{max} of TEG is given by the next equation [9][13]:

$$\eta_{max} = \frac{T_H - T_C}{T_H} \frac{(1+ZT_M)^{1/2}-1}{(1+ZT_M)^{1/2}+\frac{T_C}{T_H}} \qquad (18)$$

Where T_H, T_c are the temperature at the hot and cold side, respectively and ZT_M is the average ZT.

The efficiency of a TE device is determined by the thermoelectric performance (ZT) of the materials used in making the device. Higher efficiencies and materials that can be fabricated at reasonable cost, will revolutionize the power generation industry in the near future.

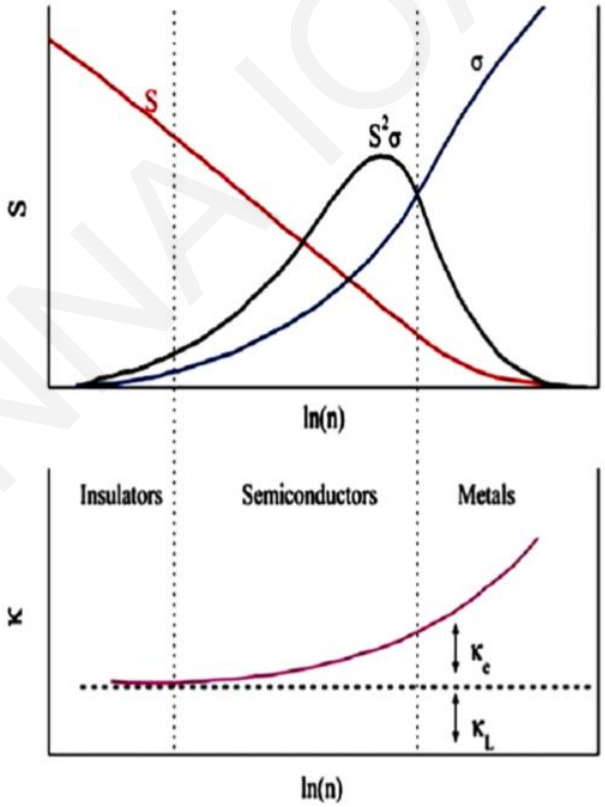

Figure 1.4: Illustration of the variation of the Seebeck coefficient (S), electrical conductivity (s), power factor ($S^2\sigma$), electronic thermal conductivity (κ_{el}), and lattice ($\kappa_{lattice}$) thermal conductivity on the charge carrier concentration, for a bulk material. Reproduced from [175].

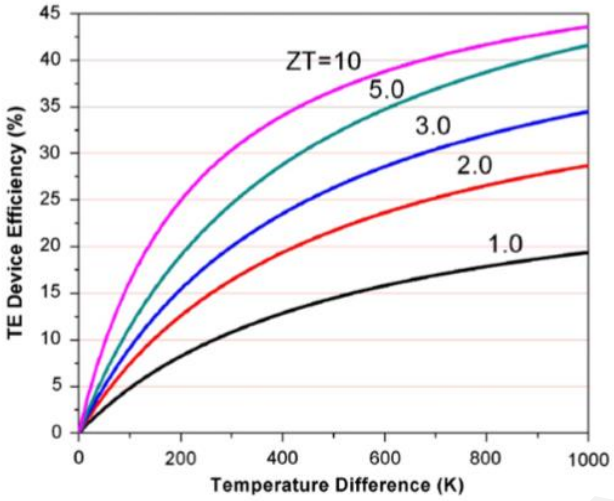

Figure 1.5: Thermoelectric energy conversion as a function of ZT at the setting of T_c=300 K [9].

.

1.2.7 Applications of TEGs

Thermoelectric generators (TEGs) can be used in a wide variety of applications including electricity generation in extreme environments, waste heat recovery in transport and industry, domestic production in developing and developed countries, micro-generation for sensors and microelectronics and solar thermoelectric generators [14]. The fact that TEGs have no moving parts, require no maintenance, have inherently high reliability and long service-free lifetimes, makes them well suited for equipment with low to modest power needs in remote uninhabited or inaccessible locations such as mountaintops, the vacuum of space, or the deep ocean. Space industry has also used TEGs in combination with thermal generators based on nuclear technology (radioisotope thermoelectric generators or RTGs). RTGs can provide electricity for distant and long-term missions when the solar energy is limited. Recently, cement-based thermoelectric materials identified as promising materials for waste solar energy harvesting and thermal sensing[15]. Their applications could be exploited in structures such as buildings, roads, housing, dams, and bridges. The enormous exposure of solar energy over the area of civil infrastructures is stored thermally within the construction materials and could possibly harvested when thermoelectric-based cement materials are used.

Reducing greenhouse gas emissions and limiting the ecological footprint are among the major challenges facing humanity in recent years. To this end, several studies have been

carried out for the use of TEGs in transport sector (vehicles, aircrafts, helicopters etc.). In automobiles there are many systems such engine, exhaust system and gear box that produce heat during operation. This waste heat can be recovered by using TEGs. Many multinational automobile companies like Renault, Honda, Ford etc. have developed their systems to recover exhaust heat using TEG and others such as Hyundai, Jaguar, Range Rover, Toyota, GM etc. are already using TE modules to heat/cool car seats[16]. A significant amount of heat is also released from aircraft jet engines and turbine helicopter engines. Studies have shown that a fuel reduction of 0.5% or more is achievable with TEG, which corresponds to $12 million monthly operating cost reduction, only for U.S commercial planes [14]. Maritime industry is rapidly expanding, resulting in more greenhouse gas emissions that are causing climate change. Kristiansen et al. [17], [18] reported that the development of a thermoelectric waste heat recovery system for ships is possible and can contribute to the solution of this problem. According to these studies, the heat released by the ship engine is already used to heat heavy fuel oil and accommodation areas, and to generate fresh water. These procedures decrease the temperature of waste heat to an optimum level for the use TEG.

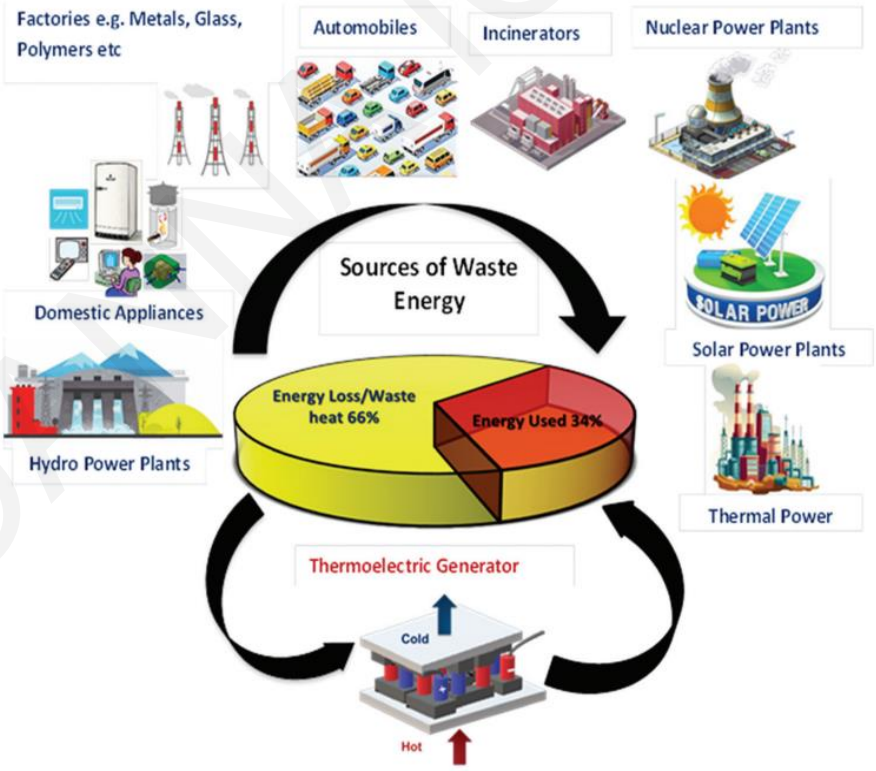

Figure 1.6: Schematic of the various types of waste energy sources and utilization of waste heat energy by a thermoelectric generator. Reproduced by [176]

2. Literature Review

2.1 Overview of thermoelectric materials

In 1950 the field of thermoelectricity grew rapidly, starting with the development of thermoelectric materials from simple metals and conventional semiconductors such as group III-V (e.g., InSb, Bi_2Te_3), IV-IV (e.g., SiGe) and group IV chalcogenides (e.g, PbTe). In middle 1950s, it was found that the thermoelectric properties can be significantly improved by doping and solid solution formation of Bi_2Te_3 and isomorphous compounds such as Sb_2Te_3 or PbTe or GeTe and related heavy-metal-based materials [19][20]. Even though, the point defects in solid solutions led to decreased lattice thermal conductivity by increasing phonons scattering, there were also reductions in the charge carrier mobility, therefore, the overall ZT enhancement was limited[21]. From 1960 to 1990, no significant progress was made and $(Bi_{1-x}\ Sb_x)_2(Se_{1-y}Te_y)_3$ alloys remained the best commercial materials with a ZT of about 1 [22].

Over the past three decades, two main concepts have been used for the enhancement of thermoelectric performance: either the investigation of new families of bulk thermoelectric materials with complex crystal structures and low lattice thermal conductivities or the development of low-dimensional thermoelectric materials systems [9]. The idea to examine complex materials first came from the conceptualization that a perfect thermoelectric material should have the low thermal conductivity of a glass in combination with the electronic properties of a single crystal. This ‘‘phonon glass electron crystal’’ (PGEC) idea was formulated by Slack, back in the mid-1990s [4]. Although the ideal thermoelectric material has yet to be found, both approaches has brought to the forefront new families of compounds, complex and nanostructured materials like skutterdites[23][24], clathrates[25][26], chalcogenides,[27] cobaltites[28], half-Heusler alloys [29][30] and many others, for which high ZTs have been recorded. As shown in Figures 2.1 and 2.2, different families of thermoelectric materials have different operation temperatures. For example, Bi_2Te_3 alloys are typically used for near-room-temperature applications, such as refrigeration and waste heat recovery for temperatures up to 473K. Materials based on group-IV tellurides (PbTe, GeTe or SnTe), skutterdites and clathrates are mainly used for mid-temperature power generation (500–900 K) while silicon–germanium and some half-Heuslers alloys can be used as high-temperature thermoelectric generators (>900 K) [10].

Low dimensional thermoelectric materials and materials with complex structures (nanostructures) can be synthesized either in bulk form or in thin film form and can achieve high ZT values basically because the scattering of phonons is stronger when the size of the sample in at least one direction is reduced, while the scattering of carriers is not affected [31]. One of the most impressive ZT values was reported by Harman et al. who achieved a ZT of 3.5 at 575K in Bi-doped n-type PbSeTe/PbTe quantum-dot superlattice [32]. High ZT values of 2.9 at 400K and 2.2 at 800K were also achieved in Bi_2Te_3/Sb_2Te_3 superlattices and lead-antimony-silver-telluride (LAST) $Ag_{1-x}Pb_{18}SbTe_2$ bulk/'nanodot', respectively [33][27]. Nevertheless, the conversion of these laboratory results into commercial efficient thermoelectric devices does not seem possible yet because of difficulties in both heat transfer and cost.

Depending on the application purposes, the candidate TE materials have to fulfill many requirements. A high ZT in the desired temperature range is not the only requirement for a potential thermoelectric material. The compatibility of the *n*- and *p*-type materials, the long-term thermal stability stability under operating conditions, the level of toxicity, the materials' cost, the mechanical strength and an easy preparation process are some other important issues that have to be addressed for the fabrication and application of modules. For instance, the most well-known high temperature TE materials; SiGe alloys, have been under study for more than 50 years and even though a high ZT=1.1 was achieved for the n-type SiGe, the overall efficiency of SiGe couples remains low due to the low ZT (peak $ZT \approx 0.6$) of the p-type counterpart [34]–[36]. For moderate temperature (T = 500–800^{o}C) applications, lead chalcogenides (PbTe and PbSe) and skutterudites have been also extensively studied. However, PbTe/PbSe materials have weak mechanical strength and high toxicity while skutterudites consist of rare-earth elements and present low thermal stability [29]. The disadvantages of the most popular thermoelectric materials give us the opportunity to further explore new candidate families of compounds with overall better thermoelectric performance.

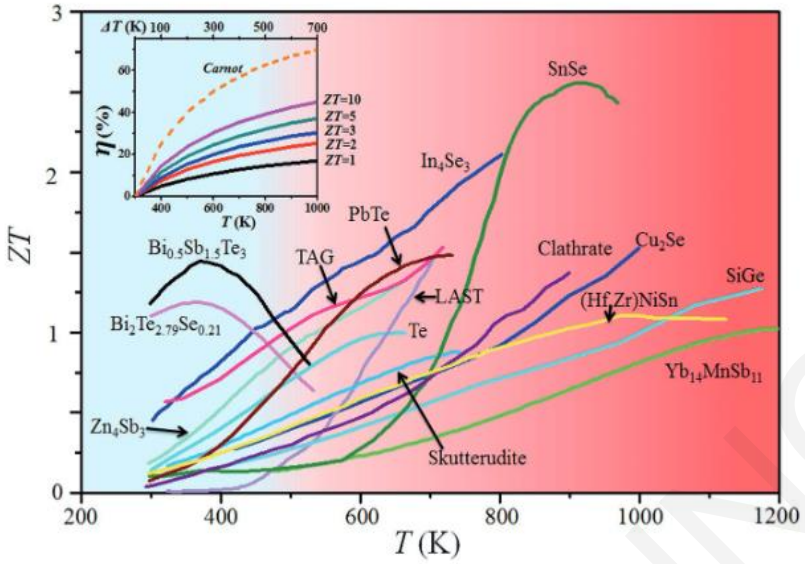

Figure 2.1: ZT as a function of temperature for typical high-efficiency thermoelectric materials and the relation between η, T, and ΔT of materials with different ZT values. Reproduced by [177].

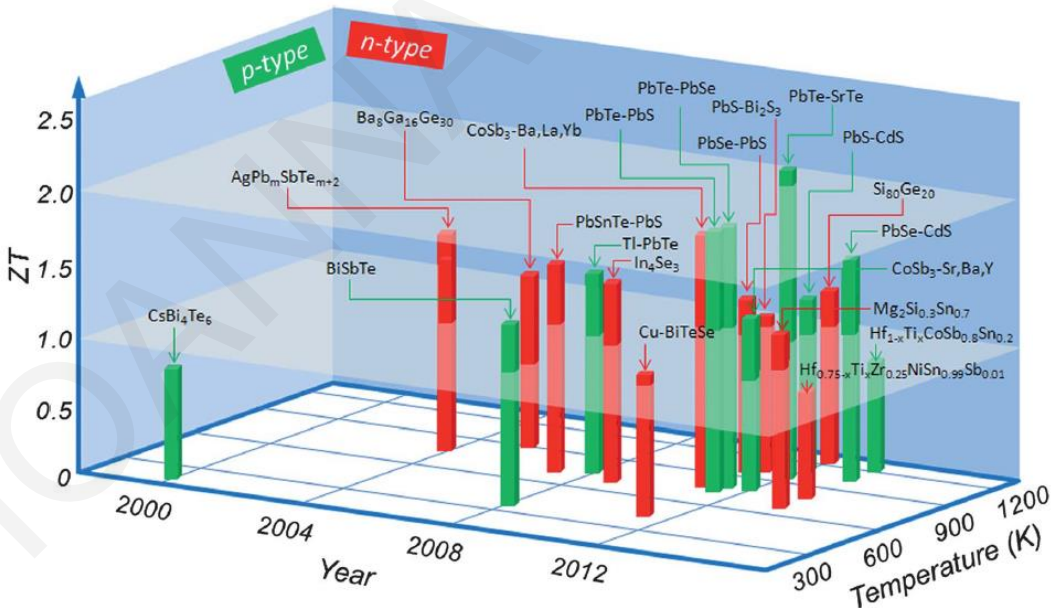

Figure 2.2: Current state-of-the-art in bulk thermoelectric materials: the thermoelectric figure-of-merit ZT as a function of temperature and year [5].

2.2 Optimization Strategies

As previously mentioned, advanced materials with complex structures have attracted great attention. Impressive thermoelectric performances have been achieved through the implementation of new optimization strategies that effectively reduce the thermal conductivity and increase the power factor. In this section, the most common optimization strategies; including nanostructuring, isoelectronic substitution, hierarchical structures, doping optimization and band structure engineering, will be discussed.

2.2.1 Thermal conductivity reduction

Some of the greatest improvements in thermoelectric performance have been achieved due to significant reductions of the lattice thermal conductivity. Impressively amorphous limit values at $\kappa_{lattice}$ = 1–2 W/mK and below were recorded due to **nanostructuring** effect [37]–[40]. There are two types of nanostructured materials. The first type consists of a single phase material of nanosized particles or grains while the second type consists of a matrix and a secondary phase in nanoscale size that is embedded in the matrix [5]. **Isoelectronic substitution** is an another effective route to reduce lattice thermal conductivity, which has been taken by many researchers for the improvement of several thermoelectric materials, such as Half-Heusler, GeSi, Bi_2Te_3 [41]–[43]. Isoelectronic alloying can contribute to the reduction of lattice thermal conductivity by creating point defects and disorder scattering without introducing charge disorders in crystal lattices. Therefore, the electrical transport is usually unaffected after an isoelectronic replacement. A large mass and radius contrast between the host atoms and impurity atoms is preferred in order to disrupt the phonon path and minimize the phonon contribution to the total thermal conductivity, while the crystalline structure is preserved [44]. Experimental investigations, as well as, theoretical calculations of the disorder scattering parameter Γ have shown that isoelectronic alloying on different sublattices greatly decreases the lattice thermal conductivities of half-Heusler alloys due to enhanced mass and strain field fluctuation scattering caused by the difference of masses and radii between the impurity atoms and substituted atoms [45]–[47]. In addition, first-principles calculations of the electronic structures and thermoelectric performance of half-Heusler (Ti,Hf,Zr)CoSb materials mention that substituting Ti with Hf or Zr does not severely change the band structures of these systems. Most of the (Ti,Hf,Zr)CoSb systems have a lower band gap value than

that of TiCoSb and especially $Ti_{0.5}Zr_{0.5}CoSb$ solid solution (0.971 eV). The isoelectronic substitution of Ti with Hf or Zr causes a slight increase of the amplitudes of the density of states in the region of the valence bands, indicating that these compounds could have better thermoelectric performance than TiCoSb. The phonon dispersion relations show that the larger mass of Zr/Hf with respect to Ti lowers the optical modes and induces mixing with the acoustic branches[48].

Nanocomposite materials usually present several kind of point defects in the matrix which result from the partial dissolution of the second phases and dopants in the matrix. The phonon mean-free-path (MFP) in most TE materials extends from nanometres to micrometres, even up to millimetres in some cases. Based on the idea that the more disorder introduced in a material, the lower its thermal conductivity will be, **hierarchical nanostructures** composed by different size of features, are expected to scatter more effectively different groups of phonon MFPs and illustrate reduced lattice thermal conductivity [38]. Defects in atomic-scale and up to a few nanometres can act as scattering points for short wavelength phonons. Nanoscale defects like dislocations, alloying, nano-precipitates, large quantum dots and second-phase islands can effectively scatter phonons of short and medium wavelength (up to ~100 nm). Long wavelength phonons (up to ~1 mm) can be scattered by micro and mesoscale defects like grain boundariess, especially at elevated temperatures [38][49][50]. All-scale hierarchical architectures can potentially reduce the thermal conductivity down to the theoretical limits due the presence of many features like solid solution point defects, nanostructures and grain boundary interfaces, all integrated in a single sample resulting in an effective scattering of all MFP ranges from nano- to micro-length scales (Fig 2.3).

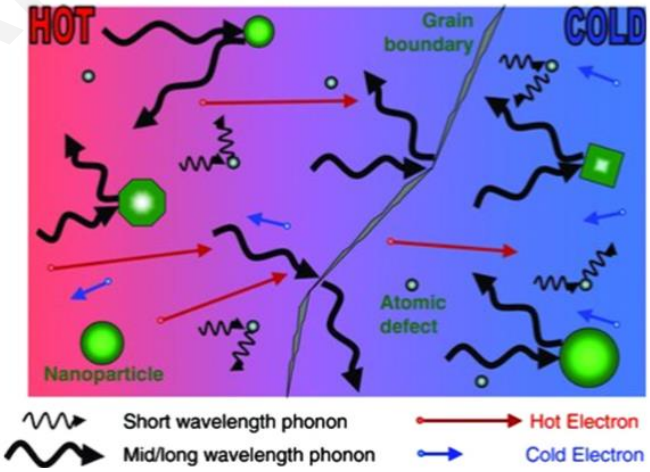

Figure 2.3: Schematic diagram illustrating phonon scattering mechanisms and electronic transport of hot and cold electrons within a thermoelectric material. Reproduced from Ref [178].

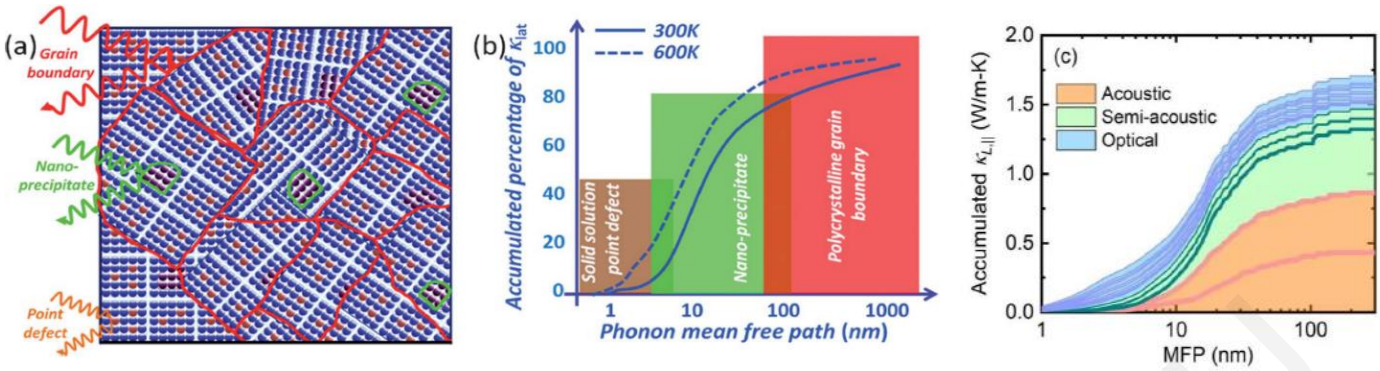

Figure 2.4: All-scale hierarchical architectures and lattice thermal conductivity: (a) all-scale hierarchical architectures, and (b) accumulative distribution function of lattice thermal conductivity with respect to the phonon mean free path in Si or PbTe bulk [5] and (c) Room-temperature $kL_{,\|}$ accumulation function of bulk Bi_2Te_3 decomposed for three ranges of phonon branches [166]

2.2.2 Power factor optimization

Carrier concentration optimization (n) has profound influences on materials' thermoelectric performance and ZT. Increasing n increases the electrical conductivity and electronic thermal conductivity but decreases the Seebeck coefficient *S*. High power factors and ZTs are usually reached by heavily doped semiconductors, either narrow band gab or degenerate semiconductors with carrier concentrations between 10^{19}-10^{20} cm^{-3}. The optimized carrier concentration (n_{opt}) increases rapidly with increasing temperature, according to the relation $n_{opt} \sim m_d{*}T$ (where $m_d{*}$ is the density of states effective mass). A common way to manipulate the carrier concentration is by chemical doping via intentionally introducing extrinsic dopants, which usually act as donors or acceptor in materials. In Bi_2Te_3 material, doping Sb on the Bi site and Se on the Te site leads the formation of p-type and n-type semiconductors, respectively. The dopants (extrinsic point defects) first facilitate the formation of intrinsic point defects (antisites, interstitials, and vacancies), and then the intrinsic point defects directly determine the carrier concentration, thereby enhancing the material performance[51]. However, this strategy will only optimize the carrier concentration for a limited temperature range, prior to the occurrence of bipolar conduction due to intrinsic excitation[52], [53].

When it comes to complex structures like hierarchical materials, the power factor optimization is even more complicated. The previously discussed strategies (2.4.1) are mainly applied to reduce the lattice thermal conductivity through the effective phonon scattering. However, in most of these cases, the electronic properties are affected due

to increased carrier scattering. This lowers the carrier mobilities and reduces the power factor [5]. **Matrix/precipitate band alignment and band structure engineering** can be used to address this problem. This strategy allows carriers to transmit via small band offsets (between two phases) without reducing their mobilities. This concept can be used to create complex materials in which the valence and conduction band energies can be aligned between matrix and inclusions. The inclusions/nanostructures simultaneously scatter phonons but due to successful band engineering the power factor remains almost unaffected.

2.3 Half-Heusler compounds as thermoelectric materials

Over the past two decades, half-Heusler compounds and especially **M**CoSb, **M**NiSn (M = Ti Zr,Hf) and Fe**R**Sb (R=V,Nb) have attracted great interest for medium-high temperature range applications due to their excellent mechanical and electrical properties, thermal stability, low toxicity, as well as the recent good progress in enhancing their thermoelectric performance [29][30]. The half-Heusler phase is represented by the general formula XYZ, where X and Y are transition metals or noble metals and Z is an *sp* metalloid or metal [54]. These compounds crystallize in the MgAgAs-type structure with space group $F\bar{4}3m$ which is built from three interpenetrating face-centered cubic (fcc) sublattices of equal size and one vacant fcc sublattice (Fig. 2.5). A rock salt structure is formed by the least and most electropositive element *Y* and *Z* and the tetrahedral holes are stuffed with *X* element [30]. In addition, if the vacant sublattice is also filled by the transition metal *Y* then a full Heusler structure with formula XY_2Z is created.

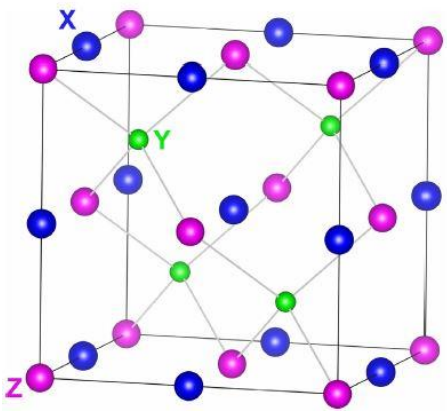

Figure 2.5: Crystal structure of a half-Heusler XYZ. The blue, green and pink dots correspond to X, Y, and Z atoms respectively.

The band structure and physical properties of these compounds depend strongly on the valence electron count (VEC) of the constituent atoms. For instance, materials with VEC = 22, like NiMnSb are half-metallic ferromagnets while materials with VEC = 18, such as ZrNiSn, TiCoSb and FeNbSb, present semiconducting behavior and have excellent thermoelectric properties [55][56]. Most HH compounds with VEC=18, display good electrical properties resulting from the narrow band gap and sharp slope of the density of states near the Fermi level. Based on theoretical calculations by Gandi et al., TiCoSb, ZrCoSb and HfCoSb are indirect bandgap semiconductors with a non-degenerate conduction band minimum (CBM) at the X point (see Fig. 2.6) [57]. The calculated energy bandgap of TiCoSb, HfCoSb and ZrCoSb are 1.05eV, 1.13eV and 1.06eV respectively, whereas the indirect band gap of TiNiSn lies between 0.45 eV and 0.61 eV [58][59]. (Ti/Hf/Zr)NiSn and (Ti/Hf/Zr)CoSb are excellent TE materials and both intrinsically *n*-type semiconductors. However, (Ti/Hf/Zr)CoSb is a much better starting material for *p*-type doping than TiNiSn. The larger band gap of (Ti/Hf/Zr)CoSb suppresses the onset of bipolar conduction at high temperatures whilst the Seebeck coefficient in Sc-doped ZrNiSn illustrates a drop around 600K. Moreover, the band structure of (Ti/Hf/Zr)CoSb exhibits several pockets with high degeneracy in the valence band and upon doping with holes, the fermi level is shifted in the valence band resulting to large positive Seebeck coefficients [60].

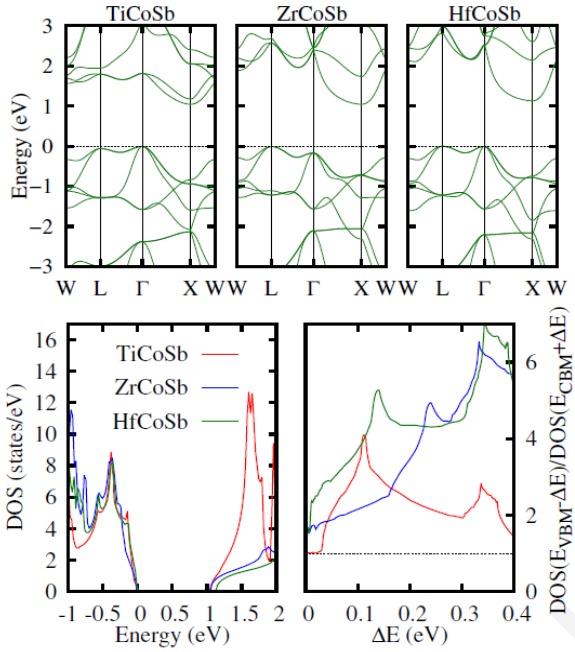

Figure 2.6: Electronic band structure and density of states for TiCoSb, ZrCoSb and HfCoSb. [57].

Despite the promising electronic properties and high power-factor of HH materials, the relative high lattice thermal conductivity remains a barrier for further improvement on their thermoelectric performance. Several approaches have been employed for the optimization of this family of compounds. Alloy effect, micrometer-phase separation and nanostructuring are some of the most common ways to increase phonon scattering and therefore decrease lattice thermal conductivity [61]–[64]. HH compounds, also provide the opportunity of substitutability at each of their three crystallographic sites, which has been found extremely useful for tuning TE transport properties [65]. Significant doping in these compounds can modify the carrier concentration, introduce point defects and optimize the scattering of phonons in order to reduce the lattice thermal conductivity [66][67][68]. The charge carrier concentration in mostly modified by substituting the Z-position element by another main-group element while the substitution of the X and Y elements will cause mass fluctuations and eventually a decrease of thermal conductivity.

The MNiSn (for n-type leg) and MCoSb (for p-type leg) are considered as the state-of-the-art HH thermoelectric materials. Where M, can be either Ti, Zr, or Hf or a combination of these elements. An extremely high ZT(700K) of 1.5 was recorded for the *n*-type (Ti/Zr/Hf)NiSn, in 2005 [69]. Few years later, in 2013 Schwall and Balke

managed to reproduced this result. A ZT(830 K) of 1.2 at was achieved for the n-type $Ti_{0.5}Zr_{0.25}Hf_{0.25}NiSn$ due to its extremely low thermal conductivity resulted from a phase-separation effect [64]. Ever since, the concept of intrinsic micrometer-scale phase separation has come to the forefront as another successful way to reduce thermal conductivity due to the increased boundary scattering at the interfaces. An intrinsic phase separation in p-type and n-type half-Heusler systems can be obtained by applying isoelectronic replacement of Ti with its heavier homologues Hf and Zr [62] [64] [67]. E. Rausch et al. achieved one of the most impressive ZTs(900K)~1.2 in a phase-separated p-type $Ti_{0.25}Hf_{0.75}CoSb_{0.85}Sn_{0.15}$ material by combining two successful approaches to enhance the thermoelectric performance, namely carrier concentration optimization by the replacement of Sb with Sn and intrinsic phase separation by substituting Ti with Hf [70]. Phase separation effect is relatively common in p-type arc-melted HH compounds and it is mainly revealed by the presence of several HH phases with slightly different lattice parameters [70]–[73]. A splitting of the main xrd reflection into a triple peak has also been reported for the n-type $Ti_{0.5}Zr_{0.25}Hf_{0.25}NiSn$, suggesting that phase-separation effect is common in both n-type and p-type half-Heusler solid solutions prepared by arc-melting and can be the origin of an impressively low lattice thermal conductivity [62].

For an effective isoelectronic substitution, the atoms must be selected based on important critiria. Yan et al. [74] mentioned that a lower thermal conductivity in p-type $(Zr,Hf,Ti)CoSb_{0.8}Sn_{0.2}$ systems can be achieved when the atoms forming the compounds exhibit large differences in their size and mass. Alloyed ingots with $Hf_{1-x}T_xCoSb_{0.8}Sn_{0.2}$ compositions were formed by arc melting followed by ball milling and hot-press method. As a result, a peak ZT(1073K)~ 1 at was reached in a nanocomposite p-type $Hf_{0.8}Ti_{0.2}CoSb_{0.8}Sn_{0.2}$ material [74]. E. Rausch et al. have also confirmed that the Ti-Hf combination is more effective in increasing the alloy scattering, than the Zr-Hf combination, due to larger differences in the atomic size and mass of Hf and Ti [71].

Nanostructuring approach has been also applied and effectively demonstrated in reducing thermal conductivity because of the increased phonon scattering at the grain boundaries [75]–[77]. A peak ZT(1073K) ≥ 1.0 has been also achieved in nanostructured $Hf_{0.44}Zr_{0.44}Ti_{0.12}CoSb_{0.8}Sn_{0.2}$ prepared by arc-melting and ball milling [75]. This high ZT is as well, attributed to the reduction of thermal conductivity due to the increased phonon scattering by both alloy and nanostructure effect. Recently, the concept of bulk HH nanocomposites has attract major attention [78][79][80]. Poon et

al. investigated the microstructure and TE properties of p-type $Hf_{0.3}Zr_{0.7}CoSn_{0.3}Sb_{0.7}$ with 20–300nm ZrO_2 nanocomposites[81]. The ZrO_2 nanoparticles dispersed in the HH grain boundaries and caused reduced electronic or lattice thermal conductivity. A high ZT(900K)~0.8 recorded for the sample with 1 vol% of ZrO_2 nanoinclusions, which corresponds to 23% increase compared to that of matrix ingot. Hu et al. also reported a high ZT(1023K)~0.93 in $Hf_{0.5}Zr_{0.5}CoSb_{0.8}Sn_{0.2}$ prepared via levitation melting followed by ball milling and SPS [82]. However, a high ZT(973K)~0.9 for the same composition prepared only via arc-melting and annealing was first reported by E.Rausch et al. back in 2014[71] .

As mentioned above, arc-melting followed by annealing is the typically applied method for the synthesis of both n-type and p-type half-Heusler materials [41], [66], [70], [71], [75], [83]–[85]. To ensure phase homogeneity the arc-melted ingots must be re-melted several times and the annealing process that follows may last up to a week, at temperatures above 900°C. During the arc-melting process the evaporation of the elements with high vapor pressures is possible, and therefore the deviation from the desired alloy composition is a frequent problem [86][41]. Single-phase half-Heusler materials, containing low melting point elements such as Sn and Sb, are intrinsically difficult to be produced by using a high temperature synthesis process. Solid state reactions at low temperatures can be used to address this problem and eliminate the material loss. Nevertheless, there are only few recorded attempts synthesizing half-Heusler compositions by using mechanical alloying and the results are not encouraging enough. Surprisingly, the p-type state-of-the-art $MCoSb_{0.8}Sn_{0.2}$ (M=Ti, Hf, Zr) system has never been synthesized using mechanical alloying (MA) method [87]–[90] . In particular, to the best of our knowledge MA method has never been applied for highly-efficient half-Heusler compositions.

Table 2.1: Selected publications with high ZTs in p-type HH solid solutions.

Publication	Composition	Fabrication Method	Maximum ZT
Rausch et al. (2015)	$Ti_{0.25}Hf_{0.75}CoSb_{0.85}Sn_{0.15}$	Arc-melting followed by annealing at 1173K for seven days	1.2 at 983K
Yan et al. (2012)	$Hf_{0.8}Ti_{0.2}CoSb_{0.8}Sn_{0.2}$	Arc melting followed by ball milling and hot-press	1 at 1073K
Yan et al. (2013)	$Hf_{0.44}Zr_{0.44}Ti_{0.12}CoSb_{0.8}Sn_{0.2}$	Arc melting followed by ball milling and hot pressing	1 at 1023K
Hu et al. (2018)	$Hf_{0.5}Zr_{0.5}CoSb_{0.8}Sn_{0.2}$	Levitation melting followed by ball milling and SPS	0.93 at 1123K
Poon et al. (2011)	$Hf_{0.3}Zr_{0.7}CoSn_{0.3}Sb_{0.7}$ &1 vol% ZrO_2	Arc melting followed by SPS	0.8 at 1123K

2.4 Thermoelectric $Bi_{2-X}Sb_XTe_3$ (BST)

Bismuth tellurides were first discovered by Goldsmith in 1954 and since ever are considered as the best thermoelectric materials near room temperature. Their excellent thermoelectric properties are attributed to the large mean molecular mass (low lattice thermal conductivity), the partial degeneracy of the conduction and valence bands and the narrow gap of approximately 0.15 eV [4]. $Bi_{2-X}Sb_XTe_3$, Bi_2Te_3 and Sb_2Te_3 crystallize in a layer structure with rhombohedral–hexagonal symmetry (space group D_{3d}^5 ($R\bar{3}m$)) with unit cell dimensions at room temperature: a =3.8 Å and c =30.5 Å (Fig. 2.7) [91]. The hexagonal unit cell is consisting of three quintuples, each one composed of five atomic layers in the following order: Te(I)-Bi/Sb-Te(II)-Bi/Sb-Te(I). Bi/Sb and Te layers are held together by strong ionic-covalent bonds whereas the bonds between neighboring Te layers are van-der-Waals. The weak van-der-Waals bonding is responsible for the anisotropic thermoelectric properties of this family of compounds. Specifically, when the thermal conductivity is measured perpendicular to the c-axis has a value around 1.5 W m^{-1} K^{-1}, nearly twice of that along the c-axis direction (0.7 W m^{-1} K^{-1}).

The formation of antisite defects during crystal growth, sintering and milling processes significantly affects the thermoelectric performance of both Bi_2Te and Sb_2Te compounds. The carrier concentration alteration in $Bi_xSb_{2-x}Te$ with varying Sb/Bi content is explained by the existence of various antisite defects of Sb'_{Te} and Bi'_{Te} types [92]. A small difference in the electronegativity of the atoms forming the compound (X_{Sb}=1.9, X_{Bi}=1.8 and X_{Te}=2.1) leads to low bond polarity and the formation of several defects [93]. The understoiciometry of Te is liable for most of the antisite defects and the remarkable change of carrier concentration [94]. Navratil et al. [95] described the interaction of vacancies with the antisite defects in p-type $Bi_xSb_{2-x}Te_3$ solid solution. This interaction can lead to a decrease of hole carrier concentration as described below:

$$\mathbf{2V'_{Bi} + 3V_{Te} + Bi'_{Te} = V'_{Bi} + Bi^{x}_{Bi} + 4V_{Te} + 3e'} \quad \mathbf{(17)}$$

$$\mathbf{2V'_{Sb} + 3V_{Te} + Sb'_{Te} = V'_{Bi} + Sb^{x}_{Sb} + 4V_{Te} + 3e'} \quad \mathbf{(18)}$$

Where Bi^{x}_{Bi} denotes a Bi atom on a regular Bi site and Sb^{x}_{Sb} denotes a Sb atom on a regular Sb site, V_{Te} is a Te vacancy, V'_{Bi} is Bi vacancy, V'_{Sb} is a Sb vacancy and e′ is the produced electron, which can compensate and cause a decrease of hole concentration.

The increase of carrier concentration in Bi_2Te_3 compounds due to antisite defects can be explained by the following equation:

$$\mathbf{Bi_{Bi} + V_{\ddot{Te}} + 2e' \rightarrow Bi'_{Te} + V'''_{Bi} + 4h} \quad \mathbf{(19)}$$

Where, $V_{\ddot{Te}}$ are Te vacancies carrying two positive charges, Bi'_{Te} are antisite defects carrying one negative charge, V'''_{Bi} are Bi vacancies carrying three negative charges and 4h is the creation of 4 extra holes resulting in an increase of carrier concentration. Figure 2.8 presents a schematic diagram of the most common antisite defect in these materials.

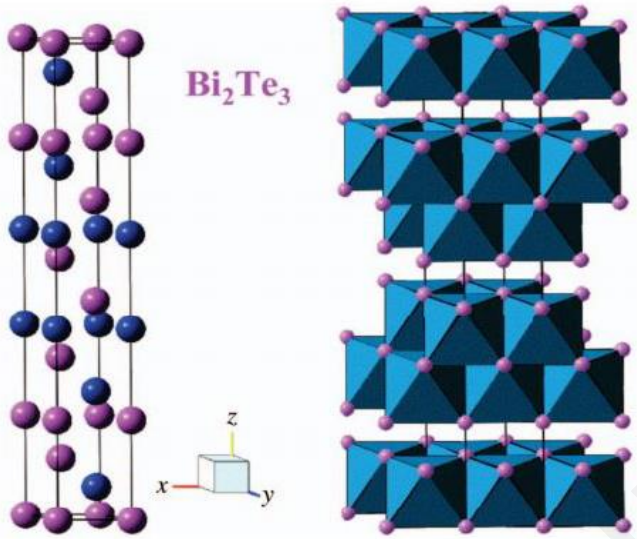

Figure 2.7: Crystal structure of the state-of-the-art thermoelectric material, Bi_2Te_3.The blue atoms are Bi and the pink atoms are Te [91].

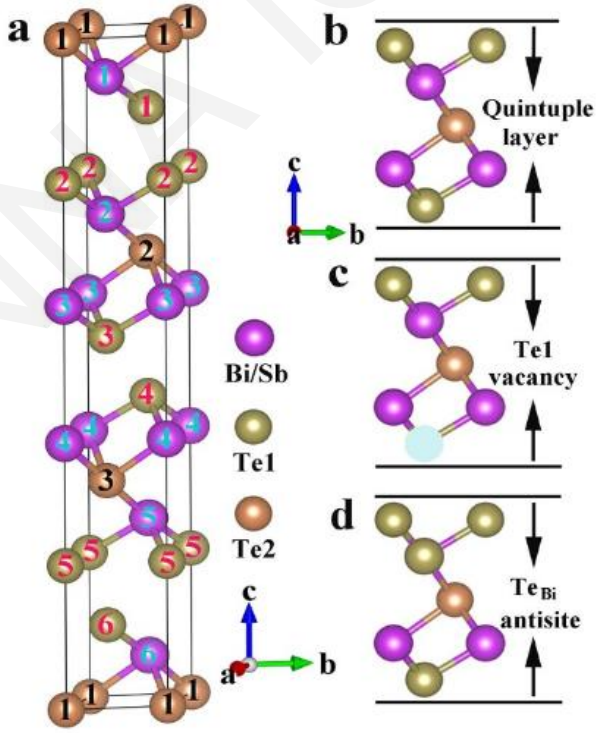

Figure 2.8 a) The hexagonal conventional unit cell of $(Bi_{1-x}Sb_x)_2Te_3$, and (b) side view of the quintuple layer structure of perfect bulk, (c) Te vacancy, and (d) Te_{Bi} antisite [179].

Even though BST is by far the most studied thermoelectric material, its ZT had remained around 1 for more than 50 years. During the past decade, several groups have reported enhanced ZT values because of reductions in the lattice thermal conductivity and enhancements in power factor. The peak ZT of $Bi_{2-x}Sb_xTe_3$ alloys has recently been reported to reach values of 1.2–1.86. Two main approaches were employed for the optimization of BST bulk materials: bottom-up and top-down. The bottom-up approach entails the incorporation of nanostructures into bulk materials via ball-milling [96] , hydrothermal synthesis [97] or melt spinning [98] followed by hot-pressing or spark plasma sintering to obtain bulk materials. The top-down approach involves hot-press or spark plasma sintering followed by hot-deformation to induce in-situ nanostructures and lattice defects in order to reduce lattice thermal conductivity and orientation [99][100][101]. A bottom-up approach was used by Poudel et al., who achieved a peak ZT(373K) ~1.4 in a p-type nanocrystalline BiSbTe bulk alloy prepared by ball-milling and hot-press sintering [102]. In 2014, a high ZT(323K)~1.56 reported by Qinghui Jiang et al. [103] for a nanostructured p-type $Bi_{0.5}Sb_{1.5}Te_3$ alloy prepared via hot forging. Furthermore, Li-Peng Hu et al. reported a ZT(380K)~1.3 for a hot-deformed $Bi_{0.3}Sb_{1.7}Te_3$ alloy. In this case both enhanced textures and donor-like effects induced by this top-down method, improved the electrical transport properties and multiple phonon scattering centers significantly reduced the lattice thermal conductivity [104]. In 2010, a maximum ZT(313K)~1.80 was reached for the nanocomposite $Bi_{0.4}Sb_{1.6}Te_3$ consisting of 40 wt % nanoinclusions [105]. Nanocomposites were obtained via melt spinning and micron-size particles obtained via solid state reaction. The low thermal conductivity due to the effective scattering of phonons and the moderately good power factor played an important role in achieving such a high ZT. Kim et al. reported an impressively improved performance in $Bi_{0.5}Sb_{1.5}Te_3$. A peak ZT(320 K) ~1.86 was reached by applying a promising phonon engineering strategy [106]. A modified traditional liquid-phase compaction technique was used to introduce dense dislocation arrays at low energy grain boundaries, which effectively scatter midfrequency phonons, leading to a substantially lower lattice thermal conductivity ($0.33 Wm^{-1} K^{-1}$) while maintaining high carrier mobility. To sum up, different fabrication methods can give different results for samples with similar compositions.

Table 2.2: Selected publications with high ZTs reported for BST solid solutions.

Publication	Composition	Fabrication Method	Maximum ZT
Symeou et al. (2019)	$Bi_{0.4}Sb_{1.6}Te_3$	Melting and hot deformation	1.24 at 375K
Kim et al. (2015)	$Bi_{0.5}Sb_{1.5}Te_3$	Liquid phase compaction technique	1.86 at 320K
Fan et al. (2012)	$Bi_{0.4}Sb_{1.6}Te_3$	Solid state reaction/melt spinning followed by ball-milling and hot pressing	1.8 at 320K
Poudel et al (2008)	$Bi_{2-x}Sb_xTe_3$	Melting-ball milling-hot press	1.4 at 370K
Jiang et al. (2014)	$Bi_{0.5}Sb_{1.5}Te_3$	Mechanical alloying- hot forging	1.56 at 320 K
Hu et al. (2014)	$Bi_{0.3}Sb_{1.7}Te_3$	Hot deformation	1.3 at 380K

2.5 Motivation and Objectives

2.5.1 Half-Heusler

As previously discussed, high figure-of-merit (ZT=1.0) near 1000K has been achieved for both n-type and p-type HH compounds which underlines the possibility of future application in the medium-high temperature power generation such as in transport sector [36]. Despite the many advantages of HH alloys, their relatively high thermal conductivity, the disadvantages of arc-melting method that is commonly used for the fabrication of this family of compounds and the high cost of Hf remain barriers for their applicability in commercial thermoelectric devices [66], [70], [81], [85]. On the other hand, a solid-state preparation method like MA has several advantages such as possibility of scaling up, inexpensive equipment, reduction of processing steps and easy preparation of nanostructured samples with decreased lattice thermal conductivity values. The objective of the first part of this work was the synthesis and characterization of p-type half-Heusler MCoSb (M=Ti, Hf, Zr) thermoelectric solid solutions prepared via mechanical alloying followed by hot-press sintering. Different optimization strategies have been applied: isoelectronic substitution and nanostructuring for the

lattice thermal conductivity reduction, doping adjustment for the power factor optimization and Hf replacement for the cost reduction. The adjustment of Ti/Hf and Hf/Zr ratio as well as the carrier concentration optimization by the substitution of Sb with Sn were examined. At last, the long-term thermal stability of the most efficient HH compound was investigated.

2.5.2 $Bi_{0.3}Sb_{1.7}Te_3$ (BST)

The best commercial thermoelectric materials for applications near room temperature are still bismuth telluride-based alloys. High ZTs were achieved by nanocomposite materials consisting of both nanosized and micronsized particles, underlining that the effective scattering of phonons and the moderately good power factor play an important role in achieving a good thermoelectric performance. According to recent reported results it is worthwhile to "revisit" this material system. To this end, the aim of the second part of this work was the improvement of the thermoelectric efficiency of bismuth telluride-based materials by tuning both the microstructure and the carrier concentration. P-type $Bi_xSb_{2-x}Te_3$ (x = 0.2,0.3,0.4,0.5) alloy powders were fabricated via mechanical alloying, and consequently consolidated by hot-press sintering. The effect of Sb/Bi ratio on the microstructure and TE properties was investigated. In a second step, p-type $Bi_{0.3}Sb_{1.7}Te_3$ bulk materials have been prepared by different methods: melting and mechanical alloying. Powders, prepared by hand grinding and ball milling, were compacted into high density pellets by hot pressing. The temperature dependence of all thermoelectric properties was measured along the same in-plane direction and reliable thermoelectric power factor and dimensionless figure of merit values were calculated. Finally, the fabrication of nanocomposite $Bi_{0.3}Sb_{1.7}Te_3$ materials consisting of 50% nano-powders and 50% micro-grained powders was attempted, with the aim to further reduce the lattice thermal conductivity without significantly affect the electrical conductivity and Seebeck coefficient.

3. Experimental Methods

This chapter gives an outline of experimental methods that were used in this work. It provides information on the fabrication techniques for both BST and half-Heusler materials and explains the basic characterization techniques that were used.

3.1 Sample preparation

Half Heusler materials were exclusively synthesized via mechanical alloying while for the fabrication of BST pellets different methods were applied: melting followed by hand-grinding, melting followed by ball-milling and mechanical alloying. All samples (HHs and BSTs) were compacted into high-density pellets in a cylindrical graphite die via hot-press sintering.

3.1.1 Half-Heusler

The synthesis of the p-type state-of-the-art $MCoSb_{0.8}Sn_{0.2}$ system via **mechanical alloying (MA)** method was attempted for the first time, while to the best of our knowledge this method has never been applied for highly-efficient half-Heusler compositions. Mechanical alloying (MA) is a solid-state synthesis method and powder processing technique involving repeated cold welding, fracturing, and re-welding of blended powder particles in a high-energy ball mill to produce a homogeneous material. The actual process of MA starts with mixing of the powders in the right proportion and loading the powder mix into the mill along with the grinding medium (generally steel or tungsten balls). This mix is then milled for the desired length of time until a steady state is reached [107].

As mentioned in chapter 2.3, **arc-melting** followed by annealing is the typically applied method for the synthesis of both n-type and p-type half-Heusler materials. Arc-melting is a rapid solidification method and as the name suggests, the elements are heated by direct application of electric arc between oppositely charged electrodes [108]. The arc-melted ingots must be re-melted several times to ensure phase homogeneity and the annealing process that follows may last up to seven days at high temperatures ($T>800^oC$). The mechanical alloying and arc melting methods are compared schematically in Figure 3.1.

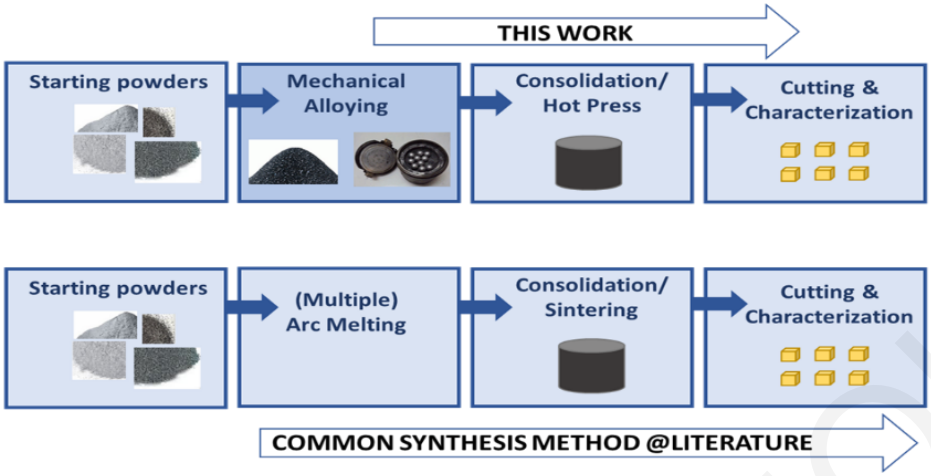

Figure 3.1: Mechanical alloying synthesis route vs the arc melting as a typical route in the literature.

For the **mechanical alloying** process, high purity elemental Hf (99.6% Alfa Johnson Matthey GmbH, Germany), Zr (99% US Research Nanomaterials Inc, USA), Ti (99.9% Alfa Johnson Matthey GmbH, Germany), Co (99.8% Alfa Johnson Matthey GmbH, Germany), Sb (99.9% Alfa Johnson Matthey GmbH, Germany), Bi (99.5% Alfa Johnson Matthey GmbH, Germany) and Sn (99.85% Alfa Johnson Matthey GmbH, Germany) were weighted under Ar atmosphere and were loaded to a tungsten carbide vial along with 10mm balls. The milling process was carried out in a planetary mill.

3.1.2 $Bi_xSb_{2-x}Te_3$

The $Bi_xSb_{2-x}Te_3$ samples were prepared via **melting** and **mechanical alloying**. For the **melting** process, high purity (5N) Bi, Sb and Te granules were weighed according to the $Bi_xSb_{2-x}Te_3$ and then an excess amount of Te (4%wt) was added to the mixture to compensate for its loss during heating due to its low vapor point (277℃ at 10^{-4} Torr). The metal mixture was loaded into an evacuated quartz-sealed tube and melted at temperatures over 800℃ for 10 hours to ensure composition homogeneity. At the end of the process the mixture/ingot was slowly cooled down to room temperature. The ingots were hand-grounded multiple to to obtain powders with different particle sizes. For the **mechanical alloying process**, high purity (5N) Bi, Sb and Te elements were weighted following the nominal compositions, in a glovebox under Ar atmosphere and were loaded to a tungsten carbide vial along with 10mm balls. The milling process lasted 20 hours at 300rpm and was carried out in a planetary mill.

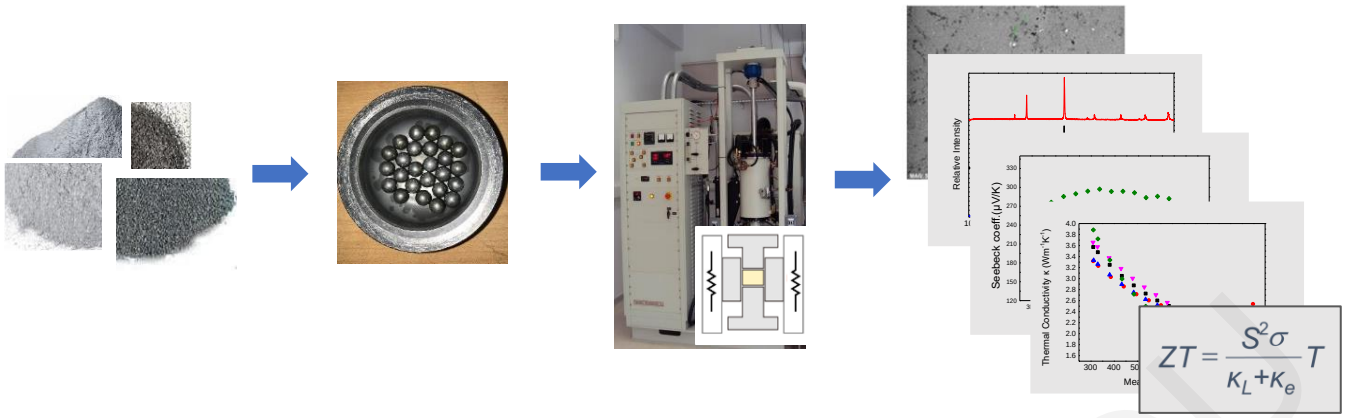

Figure 3.2 Typical experimental route for HH and BST samples prepared via mechanical alloying: 1) mixing of elements in a glovebox, 2) mechanical alloying, 3) hot-pressing in a graphite die and 4) characterization.

3.2 Structural Characterization

3.2.1 X-ray diffraction (XRD)

The crystal structure of all samples and powders was analysed by **X-ray diffraction** (XRD) at room temperature. X-ray diffraction is a technique typically used for qualitive/quantitative determination of the crystallographic structure of the investigated samples. It provides information on structures, phases, preferred crystal orientations (see **Error! Reference source not found.**c), and other structural parameters, such as a verage grain size, crystallinity, strain, and crystal defects. **Error! Reference source not found.** presents an example of a theoretical x-ray diffraction pattern for both the half-Heusler TiCoSb composition and BST solid solution and an experimental pattern of BST sample for both in-plane and cross-plane direction. In this work, two different instruments were used: a 9kW rotating anode Rigaku SmartLab diffractometer and a Rigaku Miniflex diffractometer.

Theoretical Background of X-ray diffraction:

Crystal structures diffract wavelengths similar to the spacing of planes of the crystal lattice. X-rays are generated by a cathode ray tube, filtered to produce monochromatic radiation, and directed toward the investigated sample. The interaction of the incident X-rays with the sample produces constructive interference (and a diffracted ray) when conditions satisfy Bragg's Law ($n\lambda=2d\sin\theta$), which relates the diffraction angle (2θ) and lattice spacing (d) to the wavelength of electromagnetic radiation (λ) (Fig.3.2). The diffracted X-rays are then detected, processed and counted to give a diffraction pattern.

By scanning the sample through a wide range of 2θ angles, all possible diffraction directions of the lattice are attained [109].

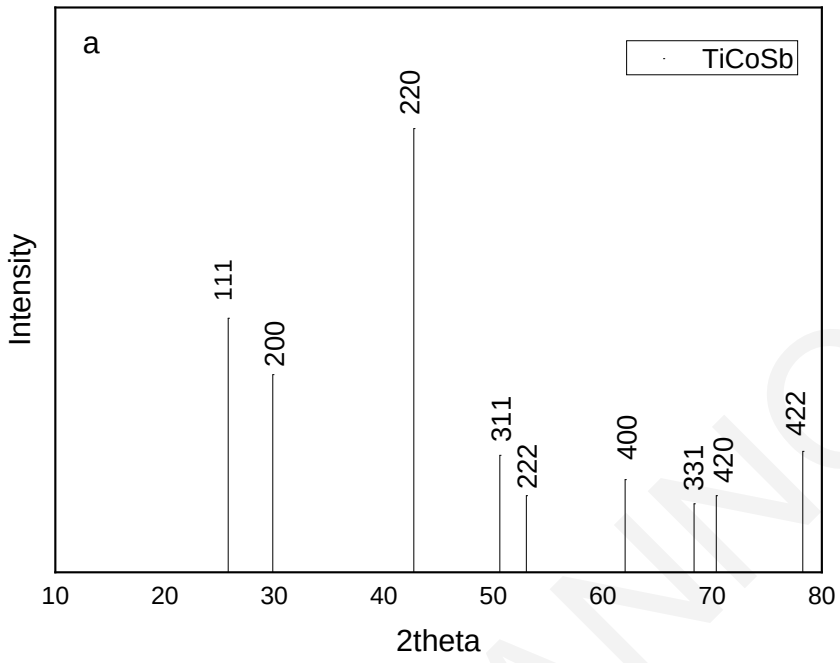

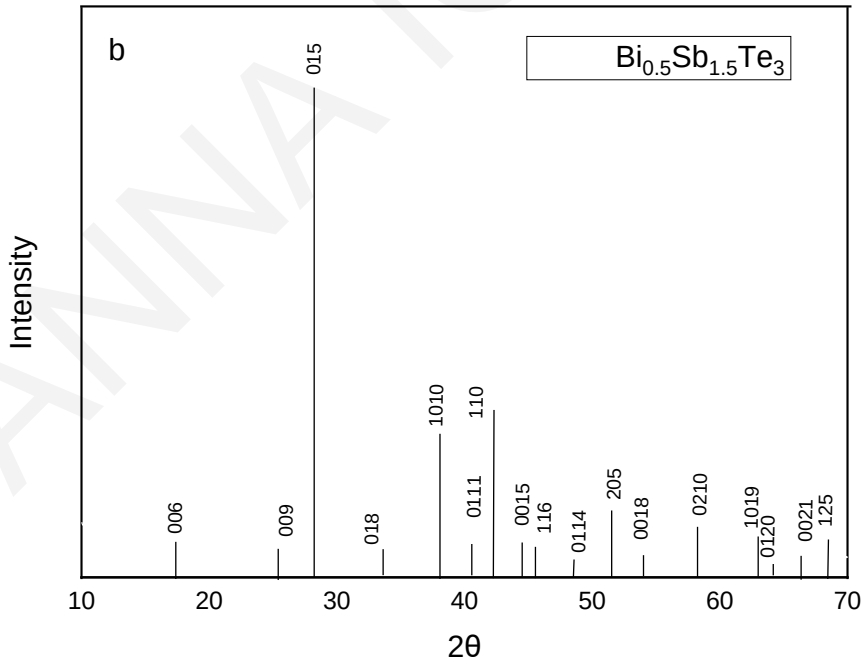

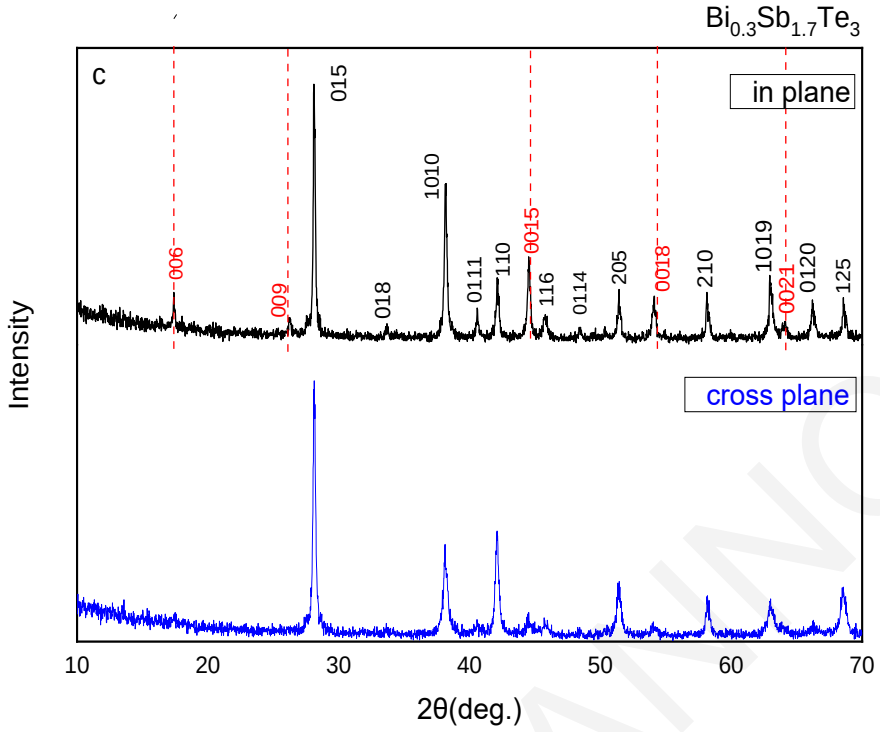

Figure 3.3: Theoretical X-ray diffraction pattern of the half-Heusler TiCoSb (a) and $Bi_{0.5}Sb_{1.5}Te_3$ (b). Experimental XRD diffraction patterns of the hot-pressed $Bi_{0.3}Sb_{1.7}Te_3$ samples for both in-plane and cross-plane direction (c). The dash lines correspond to (00l) peaks, which reveal the presence of preferred orientation.

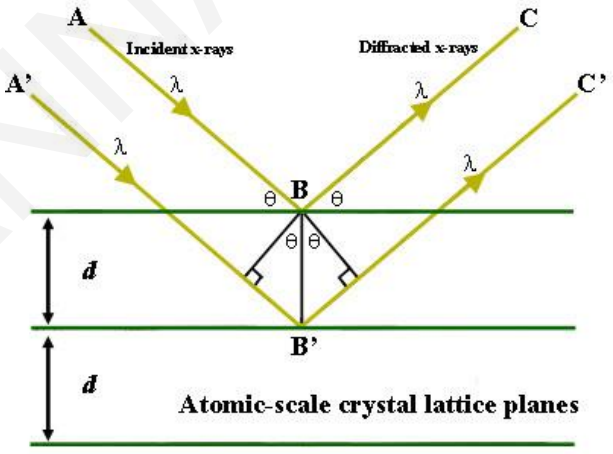

Figure 3.4 Bragg's Law. Reproduced by [109]

Lotgering Factor-Preferred orientation:

The existence of preferred orientation in the in-plane configuration of Bismith-Teluride alloys is revealed by the (00l) diffraction intensities which are higher than the ones in the cross-plane pattern. The degree of preferred orientation can be evaluated by calculating the Lotgering factor (LF) [110]:

$$f = \frac{P - P_0}{1 - P_0} \quad P = \frac{\sum I(00l)}{\sum I(hkl)} \quad P_0 = \frac{\sum I_o(00l)}{\sum I_o(hkl)}$$

Where, I_o(hkl) and I(hkl) are the peak intensities of a randomly oriented sample and the measured sample respectively.

Sherrer equation-Crystallite size:

The well-known Scherrer formula, was used to calculate the mean crystallite size of BST powders generated by ball milling and mechanical alloying:

$$\beta(2\theta) = \frac{K\lambda}{Lcos\theta}$$

Where, L is the mean grain size, K is a dimensionless shape factor with value of about 0.9, λ is the X-ray wavelength, θ is the Bragg angle and β is the line broadening at half the maximum intensity (FWHM).

Scherrer equation relates the size of sub-micrometre particles, or crystallites to the broadening of a peak in a diffraction pattern and it is used in the determination of size of crystallites in the form of powder. In order to analyse the crystallite size, the instrumental broadening should be considered. An XRD pattern of a large crystallite size, defect-free powder specimen (powder of a hand-grounded $Bi_{0.3}Sb_{1.7}Te_3$ ingot) was used to calculate the instrument contribution.

3.2.2 Scanning Electron Microscopy (SEM) and Energy Dispersive X-ray Spectroscopy (EDX)

Scanning electron microscopy technique can provide information on surface topography, morphology and chemical composition a specimen [111]. A scanning electron microscope (SEM) produces images of a sample by scanning the surface with a focused beam of electrons that is produced at the top of the microscope by an electron gun. The electron beam follows a vertical path through the microscope, which is held within a vacuum. The beam travels through electromagnetic fields and lenses, which

focus the beam down toward the sample. Once the beam hits the sample, electrons (backscattered and secondary) and X-rays are ejected from the sample. Detectors collect these X-rays, backscattered electrons, and secondary electrons and convert them into a digital signal[112].

The most common imaging mode collects low-energy (<50 eV) secondary electrons that are ejected from conduction or valence bands of the specimen atoms by inelastic scattering interactions with beam electrons. Due to their low energy, these electrons originate from within a few nanometers below the sample surface and are very useful for the inspection of the topography of the sample's surface[113]. Backscattered electrons originate from a broad region within the interaction volume. They are a result of elastic collisions of electrons with atoms, which result in a change in the electrons' trajectories. The number of the backscattered electrons reaching the detector is proportional to their atomic number. This dependence of the number of BSEs on the atomic number helps us differentiate between different phases, providing imaging that carries information on the sample's composition[114].Figure *3.6* present a typical secondary electron image and a typical back-scattered electron image for a hot-pressed HH solid solution.

Energy-dispersive X-ray spectroscopy (**EDX**) is an analytical technique used for the elemental analysis or chemical characterization of a sample. It relies on the emission of characteristic X-rays from a specimen a beam of electrons which is focused into the sample being studied. At rest, an atom within the sample contains ground state (or unexcited) electrons in discrete energy levels or electron shells bound to the nucleus. The incident beam may excite an electron in an inner shell while creating an electron hole where the electron was. An electron from an outer, higher-energy shell then fills the hole, and the difference in energy between the higher-energy shell and the lower energy shell may be released in the form of an X-ray. The number and energy of the X-rays emitted from a specimen can be measured by an energy-dispersive spectrometer. As the energies of the X-rays are characteristic of the difference in energy between the two shells and of the atomic structure of the emitting element, EDS allows the elemental composition of the specimen to be measured [113].Figure *3.5* shows a typical EDX spectra for $Bi_{0.3}Sb_{1.7}Te_3$ solid solution.

In this work, the microstructure and the chemical composition of the samples were studied using scanning electron microscopy (SEM; JEOL JSM-6610LV or Tescan Vega LSU-20kV) and energy dispersive X-ray spectroscopy (EDS; Bruker. nano 129eV XFLASH Detector 5010) respectively. The chemical composition was determined by choosing several areas of the same sample and averaging the composition.

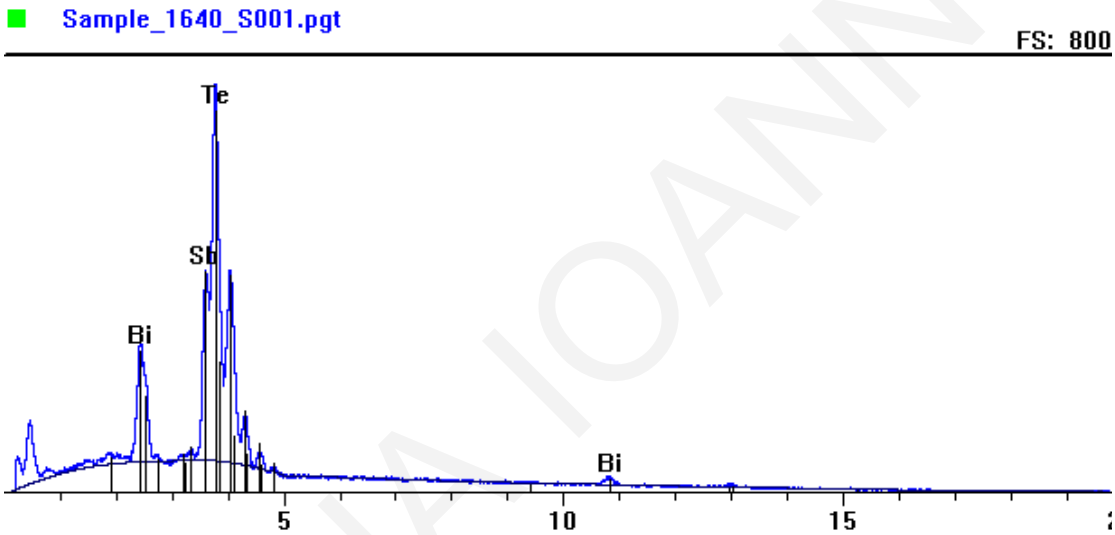

Figure 3.5: A typical EDX spectra of BST sample.

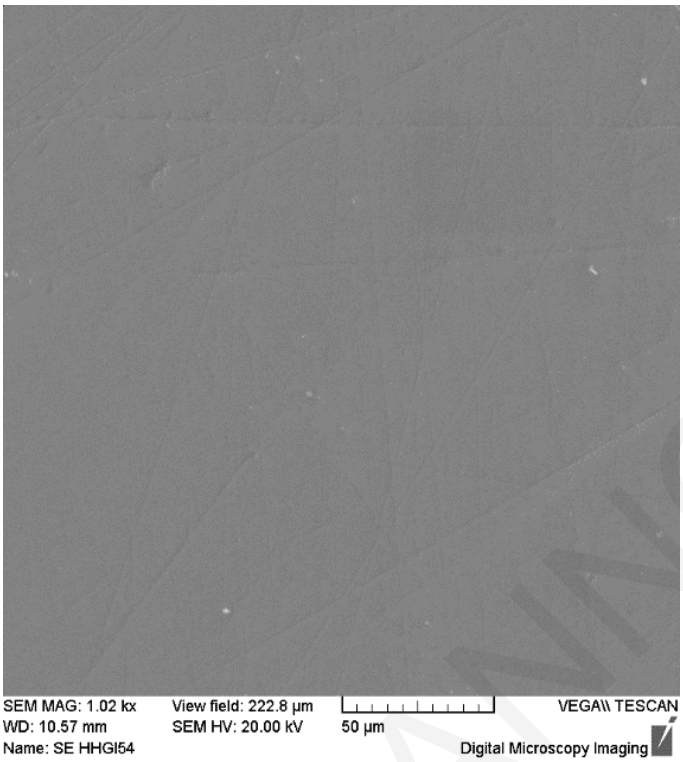

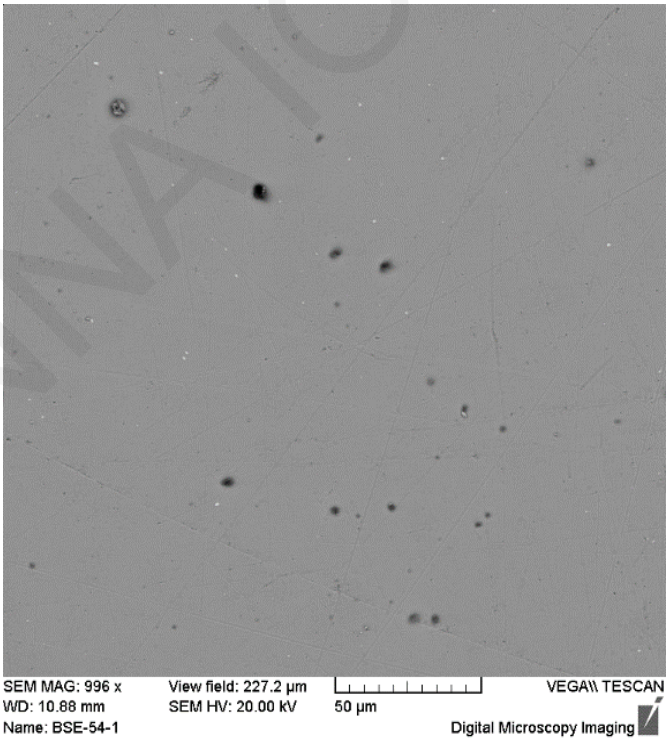

Figure 3.6: Typical secondary electron image (a) and backscattered electron image of a hot-pressed (Hf,Ti,Zr)Co(Sb,Sn) solid solution.

3.2.3 Transmission Electron Microscopy (TEM)

The **Transmission Electron Microscope** operates on the same basic principles as the light microscope but uses electrons instead of light. The wavelength of electrons is much smaller than that of light, therefore the optimal resolution attainable for TEM images is many orders of magnitude better than that from a light microscope. TEMs can reveal the finest details of internal structure - in some cases as small as individual atoms. TEMs employ a high voltage electron beam in order to create an image. An electron gun at the top of a TEM emits electrons that travel through the microscope's vacuum tube. A series of electromagnetic lens focus the electrons into a very fine beam. This beam then passes through a very thin specimen, and the electrons either scatter or hit a fluorescent screen at the bottom of the microscope. An image of the specimen with its assorted parts shown in different shades according to its density appears on the screen. Figure 3.7 presents an example of bright field (BF), in (a) and dark field (DF), in (b) images of a HH sample. The nanograins are clearly illustrated in the latter with white arrows, as bright regions against an overall dark background. In this work, a JEOL 2011 microscope, operating at an accelerating voltage of 200 kV with a point resolution of 0.25 nm and equipped with an EDS detector (EDAX Apollo XLT TEM-SDD) was employed for transmission electron microscopy (TEM, HRTEM) experiments. Samples suitable for TEM-HRTEM were prepared by dispersing crushed material on ultrathin lacey C-films supported on 3.05 mm copper grids.

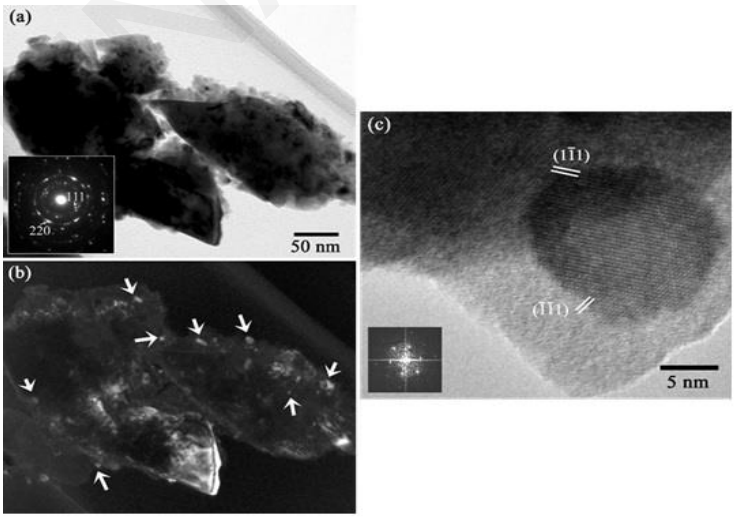

Figure 3.7: Typical TEM-BF and DF images, respectively, from a HH solid solution sample acquired using the arrowed 220 reflection at the SAD pattern, inset in (a) and c) HRTEM image of a representative nanocrystalline particle, viewed along its [011] crystallographic direction.

3.3 Thermoelectric properties

3.3.1 Electrical conductivity and Seebeck coefficient

The **electrical conductivity and Seebeck coefficient** were measured by a standard four-probe method (ZEM-3, Ulvac-Riko, Japan) in a He atmosphere to ensure homogeneous distribution of heat inside the furnace and prevent oxidation at elevated temperatures.

Measurement principle of four probe method: A prism or cylindrical sample is set in a vertical position between the upper and lower blocks in the heating furnace. While the sample is heated, and held, at a specified temperature, it is heated by the heater in the lower block to provide a temperature gradient. Seebeck coefficient is measured by measuring the upper and lower temperatures T_1 and T_2 with the thermocouples pressed against the side of the sample, followed by measurement of thermal electromotive force dE between the same wires on one side of the thermocouple. Electric resistance is measured by the dc four-terminal method, in which a constant current I is applied to both ends of the sample to measure and determine voltage drop dV between the same wires of the thermocouple by subtracting the thermo-electromotive force between leads.

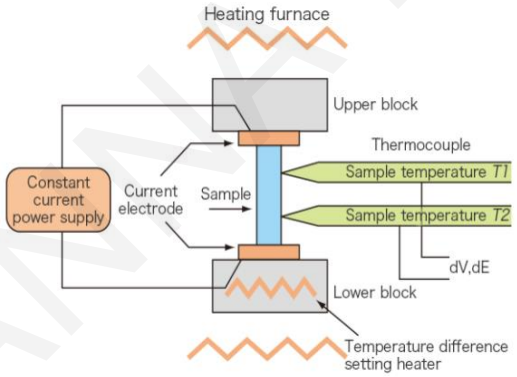

Figure 3.8: Schematic diagram of four probe method (Ulvac ZEM-3).

3.3.2 Hall measurement

The **Hall coefficient** at 300K was measured using a commercial Physical Properties Measurement System (PPMS, Quantum Design). The Van der Pauw technique was used under a magnetic field of 2T and a dc current of 20mA. The currents were applied on the surface of the samples with a four-point probe placed around the perimeter of the sample. By combining the Hall coefficient (R_H) and the electrical resistivity (ρ), the

carrier density (n_H) and the carrier mobility (μ_H) were calculated according to the following equations:

$$n_H = \frac{-1}{e \cdot R_H}, \mu_H = \frac{1}{e \cdot n_H \cdot \rho}$$

Van der Pauw technique:

The **van der Pauw Method** is a technique commonly used to measure the resistivity and the Hall coefficient of a sample. Its power lies in its ability to accurately measure the properties of a sample of any arbitrary shape, as long as the sample is approximately two-dimensional (i.e. it is much thinner than it is wide), solid and the electrodes are placed on its perimeter. The van der Pauw method employs a four-point probe placed around the perimeter of the sample, to provide an average resistivity of the sample. To make a measurement, a current is caused to flow along one edge of the sample (for instance, I_{12}) and the voltage across the opposite edge (V_{34}) is measured. From these two values, a resistance ($R_{12,34}$) can be found using Ohms law. The resistance of samples with arbitrary shapes can be determined from two of these resistances - one measured along a vertical edge, such as $R_{12,34}$ and a corresponding one measured along a horizontal edge, such as $R_{23,41}$ (see Figure 3.9). It is possible to obtain a more precise value for the resistance by making two additional measurements of their reciprocal values and averaging the result. Then, the van den Pauw formula becomes: $e^{-\pi R_{vertical}/Rs} + e^{-\pi R_{horizontal}/Rs} = 1$.

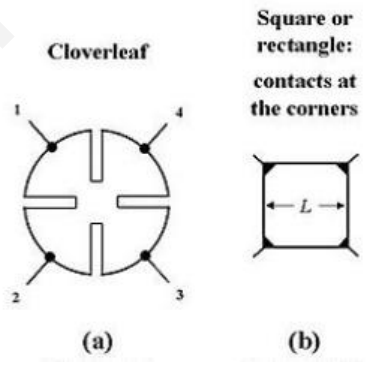

Figure 3.9: Possible contact placements for samples with different shapes.

3.3.3 Thermal conductivity

The thermal conductivity ($\kappa=D\cdot C_p\cdot\rho$) was calculated from diffusivity (D) and Specific heat (C_p) measurements by a Netzsch LFA 457 and the geometrical density (ρ) of the samples. A standard pyroceram 9606 sample was used as a reference for calculations of the specific heat capacity. Prior measurement, samples were coated with graphite to maximize the signal and the amount of thermal energy transmitted from the font surface to the back surface of the sample. The thermal diffusivity can be carried out within an error of ±3% and the specific heat capacity can be determined within an error of ±5%.

Principle of the LFA Method:

The front side of a plane-parallel sample is heated by a short laser pulse. The absorbed heat induced propagates through the sample and causes a temperature increase on the rear surface. This temperature rise is measured versus time using an infrared detector. To calculate the thermal diffusivity, the half time $t_{1/2}$ (time corresponding to half the step height) is used. The total temperature increase (step height) can be used to determine the specific heat. It is indirectly proportional to the heat capacity of the sample (Figure 3.10). The C_p of an unknown material can be calculated by comparing the signal heights between sample and reference as follows:

$$C_p(T) = \frac{T_\infty^{ref} \cdot Q^{sample} \cdot V^{sample} \cdot \rho^{ref} \cdot t^{ref} \cdot d^2_{sample\ aperture}}{T_\infty^{sample} \cdot Q^{ref} \cdot V^{ref} \cdot \rho^{sample} \cdot t^{sample} \cdot d^2_{ref\ aperture}} \cdot C_p^{ref}(T)$$

Where, T the height of the detector signals, Q the laser energy, V the amplification factor, ρ the density, t the thickness of the sample or reference and d the opening diameter of the sample holder

If the density (ρ) is known, the thermal conductivity (κ) can be determined as follows:

$\kappa=D.C_p.\rho$

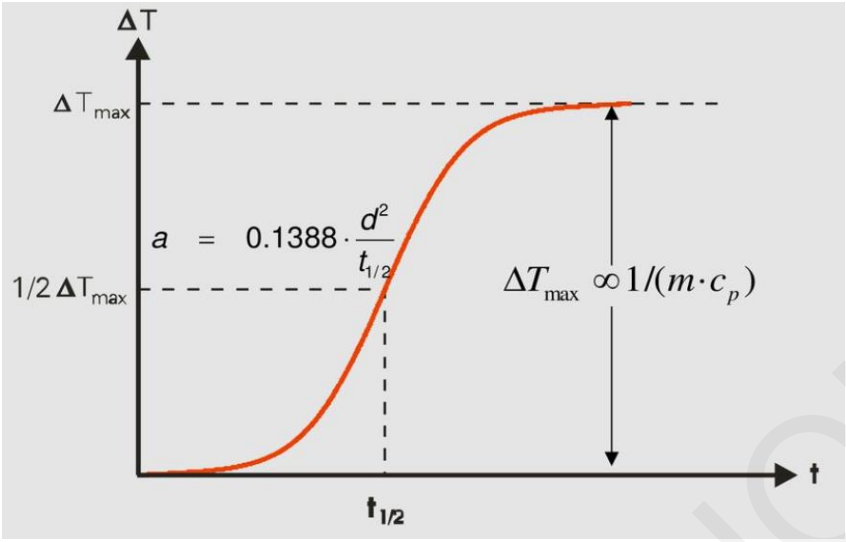

Figure 3.10: Theoretical signal of LFA method.

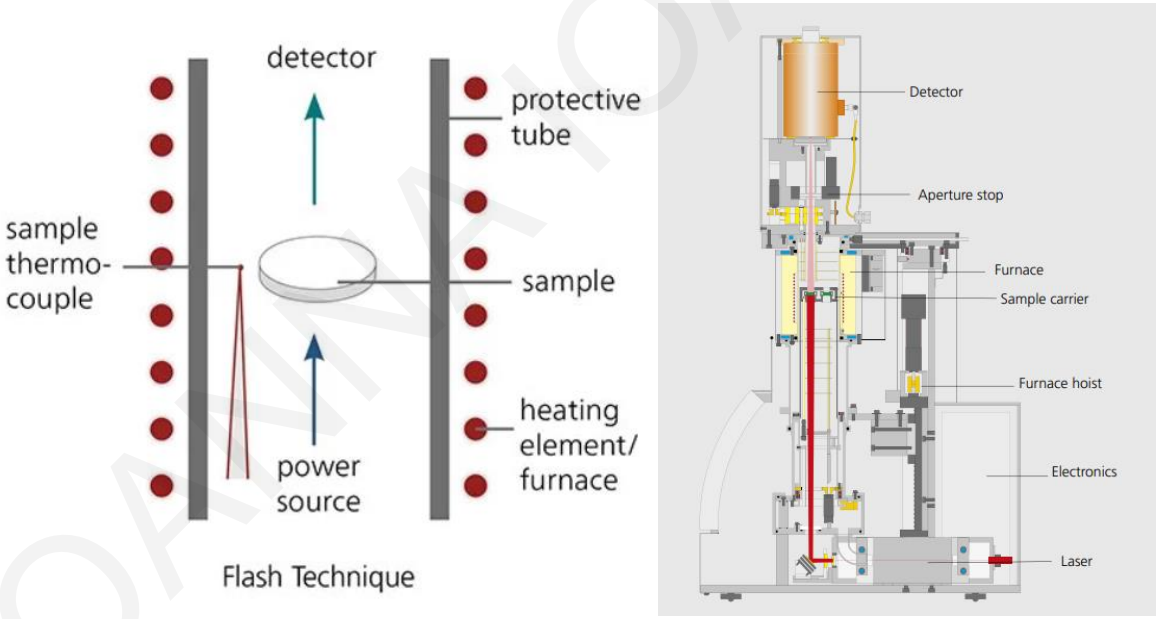

Figure 3.11: Schematic diagram of Laser Flash technique.

4. Results of half-Heusler materials

4.1 Synthesis of MCo(Sb,Sn) (M=Hf,Ti,Zr) via mechanical alloying

As mentioned above, half-Heusler compounds and especially MCoSb and MNiSn (M = Ti, Zr, Hf), have been recently identified as promising thermoelectric materials for medium-high temperature range applications due to their excellent electronic properties and high power-factor. Arc-melting is the typical method used for the synthesis of this family of compounds. However, this time-consuming technique has several disadvantages. For instance, single-phase half-Heusler materials containing low melting point elements such as Sn and Sb, are intrinsically difficult to be produced by using a high temperature synthesis process. Additionally, the ingots must be re-melted several times to ensure homogenous materials and an annealing step is most of the times required [70]–[72].

Solid state reactions at low temperatures can be used to address this problem and eliminate the material loss. Mechanical alloying (MA) is an alternative, single-step and less time-consuming synthesis method, which provides the important possibility of scaling-up and an easy preparation of nano-powders. MA describes the process when mixtures of powders (of different metals or alloys/compounds) are milled together[107] (see Figure 4.1).Interestingly, there are just few recorded attempts synthesizing half-Heusler TiCoSb-based compositions by mechanical alloying and the results were not encouraging enough [87]–[89], [115]. Currently, 20% substitution of Sb by Sn in MCoSb has achieved the best p-type Heusler compounds [41], [63], [71], [75]. Even though, the TiCoSb system was attempted to be synthesized via MA [87], [88], [115], surprisingly the p-type state-of-the-art $MCoSb_{0.8}Sn_{0.2}$ has never been synthesized by this method, while to the best of our knowledge MA has never been applied for highly-efficient half-Heusler compositions.

In this chapter, the synthesis of $MCoSb_{0.8}Sn_{0.2}$ (M=Ti,Zr,Hf) solid solutions via mechanical alloying followed by hot pressing was attempted for the first time and their thermoelectric properties were studied.

4.1.1 Synthesis and consolidation conditions

The milling/synthesis process was carried out in a planetary mill at 450rpm for 6 hours and the ball to material ratio was 15:1. The as-milled powders were loaded in graphite dies and hot-pressed into high density pellets under the same compaction conditions, at temperatures 1160K- 1180K for 1hr under pressure of 50MPa.

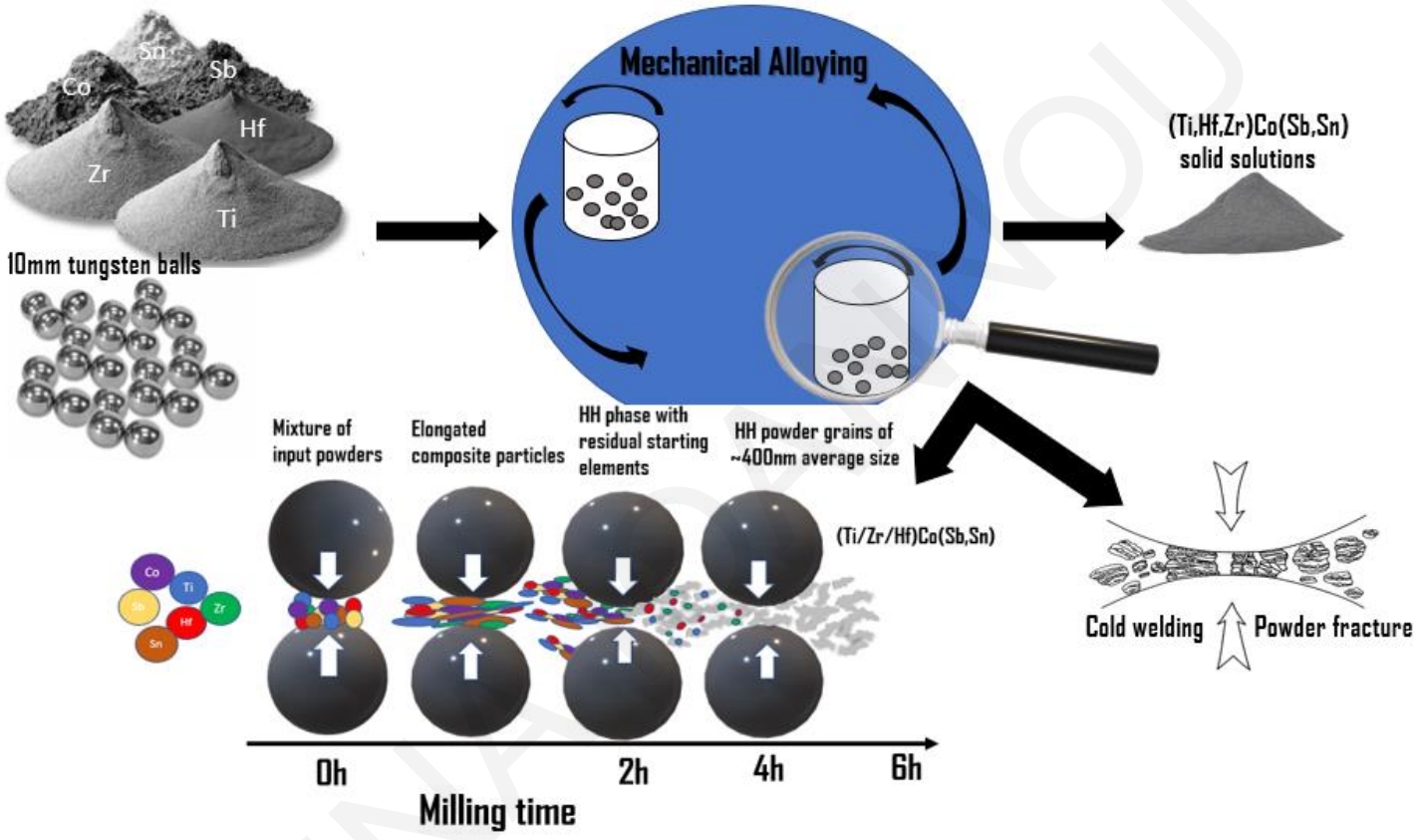

Figure 4.1:Schematic presentation of mechanical alloying method for the synthesis of HH solid solutions

4.1.2 Results of MCo(Sb,Sn)

In this section, the MA synthesis of $MCoSb_{0.8}Sn_{0.2}$ (M=Ti,Hf,Zr) materials and their thermoelectric properties are discussed. This is the first reported attempt to synthesize the p-type state-of-the-art $MCoSb_{0.8}Sn_{0.2}$ (M=Ti,Hf,Zr) system by this method.

Figure 4.1 describes the mechanisms of the technique used; MA. During high-energy milling the powder particles are repeatedly flattened, cold welded, fractured and rewelded. Every time two tungsten balls collide; some amount of powder is trapped in between them. The impact plastically deforms the particles leading to work hardening and fracture. At first, particles of different elements weld together and this leads to an increase in particle size (t<1h). The ductile metal powder particles (Hf, Zr, Co,Sn) get

flattened by the ball-powder-ball collisions, while the brittle particles (Sb,Ti) get fragmented. In the early stages of milling, the particles are still soft (if we are using either ductile-ductile or ductile-brittle material combination), their tendency to weld together and form large particles is high. As a result, a broad range of particle sizes is usually developed. Due to the continued deformation, the particles get work hardened and at some point, fracture. After milling for a certain length of time, steady-state equilibrium is attained when a balance is achieved between the rate of welding and the rate of fracturing. At this stage, each particle contains substantially all of the starting ingredients, in the proportion they were mixed together. The refined microstructural features decrease the diffusion distances while the slight rise in temperature during milling further aids the diffusion behaviour, and consequently, true alloying takes place amongst the constituent elements[107]. In this case, after 2 hours the desired HH phase starts to develop but residual starting elements may also be present. Single-phase (Ti,Zr,Hf)$CoSb_{0.8}Sn_{0.2}$ solid solutions are successfully developed after 4 hours of milling and no change is observed in HH phase for longer milling (up to 8 hours). However, the best thermoelectric properties were reported for samples prepared by 6 hours milling, which are presented in this chapter.

The products of the milling process strongly depend on the milling conditions. Using different ball mills or different conditions of the same ball mill induces different reactions pathways. In general, milling conditions strongly affect the way by which energy is transferred to the milled powder and hence the nature of the final products. For example, the time required for a chemical reaction to be completed decreases with an increase in the ball-to-material ratio, while the ignition time for a combustion reaction decreases with increasing ball diameter[107].

The energy transfer from the mill to the system constituted by the powder, the balls and the vial have been evaluated by theoretical-empirical approach proposed by N. Burgio et al. [116]. According to this study, when a ball is launched, carries an amount kinetic energy. During the first collision event a fraction of this kinetic energy is released. The energy release manifests itself as deformation of the materials and an instant rise of temperature [116]. Figure 4.2 presents the calculated weight-normalized energy transferred to powder as a function of milling time for the MA process of HH system. The transferred energy linearly increases with increasing milling time and reaches the value of 130 kJ/g for 8 hours milling at 450 rpm.

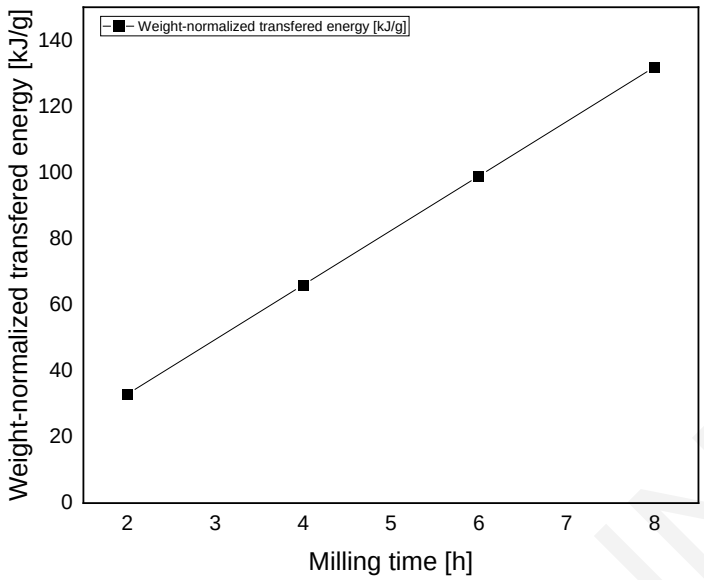

Figure 4.2: Weight-normalized transferred energy as a function of milling time.

Structural characterization:

(Hf/Ti/Zr)$CoSb_{0.8}Sn_{0.2}$ samples were studied using X-ray diffraction method (XRD), scanning electron microscopy (SEM) and energy-dispersive X-ray spectroscopy (EDX). Figure 4.3 illustrates the xrd patterns of hot-pressed samples for different milling times (4,6 and 8 hours), the X-ray diffraction patterns of (Hf/Ti/Zr)$CoSb_{0.8}Sn_{0.2}$ samples prepared by 6 hours of mechanical alloying followed hot-press sintering. The XRD measurements clearly show a successful formation of the desired a cubic half-Heusler phase ($F\bar{4}3$) in all compounds. The lattice parameter based on the XRD diffraction peaks, geometrical density calculations and theoretical density based on Joshi et al. [117] are shown in Table 4.1. Our lattice parameter values agree with theoretical calculations, which predicted the lattice constants to be 0.588, 0.609 and 0.605 nm for TiCoSb, ZrCoSb and HfCoSb, respectively [118].

SEM images and EDS results are presented in Figure 4.4 and Table 4.2, respectively. The back-scattered images illustrate homogeneous single-phase materials. EDS analysis shows that the chemical composition is close to the nominal composition of the samples. There is a small deviation in Hf and Sn percentage. The slight loss of Hf and Sn can be explained by the behavior of these powders that stick on the vial's and balls' surface during milling, resulting in a small deviation from the desired alloy composition. Considering that the relative error of EDS results is ~5% and that there is

an overlap between Sn and Sb in the EDS spectra, all three samples can be considered as nearly stoichiometric and single phase. On the other hand, samples prepared via arc-melting undergo an intrinsic phase separation into two half-Heusler phases. The composition of the matrix (phase I) and a second half-Heusler phase (phase II). For instance, according to EDX results of the arc-melted $TiCoSb_{0.85}Sn_{0.15}$ two different phases were detected: one rich in Ti and Sb ($Ti_{1.07}Co_{0.98}Sb_{0.91}Sn_{0.05}$) and one rich in Sn and Co ($Ti_{0.97}Co_{1.18}Sb_{0.28}Sn_{0.57}$)[72]. As it will be discussed in the following chapters, the phase separation effect is more prominent in HH solid solutions in which isoelectronic substitution is attempted.

Table 4.1: Lattice parameter, theoretical density and measured density of $(Hf/Ti/Zr)CoSb_{0.8}Sn_{0.2}$

Sample	Lattice Parameter α (nm)	Theoretical Density (g/cm³)	Measured Density (g/cm³)
Ti	**0.592**	**7.45**	**6.88**
Hf	**0.608**	**10.73**	**9.96**
Zr	**0.607**	**7.99**	**7.65**

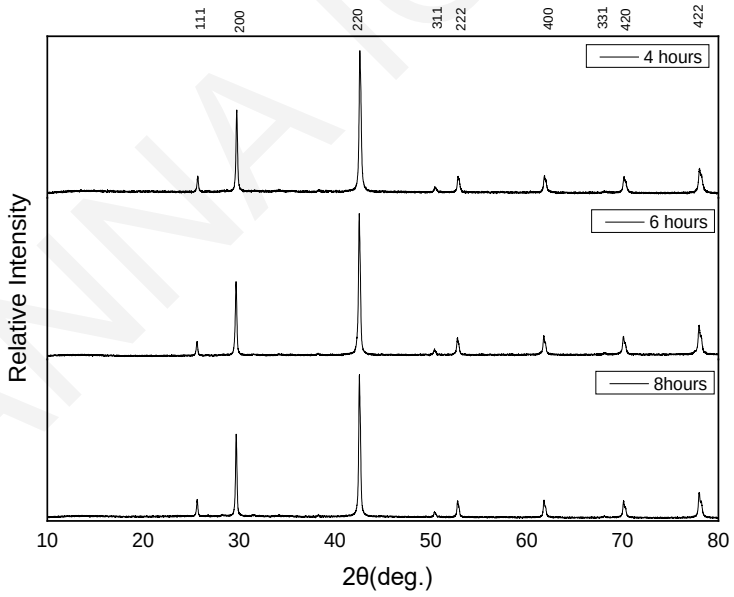

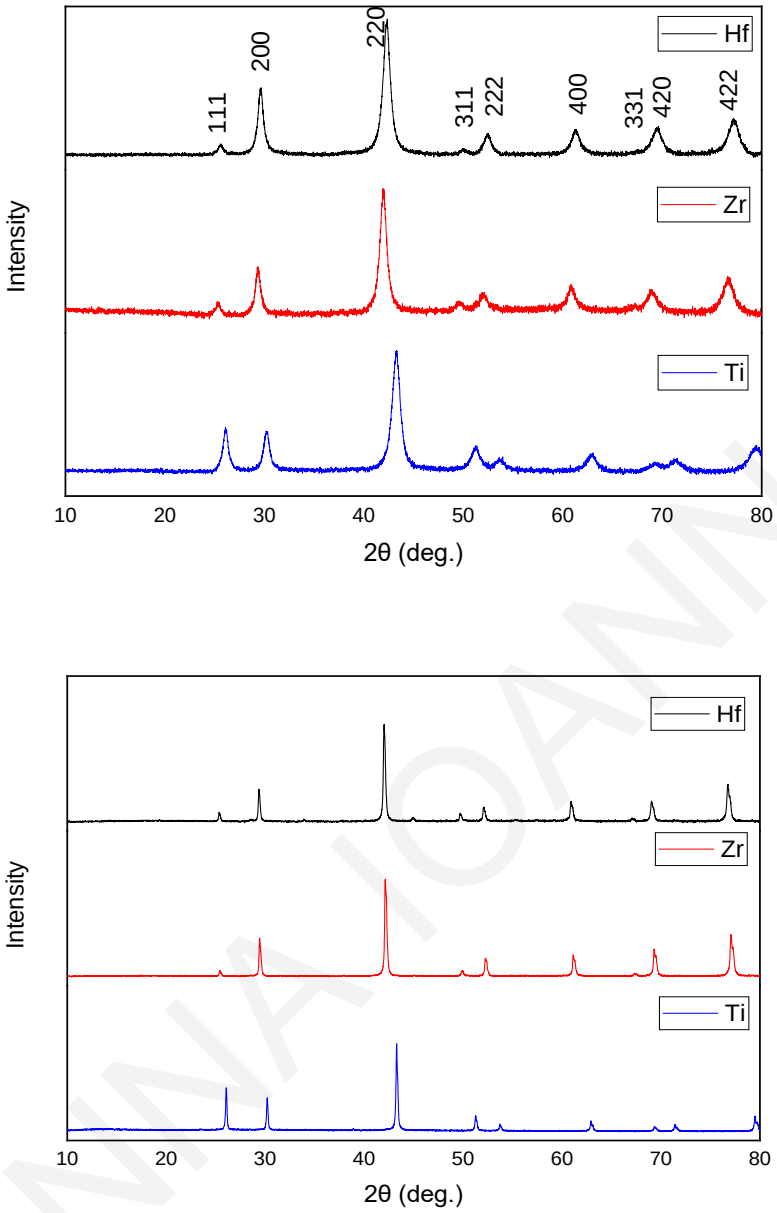

Figure 4.3: a) X-ray diffraction patterns of hot-pressed samples for different milling times (4,6 and 8 hours),b) X-ray powder diffraction patterns of (Hf/Ti/Zr)$CoSb_{0.8}Sn_{0.2}$ powders prepared by 6 hours mechanical alloying and c) the X-ray powder diffraction patterns of hot-pressed (Hf/Ti/Zr)$CoSb_{0.8}Sn_{0.2}$ pellets.

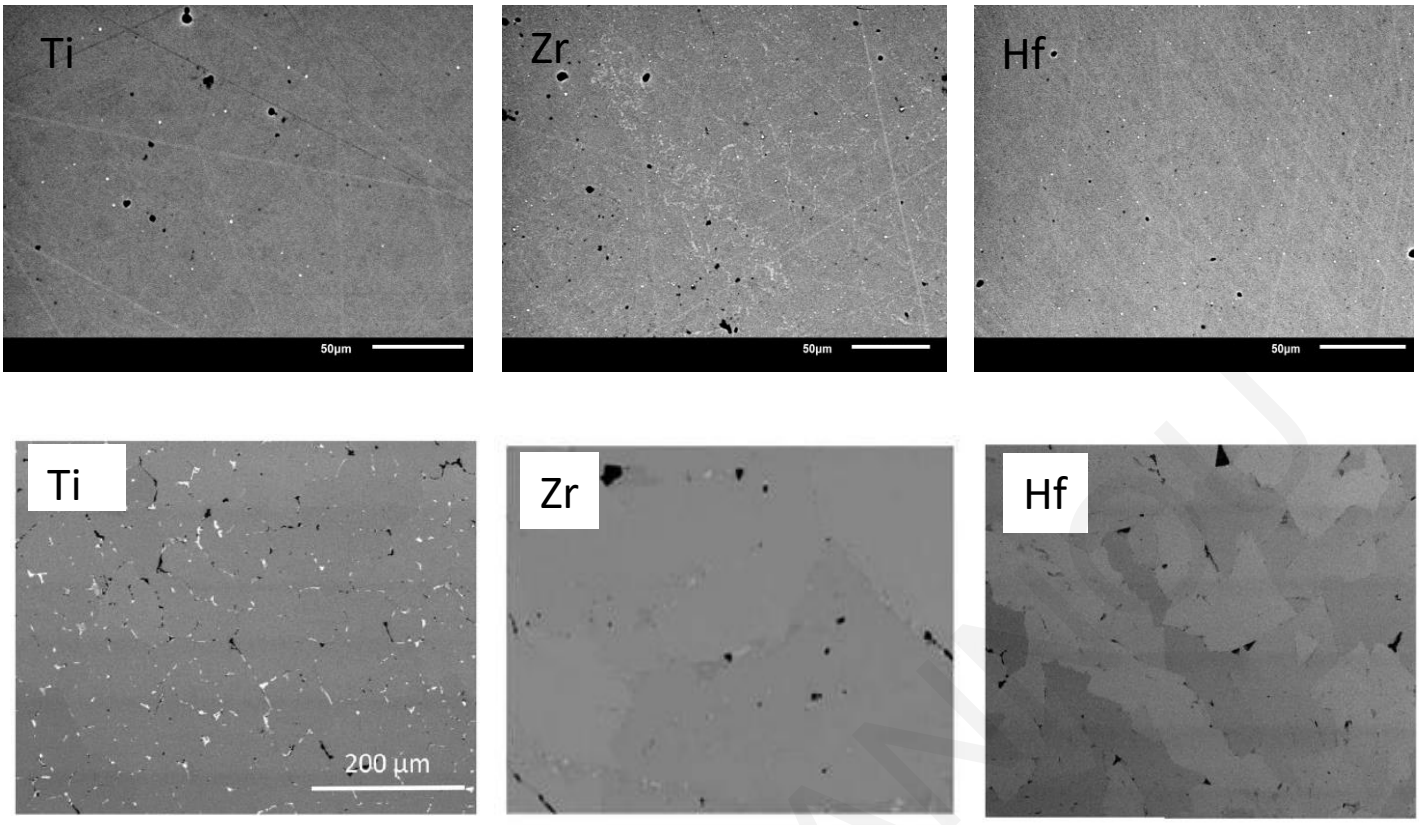

Figure 4.4: Back-scattered electron images of (Ti/Zr/Hf)$CoSb_{0.8}Sn_{0.2}$ samples prepared via MA (a) and back-scattered electron images of (Ti/Zr/Hf)$CoSb_{0.85}Sn_{0.15}$ prepared via arc-melting (reproduced by [70], [72]) (b).

Table 4.2: Chemical composition of (Ti/Zr/Hf)$CoSb_{0.8}Sn_{0.2}$ samples as determined by EDS spectroscopy.

Nominal composition	Area	Hf	Zr	Ti	Co	Sb	Sn
$TiCoSb_{0.8}Sn_{0.2}$	**Overall**	**-**	**-**	**1.09**	**0.99**	**0.81**	**0.11**
$HfCoSb_{0.8}Sn_{0.2}$	**Overall**	**0.95**	**-**	**-**	**1.03**	**0.85**	**0.17**
$ZrCoSb_{0.8}Sn_{0.2}$	**Overall**	**-**	**1.04**	**-**	**0.96**	**0.83**	**0.17**

Thermoelectric properties:

The Seebeck coefficient (S), electrical conductivity (σ) and power factor of the hot-pressed (Hf/Zr/Ti)$CoSb_{0.8}Sn_{0.2}$ samples were determined in the temperature range of 300-960K. The temperature dependence of S, σ and PF are plotted in Figure 4.5 in comparison with values of analogous (Hf/Zr/Ti)$CoSb_{0.8}Sn_{0.2}$ arc-melted samples by E.Rausch et al. [71]. All examined samples present positive S values indicating holes as majority carriers. $TiCoSb_{0.8}Sn_{0.2}$ recorded the highest Seebeck coefficient, S=283μV/K at 780K, whilst $HfCoSb_{0.8}Sn_{0.2}$ and $ZrCoSb_{0.8}Sn_{0.2}$ follow with almost similar S values. The highest S for $ZrCoSb_{0.8}Sn_{0.2}$ is 221μV/K at 960K and for

$HfCoSb_{0.8}Sn_{0.2}$ is 205μV/K at 960K. The analogous arc-melted samples recorded slightly lower S values especially at room temperature. This discrepancy can be explained by the possible loss of Sn, which is a quite soft metal, during milling resulting in lower carrier concentration in MA samples.

The electrical conductivity (σ) measurements are shown in Figure 4.5b. At room temperature, $HfCoSb_{0.8}Sn_{0.2}$ presents the highest electrical conductivity, while $TiCoSb_{0.8}Sn_{0.2}$ presents the lowest electrical conductivity values. The same trend is observed for the arc-melted materials. Interestingly, the electrical conductivity of $HfCoSb_{0.8}Sn_{0.2}$ and $ZrCoSb_{0.8}Sn_{0.2}$ drops with temperature, indicating metal-like behavior. On the other hand, the σ values of $TiCoSb_{0.8}Sn_{0.2}$ increase with temperature, showing a semiconductor-like behavior. The σ values of the arc-melted compositions are higher than those of the mechanically-alloyed materials. This can be attributed to the lower hole mobility in nanostructured materials due to the presence of high-density boundaries which consequently increase the carrier scattering as well as to the possible deviation from the nominal composition due to Sn loss in MA samples resulting in lower carrier concentration.

The calculated power factors ($PF=S^2\sigma$) are presented in Figure 4.5c. The highest power factor was achieved by $HfCoSb_{0.8}Sn_{0.2}$ ($PF= 25\mu W/cmK^2$ at 960K) and it is mainly attributed to its high electrical conductivity. Overall, the arc-melted materials have higher PF due to their higher electrical conductivity values.

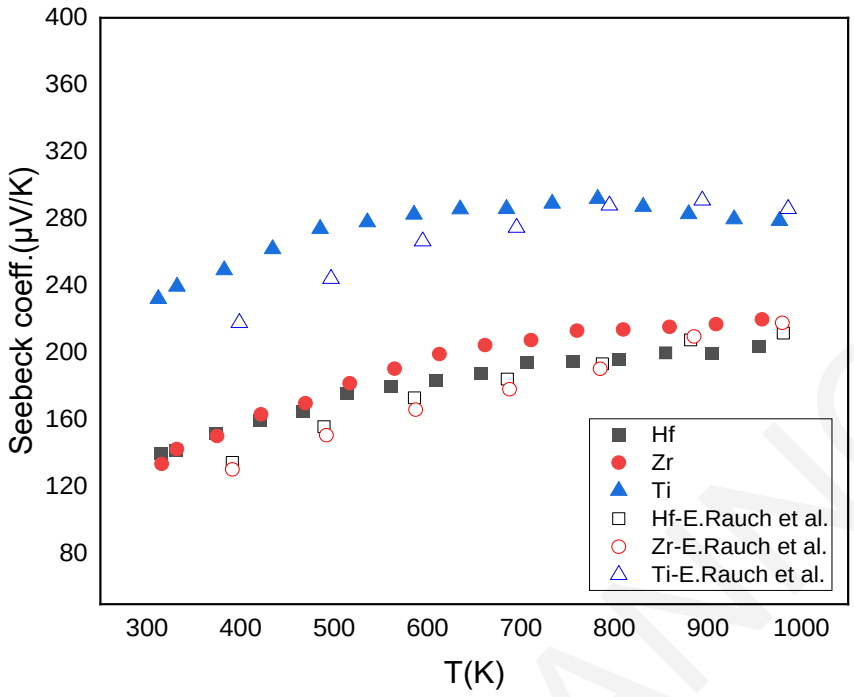

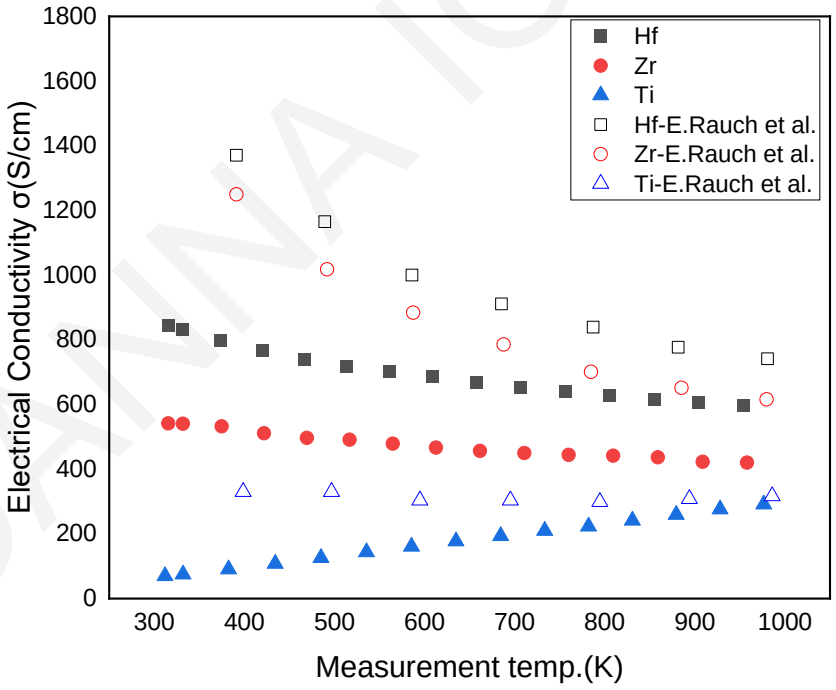

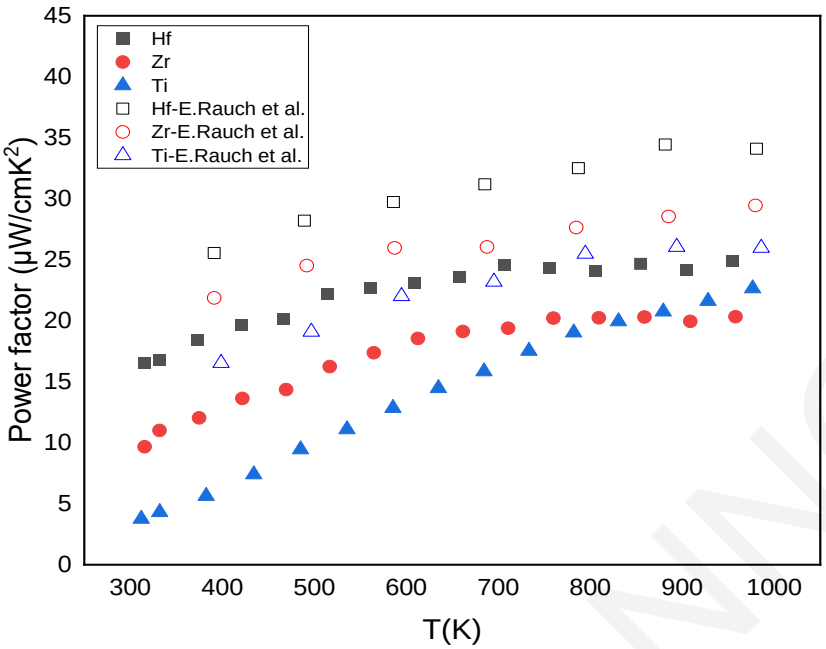

Figure 4.5: Temperature dependent Seebeck coefficient-S (a), electrical conductivity-σ (b) and power factor (PF) of hot-pressed (Hf/Ti/Zr)$CoSb_{0.8}Sn_{0.2}$ samples in comparison with values of analogous arc-melted samples reported by E.Rausch et al [71].

The temperature dependence of the total thermal conductivity and the lattice thermal conductivity of (Hf,Ti,Zr)$CoSb_{0.8}Sn_{0.2}$ samples are plotted in Figure 4.6 The lowest thermal conductivity (κ~ 3.3 W/mK at 960K) was achieved by $HfCoSb_{0.8}Sn_{0.2}$ while $TiCoSb_{0.8}Sn_{0.2}$ and $ZrCoSb_{0.8}Sn_{0.2}$ recorded higher κ values (κ~ 3.8 W/mK at 960K). It is evident that samples prepared via mechanical alloying have lower thermal conductivity than the arc-melted materials. Specifically, the mechanically-alloyed $HfCoSb_{0.8}Sn_{0.2}$ has 39% lower κ in comparison with the same arc-melted sample. This attributed to the lower electronic thermal conductivity (resulting from the decreased σ) as well as the lower lattice thermal conductivity compared to the analogous arc-melted sample. We also observe that the bigger the atom at the M site (Ti<Zr<Hf), the weakest the temperature dependency of thermal conductivity. The thermal conductivity of the mechanically-alloyed $HfCoSb_{0.8}Sn_{0.2}$ presents an almost independent temperature behavior while $ZrCoSb_{0.8}Sn_{0.2,}$ $TiCoSb_{0.8}Sn_{0.2}$ and all arc-melted materials reveal a thermal conductivity that drops with temperature. A theoretical analysis by Joshi et. al [118] predicted that TiCoSb should have higher thermal conductivity than ZrCoSb and HfCoSb. The difference in the contribution to the phonon DOS by different atoms

occurs due to the difference of mass of the atoms. A heavier atom contributes to the low modes of frequencies while a light atom contributes to the higher ones. According to this study, ZrCoSb and HfCoSb show a mixing of the acoustic (low) modes with the optical (high) modes of phonons, which indicates increased phonon-phonon scattering and reduced lattice thermal conductivity [118].

To gain a better understanding of how different elements (Ti,Zr,Hf) in M position affect the heat transport in $MCoSb_{0.8}Sn_{0.2}$ materials, the lattice thermal conductivity was estimated. Thermal conductivity is the sum of two contributions, one due to phonons and the other due to charge carriers. The electronic contribution, κ_e was calculated by the electrical conductivity σ by using Wiedemann-Franz's law $\kappa_e = L\sigma T$ and the Lorentz factor was calculated from Seebeck coefficient values:

$$L = \left[1.5 + \exp\left[-\frac{|S|}{116}\right]\right] x10^{-8} W\Omega K^{-2} ,$$

as proposed by Kim et al [12]. The lattice thermal conductivity (κ-κ_e) was estimated by subtracting κ_e from κ. From the presented figures, it is obvious that the lattice thermal conductivity ($\kappa_{lattice}$) has the major contribution in total thermal conductivity and follows almost the same trends with κ. The lattice thermal conductivity of $TiCoSb_{0.8}Sn_{0.2}$ and $HfCoSb_{0.8}Sn_{0.2}$ samples prepared via mechanical alloying are significantly lower than those of similar samples prepared via arc-melting. This reduction in $\kappa_{lattice}$ can be attributed to the effective scattering of phonons at the grain boundaries in nanostructured materials. On the other hand, $ZrCoSb_{0.8}Sn_{0.2}$ presents identical lattice thermal conductivity for both methods. However, the previously discussed impressive reduction of lattice thermal conductivity suggests that mechanical alloying can be consider as an effective method for the fabrication of HH solid solutions and can be further explored in different compositions; especially for the isoelectric substitution at the M site of $MCoSb_{0.8}Sn_{0.2,}$ which is expected to cause even lower thermal conductivity values.

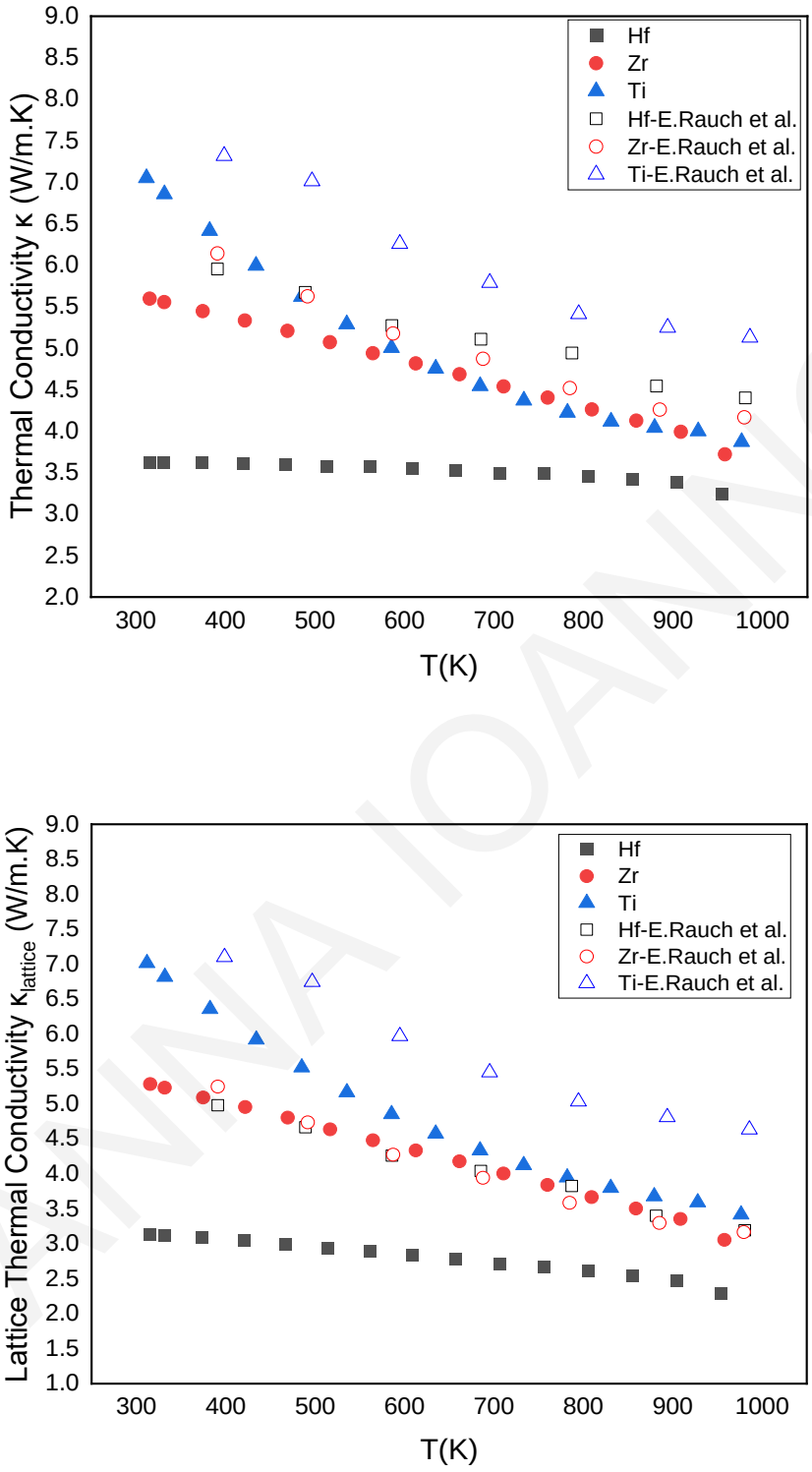

Figure 4.6: Temperature dependent thermal conductivity-κ (a) and lattice thermal conductivity-$\kappa_{lattice}$ (b) of hot-pressed (Hf/Ti/Zr)$CoSb_{0.8}Sn_{0.2}$ samples in comparison with values of analogous arc-melted samples reported by E.Rausch et al [71].

The thermoelectric figure-of-merit (ZT) is shown in Figure 4.7 as a function of temperature. Despite the lower PF of the mechanically alloyed materials, a relatively good ZT was achieved for all three samples due to their low thermal conductivity values. The highest ZT~0.74 at 960K was recorded by $HfCoSb_{0.8}Sn_{0.2}$. $TiCoSb_{0.8}Sn_{0.2}$ and $ZrCoSb_{0.8}Sn_{0.2}$ prepared via MA reached almost identical ZTs, near 0.55 at 960K.

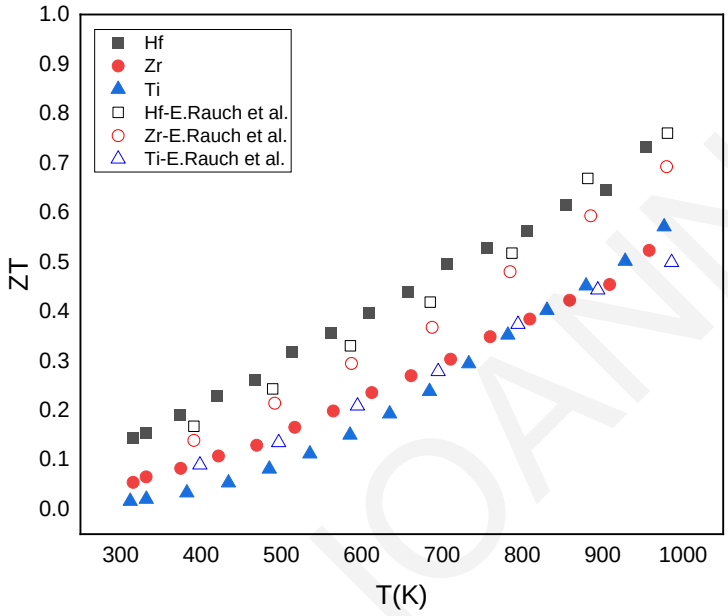

Figure 4.7: Thermoelectric figure of merit-ZT as a function of temperature of hot-pressed (Hf/Ti/Zr)$CoSb_{0.8}Sn_{0.2}$ samples in comparison with values of analogous arc-melted samples reported by E.Rausch et al [71].

4.1.3 Conclusion

In this chapter, single-phase $MCoSb_{0.8}Sn_{0.2}$ (M=Ti,Zr,Hf) materials were successfully synthesized via mechanical alloying followed by hot-pressing for the first time and their thermoelectric properties were studied and compared with similar arc-melted solid solutions. Materials prepared via MA had similar Seebeck coefficient values but lower electrical conductivity values than the arc-melted materials. However, the low thermal conductivity of the nanostructured mechanically-alloyed solid solutions contributed in achieving a relatively good ZT for all three compositions. The highest ZT~0.74 at 960K was recorded for $HfCoSb_{0.8}Sn_{0.2}$. The successful application of MA method for the fabrication of HH solid solutions with low lattice thermal conductivity values indicates that it is worthwhile to further explore this technique in more complicated HH compositions.

4.2 (Hf,Ti)Co(Sb,Sn) solid solutions

The high lattice thermal conductivity of HH compounds is one of the main obstacles in achieving a high thermoelectric performance. There are several works pointing out that the Ti/Hf combination is more effective in increasing the alloy scattering and reducing the lattice thermal conductivity than the Zr/Hf combination, due to larger differences in the atomic size and mass of Hf and Ti in p-type (Hf,Ti,Zr)CoSb solid solutions [74][70][72].

In this chapter, the synthesis of (Hf,Ti)Co(Sb,Sn) solid solutions via mechanical alloying followed by hot pressing was attempted and their thermoelectric properties were studied. At first, $Hf_xTi_{1-x}CoSb_{0.8}Sn_{0.2}$ (0, 0.2, 0.4, 0.6, 0.8) samples were prepared to investigate the effect of isoelectronic substitution. Then, the effect of charge carrier concentration was investigated by preparing $Hf_{0.6}Ti_{0.4}CoSb_{1-y}Sn_y$ samples in order to evaluate the effect of Sn/Sb doping on the thermoelectric properties.

4.2.1 Synthesis and consolidation conditions

The milling/synthesis process was carried out in a planetary mill at 450rpm and the ball to material ratio was 15:1. Different milling times (2,4,6 and 8 hours) were tested. The as-milled powders were loaded in graphite dies and hot-pressed into high density pellets under the same compaction conditions, at temperature 1180K for 1 hour under pressure of 50MPa.

4.2.2 Results of (Hf,Ti)$CoSb_{0.8}Sn_{0.2}$ Solid Solution Series

In this section, the MA synthesis of $Hf_xTi_{1-x}CoSb_{0.8}Sn_{0.2}$ (0, 0.2, 0.4, 0.6, 0.8) materials and the effect of Ti substitution with its heavier homologue Hf on their microstructure and thermoelectric properties are discussed. This is the first reported attempt to synthesize the p-type $Hf_xTi_{1-x}CoSb_{0.8}Sn_{0.2}$ system by this method.

Structural Characterization:

$Hf_xTi_{1-x}CoSb_{0.8}Sn_{0.2}$ samples were studied using X-ray diffraction method (XRD), scanning electron microscopy (SEM) and energy-dispersive X-ray spectroscopy (EDX). Figure 4.8a presents the powder X-ray diffraction patterns of the $Hf_xTi_{1-x}CoSb_{0.8}Sn_{0.2}$ series for different milling times. The half-Heusler phases were observed after only 2 hours of milling. However, small impurity peaks revealed the presence of residual Hf. After 4 hours of milling the desired half-Heusler phases were completely formed and no residual starting elements or other secondary phases were detected while there were no further changes for longer milling. Therefore, for the preparation of

$Hf_xTi_{1-x}CoSb_{0.8}Sn_{0.2}$ (0, 0.2, 0.4, 0.6, 0.8) samples was based on 4 hours alloying followed by hot press sintering. Figure 4.8b illustrates the X-ray diffraction patterns of $Hf_{1-x}Ti_xCoSb_{0.8}Sn_{0.2}$ samples after hot-pressing. The XRD measurements Figure 4.8b clearly show a cubic half-Heusler phase ($F\bar{4}3$) in all compounds. A careful examination revealed that the main reflection (220) shifts to a lower scattering angle with increasing Hf, suggesting that Hf replaces Ti and therefore the lattice parameter increases, following Vegard's law Figure 4.8c and d. The lattice parameter based on the XRD diffraction peaks, geometrical density calculations and theoretical density based on Joshi et al. [117] are shown in Table 4.3. Our calculations agree with a previous study on nanostructured arc-melted $Hf_{1-x}Ti_xCoSb_{0.8}Sn_{0.2}$ materials[74].

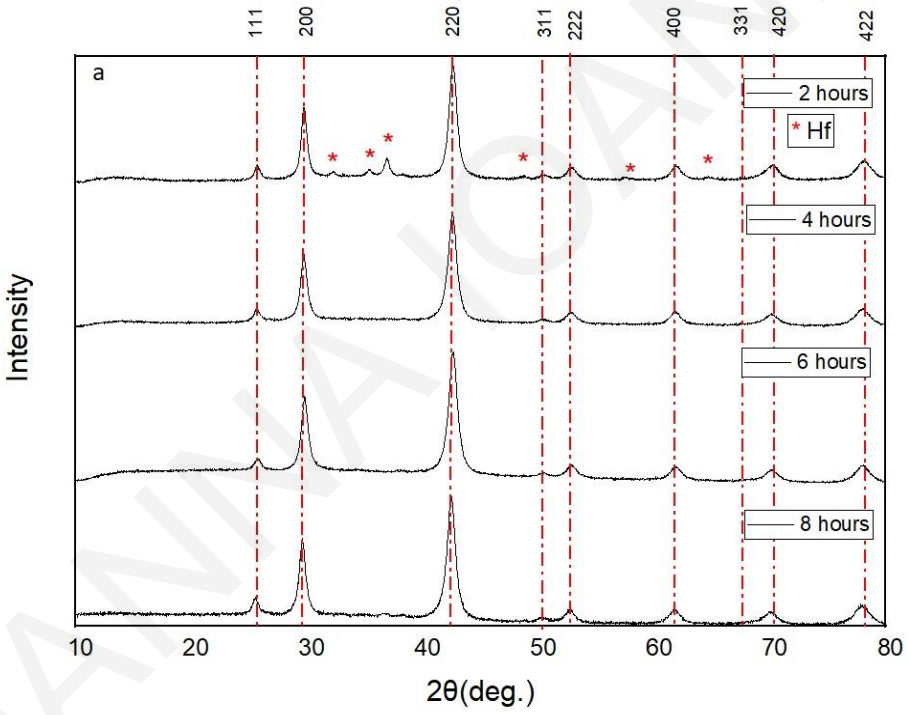

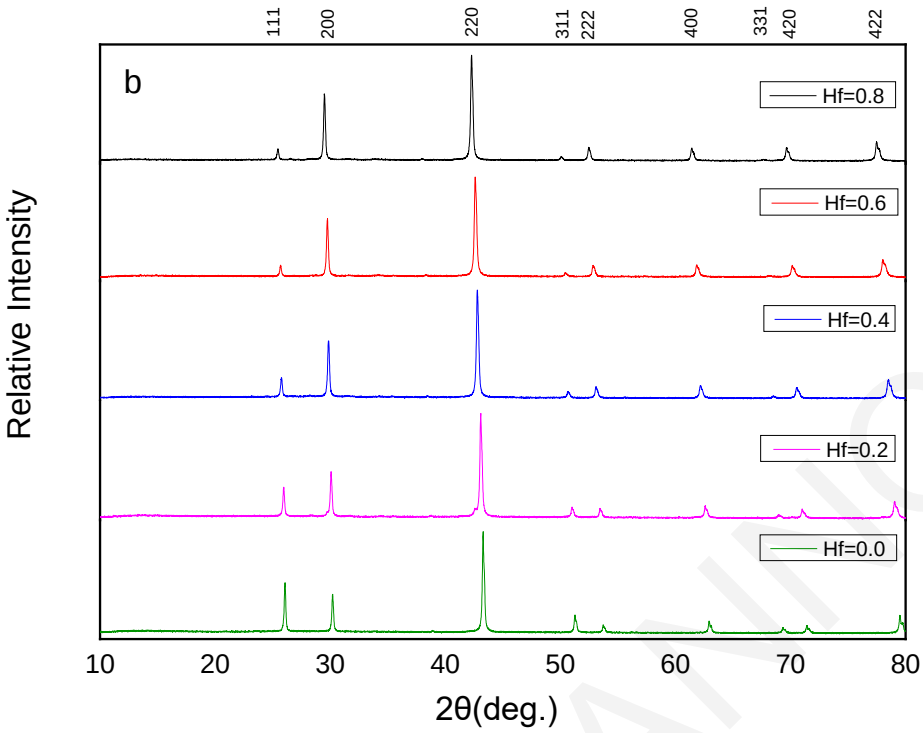

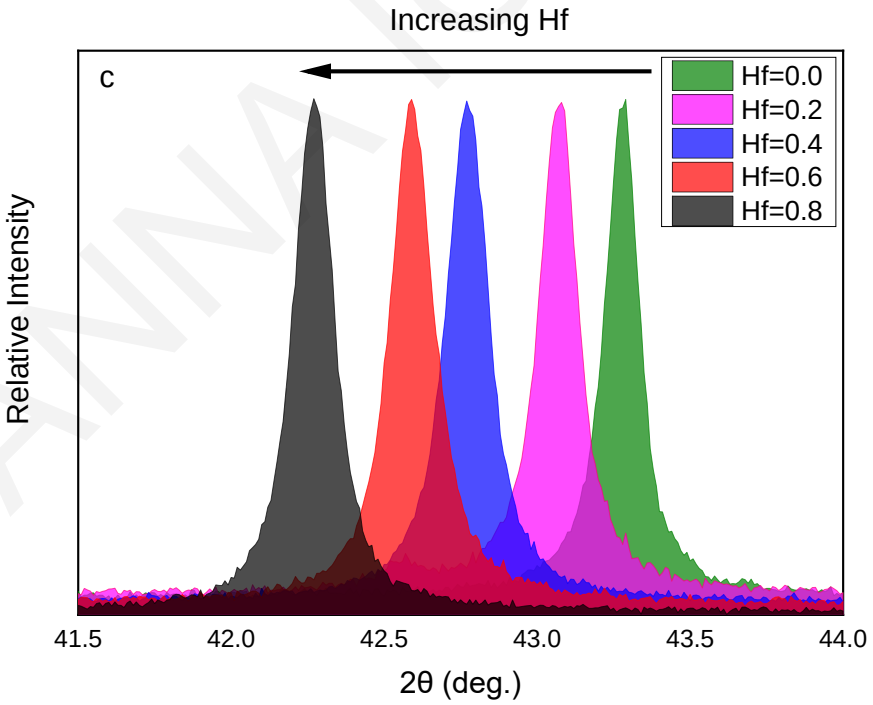

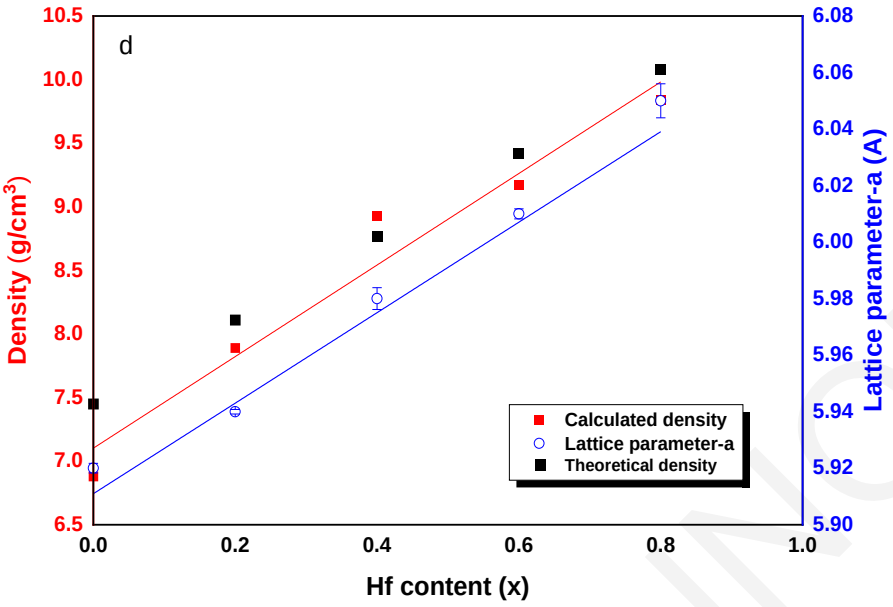

Figure 4.8: a) X-ray powder diffraction patterns of $Hf_xTi_{1-x}CoSb_{0.8}Sn_{0.2}$ powders prepared by 2,4,6 and 8 hours mechanical alloying b) the X-ray powder diffraction patterns of hot-pressed $Hf_xTi_{1-x}CoSb_{0.8}Sn_{0.2}$ pellets, c) the main (220) reflection of Hf_xTi_{1-x} $CoSb_{0.8}$ $Sn_{0.2}$ and d) the lattice parameter and the density of the pellets as a function of Hf content (x).

Table 4.3: Lattice parameter, pellet density and theoretical density of $Hf_xTi_{1-x}CoSb_{0.8}Sn_{0.2}$ samples.

Hf (x)	Lattice Parameter-α (nm)	Measured Density (g/cm^3)	Theoretical Density (g/cm^3)
0.00	0.592	6.88	7.45
0.20	0.594	7.89	8.11
0.40	0.598	8.93	8.77
0.60	0.601	9.17	9.42
0.80	0.605	9.84	10.08

SEM images and EDS results are presented in Figure 4.9 and Table 4.4, respectively. Back-scattered images of Hf=0, 0.2, 0.4, 0.6, 0.8 samples illustrate homogeneous single-phase materials. EDS analysis shows that the chemical composition is close to the nominal composition of the samples. The slight loss of Hf can be explained by the behavior of Hf powder during milling that sticks on the surface of the vial and balls resulting a small deviation from the desired alloy composition. Considering that the relative error of EDS results is ~5% and that there is an overlap between Sn and Sb in the EDS spectra, the samples can be considered as nearly stoichiometric and single phase. These results are in contrast to similar structural investigations of analogous arc-melted $Ti_{1-x}Hf_xCoSb_{0.85}Sn_{0.15}$ compounds, which revealed the presence of several HH phases with slightly different lattice parameters [72] (Fig. 4.10). A splitting of the main xrd reflection into a triple peak has also been reported for the n-type $Ti_{0.5}Zr_{0.25}Hf_{0.25}NiSn$, indicating that phase-separation effect is common in both n-type and p-type half-Heusler solid solutions prepared by arc-melting [64].

Table 4.4: Nominal and chemical composition of hot-pressed $Hf_xTi_{1-x}CoSb_{0.8}Sn_{0.2}$ samples as determined by EDS spectroscopy.

Nominal Composition (at%)	**SEM/EDS Composition (at%)**				
	Hf	**Ti**	**Co**	**Sb**	**Sn**
$TiCoSb_{0.8}Sn_{0.2}$	**-**	**1.03**	**1.06**	**0.73**	**0.19**
$Hf_{0.2}Ti_{0.8}CoSb_{0.8}Sn_{0.2}$	**0.16**	**0.81**	**1.07**	**0.74**	**0.22**
$Hf_{0.4}Ti_{0.6}CoSb_{0.8}Sn_{0.2}$	**0.35**	**0.62**	**1.07**	**0.72**	**0.24**
$Hf_{0.6}Ti_{0.4}CoSb_{0.8}Sn_{0.2}$	**0.54**	**0.41**	**1.08**	**0.76**	**0.20**
$Hf_{0.8}Ti_{0.2}CoSb_{0.8}Sn_{0.2}$	**0.78**	**0.23**	**1.06**	**0.75**	**0.18**

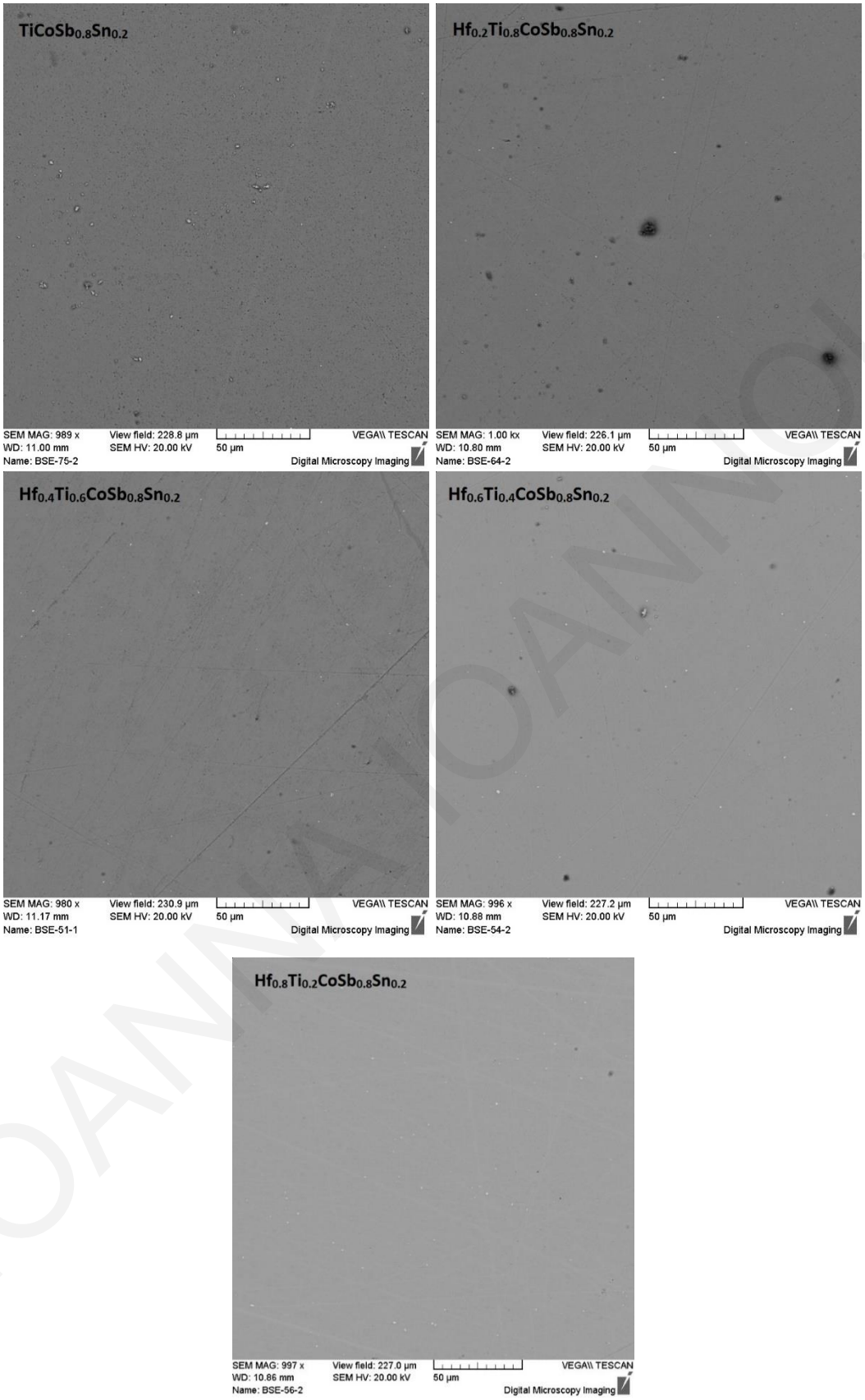

Figure 4.9: Back-scattered electron images of hot-pressed $Hf_xTi_{1-x}CoSb_{0.8}Sn_{0.2}$ samples.

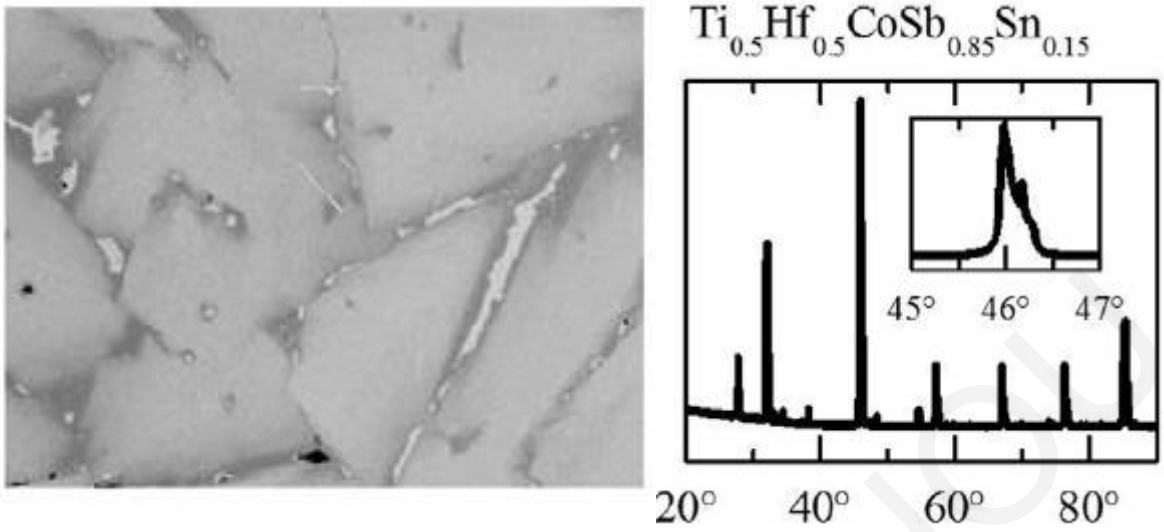

Figure 4.10: Back-scattered electron image of the arc-melted $Hf_{0.5}Ti_{0.5}CoSb_{0.85}Sn_{0.15}$ sample and splitting of the main XRD peak revealing the presence of phase-separation [72].

Thermoelectric Properties:

The temperature dependent electrical conductivity, Seebeck coefficient and Power factor ($S^2\sigma$) of the hot-pressed $Hf_xTi_{1-x}CoSb_{0.8}Sn_{0.2}$ samples in comparison with that of arc-melted $Hf_{0.8}Ti_{0.2}CoSb_{0.8}Sn_{0.2}$[74] are presented in Figure 4.11. The S values of all hot-pressed samples are positive indicating a p-type conduction behaviour. The highest value of 292μV/K was observed for TiCoSb0.8Sn0.2 at 780K and decreased with Hf. Although the replacement of Ti with Hf is an isoelectronic substitution, there is a sharp suppression of S values when Hf is added to the composition and this can be attributed to the change of electronic structure which consequently affects the carrier concentration and their effective mass [72]. Moreover, the Seebeck coefficient of samples with Hf=0.0 and Hf=0.2 raises with increasing temperature, reaches a peak value at around 780K and then starts to decrease, suggesting the onset of bipolar conduction. On the other hand, the S values of samples with higher Hf content, increase with temperature and stabilize above 750K. In the temperature range of 300-800 K, $Hf_{0.8}Ti_{0.2}CoSb_{0.8}Sn_{0.2}$ [74] by X.Yan et al. showed lower S values in comparison with our $Hf_{0.8}Ti_{0.2}CoSb_{0.8}Sn_{0.2}$ sample.

Interestingly, the electrical conductivity increases with increasing temperature due to the relatively low doping level of these materials. However, the aforementioned Seebeck coefficient does not significantly decrease with intrinsic excitation suggesting the existence of additional mechanism that affects the electrical conductivity. This

mechanism can be related to the enhanced grain boundary scattering that appears in nanostructured materials resulting in a "thermally activated mobility". This effect has been discussed in other thermoelectric systems, such as Mg_3Sb_2–Mg_3Bi_2 solid solution and $NaPb_mSbQ_{m+2}$ (Q = S, Se, Te) [119]–[121]. The replacement of Ti with Hf resulted an increase in electrical conductivity, probably due to an enhancement of carrier concentration and mobility. Specifically, electrical conductivity roughly increases from Hf=0.0 to Hf=0.4 and then stabilizes for samples with Hf ≥0.4. The σ alteration with changing Ti/Hf ratio is attributed to the change of electronic structure which consequently affects the carrier concentration and effective mass of charge carriers [72]. However, electrical conductivity investigations of most of the analogous arc-melted $(Ti,Hf)CoSb_{0.8}Sn_{0.2}$ and $(Ti,Hf,Zr)CoSb_{0.8}Sn_{0.2}$ samples showed a metallic behaviour and higher values compare to our samples [63], [72], [74], [75]. The difference is smaller at higher temperatures[74]. Moreover, Hu et. al mentioned that the electrical conductivity of $Zr_{0.5}Hf_{0.5}CoSb_{1-x}Sn_x$ samples prepared via levitation melting exhibit a metal-like behaviour and follow a typical $T^{-0.5}$ exponent relationship, suggesting that the alloying scattering in HH arc-melted materials might be the dominant scattering mechanism of charge carrier[82]. In contrast to that, Culp et al. reported that the temperature dependence of the resistivity of similar arc-melted $Zr_{0.5}Hf_{0.5}CoSb_{1-x}Sn_x$ compounds was found to be semi-metallic or degenerate semiconductor behaviour [61].

The calculated Power factors ($PF=S^2\sigma$) are presented in Figure 4.11 (c). Despite the low electrical conductivity of $TiCoSb_{0.8}Sn_{0.2}$, the high Seebeck coefficient contributed in achieving the highest PF= 22.7 $\mu W/K^2cm$ at 980K. The second highest PF= 21.6 $\mu W/K^2cm$ was obtained for $Hf_{0.8}Ti_{0.2}CoSb_{0.8}Sn_{0.2.}$ This value is lower than that of the arc-melted $Hf_{0.8}Ti_{0.2}CoSb_{0.8}Sn_{0.2}$ (PF= 25.7 $\mu W/K^2cm$ at 1073K) by X. Yan et al. due to its lower electrical conductivity [74].

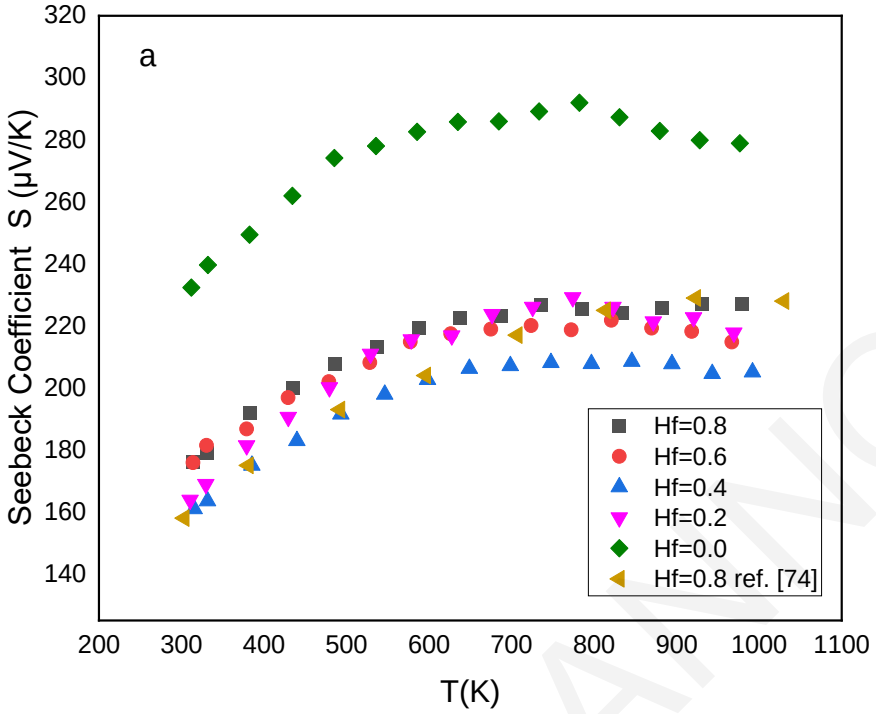

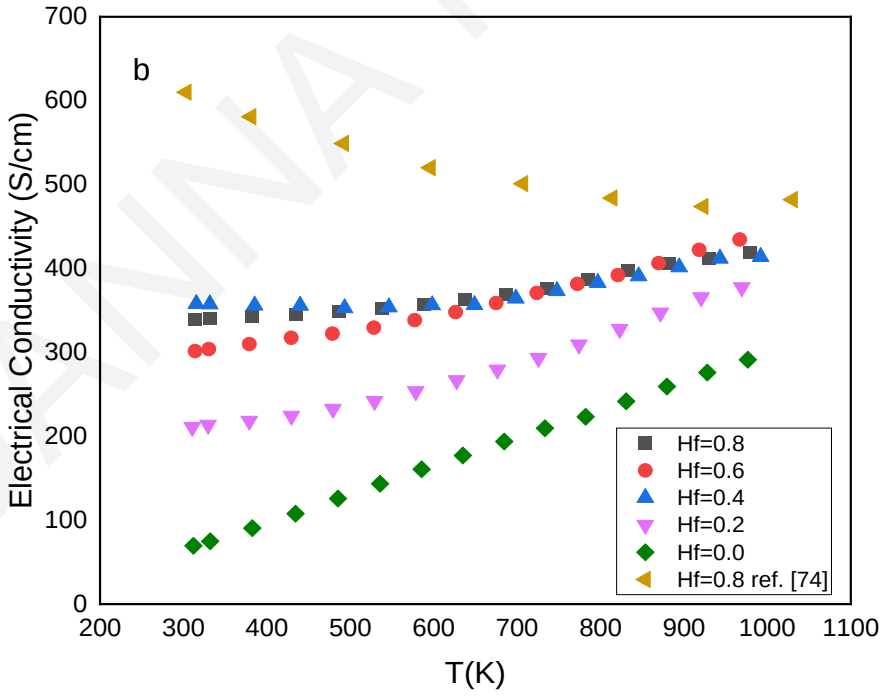

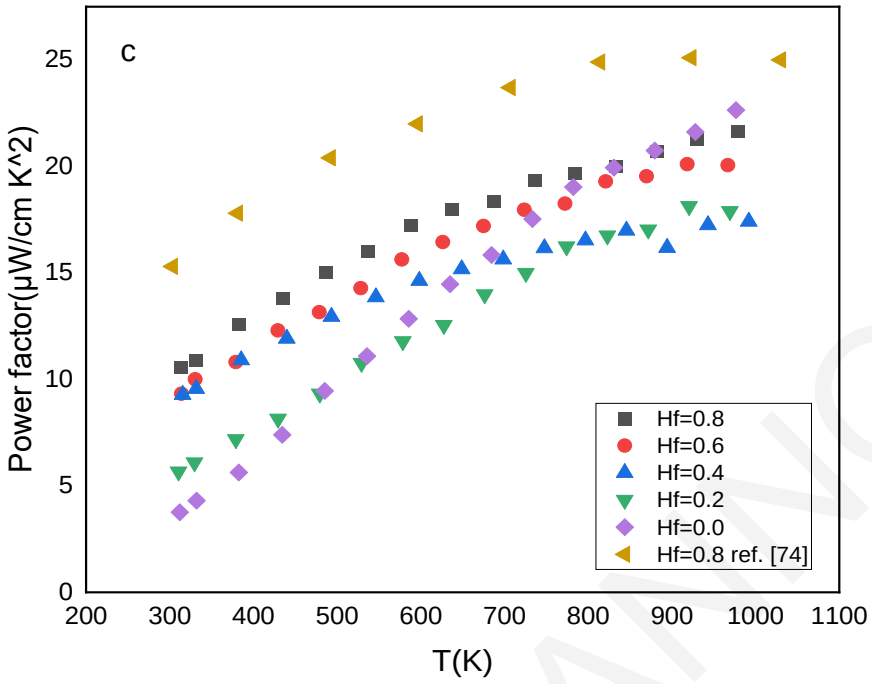

Figure 4.11: a) Seebeck coefficient S b) Electrical conductivity σ and c) Power Factor PF as a function of temperature for hot-pressed $Hf_xTi_{1-x}CoSb_{0.8}$ $Sn_{0.2}$, synthesized by mechanical alloying and arc-melted $Hf_{0.8}Ti_{0.2}CoSb_{0.8}$ $Sn_{0.2}$ [74]

The temperature dependence of the total thermal conductivity and the lattice thermal conductivity of $Hf_xTi_{1-x}CoSb_{0.8}Sn_{0.2}$ samples are plotted in Figure 4.12. It is evident that the κ values of samples containing both Hf and Ti have minor differences and are much lower than the thermal conductivity values of $TiCoSb_{0.8}Sn_{0.2}$, as expected. The lowest thermal conductivity with a value of 2.29 W/mK was achieved by $Hf_{0.4}Ti_{0.6}CoSb_{0.8}Sn_{0.2}$ at 971K. Similar trends were observed in previously reported arc-melted $Ti_{1-x}Hf_xCoSb_{0.85}Sn_{0.15}$ compounds[72].

The electronic thermal conductivity (κ_e) and consequently the lattice thermal conductivity ($\kappa_{lattice}$) were again calculated as in chapter 4.1. The electronic thermal conductivity values increased upon replacement of Ti with the heavier Hf, because of an increase in the electrical conductivity. It is worth mentioning that the conventional Wiedemann-Franz's law often leads to an overestimation of the lattice contribution, especially when it is applied for materials with high nanocrystallinity and resistive

grain-boundaries. The fundamental cause of this overestimation is mainly attributed to the conventional assumption of sample homogeneity, which treats electrons and phonons as independent channels of heat transport [122].

From the Figure 4.12, it is obvious that the major contribution in the total thermal conductivity originates from the lattice part. It is remarkable that the lattice thermal conductivity of the Hf/Ti solid solutions are almost three times lower than the $TiCoSb_{0.8}Sn_{0.2}$, indicating that the Hf/Ti combination significantly contributes to the reduction of the phonon mean free path as expected, by creating defect scattering for phonons due to mass differences and strain field variations. At room temperature (Figure 4.12c), the lattice thermal conductivity decreases with increasing Hf from 0% to 60 % and then for $Hf_{0.8}Ti_{0.2}CoSb_{0.8}Sn_{0.2}$ (Hf=80%) slightly increases, as expected. Specifically, $Hf_{0.6}Ti_{0.4}CoSb_{0.8}Sn_{0.2}$ exhibits the lowest lattice thermal conductivity at room temperature which is 65% lower than the $TiCoSb_{0.8}Sn_{0.2}$ sample. This minimal lattice thermal conductivity ($\kappa_{lattice}$=1.6 W/m·K at 970K) suggests that the $Hf_{0.6}Ti_{0.4}CoSb_{0.8}Sn_{0.2}$ composition would be a good selection for further studies in terms of the thermoelectric figure-of-merit.

Lattice thermal conductivity arises from several phonon scattering processes like grain boundary scattering, point defect scattering, scattering on dislocations, and Umklapp scattering processes [123]. In solid solutions, the point defect scattering originates from the mass and strain field fluctuations. Based on Slack's [124] and Abeles' [125] models, the disorder scattering parameter Γ describes the point defect scattering of phonons and it has two components: the scattering parameter due to mass fluctuations Γ_M and the scattering parameter due to strain field fluctuations Γ_S ($\Gamma=\Gamma_M+\Gamma_S$)[125]. The Γ parameter (Figure 4.12d) was calculated based on the following equations[45]:

$$\Gamma_M = \frac{\sum_{i=1}^{n} c_i \left(\frac{\overline{M_i}}{\overline{M}}\right)^2 \Gamma_M^i}{\sum_{i=1}^{n} c_i}, \quad \Gamma_S = \frac{\sum_{i=1}^{n} c_i \left(\frac{\overline{M_i}}{\overline{M}}\right)^2 f_i^1 f_i^2 \varepsilon_i \left(\frac{r_i^1 - r_i^2}{\overline{r_i}}\right)^2}{\sum_{i=1}^{n} c_i}$$

where the mass fluctuation parameter for the i_{th} sublattice is:

$$\Gamma_M^i = \sum_k f_k \left(1 - \frac{M_i^k}{\overline{Mi}}\right)^2$$

The k^{th} atom of the i^{th} sublattice has mass M_i^k, radius r_i^k and fractional occupation f_i^k. The average mass and radii of atoms on the i^{th} sublattice is given by:

$$\overline{M_i} = \sum_k f_i^k M_i^k, \quad \overline{r_i} = \sum_k f_i^k r_i^k$$

The average atomic mass of the compound is:

$$\overline{\overline{M}} = \frac{\sum_{i=1}^{n} c_i \ \overline{M_i}}{\sum_{i=1}^{n} c_i}$$

Where, c_i are the relative degeneracies of the respective sites (For instance, in TiCoSb $c_1=c_2=c_3=1$). The parameter ε_i is a phenomenological parameter, which characterizes the anharmonicity of the lattice and normally ranges from 10 to 100.

If we only consider the isoelectronic alloying of M-sites in half-Heusler compounds, Γ can be simply written as [46]:

$$\Gamma = \frac{1}{3}\left(\frac{\overline{M_i}}{\overline{\overline{M}}}\right)^2 \left[\sum_k f_k \left(1 - \frac{M_i^k}{\overline{Mi}}\right)^2 + \varepsilon \sum_k f_k \left(1 - \frac{r_i^k}{\overline{ri}}\right)^2\right]$$

In Figure Figure 4.12d, the results from the Γ parameter calculations are presented as a function of Hf concentration. Γ sharply increases with increasing Hf percentage up to 40% and then gradually decreases for higher percentages. It is also confirmed that the decreased mass fluctuation (Γ_M is significantly higher than Γ_S) is the main reason for the $\kappa_{lattice}$ reduction. High Γ suggests higher scattering for phonons and therefore lower lattice thermal conductivity. The experimental results of the lattice thermal conductivity, which revealed lower values for H=0.6 and Hf=0.4, agree with the previous calculations.

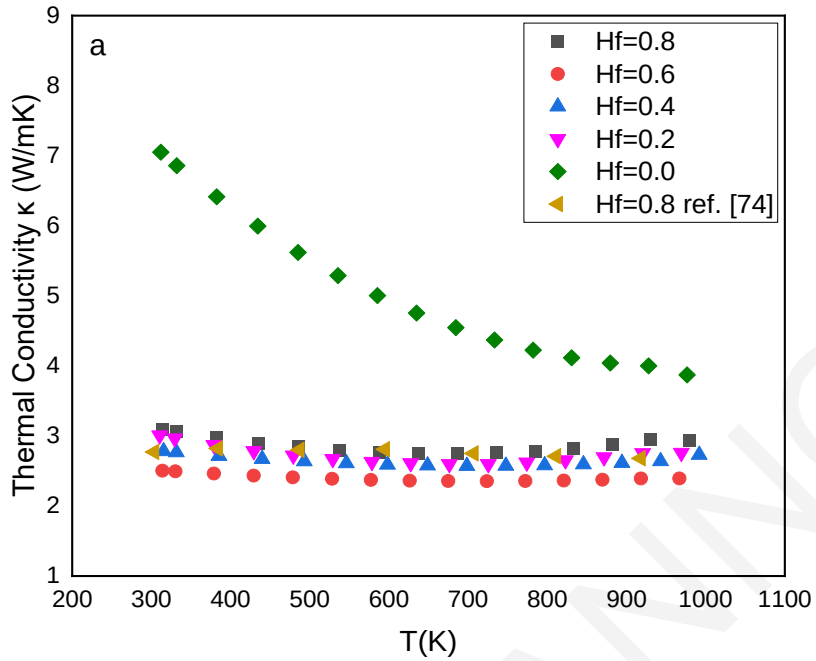

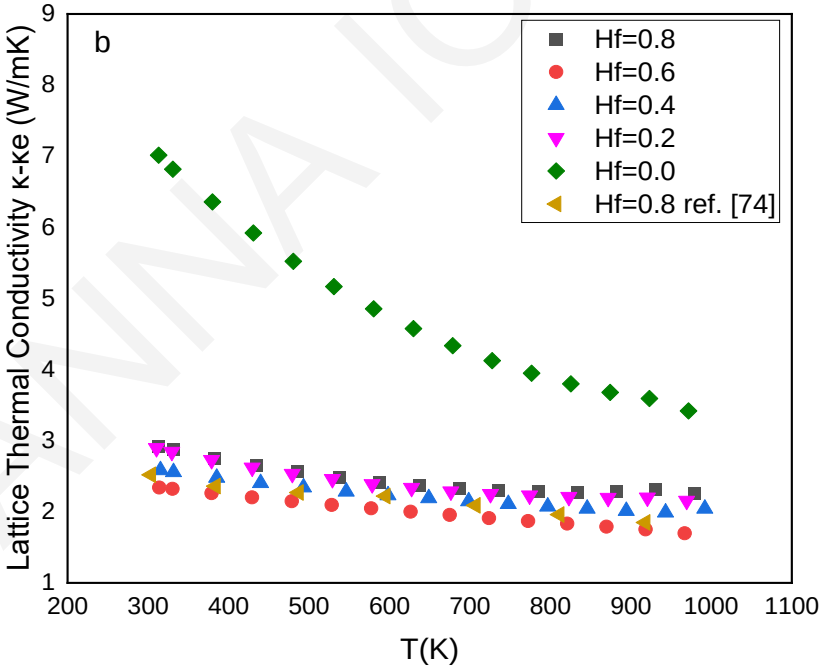

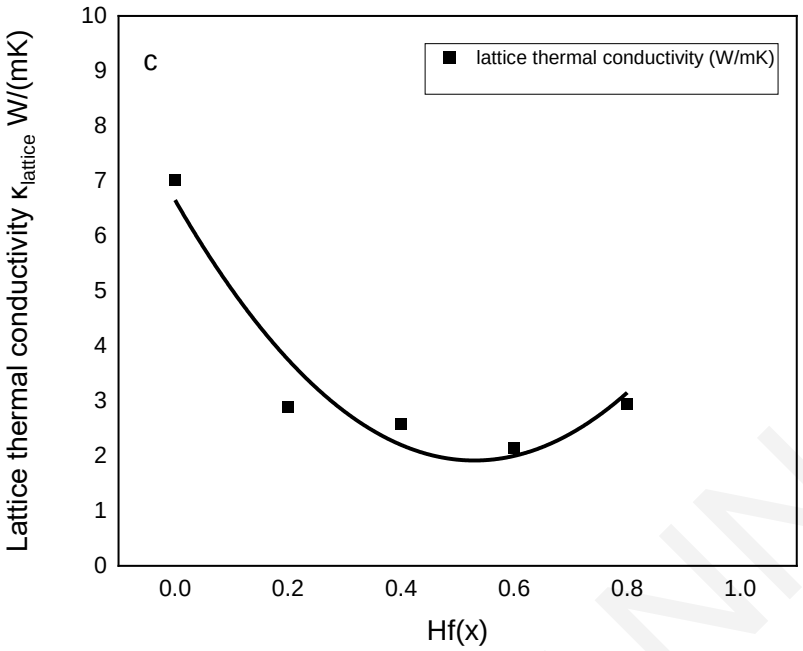

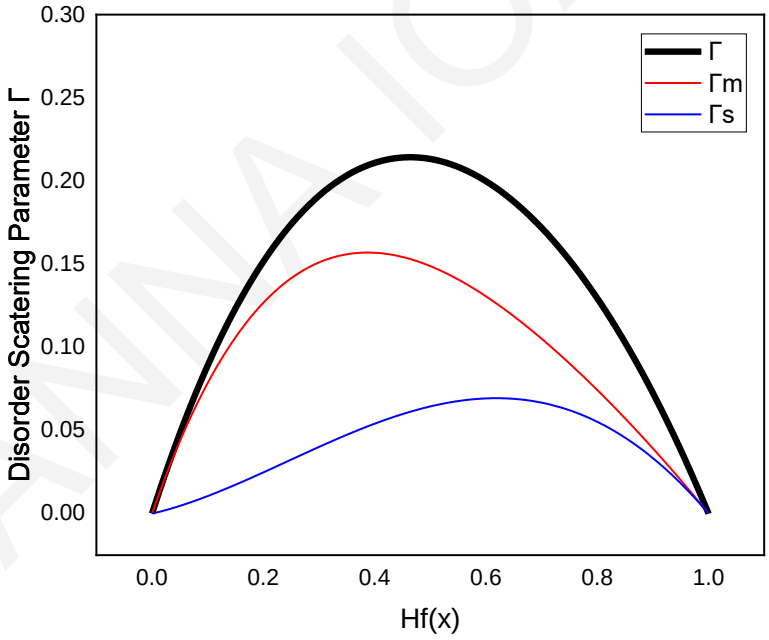

Figure 4.12: (a) Thermal conductivity κ, (b) lattice thermal conductivity κ-κ_e as a a function of temperature of $Hf_xTi_{1-x}CoSb_{0.8}Sn_{0.2}$, synthesized by mechanical alloying and arc-melted $Hf_{0.8}Ti_{0.2}CoSb_{0.8}Sn_{0.2}$ [74], (c) lattice thermal conductivity at room temperature as a function of Hf(x) (the line is guide to the eye) and (d) scattering parameter Γ as a function of Hf(x).

By combining all the previously discussed properties, the thermoelectric figure-of-merit ZT was calculated. The results are presented as a function of temperature in Figure 4.13 where it is clear that the optimization of Ti/Hf ratio has a significant impact on the thermoelectric performance of p-type $Hf_xTi_{1-x}CoSb_{0.8}Sn_{0.2}$ solid solutions. Although $TiCoSb_{0.8}Sn_{0.2}$ exhibits higher power factor, a maximal ZT of 0.84 at 970 K was achieved by $Hf_{0.6}Ti_{0.4}CoSb_{0.8}Sn_{0.2}$ originated from the significant reduction of the lattice thermal conductivity in the Hf/Ti member. The high ZT of $Hf_{0.6}Ti_{0.4}CoSb_{0.8}Sn_{0.2}$ as well as minimum lattice thermal conductivity leads to the conclusion that further investigation is desired in order to modify and improve the power factor and achieve even higher ZT.

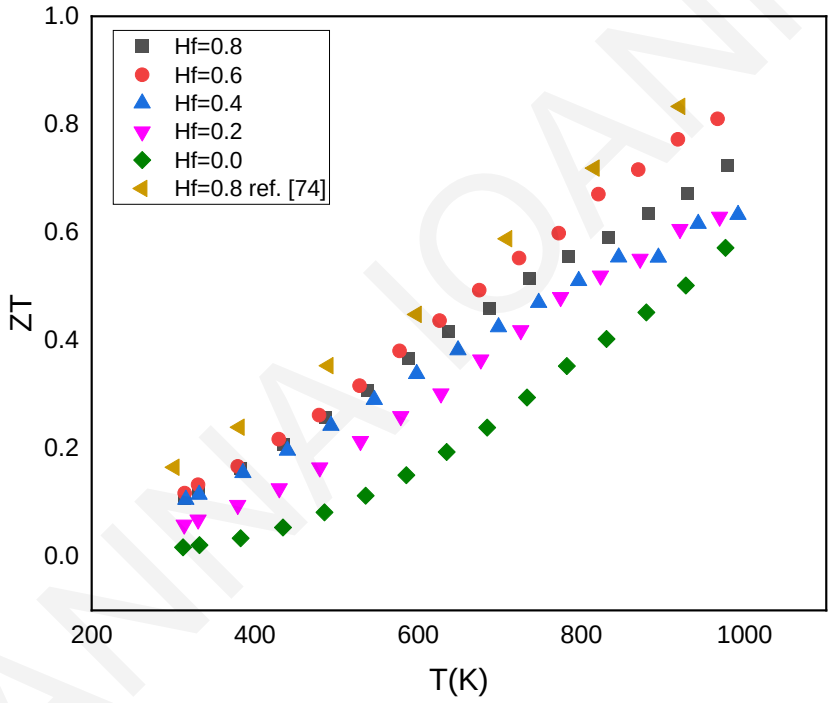

Figure 4.13: Thermoelectric figure of merit ZT as a function of temperature for $Hf_xTi_{1-x}CoSb_{0.8}Sn_{0.2}$ and arc-melted $Hf_{0.8}Ti_{0.2}CoSb_{0.8}Sn_{0.2}$ [74] with the indicated compositions of Hf.

4.2.3 Results of $Hf_{0.6}Ti_{0.4}CoSb_{1-y}Sn_y$ solid solution series

A fundamental way to further enhance the performance of thermoelectric materials is by optimizing the carrier concentration. In this part, we investigate the adjustment of doping level by the partial substitution of Sb with Sn in $Hf_{0.6}Ti_{0.4}CoSb_{1-y}Sn_y$ (y = 0.15, 0.17, 0.20, 0.23, 0.25) series.

Structural characterization:

The XRD patterns of the synthesized, hot-pressed $Hf_{0.6}Ti_{0.4}CoSb_{1-y}Sn_y$ solid solutions are shown in Figure 4.14. As in the previous studies, the diffraction peaks of all samples match well with the half-Heusler phase (space group $F\bar{4}3$) and no residual starting elements were detected. The calculated lattice parameter and the measured density (corresponds to > 94% of $\rho_{theoretical}$ = 9.42 g/cm^3) of the samples are presented in Table 4.5. The lattice parameter does not significantly change with Sb/Sn substitution, as it was expected. The back-scattered SEM images and chemical compositions are illustrated in Figure 4.15 and Table 4.6, respectively. The SEM images of $Hf_{0.6}Ti_{0.4}CoSb_{1-y}Sn_y$ samples showed homogeneous single-phase materials and the EDS analysis revealed that the chemical compositions are close to the nominal compositions of the compounds. Small deviations are due to the relative error of EDS and a possible Hf/Sn slight loss during milling as in previous chapters.

Table 4.5: Lattice parameter a, measured density and relative density of $Hf_{0.6}Ti_{0.4}CoSb_{1-y}Sn_y$ samples.

Nominal composition	Lattice Parameter α (nm)	Measured Density (gr /cm^3)
$Hf_{0.6}Ti_{0.4}CoSb_{0.75}Sn_{25}$	**0.603**	**9.23**
$Hf_{0.6}Ti_{0.4}CoSb_{0.77}Sn_{23}$	**0.601**	**9.03**
$Hf_{0.6}Ti_{0.4}CoSb_{0.80}Sn_{20}$	**0.602**	**9.13**
$Hf_{0.6}Ti_{0.4}CoSb_{0.83}Sn_{17}$	**0.601**	**8.83**
$Hf_{0.6}Ti_{0.4}CoSb_{0.85}Sn_{15}$	**0.601**	**8.88**

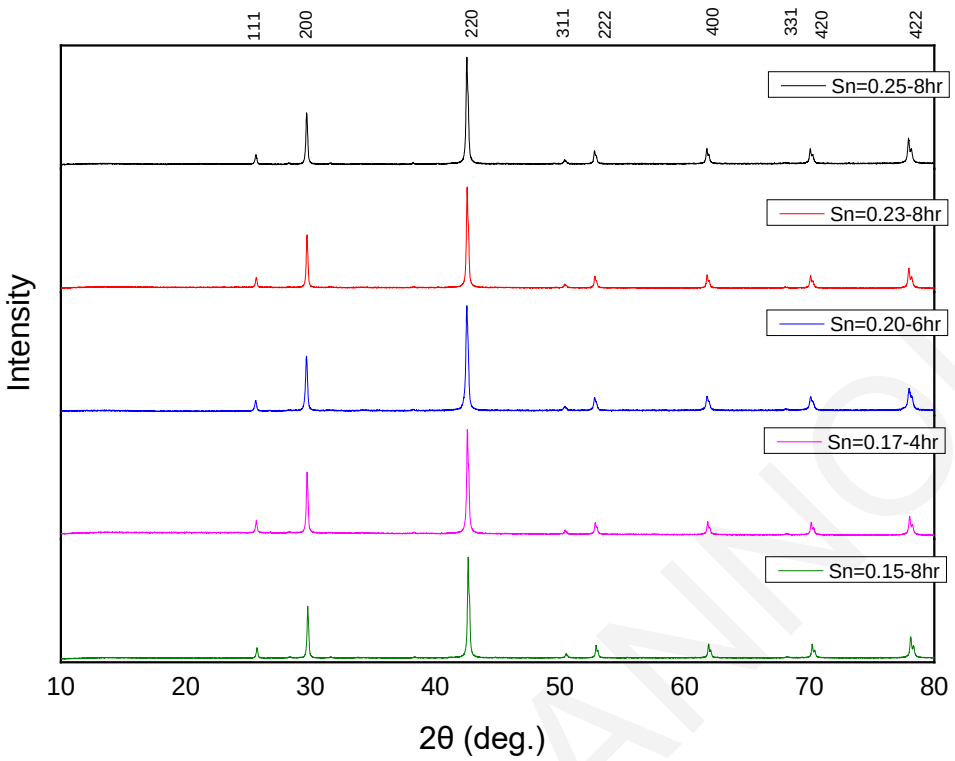

Figure 4.14: XRD patterns of $Hf_{0.6}Ti_{0.4}CoSb_{1-y}Sn_y$ samples prepared by mechanical alloying followed by hot-pressing.

Table 4.6: Nominal and chemical composition of hot-pressed $Hf_{0.6}Ti_{0.4}CoSb_{1-y}Sn_y$ samples as determined by EDS spectroscopy.

Nominal Composition (at%)	**SEM/EDS Composition (at%)**				
	Hf	**Ti**	**Co**	**Sb**	**Sn**
$Hf_{0.6}Ti_{0.4}CoSb_{0.85}Sn_{0.15}$	**0.54**	**0.44**	**1.08**	**0.80**	**0.14**
$Hf_{0.6}Ti_{0.4}CoSb_{0.83}Sn_{0.17}$	**0.54**	**0.42**	**1.11**	**0.76**	**0.18**
$Hf_{0.6}Ti_{0.4}CoSb_{0.80}Sn_{0.20}$	**0.55**	**0.41**	**1.08**	**0.75**	**0.21**
$Hf_{0.6}Ti_{0.4}CoSb_{0.77}Sn_{0.23}$	**0.54**	**0.42**	**1.08**	**0.72**	**0.24**
$Hf_{0.6}Ti_{0.4}CoSb_{0.75}Sn_{0.25}$	**0.58**	**0.41**	**1.07**	**0.70**	**0.23**

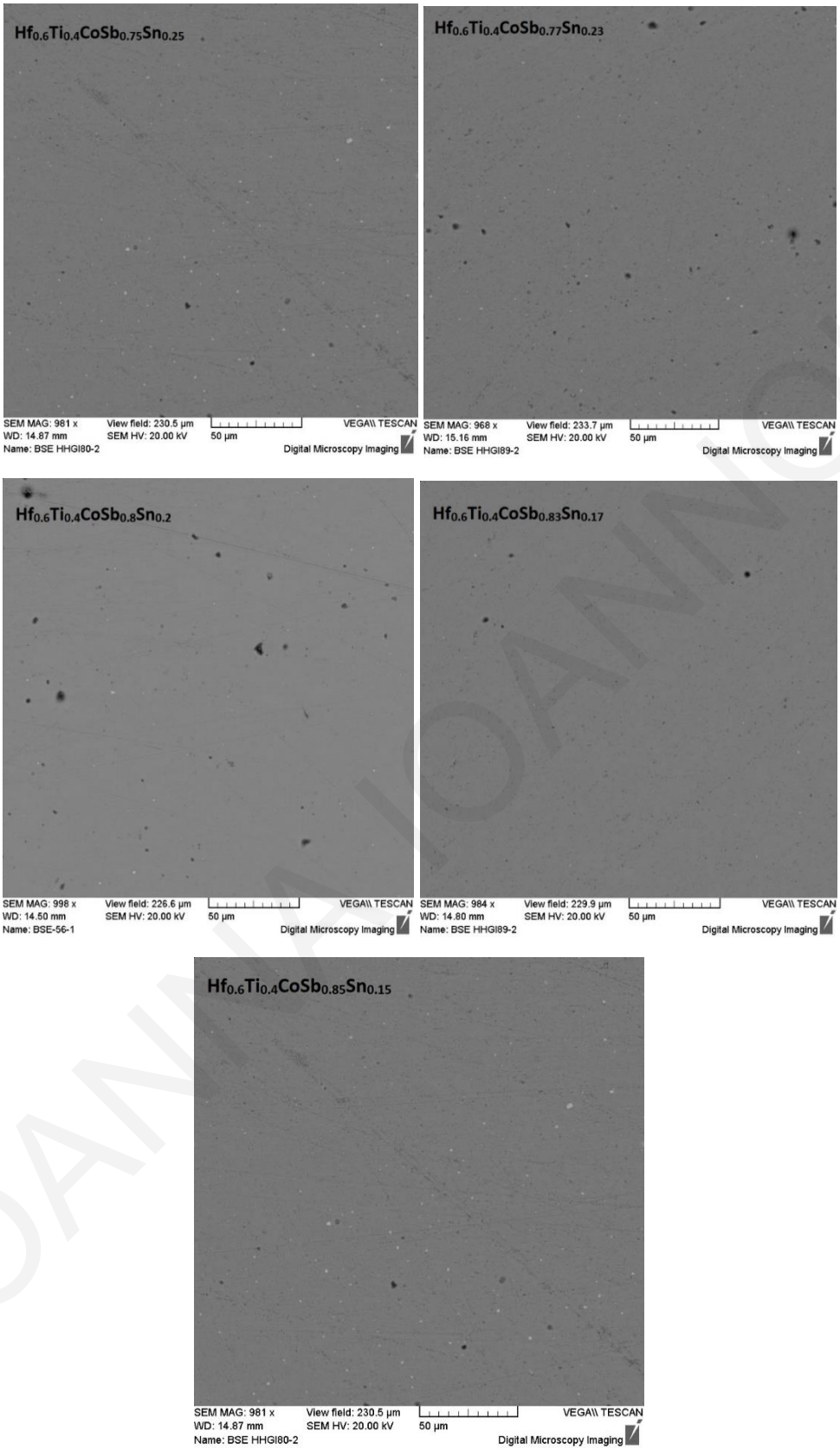

Figure 4.15: Back-scattered electron images of hot-pressed $Hf_{0.6}Ti_{0.4}CoSb_{1-y}Sn_y$ samples.

In order to systematically assess the nanostructured morphology, as well as potential discrete phase formation, transmission electron microscopy experiments (TEM/HRTEM) were carried out in the $Hf_{0.6}Ti_{0.4}CoSb_{0.83}Sn_{0.17}$ sample and a characteristic TEM image is presented in Figure 4.16. The primary particles of the material have a size of 350 nm, on average, although some up to 1 μm have been also detected. As a consequence of the ball milling, the material exhibits a substantial percentage of nanocrystallinity, demonstrated both by the selected area diffraction (SAD) ring pattern, inset in Figure 4.16a, as well as by the complementary bright field (BF), in (a) and dark field (DF), in (b) images. The nanograins are clearly illustrated in the latter with white arrows, as bright regions against an overall dark background. The BF and DF images were obtained using the 220 reflection of $Hf_{0.6}Ti_{0.4}CoSb_{0.83}Sn_{0.17}$.

The nanograins have a size range of up to 12 nm and are single crystalline. A typical one is shown at the HRTEM image of Figure 4.16c, oriented along the $Hf_{0.6}Ti_{0.4}CoSb_{0.83}Sn_{0.17}$ [011] crystallographic direction. Experimental measurements of the (200) and {111} lattice fringe distance provided d_{200}=0.294 nm and d_{111}=0.339 nm, respectively; this results in a lattice constant of a=0.588 nm, an average, which is in good agreement with the XRD results (a=0.601 nm). In addition, this value aligns very well with the theoretical lattice parameter of the $Hf_{0.6}Ti_{0.4}CoSb_{0.83}Sn_{0.17}$ sample, taking into account Vegard's law and the constants of the two distinct members, $HfCoSb_{0.85}Sn_{0.15}$ (a=0.604 nm) and $TiCoSb_{0.85}Sn_{0.15}$ (a=0.589 nm), i.e. $a_{theor.}$= 0.598 nm [70].

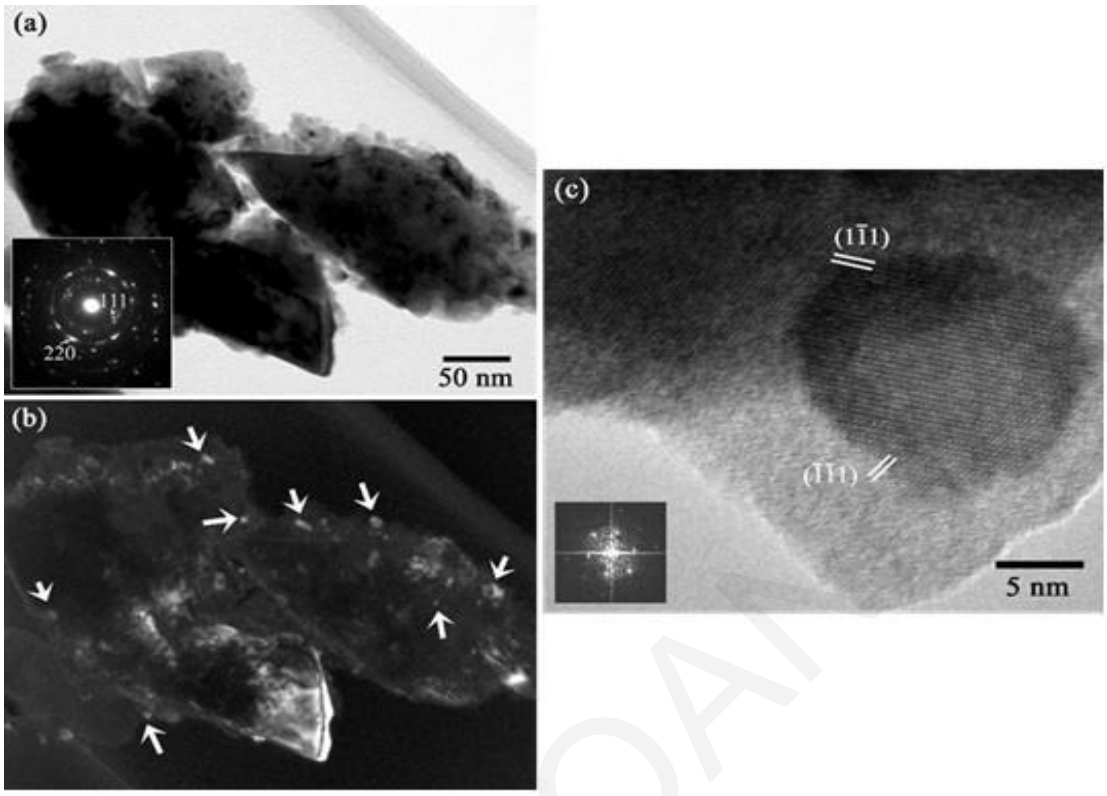

Figure 4.16: a-b) Complementary TEM-BF and DF images, respectively, from the $Hf_{0.6}Ti_{0.4}CoSb_{0.83}Sn_{0.17}$ sample, acquired using the arrowed 220 reflection at the SAD pattern, inset in (a) and c) HRTEM image of a representative nanocrystalline particle, viewed along its [011] crystallographic direction.

Thermoelectric properties:

The electrical conductivity, Seebeck coefficient and thermal conductivity measurements were performed in order to assess the thermoelectric performance of the $Hf_{0.6}Ti_{0.4}CoSb_{1-y}Sn_y$ series. The obtained data from the electrical conductivity and Seebeck coefficient measurements along with the calculated Power factors are summarized in Figure 4.17. The Sb substitution with Sn in p-type half- Heusler solid solutions introduces holes into the system, thus the carrier concentration increases. The Seebeck coefficient is highest for Sn = 0.15 and decreases upon substitution of Sb with Sn up to y=0.23 suggesting the incorporation of the Sn in Sb sublattice. Samples with Sn = 0.23 and 0.25 present similar Seebeck coefficient values, suggesting similar charge carrier concentrations but different carrier mobilities according to electrical conductivity measurements. Figure 4.17b demonstrates that the electrical conductivity

increases with increasing Sn content from 0.15 to 0.23 and then decreases when Sn = 0.25. The electrical conductivity of the sample with Sn = 0.15 linearly increases with increasing temperature, as a consequence of the lower doping level as well as the thermally activated mobility that resulted by the enhanced grain boundary scattering of these nanostructured materials. However, this behaviour changes as the Sn content increases due to the higher doping level. Consequently, the temperature dependence of σ values of $Hf_{0.6}Ti_{0.4}CoSb_{0.75}Sn_{0.25}$ and $Hf_{0.6}Ti_{0.4}CoSb_{0.77}Sn_{0.23}$ exhibit smaller slope. The calculated power factors (Figure 4.17c) of samples with $0.17 \leq Sn \leq 0.23$ are higher than that of $Hf_{0.6}Ti_{0.4}CoSb_{0.75}Sn_{0.25}$ and $Hf_{0.6}Ti_{0.4}CoSb_{0.85}Sn_{0.15}$ samples suggesting that Sn concentration between 0.17 and 0.23 results an optimum range of carrier concentration. The highest PF ~ 24μW/cmK^2 was reached by $Hf_{0.6}Ti_{0.4}CoSb_{0.77}Sn_{0.23}$ at 975 K.

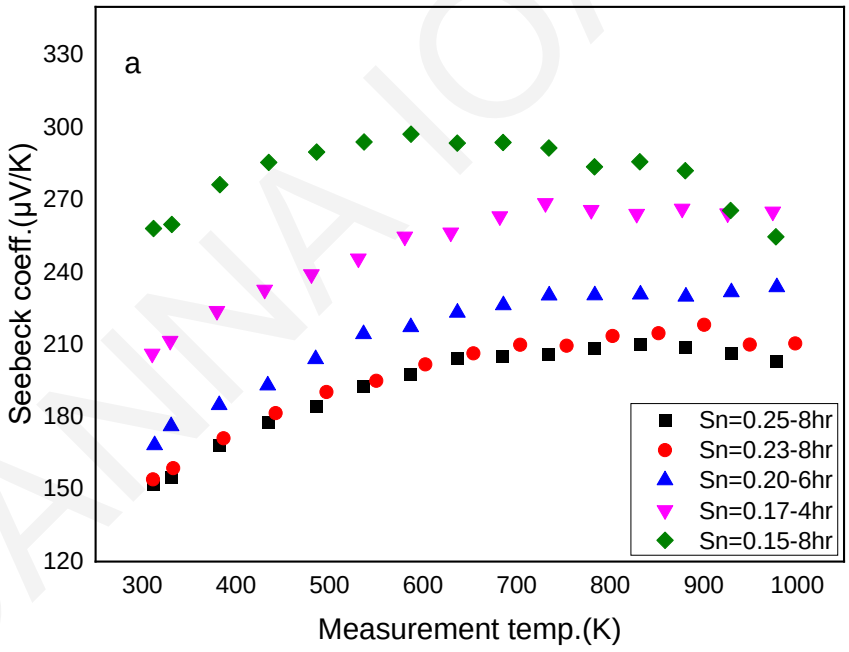

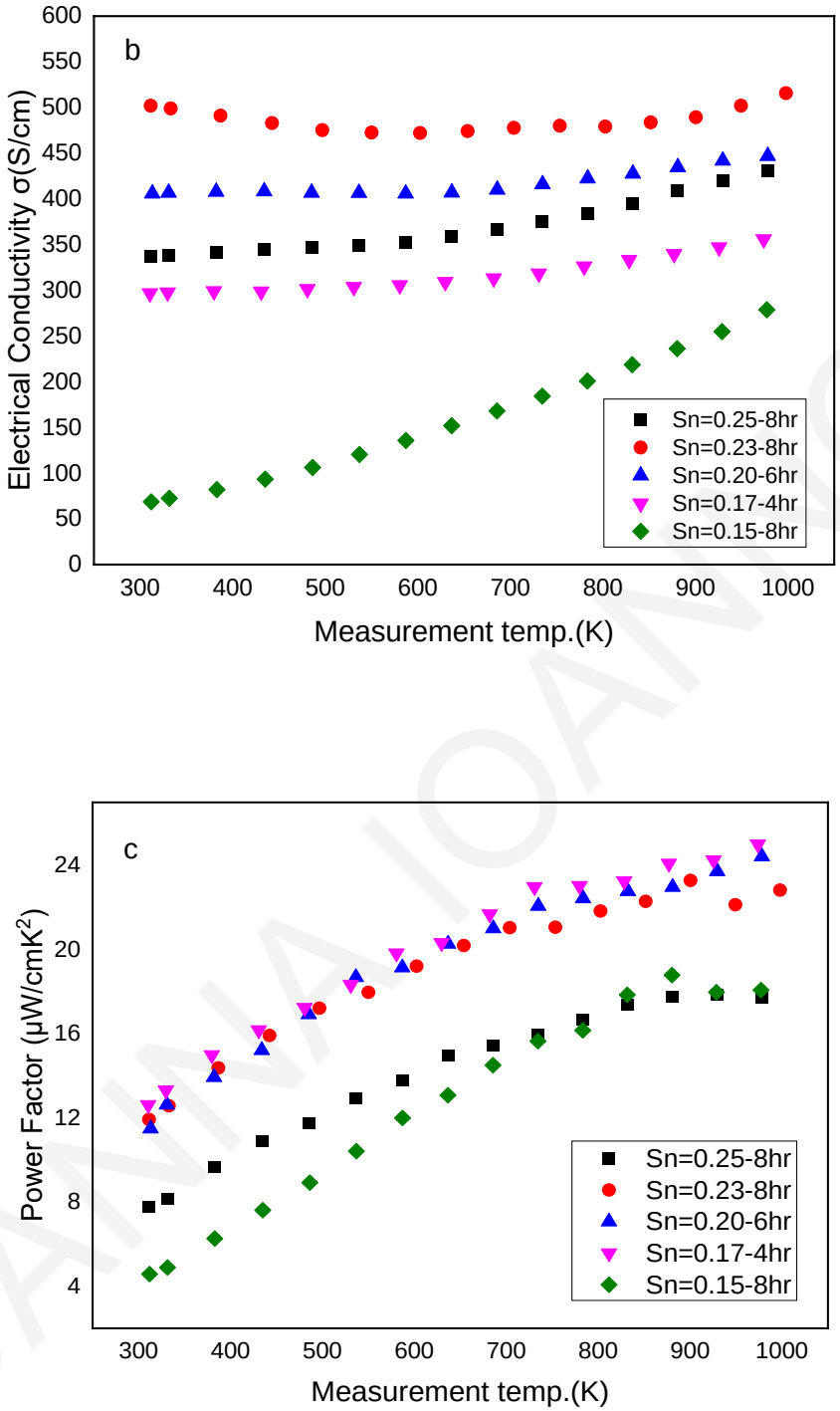

Figure 4.17: a) Seebeck coefficient S b) Electrical conductivity σ and c) Power Factor PF as a function of temperature for hot-pressed $Hf_{0.6}Ti_{0.4}CoSb_{1-y}Sn_y$ alloys.

The total and lattice thermal conductivity plots of the investigated compounds are displayed in Figure 4.18. The thermal conductivity is successfully suppressed by the optimization of Sb/Sn ratio. At room temperature, samples with Sn = 0.20,0.23 present lower κ values than the other samples. To further understand the influence of substitution level, the lattice thermal conductivity was calculated as previously. The lowest $\kappa_{lattice}$ = 1.68 W/mK was achieved by $Hf_{0.6}Ti_{0.4}CoSb_{0.77}Sn_{0.23}$ at 970 K. This minimal lattice thermal conductivity is a result of the partial substitution optimization in combination with nanostructuring, which increased the effective scattering of phonons.

The thermoelectric figure of merit ZT calculation reveals that the best thermoelectric properties are obtained for $Hf_{0.6}Ti_{0.4}CoSb_{0.83}Sn_{0.17}$ composition (Figure 4.19). The mechanically alloyed compounds with the optimal Hf/Ti and Sn/Sb ratios lead to an impressive ZT of 1.1 at 975 K. This value corresponds to an improvement of 22% with respect to that of $Hf_{0.6}Ti_{0.4}CoSb_{0.8}Sn_{0.2}$. It turned out that a substitution level of 17% Sn for Sb is more effective in $Hf_{0.6}Ti_{0.4}CoSb_{1-y}Sn_y$ materials prepared by mechanical alloying than that of 15% and 20% which have been suggested in the past for materials prepared by arc-melting [61], [66], [75].

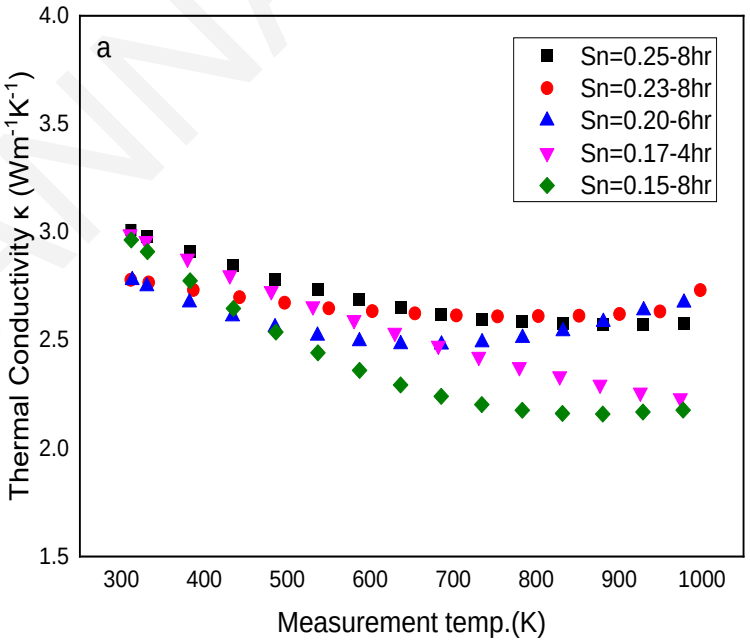

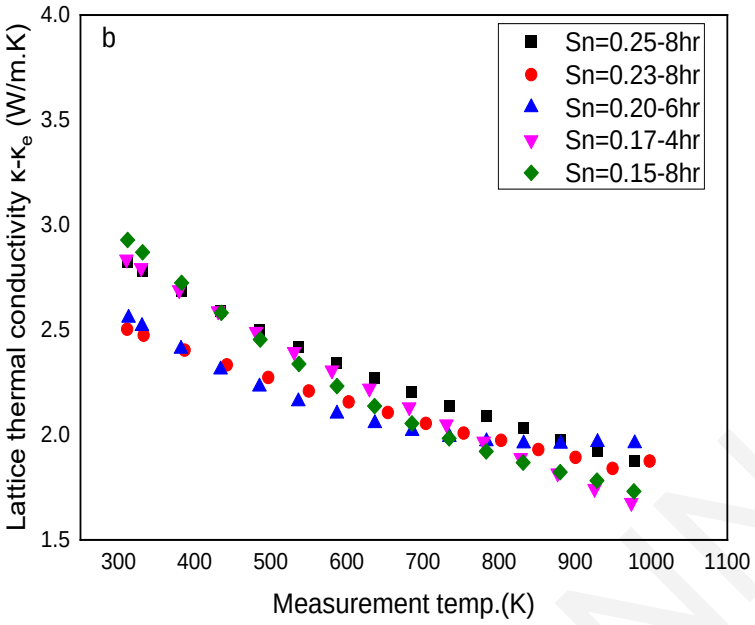

Figure 4.18: a) Thermal conductivity κ and (b) Lattice thermal conductivity κ-κ_e of hot-pressed $Hf_{0.6}Ti_{0.4}CoSb_{1-y}Sn_y$ samples.

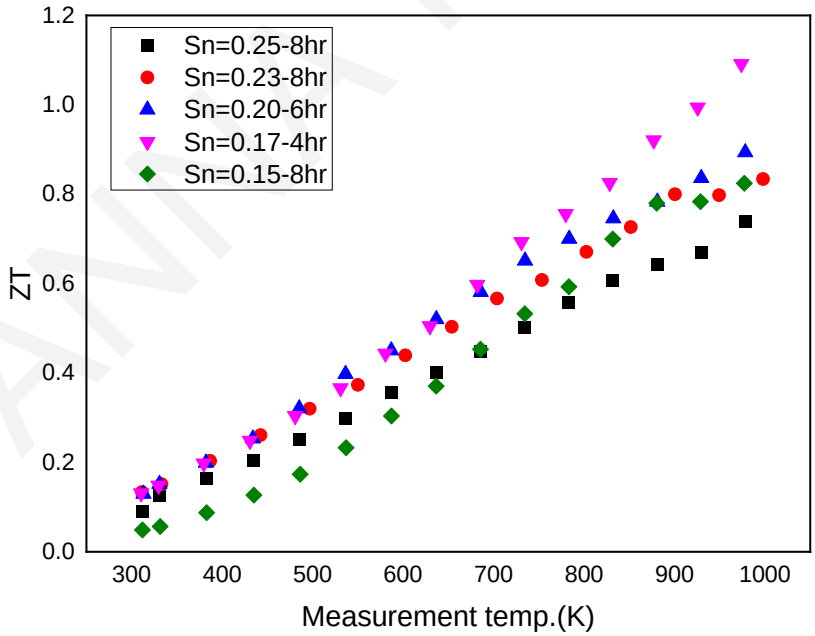

Figure 4.19: Thermoelectric figure of merit ZT for hot-pressed $Hf_{0.6}Ti_{0.4}CoSb_{1-y}Sn_y$ samples.

4.2.4 Conclusion

In this chapter, mechanical alloying was successfully applied for the synthesis of half-Heusler ($Hf_xTi_{1-x}CoSb_{0.8}Sn_{0.2}$) compositions, suggesting the potential of replacing the time-consuming arc-melting followed by several days of annealing method by an advantageous, single step process. Two different methods were applied to enhance the thermoelectric performance of p-type (Hf,Ti)Co(Sb,Sn) materials: adjustment of the Ti/Hf ratio to affect the lattice thermal conductivity and fine tuning of carrier concentration by the substitution of Sb with Sn. The isoelectronic replacement of Ti with Hf in combination with nanostructuring approach via mechanical alloying led to an important reduction in the lattice thermal conductivity. Consequently, a high ZT~0.85 at 980K was recorded by the hot-pressed $Hf_{0.6}Ti_{0.4}CoSb_{0.8}Sn_{0.2}$ sample prepared by 4 hours milling. The effect of charge carrier concentration was also investigated by preparing $Hf_{0.6}Ti_{0.4}CoSb_{1-y}Sn_y$ (0.15, 0.17, 0.20, 0.23, 0.25) samples. It turned out that a substitution level of 17% Sn for Sb is the most effective in $Hf_{0.6}Ti_{0.4}CoSb_{1-y}Sn_y$ materials prepared by mechanical alloying. $Hf_{0.6}Ti_{0.4}CoSb_{0.83}Sn_{0.17}$ sample, reached a maximum ZT~1.1 at 973K. It is noteworthy, that this ZT value is among the highest ever reported for p-type MCo(Sb,Sn). When it comes to (Ti,Hf)Co(Sb,Sn) system, previous investigations have shown that high thermoelectric figure of merit ($ZT \geq 1$) can be achieved in arc-melted $Hf_{0.8}Ti_{0.2}CoSb_{0.8}Sn_{0.2}$ and $Ti_{0.25}Hf_{0.75}CoSb_{0.85}Sn_{0.15}$. $Hf_{0.6}Ti_{0.4}CoSb_{0.83}Sn_{0.17}$ composition has the advantage of less Hf, which is much more expensive than Ti and Zr. Achieving a high ZT in a less expensive composition can be crucial for large-scale application of half-Heusler materials**.** Overall, this study indicates that single-phase, p-type (Hf,Ti)Co(Sb,Sn) alloys can be synthesized by the advantageous mechanical alloying method and high ZT values can be obtained by the optimization of phonon scattering and carrier concentration using Hf/Ti as well as Sb/Sn partial substitution.

4.3 Effect of Sb substitution with Bi in $Hf_{0.6}Ti_{0.4}CoSb_{0.8-x}Bi_xSn_{0.2}$

Recently, a record-high ZT ~1.42 at 973 K was achieved in $ZrCoBi_{0.65}Sb_{0.15}Sn_{0.20}$ solid solution prepared via MA and hot-press sintering [126]. As indicated by theoretical calculations, the high power-factor (PF ~ 40 μW cm^{-1} K^{-2}) achieved in ZrCoBi-based compounds is ascribed to the high band degeneracy, while the impressively low thermal conductivity (κ= 2.2 W/mK) is mainly attributed to the substantial atomic mass difference between Sn (atomic weight: ~118.71) and Bi atoms (atomic weight: ~208.98) that leads to an intense point defect scattering. Bismuth-based half-Heuslers have not been thoroughly examined for thermoelectric application, giving us the opportunity to explore a new avenue for the design of half-Heusler thermoelectric materials.

The objective of this chapter was to achieve a low lattice thermal conductivity and a high power factor in $Hf_{0.6}Ti_{0.4}Co(Sb,Bi,Sn)$ solid solutions prepared by MA. Based on the previously discussed encouraging results of $Hf_{0.6}Ti_{0.4}CoSb_{0.8}Sn_{0.2}$ in chapter 4.2, $Hf_{0.6}Ti_{0.4}CoSb_{0.8-x}Bi_xSn_{0.2}$ (x=0-0.1) samples were prepared as an attempt to partially replace Sb with Bi and to investigate the effect of that kind of isoelectronic substitution on the thermoelectric properties.

4.3.1 Synthesis and consolidation conditions

The MA process lasted 6 hours and was carried out in a planetary mill at 450rpm. The ball to material ratio was 15:1. The as-milled powders were hot-pressed into high-density pellets as in chapter 4.2.

4.3.2 Results of $Hf_{0.6}Ti_{0.4}CoSb_{0.8-x}Bi_xSn_{0.2}$ solid solution series

In this chapter the results from the structural characterization and the thermoelectric properties of the hot-pressed $Hf_{0.6}Ti_{0.4}CoSb_{0.8-x}Bi_xSn_{0.2}$ (x=0-0.1) solid solutions will be briefly discussed.

Structural Characterization:

X-ray diffraction patterns, scanning electron microscopy (SEM) images and energy dispersive X-ray analysis (EDS) were performed for the structural characterization of $Hf_{0.6}Ti_{0.4}CoSb_{0.8-x}Bi_xSn_{0.2}$ samples. The XRD diffraction patterns of all $Hf_{0.6}Ti_{0.4}CoSb_{0.8-x}Bi_xSn_{0.2}$ powders after 6 hours of milling and hot-pressed pellets

present the cubic half-Heusler phase (Figure 4.20). However, small impurity peaks revealed the presence of residual Bi in samples with x>0 after hot-press sintering (Figure 4.20b). The (220) main peak in Figure 4.20c broadens with increasing Sb substitution with Bi suggesting the presence of two or more HH phases. The broadening of the X-ray diffraction peaks was also noticed in other phase-separated HH compounds prepared via arc-melting [66][73]. The lattice parameters based on the XRD diffraction peaks and the geometrical density of samples are shown in Table 4.7. The lattice parameter does not significantly increase with increasing the Sb substitution with Bi, indicating that Bi atoms do not fully incorporate within the matrix.

SEM and EDS analysis were performed (Figure 4.21 and Table 4.8) to investigate the microscopic features in $Hf_{0.6-x}Zr_xTi_{0.4}CoSb_{0.8}Sn_{0.2}$ materials. The back-scattered images of all samples with x>0 displayed some small bright spots randomly distributed in the grey matrix. The quantitative composition estimation from the EDS analysis demonstrated that the grey half-Heusler matrix region in all samples is interspersed with some Bi-rich spots. This effect is more evident in samples with high Bi percentage (x=0.075 and 0.1). In addition, samples with x=0.025 and 0.05 are also interspersed with some darker regions, which were identified to have lower Hf and Bi percentage. The effect of intrinsic phase separation has been extensively discussed for HH compounds prepared via rapid solidification techniques like arc-melting [73][127]. However, the formation of two or three different HH phases in samples prepared via mechanical alloying has never been reported, to the best of our knowledge. Bi probably reduces the solid solubility limits under the used MA conditions (duration and speed). The levels of solid solubility may differ in different systems under the same synthesis conditions leading to the formation of secondary phases or the presence of residual starting elements. Further investigation of milling-time may provide a clearer understanding of the underling mechanisms.

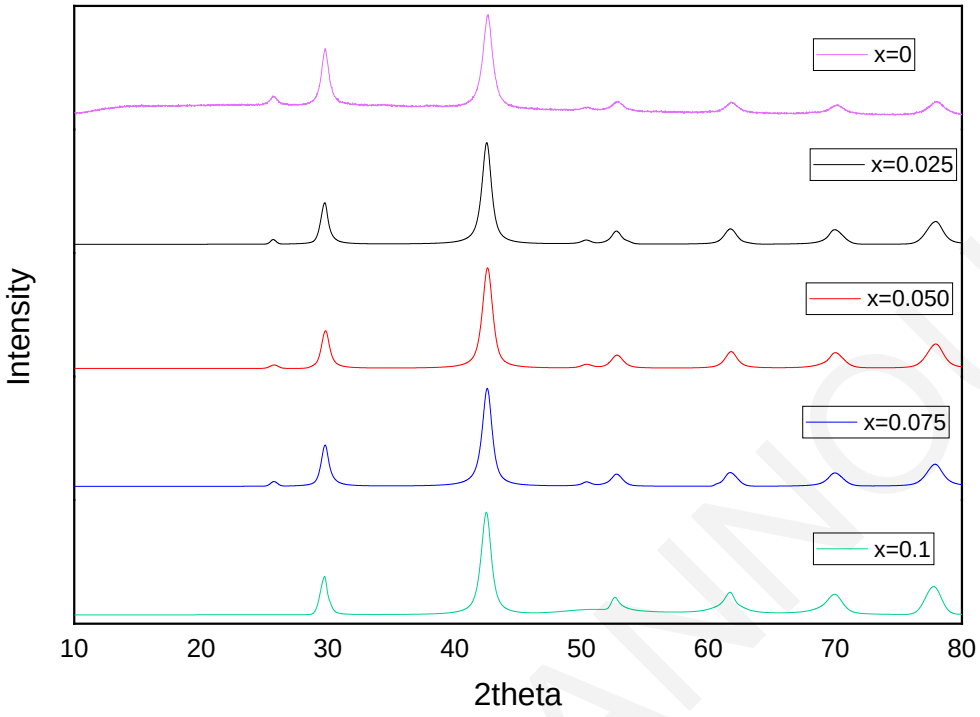

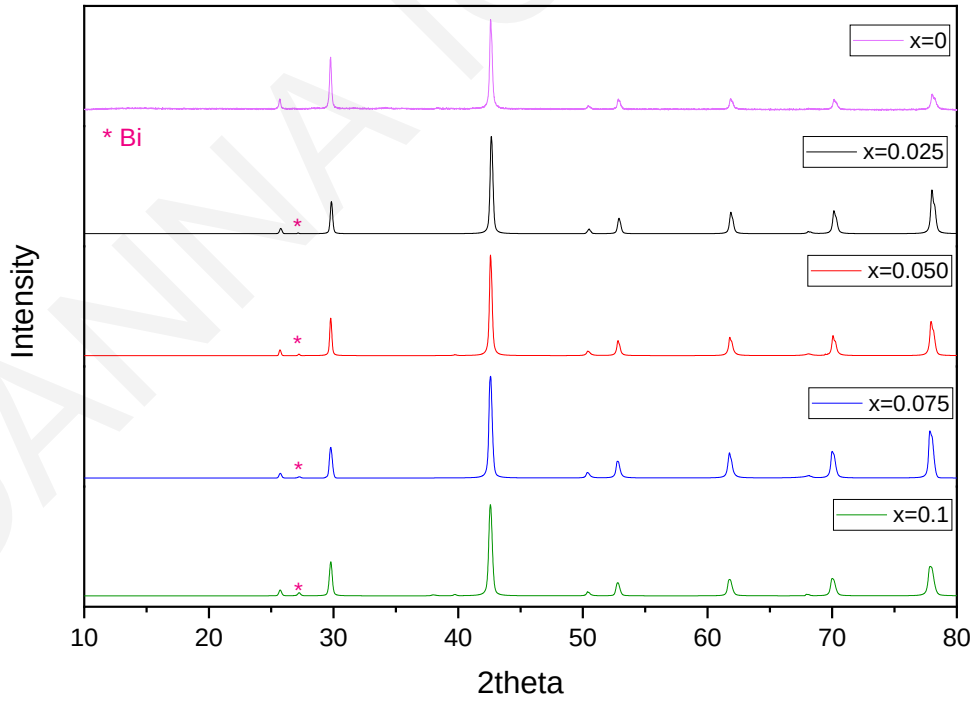

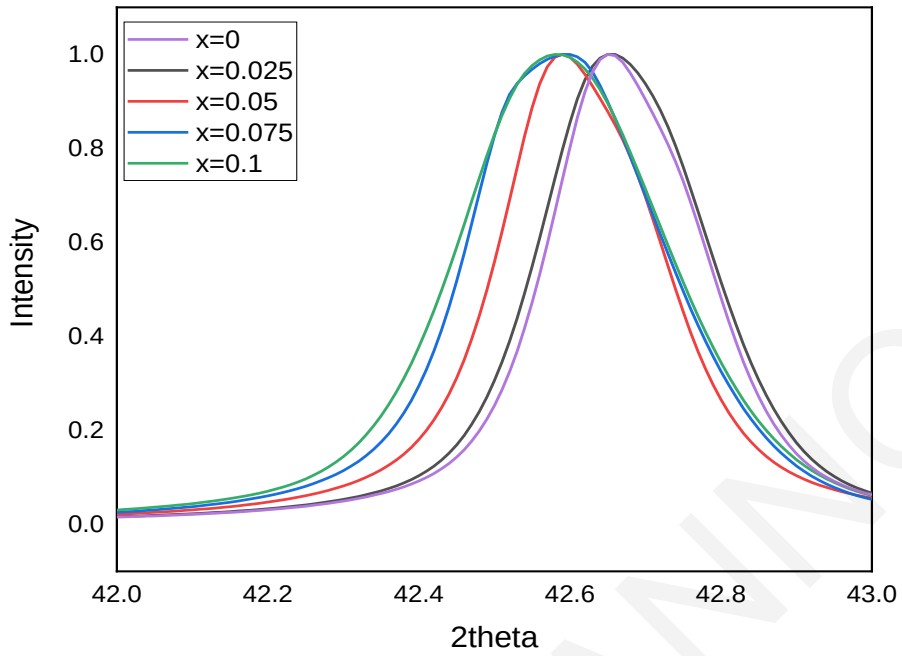

Figure 4.20: a) X-ray powder diffraction patterns of powders $Hf_{0.6}Ti_{0.4}CoSb_{0.8-x}Bi_xSn_{0.2}$ (x=0-0.1) prepared by 6 hours mechanical alloying, b) the X-ray powder diffraction patterns of hot-pressed pellets and c) the main (220) reflection of samples with x=0-0.1.

Table 4.7: The geometrical densities and lattice parameter of the hot-pressed $Hf_{0.6}Ti_{0.4}CoSb_{0.8-x}Bi_xSn_{0.2}$ (x=0-0.1) samples

Sample	Density(g/cm^3)	Lattice parameter(nm)
x=0	9.13	0.599
x=0.025	9.10	0.599
x=0.05	8.90	0.601
x=0.075	9.29	0.600
x=0.10	9.31	0.600

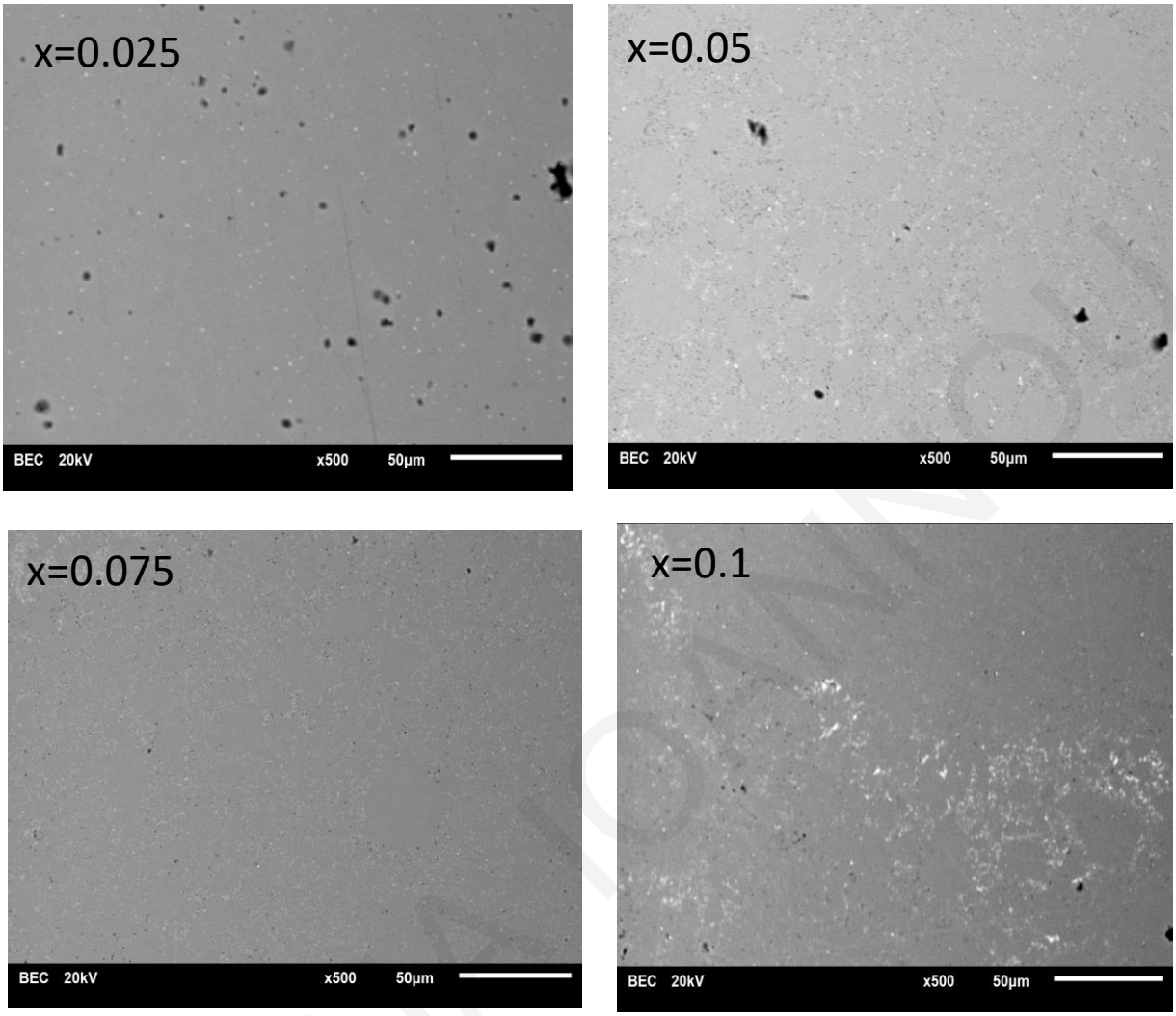

Figure 4.21: Back-scattered electron images of hot-pressed $Hf_{0.6}Ti_{0.4}CoSb_{0.8-x}Bi_xSn_{0.2}$ samples

Table 4.8: Chemical composition of hot-pressed $Hf_{0.6}Ti_{0.4}CoSb_{0.8-x}Bi_xSn_{0.2}$ samples as determined by EDS.

Sample	Area	Hf	Ti	Co	Sb	Bi	Sn
x=0.025	matrix	0.56	0.45	1.03	0.84	0.01	0.12
	black	0.46	0.39	0.88	0.97	0	0.29
	white	0.58	0.42	0.97	0.8	0.02	0.13
x=0.05	matrix	0.54	0.44	1.03	0.79	0.04	0.15
	black	0.52	0.45	0.99	0.83	0.01	0.19
	white	0.62	0.45	1.02	0.74	0.05	0.13
x=0.075	matrix	0.56	0.41	1.05	0.74	0.07	0.17
	white	0.54	0.41	0.98	0.69	0.2	0.17
x=0.1	matrix	0.55	0.43	1.03	0.79	0.08	0.13
	white	0.46	0.36	0.9	0.68	0.48	0.13

Thermoelectric properties:

The temperature dependent electrical conductivity, Seebeck coefficient and Power factor ($S^2\sigma$) of the hot-pressed $Hf_{0.6}Ti_{0.4}CoSb_{0.8-x}Bi_xSn_{0.2}$ samples are presented in Figure 4.22. All samples exhibit positive S values, indicating holes as the majority charge carriers. The highest S value of 233 μV/K was observed for $Hf_{0.6}Ti_{0.4}CoSb_{0.8}Sn_{0.2}$ at 978 K. At room temperature, the Seebeck coefficient slightly increases with increasing Bi ranging from 169μV/k for the sample with x=0 to a maximum value of 196 μV/K for the sample with x=0.075. A further increase of Bi (x=0.1) resulted in lower Seebeck coefficient. At high temperatures (T≥750K) the trend is reversed; S values decrease with increasing Bi (x). Although, the substitution of Sb with Bi is isoelectronic, the thermopower values change to some degree with changing Sb/Bi ratio. The observed increase in S probably corresponds to a slight drop in the hole density within the HH matrix upon increasing the Sb/Bi substitution due to the presence of residual elemental Bi in all samples with x>0. Bismuth is metallic in nature and electronically dope the p-type HH matrix by dumping extra electrons which partially compensate the existing holes within matrix. In addition, the Seebeck coefficient of samples with x>0 increases with increasing temperature, reaches a maximum value around 750K and then starts to decrease, revealing the onset of bipolar excitation. On the other hand, the S values of the sample without Bi (x=0) increase with temperature and almost stabilize at temperatures above 750K. The electrical conductivity (Figure 4.22b) at 300K decreases with increasing Bi and drops to the minimum value of 165 S/cm for the composition with x=0.1. The magnitude of this drop is not consistent with the Seebeck coefficient values at room temperature, indicating also a decrease in carrier mobility with increasing the level of Sb substitution with Bi, probably resulting from the presence of metallic inclusions and phase-separation within the HH matrix. Interestingly, the electrical conductivity of compounds with x>0 increases with rising temperature and this trend becomes more prominent as Bi rises suggesting a semiconductor-like behavior, whereas a nearly temperature independent electrical conductivity is observed for the sample with x=0.

Another interpretation is that the observed change in the carrier density and mobility results due to the filtering (trapping) of the low energy carriers by the energy barriers (ΔE) developed at the phase boundaries between the HH matrix and Bi inclusions, similar to the model, proposed by Faleev et al.[128]. Similar trends in S and σ have

been recorded in HH solid solutions, embedded with metallic FH nanoinclusions[129], [130]. In addition to that, Nolas et al. [131] proposed a model which relates S to the scattering factor and reduced Fermi energy as follows:

$$S = \frac{\pi^2 k_B}{3e}\left(r + \frac{2}{3}\right)\frac{1}{\xi}$$

where k_B is the Boltzmann constant, r is the scattering factor and ξ is the reduced Fermi energy. The reduced Fermi energy ξ is related to the decrease of carrier concentration, which consequently increase the S. Moreover, an increase in the scattering factor r, from the potential barrier scattering effect may also result in an increase of S of these materials. However, further studies and especially Hall measurements may be required to understand the underling mechanisms.

The calculated Power factors are shown in Figure 4.22c. All samples with x>0 presented lower power factors than $Hf_{0.6}Ti_{0.4}CoSb_{0.8}Sn_{0.2}$ (PF ~24.5 μW/cmK^2) mainly due to their lower electrical conductivities. The sample with x=0.075 follows with a PF value around 19 μW/cmK^2.

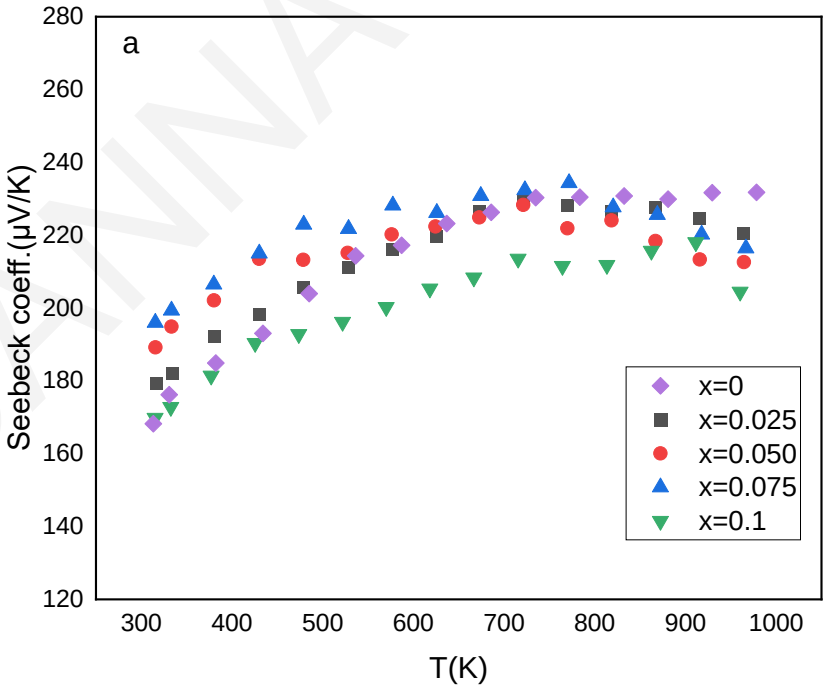

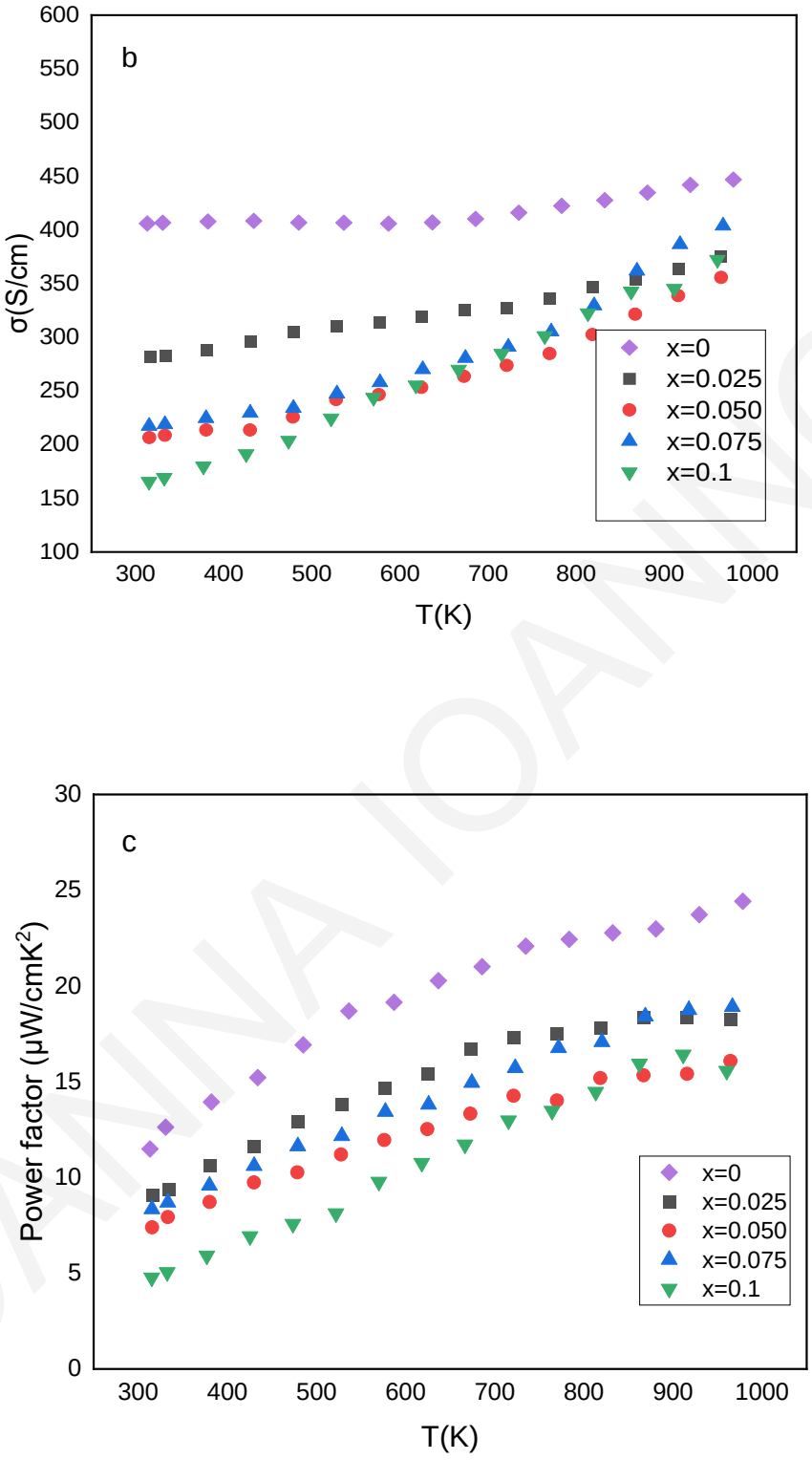

Figure 4.22: Temperature dependent Seebeck coefficient (a), electrical conductivity (b) and Power factor (c) of $Hf_{0.6}Ti_{0.4}CoSb_{0.8-x}Bi_xSn_{0.2}$ samples.

The temperature dependence of the total thermal conductivity and the lattice thermal conductivity are plotted in Figure 4.23. At room temperature, the total thermal conductivity (Figure 4.23a) decreases with increasing Bi up to 5% ($x \leq 0.05$) but then starts to increase for higher Bi percentage ($x \geq 0.075$). Specifically, the sample with $x=0.05$ present 37% lower thermal conductivity at 300K ($\kappa=1.76$ W/mK) than the sample without Bi ($x=0$) which presents a thermal conductivity value around 2.8 W/mK. It is also interesting that all samples containing Bi illustrate a totally different temperature behavior compared to the sample without Bi. The thermal conductivity of samples with $x>0$ increases with rising temperature due to the increase of electronic thermal conductivity whereas the κ_{total} values of the sample without Bi decrease with temperature, reach a minimum value at 750K and then start to increase.

The lattice thermal conductivity was also calculated as in chapter 4.1.2. It is obvious that $\kappa_{lattice}$ has the major contribution in κ_{total}, especially at low temperatures. Moreover, $\kappa_{lattice}$ of samples with Bi present an almost independent temperature behavior, leading to an extremely low $\kappa_{lattice}=1.69$ W/m.K at 980K for the sample with $x=0.05$. The significant reduction of lattice thermal conductivity is mainly attributed to the substantial atomic mass and size difference between Sb(121.76u)-Bi(208.98u) atoms that leads to an intense point defect scattering and to the increased boundary scattering at the interfaces due to the presence of phase-separation and Bi inclusions. In general, any substitution of an atom with a different one, as well as the presence of nanoinclusions in the HH matrix, tend to induce strain effects and mass fluctuations in the crystal lattice. These fluctuations contribute towards enhanced scattering of phonons with particular wavelengths resulting in suppressed lattice thermal conductivity.

The calculated ZTs are presented in Figure 4.24. The highest ZT was reported for the sample without Bi (ZT~0.9) and the second highest for the sample with $x=0.075$ (ZT~0.73). Even though, the lattice thermal conductivity of $Hf_{0.6}Ti_{0.4}CoSb_{0.75}Bi_{0.05}Sn_{0.2}$ was remarkably low, the decreased power factor prevented this compound to overcome the ZT of $Hf_{0.6}Ti_{0.4}CoSb_{0.8}Sn_{0.2}$ and remained relatively low with a value around 0.69.

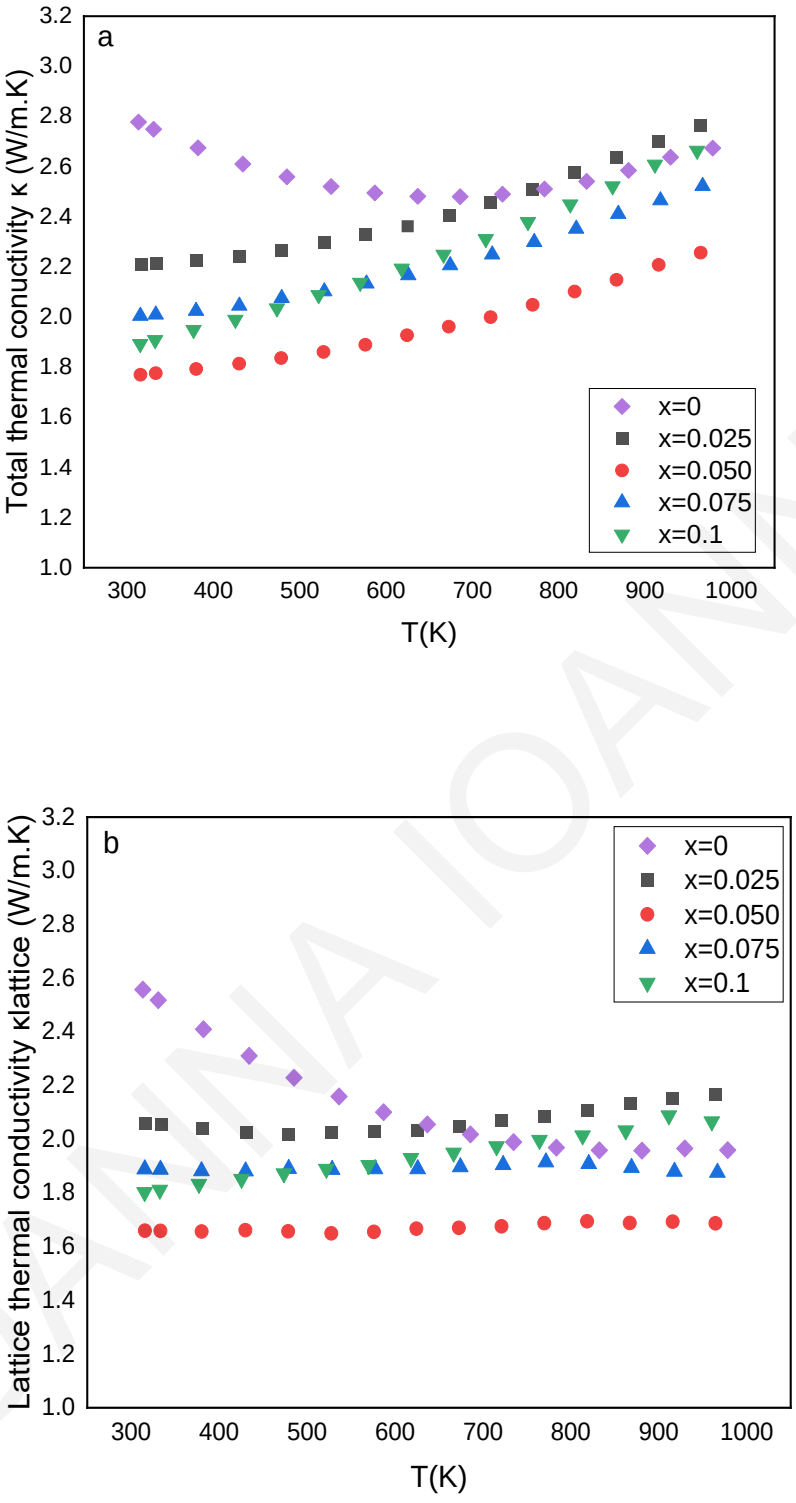

Figure 4.23: Total thermal conductivity (a) and lattice thermal conductivity (b) of $Hf_{0.6}Ti_{0.4}CoSb_{0.8-x}Bi_xSn_{0.2}$ samples.

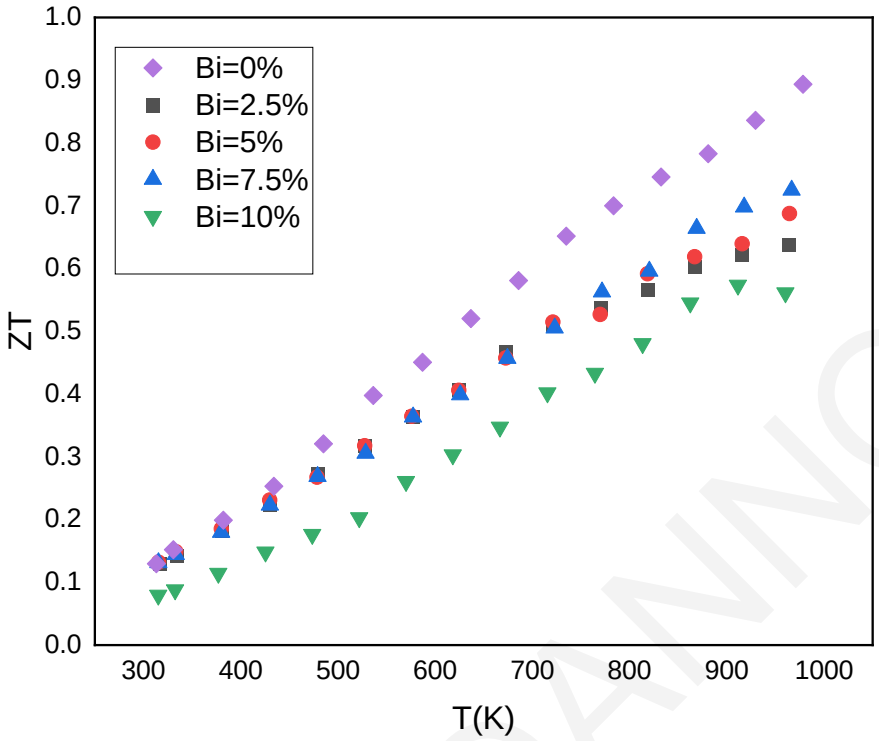

Figure 4.24: Thermoelectric figure-of-merit (ZT) as a function of temperature of $Hf_{0.6}Ti_{0.4}CoSb_{0.8-x}Bi_xSn_{0.2}$ samples.

4.3.4 Conclusion

In this chapter, the isoelectronic substitution of Sb with Bi in $Hf_{0.6}Ti_{0.4}CoSb_{0.8-x}Bi_xSn_{0.2}$ was attempted. Structural investigations revealed residual Bi element, and the presence of phase-separation in in all samples which consequently affected thermoelectric properties of the investigated materials. The increase of Bi/Sb ratio resulted in lower hole concentration and mobility and therefore decreased electrical conductivities and power factors. An extremely low $\kappa_{lattice}$=1.69 W/m.K at 980K was achieved for $Hf_{0.6}Ti_{0.4}CoSb_{0.75}Bi_{0.05}Sn_{0.2}$. This result is mainly attributed to the intense phonon point defect scattering due to mass fluctuations and the increased boundary scattering at the interfaces due to the presence of phase separation. However, the decreased power factor prevented this compound to overcome the ZT of $Hf_{0.6}Ti_{0.4}CoSb_{0.8}Sn_{0.2}$. The highest ZT was reported for the sample without Bi (ZT~0.9) and the second highest for the sample with x=0.075 (ZT~0.73).

4.4 Reduction of Hf via Hf/Zr substitution in (Hf,Zr,Ti)Co(Sb,Sn) solid solutions

In chapter 4.2, a scalable synthesis method was applied in p-type (Hf,Ti)Co(Sb,Sn) compounds and a high thermoelectric figure of merit (ZT~1.1) was reached for the hot-pressed $Hf_{0.6}Ti_{0.4}CoSb_{0.83}Sn_{0.17}$ composition, prepared by 4 hours MA. This excellent result originates from the significant reduction of the lattice thermal conductivity in the Hf/Ti member in combination with nanostructuring and the charge carrier optimization in Sb/Sn member. However, the Hf percentage in this composition is still high in order to be used in cost-effective thermoelectric devices. According to a report on metal prices in the United States through 2010, one kilogram of Hf costs approximately 53 times more than one kilogram of Ti while Zr is only 9 times more expensive than Ti[132]. Cost effectiveness is a major aspect for commercial use and has been often ignored by thermoelectric researchers. Therefore, reducing the Hf usage in HH solid solutions could be a critical step for practical applications [90].

The aim of this part was to achieve a high thermoelectric performance in (Hf,Zr, Ti)Co(Sb,Sn) solid solutions with reduced Hf concentration, prepared by MA. Based on the previously discussed encouraging results of MA in HH compounds, $Hf_{0.6-x}Zr_xTi_{0.4}CoSb_{0.8}Sn_{0.2}$ (x=0,0.1,0.2,0.3,0.4,0.5) samples were prepared as an attempt to replace Hf with Zr and to investigate the effect of isoelectronic substitution on the thermoelectric properties. Then, the charge carrier concentration was optimized by preparing $Hf_{0.4}Zr_{0.2}Ti_{0.4}CoSb_{1-y}Sn_y$ samples and the effect of Sb/Sn doping was evaluated.

4.4.1 Synthesis and consolidation conditions

For the synthesis of (Hf,Zr, Ti)Co(Sb,Sn) solid solutions, the milling process lasted 6 hours and was carried out in a planetary mill at 450rpm. The ball to material ratio was 15:1. The as-milled powders were hot-pressed into high density pellets at temperatures in the range of 1165-1180K for 1hr under pressure of 50MPa.

4.4.2 Results of (Hf,Zr,Ti)$CoSb_{0.8}Sn_{0.2}$ Solid Solution Series

In this section, the MA synthesis of $Hf_{0.6-x}Zr_xTi_{0.4}CoSb_{0.8}Sn_{0.2}$ (x=0,0.1,0.2,0.3,0.4,0.5) materials and the effect of Hf substitution with its lighter and cheaper homologue Zr on their microstructure and thermoelectric properties are discussed. The desired half-Heusler phases were completely formed after four hours of milling and there were no further changes for longer milling (up to 8 hours). According to the results of part 4.2, 6 hours of milling led to best results in terms of thermoelectric properties. Therefore, for the preparation of samples was based on 6hrs alloying followed by hot press sintering.

Structural Characterization:

Figure 4.25a presents the powder X-ray diffraction patterns of the $Hf_{0.6-x}Zr_xTi_{0.4}CoSb_{0.8}Sn_{0.2}$ series after 6 hours of milling. All diffraction peaks are matched with the cubic MgAgAs-type crystal structure indicating the formation of the desired half-Heusler phases without any residual starting elements or other secondary phases presented. The XRD results after hot-pressing show that HH remains as the only phase in all prepared samples (Figure 4.25b). The position of peaks in XRD patterns does not severely change with increasing the level of Hf/Zr substitution. Despite the notable difference between the atomic number and mass of Hf and Zr, their atomic radii are almost identical due to lanthanide contraction effect [133]. The lattice parameter as determined by XRD patterns, geometrical densities of the hot-pressed samples and theoretical densities based on Joshi et al. [117] are presented in Table 4.9. The substitution of Hf with Zr linearly decreases the geometrical density of the samples, as expected. Overall, high-density pellets were prepared with a relative density higher than 94% of the theoretical density.

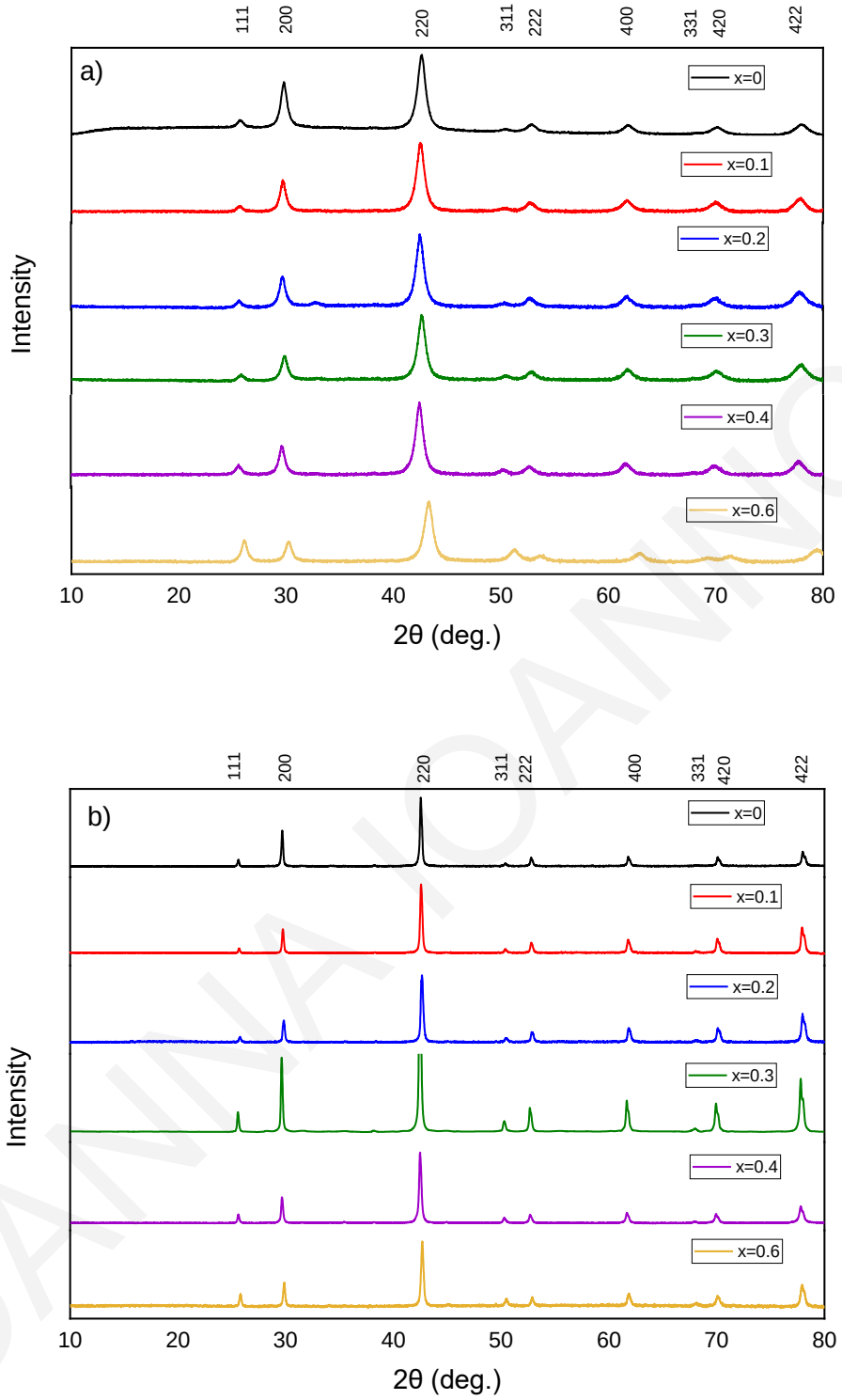

Figure 4.25: a) X-ray powder diffraction patterns of powders $Hf_{0.6-x}Zr_xTi_{0.4}CoSb_{0.8}Sn_{0.2}$ (x=0,0.1,0.2,0.3,0.4,0.5) prepared by 6 hours mechanical alloying and b) the X-ray powder diffraction patterns of hot-pressed pellets

Table 4.9: : Lattice parameter calculated from x-ray diffraction peaks, geometrical densities of the hot-pressed $Hf_{0.6-x}Zr_xTi_{0.4}CoSb_{0.8}Sn_{0.2}$ samples and relative density based on Joshi et al [117].

Composition	Lattice parameter (nm)	Geometrical density (g/cm^3)	Relative density (%)
$Hf_{0.6}Ti_{0.4}CoSb_{0.8}Sn_{0.2}$	0.599	9.13	97
$Hf_{0.5}Zr_{0.1}Ti_{0.4}CoSb_{0.8}Sn_{0.2}$	0.601	8.59	94
$Hf_{0.4}Zr_{0.2}Ti_{0.4}CoSb_{0.8}Sn_{0.2}$	0.601	8.51	96
$Hf_{0.3}Zr_{0.3}Ti_{0.4}CoSb_{0.8}Sn_{0.2}$	0.602	8.14	95
$Hf_{0.2}Zr_{0.4}Ti_{0.4}CoSb_{0.8}Sn_{0.2}$	0.601	8.12	98
$Zr_{0.6}Ti_{0.4}CoSb_{0.8}Sn_{0.2}$	0.599	7.50	96

SEM and EDS analysis were performed (Figures 4.26-4.27 and Table 4.10) to investigate the microscopic features in $Hf_{0.6-x}Zr_xTi_{0.4}CoSb_{0.8}Sn_{0.2}$ (x=0,0.1,0.2,0.3,0.4,0.5) materials. The slight loss of Hf and Sn in all samples with x<0.6 can be explained by the behaviour of Hf and Sn powders that stick on the vial's and balls' surface during milling, resulting a small deviation from the desired alloy composition. Overall, back-scattered images and EDS results revealed homogeneous, stoichiometric and single-phase materials. Contrary to our results, structural investigations in analogous (Hf,Zr,Ti)$CoSb_{0.8}Sn_{0.2}$ solid solutions prepared by arc-melting proved that the samples underwent a dendritic intrinsic phase separation and up to three different HH phases can be identified [73]. Similarly, in a previous study in arc-melted (Ti,Zr)$CoSb_{0.8}Sn_{0.2}$ materials a prominent phase-separation effect was noticed. According to N. S. Chauhan et al. Ti-rich phases were heterogeneously distributed within the Ti-deficient matrix in an arc-melted $Ti_{0.5}Zr_{0.5}CoSb_{0.8}Sn_{0.2}$ alloy [127]. A calculated thermodynamic phase-diagram of the $(Hf_{1-x-y}Zr_xTi_y)NiSn$ system suggests that Ti-rich and Ti-poor grains in arc-melted materials are non-equilibrium states created during solidification and then are kinetically trapped at lower temperatures [134]. The mechanisms by which supersaturated solid solutions form by MA and rapid solidification processing (RSP) techniques like arc-melting, are different. Therefore, the level of solid solubility is different in various systems by these two techniques. For instance, solid solutions are easy to obtained in the full composition range in the Cu-Fe, AlSb-InSb, and Cu-Co systems by MA but not by RSP [107].

Table 4.10: Nominal and chemical composition of hot-pressed $Hf_{0.6-x}Zr_xTi_{0.4}CoSb_{0.8}Sn_{0.2}$ samples as determined by EDS.

Nominal composition	Hf	Zr	Ti	Co	Sb	Sn
$Hf_{0.6}Ti_{0.4}CoSb_{0.8}Sn_{0.2}$	0.56	-	0.45	1.02	0.84	0.14
$Hf_{0.5}Zr_{0.1}Ti_{0.4}CoSb_{0.8}Sn_{0.2}$	0.45	0.12	0.43	1.01	0.84	0.14
$Hf_{0.4}Zr_{0.2}Ti_{0.4}CoSb_{0.8}Sn_{0.2}$	0.35	0.22	0.42	1.02	0.84	0.15
$Hf_{0.3}Zr_{0.3}Ti_{0.4}CoSb_{0.8}Sn_{0.2}$	0.27	0.33	0.43	0.98	0.86	0.13
$Hf_{0.2}Zr_{0.4}Ti_{0.4}CoSb_{0.8}Sn_{0.2}$	0.17	0.43	0.44	0.99	0.85	0.12
$Zr_{0.6}Ti_{0.4}CoSb_{0.8}Sn_{0.2}$	-	0.62	0.43	0.97	0.84	0.13

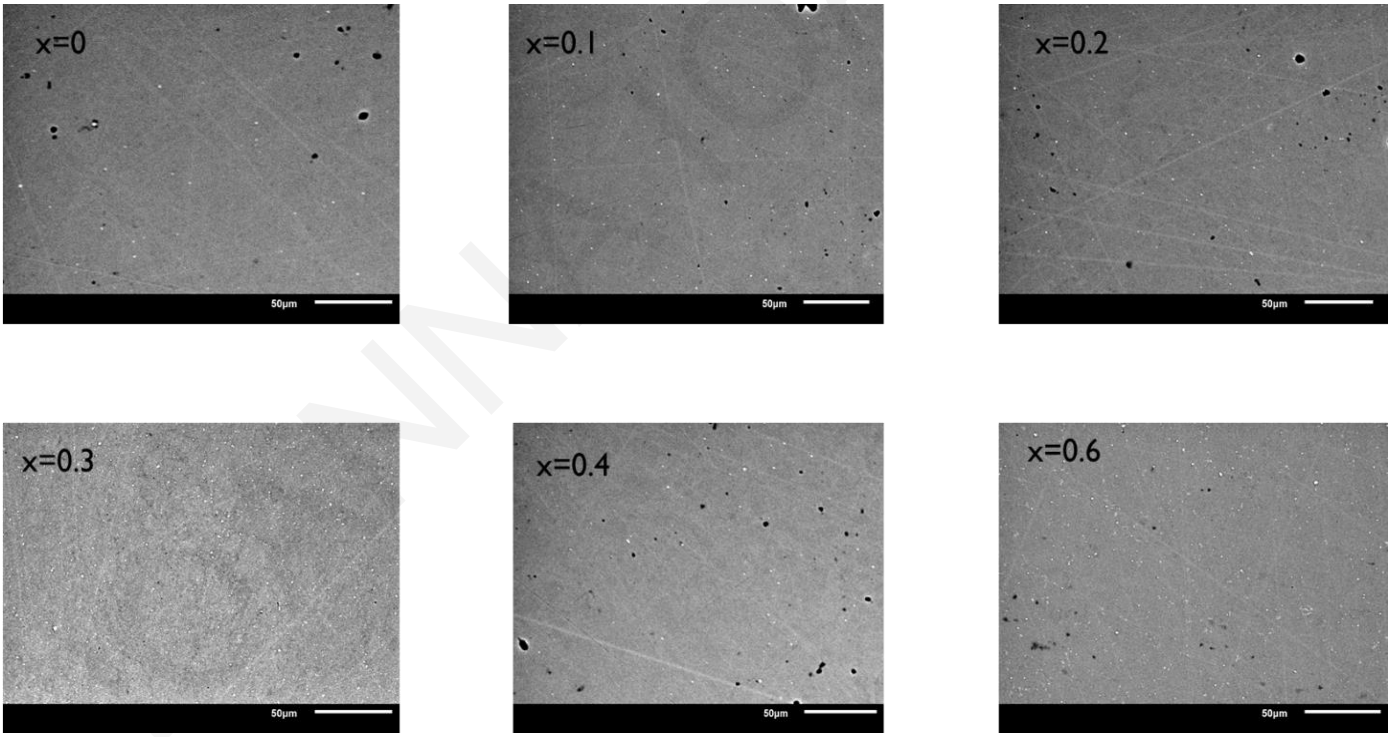

Figure 4.26: Back-scattered electron images of hot-pressed $Hf_{0.6-x}Zr_xTi_{0.4}CoSb_{0.8}Sn_{0.2}$ samples.

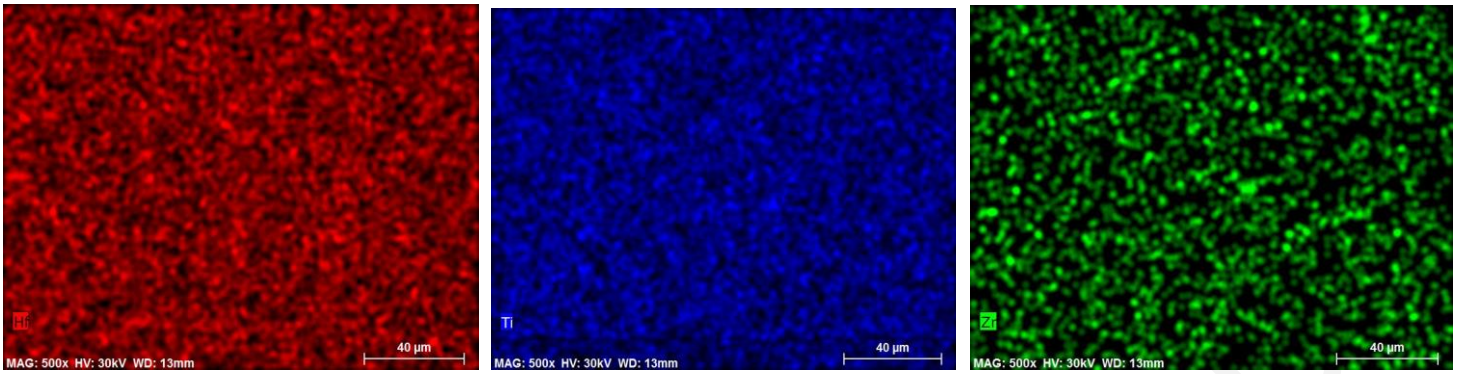

Figure 4.27: Elemental mapping (Hf-Ti-Zr) of $Hf_{0.4}Zr_{0.2}Ti_{0.4}CoSb_{0.8}Sn_{0.2}$ sample.

Figure 4.28a shows a representative image of the morphology of the $Hf_{0.4}Zr_{0.2}Ti_{0.4}CoSb_{0.8}Sn_{0.2}$ sample particles. They are typically medium sized, about 150-200 nm, on average, reaching up to 450 nm. Each one is single crystalline, as confirmed by the Selected Area Diffraction (SAD) pattern inset in Figure 4.28a, the latter viewed along the [111] zone axis. Measurements of the *d* spacings of the 220 reflections resulted in a mean lattice constant of a_{SAD}=0.604 nm, in very good agreement with the 'theoretical' lattice parameter of $Hf_{0.4}Zr_{0.2}Ti_{0.4}CoSb_{0.8}Sn_{0.2}$. The latter has been calculated using Vegard's law, taking into consideration the values of the three members, i.e., $TiCoSb_{1-x}Sn_x$ (a = 0.589 nm) $HfCoSb_{1-x}Sn_x$ (a = 0.604 nm) and $ZrCoSb_{1-x}Sn_x$ (a = 0.607 nm), resulting in $a_{theor.}$ = 0.596 nm, approximately [70]. This is also in agreement with the XRD results, where the lattice parameter of $Hf_{0.4}Zr_{0.2}Ti_{0.4}CoSb_{0.8}Sn_{0.2}$ was calculated as α_{XRD} = 0.601 nm.

A secondary morphology of the sample is in the form of smaller nanoparticles, some of which are illustrated in Figure 4.28b by arrows. These nanoparticles are crystalline, as well and have sizes of 5-15 nm, although some may reach up to 60-70 nm. Figure 4.28b shows an HRTEM image of such a crystalline nanoparticle, with a size of 61.7 nm. A thin band of nearly amorphous structure is observed at its surface, probably due to ball milling. On the crystalline region mainly (200) lattice fringes are dominant; experimental measurements of their separation provided d_{200}=0.295 nm, resulting in a lattice constant of a_{HRTEM}=0.590 nm, close to the 'theoretical' one, as well as the XRD- and SAD-deduced experimental ones. The slightly lower value calculated in Figure 4.28b and in similar HRTEM images could be attributed to small fluctuations of the elemental content in such particles, especially when it comes to its Sb percentage. This was confirmed by the EDS analysis results, too, where the average stoichiometry of this

particle deviated from the nominal $Hf_{0.4}Zr_{0.2}Ti_{0.4}CoSb_{0.8}Sn_{0.2}$ one, having in particular about 5-8 at% deficiency in Zr and Co.

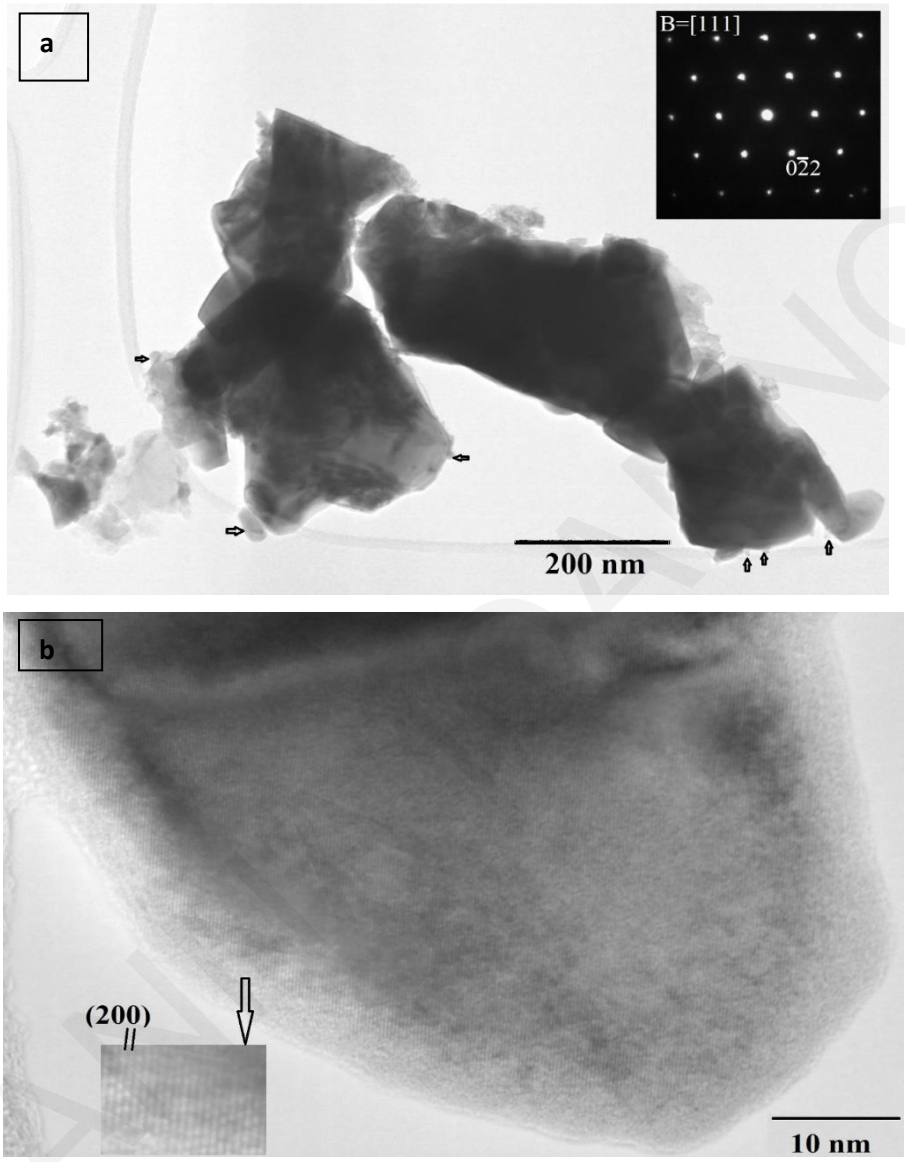

Figure 4.28: a) TEM image of the particles' morphology at the $Hf_{0.6-x}Zr_xTi_{0.4}CoSb_{0.8}Sn_{0.2}$ sample. The SAD pattern inset, coming from one of these particles, is viewed along [111]. (b) HRTEM image of a representative nanocrystalline particle, predominately revealing.

Table 4.11: Nominal and chemical composition of the hot-pressed $Hf_{0.4}Zr_{0.2}Ti_{0.4}CoSb_{0.8}Sn_{0.2}$ sample as determined by EDS and TEM.

Element	Nominal	SEM	TEM
Hf	**0.4**	**0.35**	**0.42**
Zr	**0.2**	**0.22**	**0.19**
Ti	**0.4**	**0.42**	**0.41**
Co	**1**	**1.02**	**0.99**
Sb	**0.8**	**0.84**	**0.75**
Sn	**0.2**	**0.15**	**0.23**
Sb+Sn	**1**	**0.99**	**0.98**

Thermoelectric Properties:

The temperature dependent Seebeck coefficient, electrical conductivity and power factor ($S^2\sigma$) of the hot-pressed $Hf_{0.6-x}Zr_xTi_{0.4}CoSb_{0.8}Sn_{0.2}$ samples are presented in Figure 4.29. All samples exhibit positive S values, confirming p-type materials. The highest value of 233 μV/K was observed for $Hf_{0.6}Ti_{0.4}CoSb_{0.8}Sn_{0.2}$ at 973 K and decreased with increasing Zr, indicating the increase of carrier concentration. Even though, the substitution of Hf with Zr is isoelectronic, the carrier concentration and therefore the S values change. This effect can be explained by the alteration of electronic structure which thereafter alters the carriers concentration and their effective mass [72]. The change of carrier concentration and S upon isoelectronic replacement has been reported by several previous investigations[72][85][74]. For instance, hall measurements by Chauhan et al. in (Ti/Zr)Co(Sb,Sn) solid solutions support that isoelectronic substitution influence the carrier concentration and carrier mobility [85]. Moreover, the S values of sample with x=0.6 present a stronger temperature dependence than samples with x<0.6. Gandi et al. calculated that the energy bandgap of TiCoSb, HfCoSb and ZrCoSb is 1.05eV, 1.13eV and 1.06eV respectively [57]. The smaller bandgap of TiCoSb and ZrCoSb explains the slight drop of Seebeck coefficient in samples with low Hf concentration (Hf≤0.2) at T≥750K due to bipolar excitation. Electrical conductivity decreases when Zr(x) percentage rises, leading us to the

conclusion that Hf substitution with Zr affects the carrier mobility. Moreover, samples with $x \leq 0.3$ present relatively stable σ values with increasing temperature while the σ values of samples with $x \geq 0.4$ significantly increase with temperature. The aforementioned Seebeck coefficient does not intensively decrease with intrinsic excitation, suggesting the presence of an additional mechanism that influence the electrical conductivity [121]. This mechanism can be due to the enhanced grain boundary scattering that usually appears in materials with high nanocrystallinity, resulting thermally activated mobility. In nanostructured materials, energy barriers that are known to form at the grain boundaries, result in strong carrier scattering and restrict electronic conduction at low temperatures. When the temperature rises, charge carriers are thermally excited across the energy barriers and consequently the electrical conductivity increases[121]. This effect has been discussed (chapter 4.2) in $Hf_xTi_{1-x}CoSb_{0.8}Sn_{0.2}$ materials prepared by mechanical alloying, as well as in other thermoelectric systems, such as Mg_3Sb_2–Mg_3Bi_2 solid solution and $NaPb_mSbQ_{m+2}$ (Q = S, Se, Te)[135][119][120][121]. In specific, the substantial percentage of nanocrystallinity in $Hf_xTi_{1-x}CoSb_{0.8}Sn_{0.2}$ was assessed by transmission electron microscopy experiments that proved the presence of primary particles in the size range of 350 nm and nanograins in the size range of ~12 nm [135]. While, the average particle size for this work's sample with x=0.2 was found to be a little bit lower, around 150-200 nm. The calculated power factors are shown in Figure 4.29c $Hf_{0.6}Ti_{0.4}CoSb_{0.8}Sn_{0.2}$ reached the highest PF ~24.5 $\mu W/cmK^2$ at 973 K. Samples with x=0.1-0.3 follow with PF values around 17 $\mu W/cmK^2$.

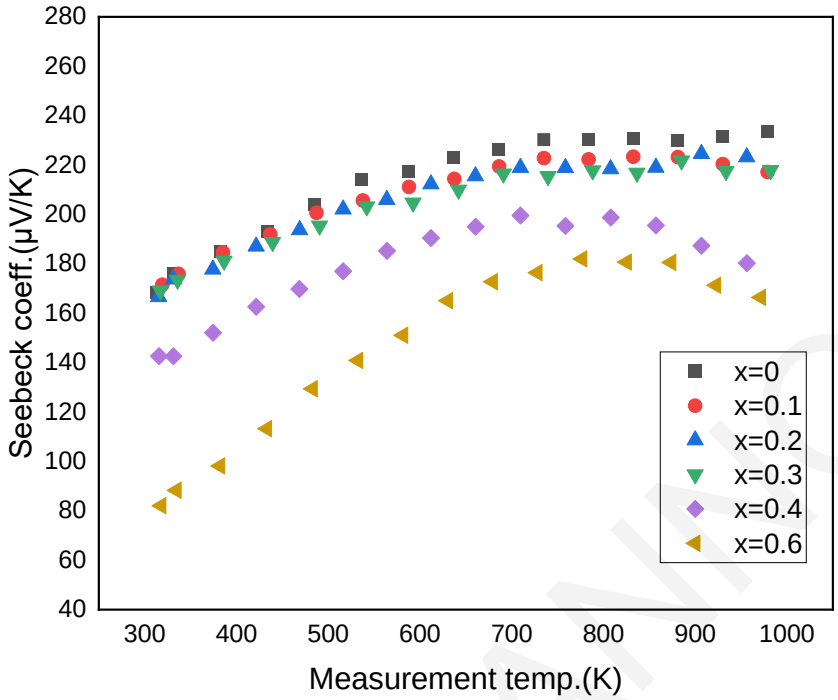

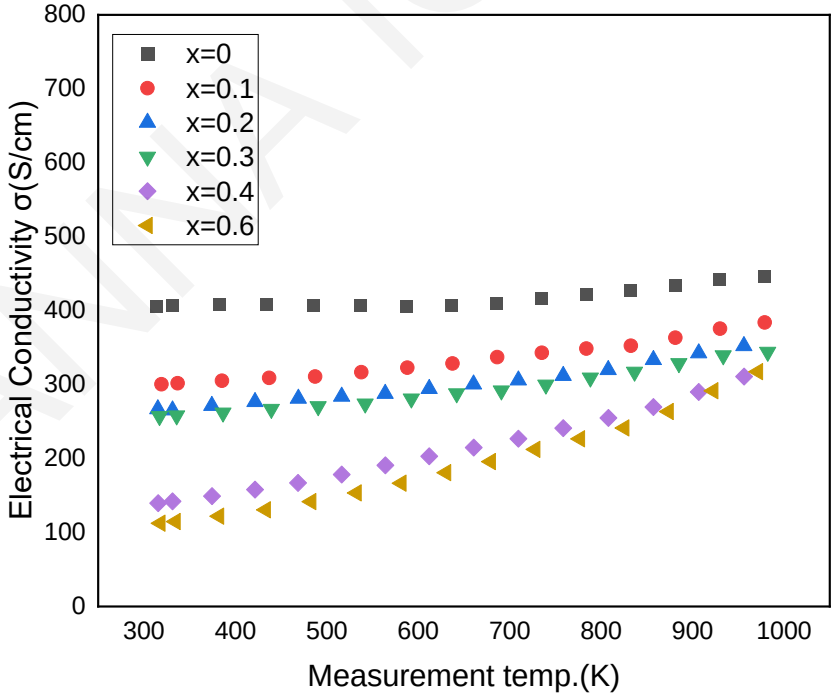

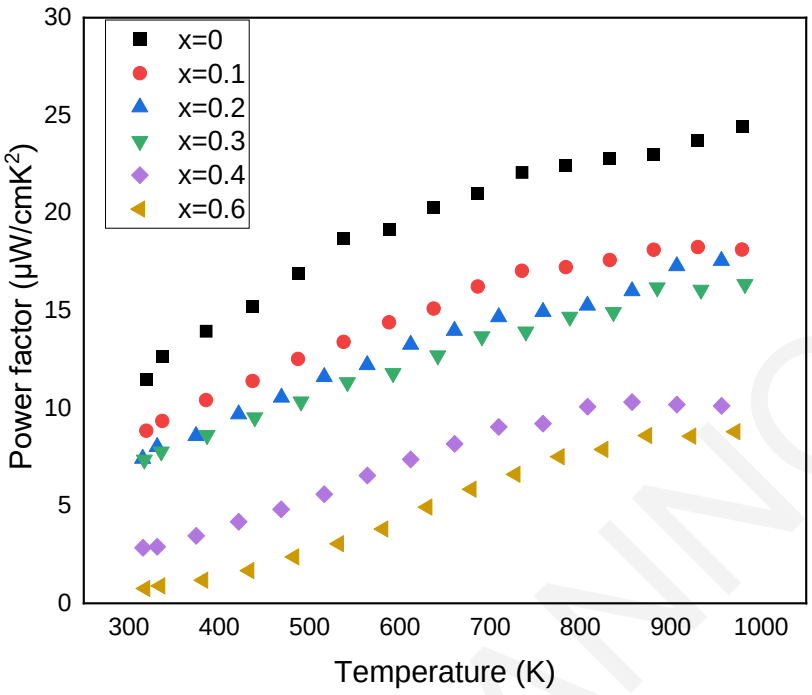

Figure 4.29: Temperature dependent Seebeck coefficient (a), electrical conductivity (b) and Power factor (c) of $Hf_{0.6-x}Zr_xTi_{0.4}CoSb_{0.8}Sn_{0.2}$ samples.

The temperature dependence of total thermal conductivity (κ) and lattice thermal conductivity ($\kappa_{lattice}$) of $Hf_{0.6-x}Zr_xTi_{0.4}CoSb_{0.8}Sn_{0.2}$ samples are presented in Figure 4.30(a-b) while the lattice thermal conductivity at room temperature as a function of Zr concentration (x) is presented in Figure 4.30c. At room temperature, samples with x=0 and x=0.6 present the highest thermal conductivity values (κ=2.8 W/m·K and κ=3.0 W/m·K respectively). On the other hand, samples with x=0.1-0.4 present lower thermal conductivity at room temperature (in the range of 2.4-2.15 W/m·K) but then slightly increases with rising temperature due to the increase of specific heat (Cp) and electronic thermal conductivity (κ_e). The lowest thermal conductivity at high temperatures with a value of 2.48 W/m·K was recorded by $Hf_{0.4}Zr_{0.2}Ti_{0.4}CoSb_{0.8}Sn_{0.2}$ at 960K. To have a better insight of how the replacement of Hf with Zr affects the heat transport in $Hf_{0.6-x}Zr_xTi_{0.4}CoSb_{0.8}Sn_{0.2}$ materials, the lattice thermal conductivity was estimated by subtracting the electronic contribution from total thermal conductivity (κ), as in previous chapters. In addition, a simple exponential function, $\kappa_{lattice} \propto A \cdot T^N$, was used to determine the exponent N in all temperature dependent $\kappa_{lattice}$ plots (Fig.4.30b).

The lattice thermal conductivity of samples with $0.1 \leq x \leq 0.4$ show a relatively stable/independent (N~0) temperature behavior, while the $\kappa_{lattice}$ of samples with x=0 and 0.6 drops with temperature (N~-0.25). The lowest $\kappa_{lattice}$ values (~1.95 W/m·K) were recorded for $Hf_{0.6}Ti_{0.4}CoSb_{0.8}Sn_{0.2}$ as expected, and $Hf_{0.4}Zr_{0.2}Ti_{0.4}CoSb_{0.8}Sn_{0.2}$ at 970K. In Figure 4.30c the $\kappa_{lattice}$ as a function of Zr (x) was plotted in comparison with $(Hf,Ti,Zr)CoSb_{0.8}Sn_{0.2}$ compositions by E.Rausch et al. and Yan et al. [66][75]. The lattice thermal conductivity of the arc-melted $Hf_{0.35}Zr_{0.35}Ti_{0.3}CoSb_{0.8}Sn_{0.2}$ by E.Rausch et al. is significantly higher than the $\kappa_{lattice}$ of this work's samples [66]. This can be attributed to the higher grain boundary density in this work's nanostructured samples as well as to the bigger atomic mass variation which results in stronger phonon scattering. The $\kappa_{lattice}$ of the nanostructured $Hf_{0.72}Zr_{0.1}Ti_{0.18}CoSb_{0.8}Sn_{0.2}$ and $Hf_{0.45}Zr_{0.45}Ti_{0.1}CoSb_{0.8}Sn_{0.2}$ by Yan et al. is lower than that of $Hf_{0.35}Zr_{0.35}Ti_{0.3}CoSb_{0.8}Sn_{0.2}$ by E.Rausch et al. due to the increased phonon-scattering at the grain boundaries in nanostructured materials [75]. However, our nanostructured samples recorded even lower $\kappa_{latttice}$ values indicating enhanced mass and strain field variations in $Hf_{0.6-x}Zr_xTi_{0.4}CoSb_{0.8}Sn_{0.2}$ compositions. Published studies usually highlight that the Hf-Ti combination in half-Heusler compounds is expected to cause increased phonon scattering and lower $\kappa_{lattice}$ than other combinations because of bigger difference in the size and mass of Ti and Hf atoms [71][136]. In this study, we show that similar lattice thermal conductivity values can be also achieved by Ti-Zr-Hf combination and this excellent result indicates that $Hf_{0.4}Zr_{0.2}Ti_{0.4}CoSb_{0.8}Sn_{0.2}$ solid solution would be a good selection for further investigation regarding thermoelectric figure-of-merit.

In a theoretical analysis by Joshi et al. was mentioned that in TiCoSb, ZrCoSb and HfCoSb materials the maximum contribution to heat transfer comes from the acoustic branch of phonons and that the mixing of acoustic and optical mode phonons causes phonon-phonon scattering which as a result reduces the lattice thermal conductivity of a compound [117]. Different atoms contribute in a different way in phonon DOS. Heavier atoms contribute to the low modes of frequencies while light atoms contribute to the higher one[117]. As in chapter 4.2, the disorder scattering parameter Γ was calculated to give us a better insight of the phonon point defect scattering due to mass fluctuations in solid solutions. The disorder scattering parameter Γ describes the point defect scattering of phonons and it has two components: the scattering parameter due to mass fluctuations Γ_M and the scattering parameter due to strain field fluctuations Γ_S

($\Gamma=\Gamma_M+\Gamma_S$) [124][125]. In this case, the Γ_S parameter was considered constant with changing the Hf/Zr ratio because of high similarity between the atomic size of Hf and Zr [82].

In Figure 4.30d, the results from the Γ_M parameter calculations are presented as a function of Zr concentration. Γ_M significantly decreases as the Zr percentage rises. Specifically, the Hf-Ti combination, as well as the Hf-Ti-Zr combination with a low Zr percentage ($x \leq 0.2$) present a Γ_M around 0.13, which is expected to cause increased phonon scattering due to high atomic mass fluctuations. On the other hand, the Ti-Zr combination presents a decrease of approximately 85% in the Γ_M parameter, suggesting lower scattering for phonons and therefore higher lattice thermal conductivity. Based on the calculated Γ_M, the $\kappa_{lattice}$ value at room temperature for $Ti_{0.4}Hf_{0.6}CoSb_{0.8}Sn_{0.2}$ is larger than expected. Interestingly, $\kappa_{lattice}$ decreases when Zr is incorporated in the lattice and then remains almost unchanged for low Zr ($x \leq 0.2$) concentration. This partially agrees with the calculated Γ_M parameter that remains almost the same at low Zr percentages since it is more affected by the presence of the Hf-Ti combination and their higher mass difference. The higher $\kappa_{lattice}$ of x=0 indicates that this theoretical model cannot fully explain the $\kappa_{lattice}$ results and that other factors may influence the $\kappa_{lattice}$ behavior. For instance, the higher relatively density of x=0 sample or a possible alteration of grain boundaries with Hf/Zr substitution could further explain the experimental values. At higher Zr concentration, Γ_M parameter strongly decreases resulting in an increasing lattice thermal conductivity.

In Figure 4.31 the dimensionless thermoelectric figure-of-merit (ZT) is presented as a function of temperature. The highest ZT value equal to 0.9 was recorded for $Hf_{0.6}Ti_{0.4}CoSb_{0.8}Sn_{0.2}$ and the second highest ZT equal to 0.68 was achieved for $Hf_{0.4}Zr_{0.2}Ti_{0.4}CoSb_{0.8}Sn_{0.2}$ at 970K and it is mainly attributed to the low lattice thermal conductivity of $Hf_{0.4}Zr_{0.2}Ti_{0.4}CoSb_{0.8}Sn_{0.2}$.

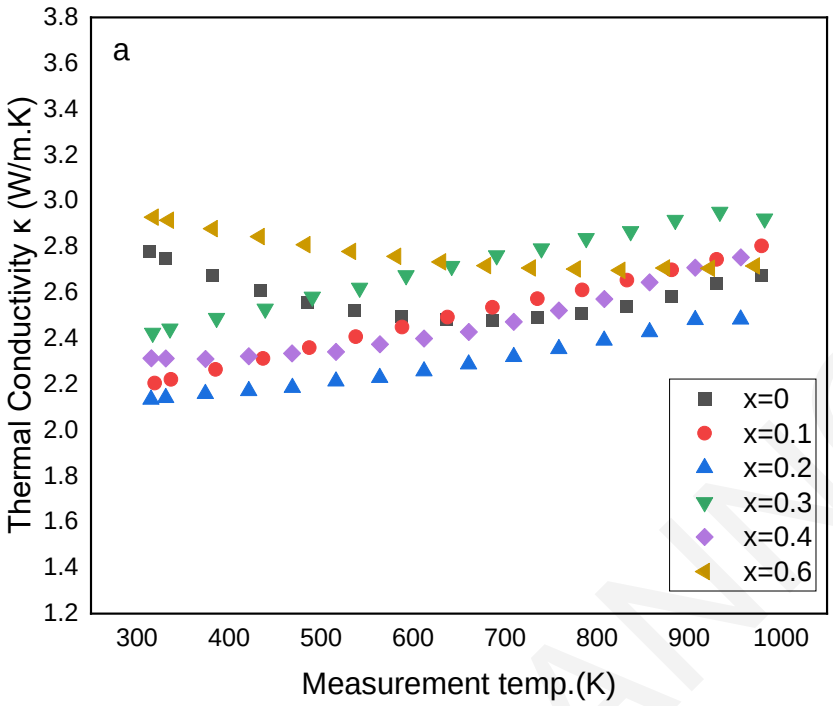

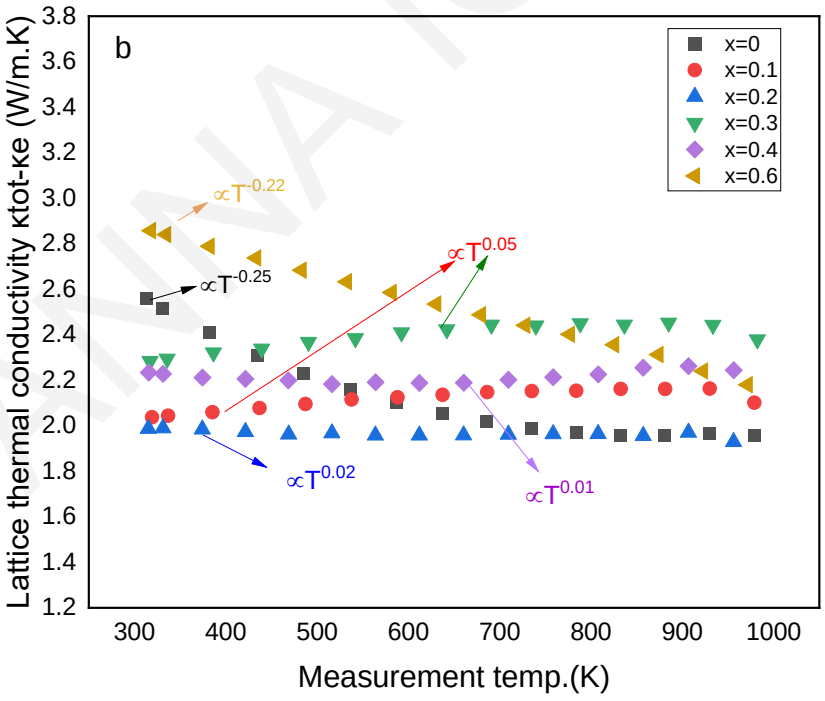

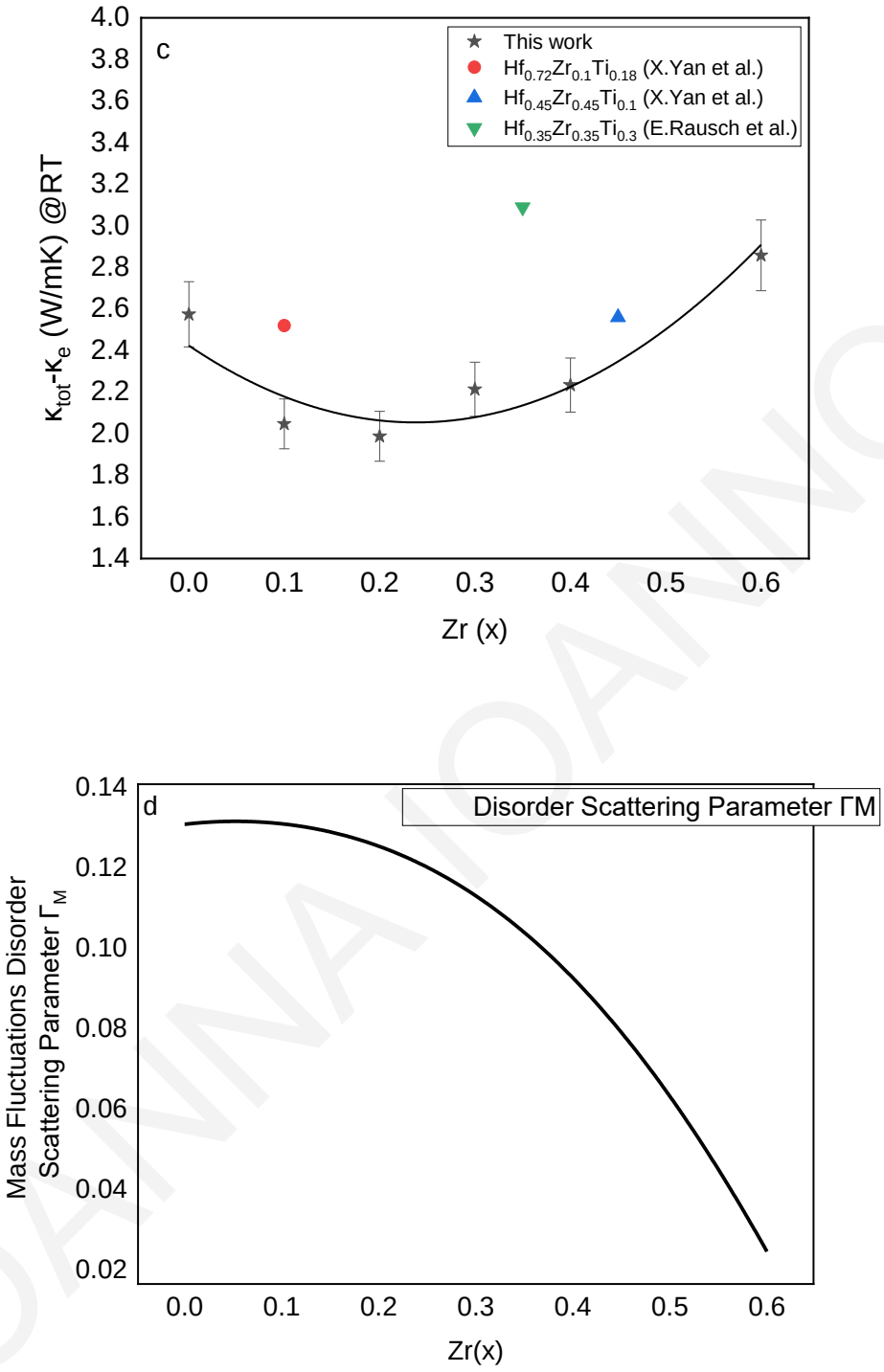

Figure 4.30: Total thermal conductivity (a) and lattice thermal conductivity (b) of $Hf_{0.6-x}Zr_xTi_{0.4}CoSb_{0.8}Sn_{0.2}$ samples as a function of temperature, the lattice thermal conductivity at room temperature in comparison with (Hf,Ti,Zr)$CoSb_{0.8}Sn_{0.2}$ compositions by E.Rausch et al. and Yan et al. [66][75] (the line is guide to the eye) (c) and the theoretical disorder scattering parameter due to mass fluctuations Γ_M as function of Zr concentration (d).

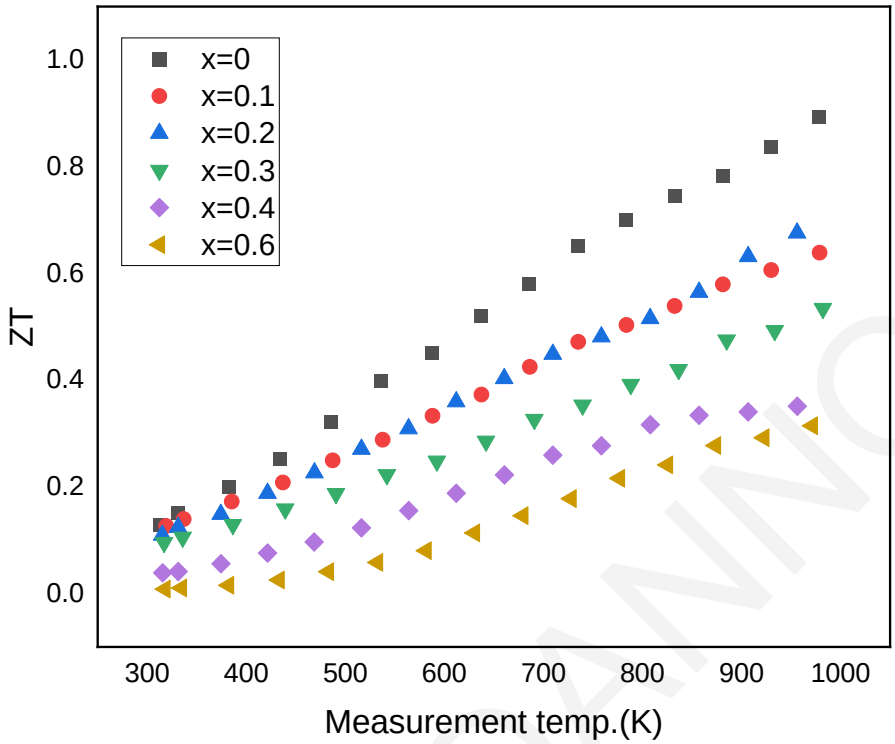

Figure 4.31: Thermoelectric figure-of-merit ZT as a function of temperature for $Hf_{0.6-x}Zr_xTi_{0.4}CoSb_{0.8}Sn_{0.2}$ samples.

4.4.3 Results of $Hf_{0.4}Zr_{0.2}Ti_{0.4}CoSb_{1-y}Sn_y$ Solid Solution Series

The optimization of carrier concentration is a typical method for further improvement in a material's TE performance. In this part, we investigate the adjustment of doping level by the partial substitution of Sb with Sn in $Hf_{0.4}Zr_{0.2}Ti_{0.4}CoSb_{1-y}Sn_y$ (y=0.15,0.17,0.20,0.23,0.25) solid solution series.

Structural Characterization:

The XRD diffraction patterns of all prepared samples after hot-pressing revealed the desired HH phase (Figure 4.32). In Table 4.12, we present the lattice parameter, the geometrical densities of the hot-pressed samples and theoretical densities based on Joshi et al.[117]. The change of Sb/Sn ratio does not significantly affect the geometrical density because of high similarity in the size and mass of the two elements. Back-scattered images and EDS results of samples with different Sb/Sn ratios show homogeneous single-phase materials. Considering that there is an overlap between Sb and Sn in the EDS spectra and that the relative error of EDS results is approximately 5%, the samples can be considered as nearly stoichiometric and single phase. In contrast to MA method, E. Rauch et al. reported that in an investigation of an analogous arc-melted system ($Ti_{0.3}Zr_{0.35}Hf_{0.35}CoSb_{1-x}Sn_x$), all samples underwent an intrinsic phase separation and inclusions of additional binary phases on a micrometer scale appeared in all samples with Sn-substitution level greater than 20%[66].

Table 4.12: The lattice parameter, geometrical densities of the hot-pressed $Hf_{0.4}Zr_{0.2}Ti_{0.4}CoSb_{1-y}Sn_y$ samples and relative density.

Sn(y)	Lattice Parameter (nm)	Geometrical density (g/cm^3)	Relative density (%)
0.15	0.601	8.47	95
0.17	0.603	8.44	95
0.20	0.599	8.51	96
0.23	0.599	8.86	100
0.25	0.599	8.30	94

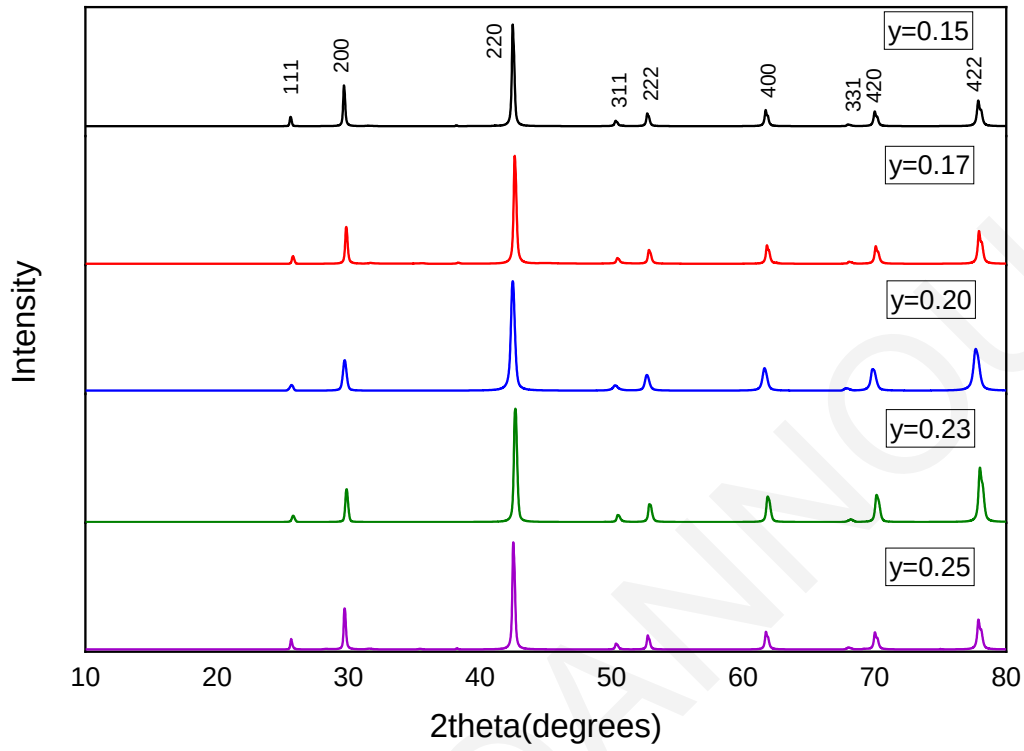

Figure 4.32: X-ray powder diffraction patterns of $Hf_{0.4}Zr_{0.2}Ti_{0.4}CoSb_{1-y}Sn_y$ hot-pressed pellets.

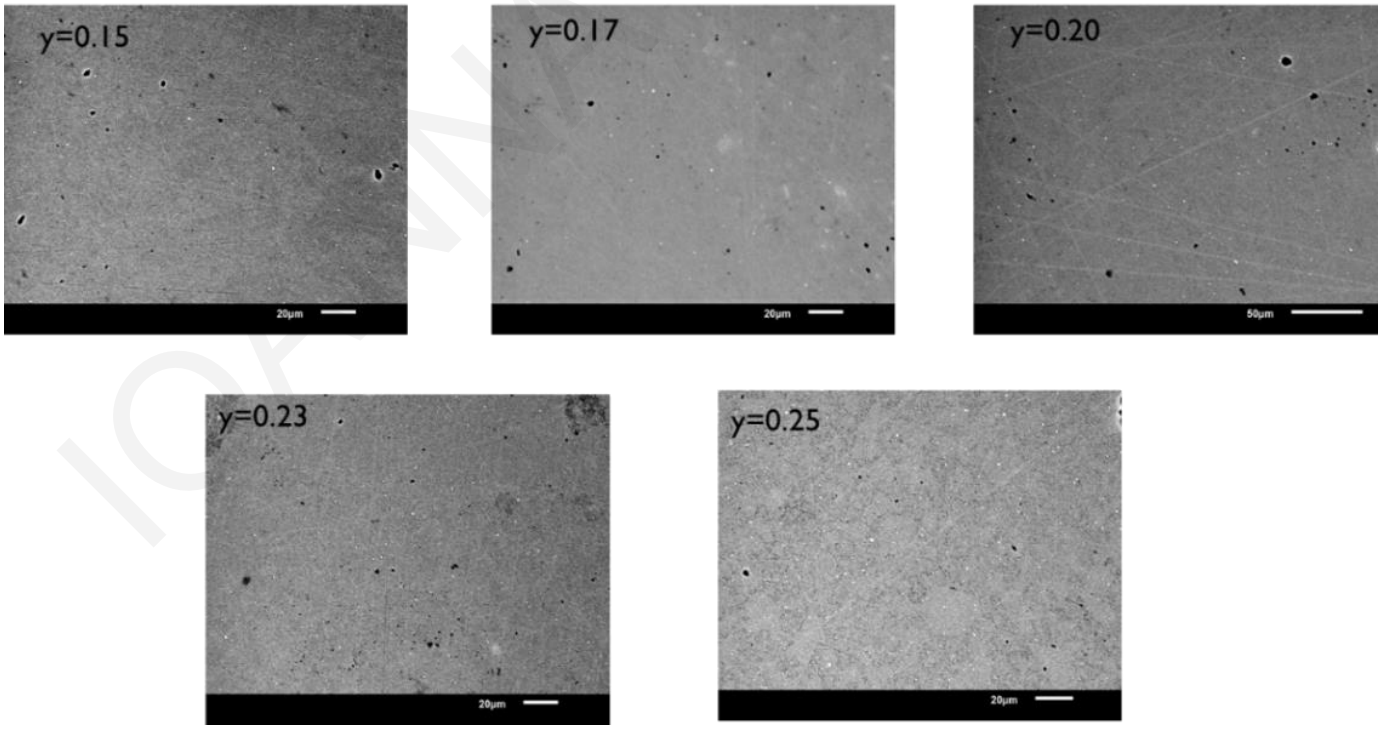

Figure 4.33: Back-scattered electron images of hot-pressed $Hf_{0.4}Zr_{0.2}Ti_{0.4}CoSb_{1-y}Sn_y$ samples.

Table 4.13: Nominal and chemical composition of hot-pressed $Hf_{0.4}Zr_{0.2}Ti_{0.4}CoSb_{1-y}Sn_y$ samples as determined by EDS.

Nominal composition	Hf	Zr	Ti	Co	Sb	Sn
$Hf_{0.4}Zr_{0.2}Ti_{0.4}CoSb_{0.85}Sn_{0.15}$	0.36	0.22	0.43	1.01	0.88	0.09
$Hf_{0.4}Zr_{0.2}Ti_{0.4}CoSb_{0.83}Sn_{0.17}$	0.36	0.23	0.44	1.00	0.87	0.11
$Hf_{0.4}Zr_{0.2}Ti_{0.4}CoSb_{0.8}Sn_{0.2}$	0.35	0.22	0.42	1.02	0.84	0.15
$Hf_{0.4}Zr_{0.2}Ti_{0.4}CoSb_{0.77}Sn_{0.23}$	0.36	0.22	0.44	1.00	0.85	0.13
$Hf_{0.4}Zr_{0.2}Ti_{0.4}CoSb_{0.75}Sn_{0.25}$	0.36	0.22	0.43	1.01	0.79	0.19

Thermoelectric properties:

In Figure 4.34 the Seebeck coefficient and electrical conductivity data along with the calculated power factors are presented. Seebeck coefficient (Fig 4.34 a) increases with increasing temperature, reaches a maximum value at around 750K and then starts to decrease suggesting the onset of bipolar excitation. The Sb substitution with Sn in $Hf_{0.4}Zr_{0.2}Ti_{0.4}CoSb_{1-y}Sn_y$ solid solutions, introduces holes into the system, thus the carrier concentration increases. Furthermore, samples with y = 0.17 and 0.15 present almost similar Seebeck coefficient values, suggesting similar charge carrier concentrations but different carrier mobilities according to electrical conductivity measurements. Additionally, samples with y = 0.23 and y = 0.25 present a higher S at room temperature than y = 0.2. This could be attributed to Sn loss during milling, resulting in a deviation from the nominal composition and therefore to lower charge carrier concentration. At high temperatures, $Hf_{0.4}Zr_{0.2}Ti_{0.4}CoSb_{0.75}Sn_{0.25}$ presented the lowest S~208μV/K, while $Hf_{0.4}Zr_{0.2}Ti_{0.4}CoSb_{0.77}Sn_{0.23}$ and $Hf_{0.4}Zr_{0.2}Ti_{0.4}CoSb_{0.8}Sn_{0.2}$ remained a little bit higher (S~225μV/K). Figure 4.34b demonstrates that the electrical conductivity increases with increasing Sn content. Despite the different doping level of samples with y=0.20 and 0.23, their σ values are almost identical at all temperatures, indicating a higher carrier mobility in $Hf_{0.4}Zr_{0.2}Ti_{0.4}CoSb_{0.8}Sn_{0.2}$ sample. Electrical conductivity rises with increasing temperature in all samples, revealing again the presence of a thermally activated carrier mobility that resulted by the enhanced grain boundary scattering. The calculated Power factors ($PF=S^2\sigma$) are presented in Figure 4.34c. Despite the low Seebeck coefficient, the high electrical conductivity of $Hf_{0.4}Zr_{0.2}Ti_{0.4}CoSb_{0.75}Sn_{0.25}$ contributed in achieving the highest PF=20 $\mu W/K^2cm$ at 980K. This result corresponds to 16% improvement in PF comparatively to $Hf_{0.4}Zr_{0.2}Ti_{0.4}CoSb_{0.8}Sn_{0.2}$, which was our starting material.

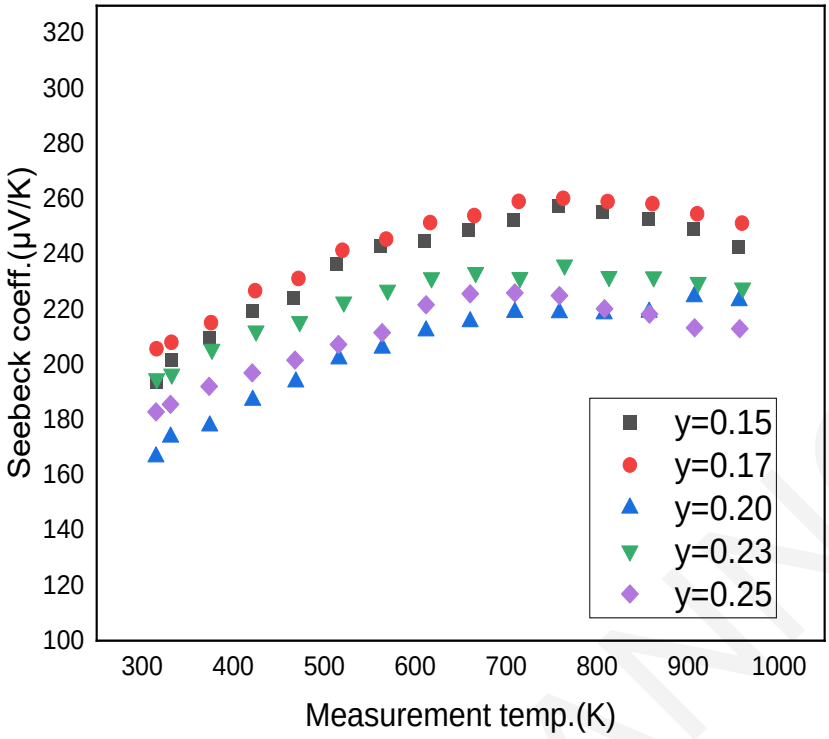

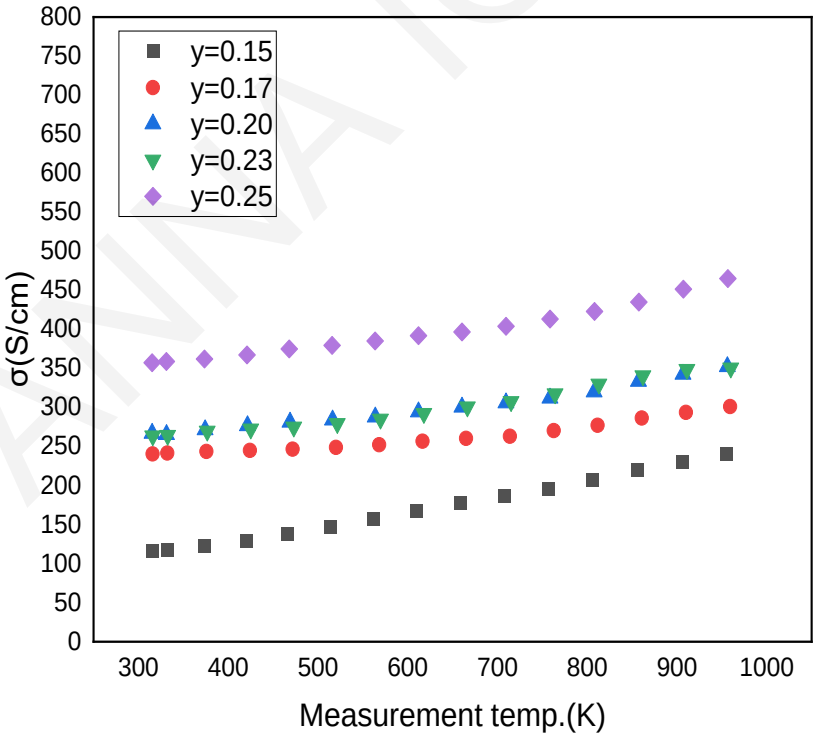

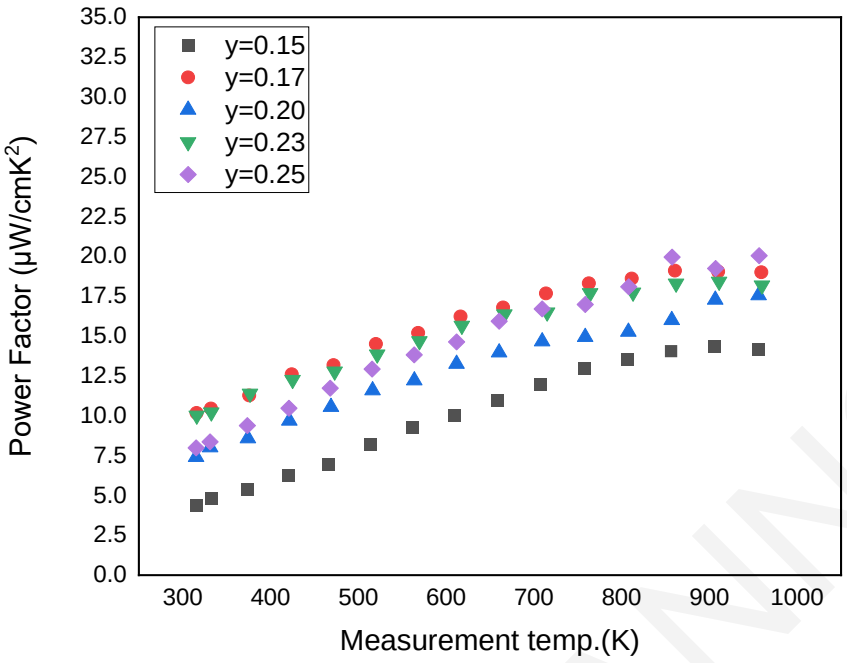

Figure 4.34: Temperature dependent Seebeck coefficient (a), electrical conductivity (b) and Power factor (c) of $Hf_{0.4}Zr_{0.2}Ti_{0.4}CoSb_{1-y}Sn_y$ samples.

The total and lattice thermal conductivity plots of the investigated compounds are displayed in Figure 4.35. At room temperature, the thermal conductivity of samples with y=0.17, 0.20,0.23 present lower κ values (~2.13 W/mK) than that of y=0.15 and 0.25. However, all samples exhibit relatively low thermal conductivity values at room temperature in the range of 2.23-2.12 W/mK. At temperatures above 500K, κ_{tot} gradually increases and reaches the highest value of 2.80 W/mK for $Hf_{0.4}Zr_{0.2}Ti_{0.4}CoSb_{0.75}Sn_{0.25}$. To further understand the influence of substitution level, the lattice thermal conductivity was again calculated. The enhanced phonon scattering with increasing temperature, lowers the heat flux and results in reduced lattice thermal conductivity. Although, the onset of bipolar diffusion at 700K results in a slight increase of lattice thermal conductivity for almost all samples. The lowest $\kappa_{lattice}$=1.85 W/mK was recorded by $Hf_{0.4}Zr_{0.2}Ti_{0.4}CoSb_{0.77}Sn_{0.23}$ at 960K.

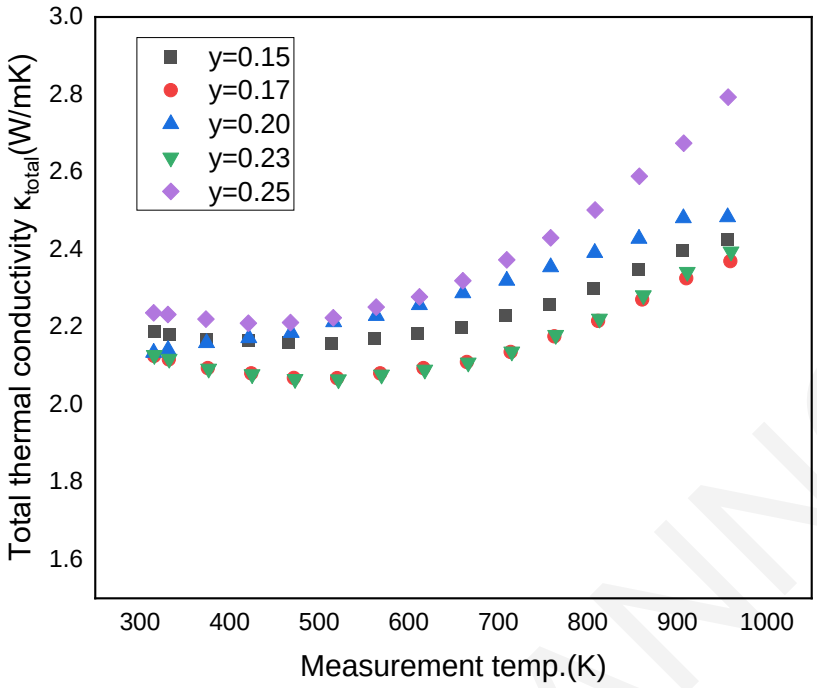

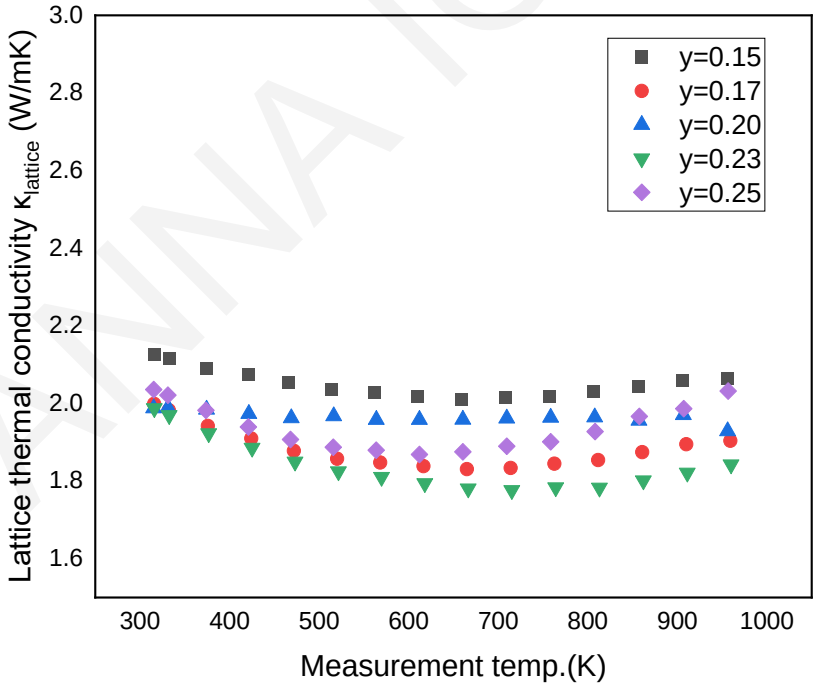

Figure 4.35:Temperature dependent total thermal conductivity (a) and lattice thermal conductivity (b) of $Hf_{0.4}Zr_{0.2}Ti_{0.4}CoSb_{1-y}Sn_y$ hot-pressed samples.

The dimensionless figure of merit ZT of all HP samples is presented in Figure 4.36. The results reveal that the best thermoelectric performance is obtained for $Hf_{0.4}Zr_{0.2}Ti_{0.4}CoSb_{0.83}Sn_{0.17}$ composition. The mechanically alloyed compounds with the optimal Hf/Zr/Ti and Sn/Sb ratios led to a high ZT of 0.77 at 960K, a value that corresponds to 15% improvement with respect to that of $Hf_{0.4}Zr_{0.2}Ti_{0.4}CoSb_{0.8}Sn_{0.2.}$ It has been found that the substitution level of 17% Sn for Sb is the most effective in $Hf_{0.4}Zr_{0.2}Ti_{0.4}CoSb_{1-y}Sn_y$ compounds prepared by mechanical alloying.

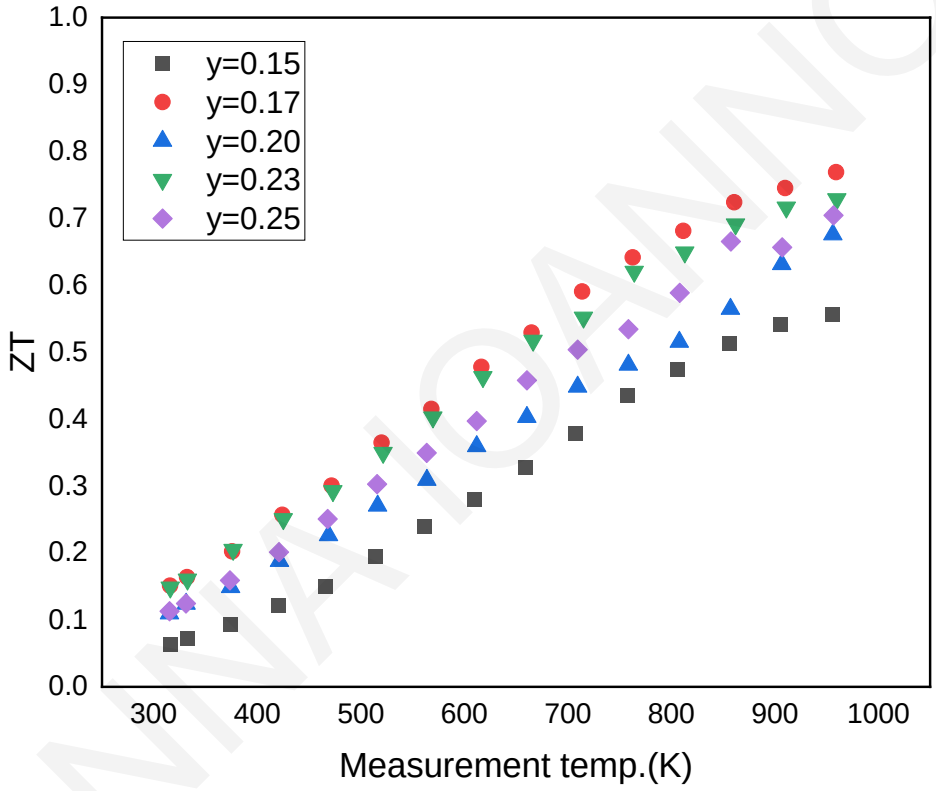

Figure 4.36: Temperature dependent thermoelectric figure-of-merit (ZT) of $Hf_{0.4}Zr_{0.2}Ti_{0.4}CoSb_{1-y}Sn_y$ hot-pressed samples.

4.4.4 Conclusion

In this chapter, $Hf_{0.6-x}Zr_xTi_{0.4}CoSb_{0.8}Sn_{0.2}$ solid solutions were prepared by MA in an attempt to reduce Hf concentration and material's cost. The isoelectronic substitution of Hf with Zr resulted in lower power factors and ZTs, as expected. However, the decreased thermal conductivity of $Hf_{0.4}Zr_{0.2}Ti_{0.4}CoSb_{0.8}Sn_{0.2}$ suggested that this composition would be a good selection for further investigation regarding thermoelectric performance. To this end, the effect of charge carrier concentration was investigated by preparing $Hf_{0.4}Zr_{0.2}Ti_{0.4}CoSb_{1-y}Sn_y$ samples in order to optimize the Sn/Sb doping. $Hf_{0.4}Zr_{0.2}Ti_{0.4}CoSb_{0.83}Sn_{0.17}$ reached the highest ZT of 0.77 at 960K, a value that corresponds to an improvement of 15% with respect to that of $Hf_{0.4}Zr_{0.2}Ti_{0.4}CoSb_{0.8}Sn_{0.2.}$ The use of a single-step and cost-effective preparation method, like mechanical alloying in combination with a decreased Hf usage without losing much of the TE conversion efficiency, will be crucial for the commercialization of half-Heusler materials in the near future.

4.5 Annealing of $Hf_{0.6}Ti_{0.4}CoSb_{0.83}Sn_{0.17}$

The practical applications of thermoelectric devices involve prolonged and large temperature gradients. Thus, it is really important to investigate the thermal stability of a candidate thermoelectric material before its applicability in commercial devices. Recently, the long-term stability of the n-type $Ti_{0.3}Zr_{0.35}Hf_{0.35}NiSn$ (ZT=0.6) was investigated by Krez et al. [137]. The properties remained unaffected after 500 cycles of repeated heating and cooling from 100 ^{o}C to 600 ^{o}C while the phase-separation was stable under long-term cycling. The long-term stability of the p-type $Ti_{0.5}Hf_{0.5}CoSb_{0.85}Sn_{0.15}$ (ZT=1.1) was also investigated by E.Rausch et al. The intrinsic phase separation that was responsible for the excellent thermoelectric performance was stable after 500 heating and cooling cycles and the standard deviation of the obtained ZT values were within 2-3% [73].

In addition to that, annealing process is commonly used in both n- and p-type arc-melted ingots before sintering to promote the crystalline order and to eliminate impurity phases such as CoTi, $(Hf,Zr)_5Sn_3$, $TiNi_2Sn$, Ti_6Sn_5, and unalloyed Sn [84], [138]–[140]. The annealing process of an arc-melted ingot may last up to 7 days at temperatures around 800 ^{o}C. As it has been discussed in previous chapters, this step is not necessary for the mechanically alloyed solid solutions because it is relatively easy to prepare single-phase HH powders via a single-step ball-milling process. However, the presence of phase separation in arc-melted HH materials which lead to reduced lattice thermal conductivity, arises a question whether this effect develops during rapid solidification or during annealing process.

Since the pseudo-ternary phase diagram of the p-type (Hf/Ti/Zr)CoSb system is not yet available, the phase diagram of the n-type (Hf/Ti/Zr)NiSn counterpart is presented to gain more information regarding the phase stability and solid solution formation of HH materials (Figure 4.37) [134]. According to A. Page et al., calculations predict a miscibility gap at low temperatures between a Ti-rich and a Ti-poor half-Heusler phase, which disappears at temperatures above 850 K. Therefore, at the high annealing temperatures used in experiments (e.g. 1175 K), the equilibrium phase is predicted to be a solid solution and interdiffusion among Ti, Zr and Hf will be negligible [134]. Thus, the commonly observed dendritic features in n-type HH materials synthesized by arc-melting are developed during the rapid solidification process and should remain unaffected after annealing.

It is obvious that the observed microstructures and solubility limits of the HH phases are highly dependent on synthesis techniques. Therefore, in order to examine if the previously mentioned predictions can be applied in p-type materials, a series of annealing experiments are needed. To this end, the effect of annealing under different durations upon thermoelectric performance of a p-type HH solid solution prepared via MA was investigated and correlated with the impact on the structural properties. For this investigation, the $Hf_{0.6}Ti_{0.4}CoSb_{0.83}Sn_{0.17}$ sample (see chapter 4.2) was selected due its outstanding thermoelectric performance (ZT=1.1 at 980K) to examine a possible phase-separation formation after an annealing step.

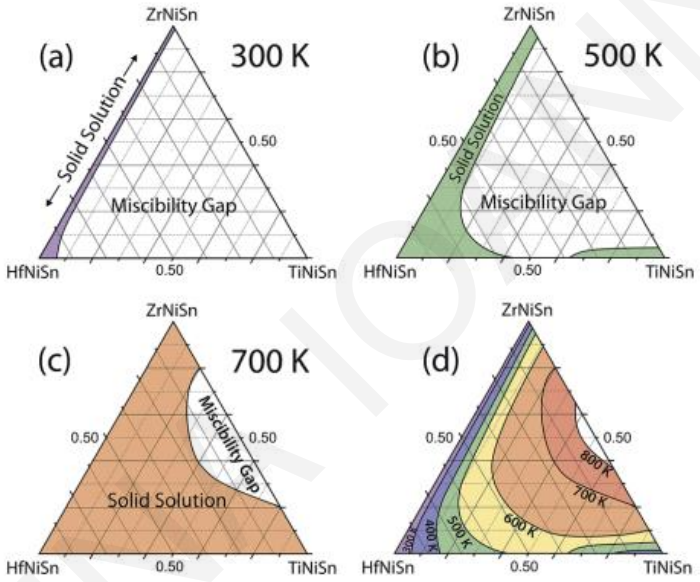

Figure 4.37: Pseudo-ternary $(Hf_{1-x-y}Zr_xTi_y)NiSn$ phase diagrams were calculated at 300 K (a), 500 K (b), 700 K (c). The solid solution region is shown in colour, and the miscibility gap region is shown in white. As the temperature increases, the miscibility gap shrinks, and completely disappears above 900 K. Part (d) shows a summary of phase boundaries calculated from 300 to 800 K. Reproduced from [134]

4.5.1 Experimental details

$Hf_{0.6}Ti_{0.4}CoSb_{0.83}Sn_{0.17}$ samples were prepared as described in chapter 4.2. Two disc-shaped hot-pressed samples were loaded into quartz-sealed tubes and annealed under vacuum at 800℃ for 3 and 10 days respectively. Another two bar-shaped samples were also annealed in a quartz-sealed tubes under vacuum for 3 days at 800^{o}C to assess the repeatability of the results.

4.5.2 Results of annealed $Hf_{0.6}Ti_{0.4}CoSb_{0.83}Sn_{0.17}$ solid solutions

Figure 4.38 presents the powder X-ray diffraction patterns of $Hf_{0.6}Ti_{0.4}CoSb_{0.83}Sn_{0.17}$ samples right after hot-press sintering and after 3 and 10 days of annealing at 800^{o}C. All diffraction peaks are matched with the cubic MgAgAs-type crystal structure (space group $F\bar{4}3m$), revealing the desired half-Heusler phases without any other secondary phases presented. SEM images and EDS results are presented in Fig. 4.39 and Table 4.12, respectively. The back-scattered images of the sample before and after 3 days of annealing illustrate homogeneous single-phase materials. EDS analysis confirmed that the chemical composition is close to the nominal composition for both samples. On the other hand, the back-scattered images of the sample after 10 days of annealing at 800^{o}C revealed two different phases: a grey matrix and some randomly distributed black spots. According to the EDS results the chemical compositions of the grey matrix deviates from the nominal composition due to the presence of higher Hf percentage and lower Ti percentage. When it comes to the black areas, EDS analysis revealed a Ti-rich phase, suggesting that further investigation is needed to fully understand this effect. Elemental mapping (Fig. 4.40) was employed in two different large black areas to examine the distribution of elements in the sample. In both cases, Hf is the only element that is homogeneously distributed in the sample. The black areas are deficient in Co, Sb and Sn and rich in Ti as it was suggested by EDS results.

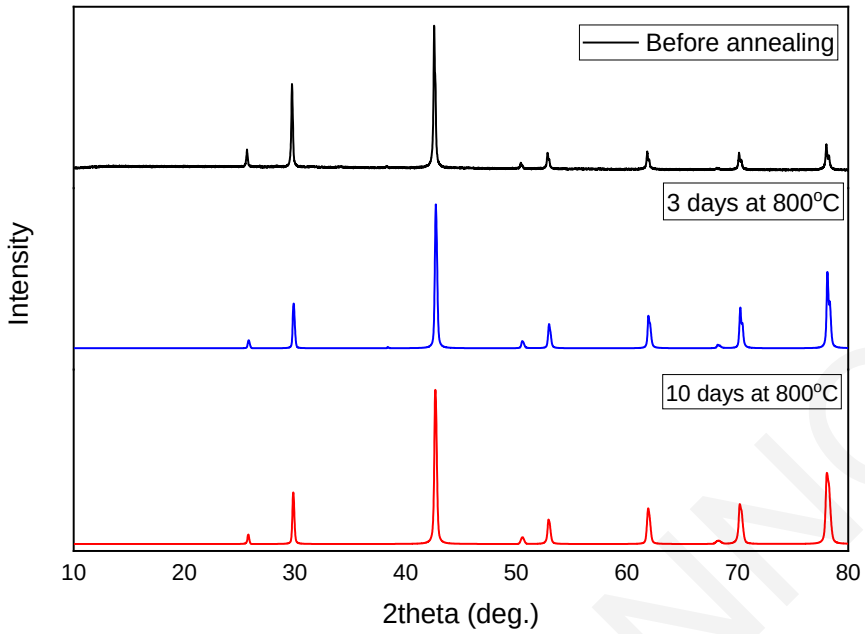

Figure 4.38: The X-ray diffraction patterns of $Hf_{0.6}Ti_{0.4}CoSb_{0.83}Sn_{0.17}$ samples before and after annealing.

Table 4.14: Chemical composition of $Hf_{0.6}Ti_{0.4}CoSb_{0.83}Sn_{0.17}$ as determined by EDS.

Sample	Area	Hf	Ti	Co	Sb	Sn
Before annealing	**Overall**	0.54	0.42	1.11	0.76	0.18
3 days at 800°C	**Overall**	0.55	0.47	1.02	0.86	0.10
10 days at 800°C	**Matrix**	0.71	0.32	1.02	0.83	0.12
	Black	0.83	1.96	0.12	0.07	0.02

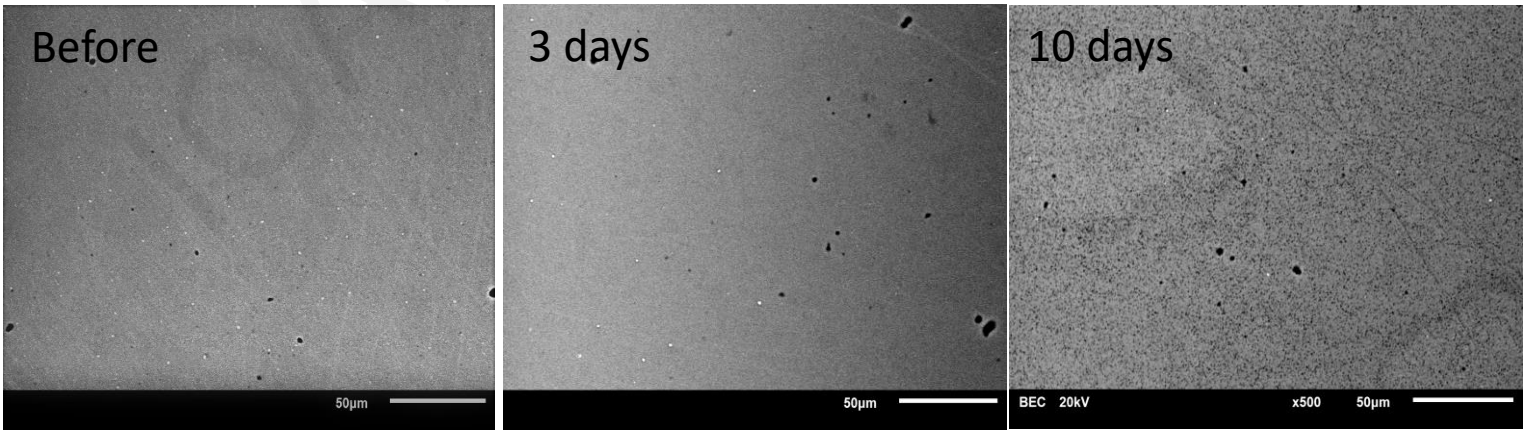

Figure 4.39: Backscattered electron images of $Hf_{0.6}Ti_{0.4}CoSb_{0.83}Sn_{0.17}$ samples before and after 3 and 10 days of annealing at 800°C

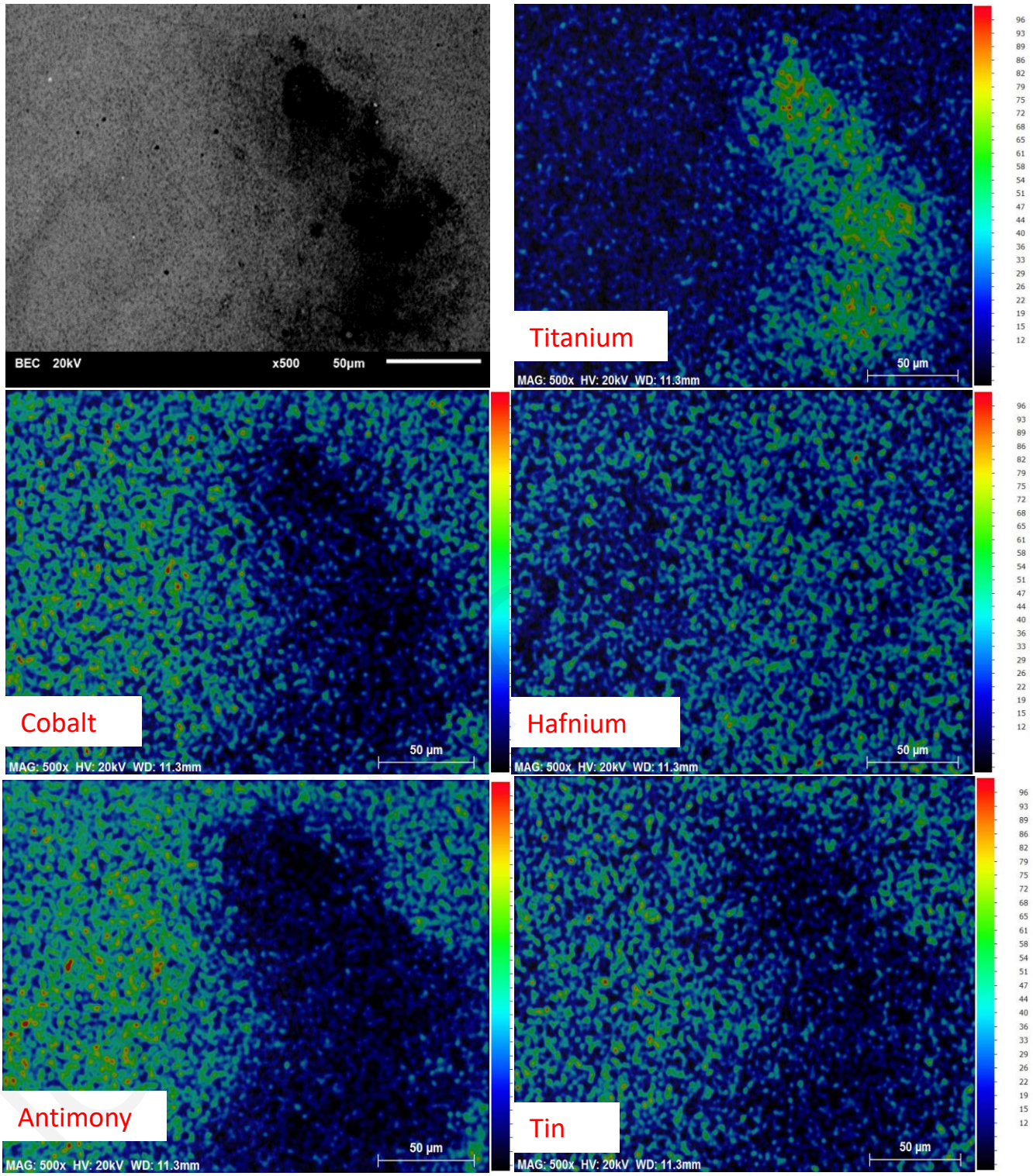

Figure 4.40: Elemental mapping of $Hf_{0.6}Ti_{0.4}CoSb_{0.83}Sn_{0.17}$ sample after 10 days of annealing at 800°C.

Thermoelectric properties:

The temperature dependent Seebeck coefficient (S), electrical conductivity (σ) and power factor are presented in Fig. 4.41. The Seebeck coefficient of samples after 3 days of annealing remains almost unaffected (S~250μV/K at 980K), indicating same charge carrier concentration after annealing. The sample that was annealed for 10 days at 800^{o}C presents a totally different behavior. At low temperatures, S values are extremely low and then gradually increase with increasing temperature, reaching the value of 230μV/K at 960K. The change of Seebeck coefficient can be attributed to the presence of a secondary Ti-rich phase which consequently affects the carrier concentration. The electrical conductivity after 3 days of annealing is nearly the same, especially for two of the three annealed samples, while for the third sample the electrical conductivity values are approximately 12% lower in comparison to the sample before annealing. After 10 days at 800^{o}C, the electrical conductivity of $Hf_{0.6}Ti_{0.4}CoSb_{0.83}Sn_{0.17}$ is severely decreased and even though there is a slight increase with increasing temperature, the highest value of σ~211S/cm is still 50% lower than that before annealing. This is attributed to the presence of a metallic Ti-rich phase, which partially compensate the existing holes within the HH matrix. The calculated power factors in 4.41c show that the PF values remain unaffected after 3 days of annealing (PF~25 μW/cmK^2 at 960K), but remarkably decrease after 10 days of annealing (PF~12 μW/cmK^2 at 970K) because of the reduction in both Seebeck coefficient and electrical conductivity.

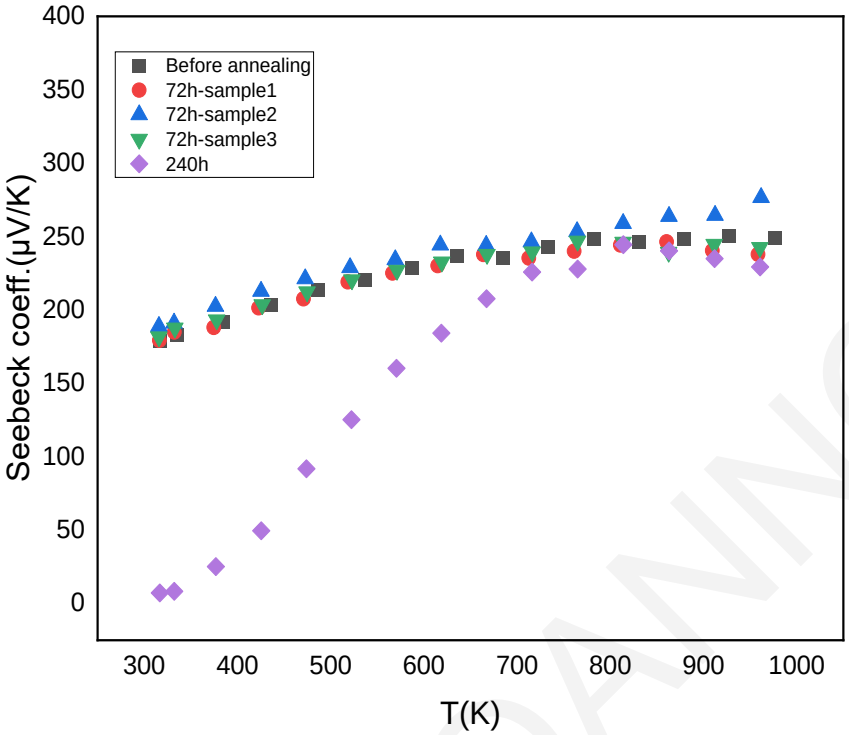

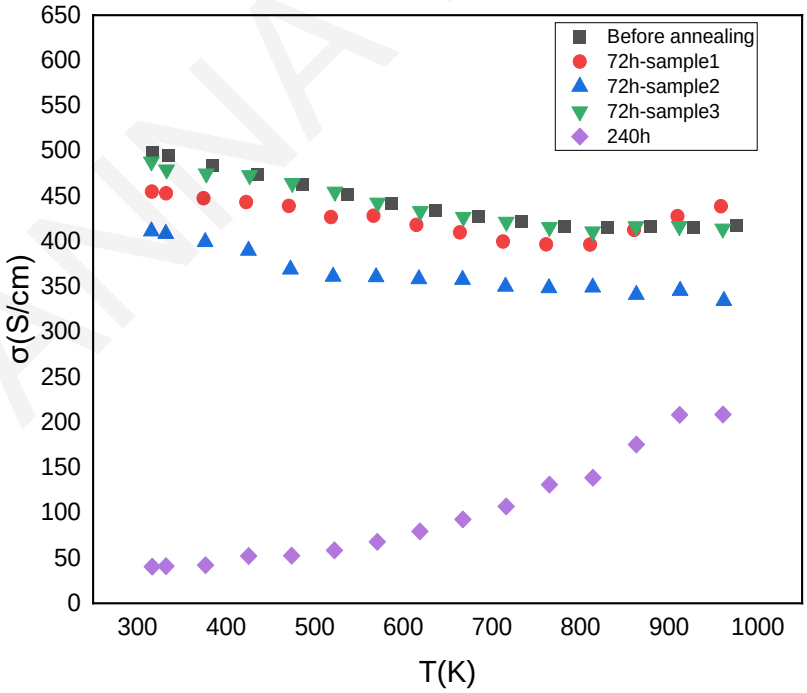

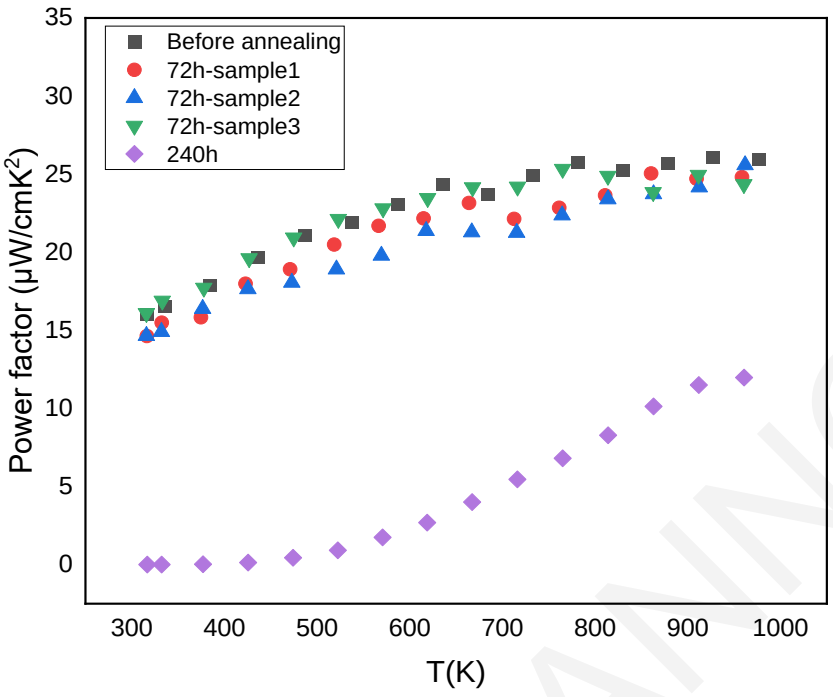

Figure 4.41: Temperature dependent Seebeck coefficient (S), electrical conductivity (σ) and power factor (PF) of $Hf_{0.6}Ti_{0.4}CoSb_{0.83}Sn_{0.17}$ sample before and after 3 and 10 days of annealing at 800°C.

The temperature dependence of the total thermal conductivity and the lattice thermal conductivity is plotted in Figure 4.42. The lattice thermal conductivity was calculated as described in chapter 4. The sample after 3 days of annealing presents a lower total thermal conductivity at room temperature (2.64 W/mK) than the sample before annealing (3 W/mK). However, the κ_{total} values before and after 3 days at 800°C are almost identical at higher temperatures (κ~2.45 W/mK). The $Hf_{0.6}Ti_{0.4}CoSb_{0.83}Sn_{0.17}$ sample after 10 days recorded higher thermal conductivity values; approximately 25% higher than that of the sample before annealing. The same trends are observed for the lattice thermal conductivity values.

By combining the previously discussed thermoelectric properties, the thermoelectric figure of merit was estimated (Fig. 4.43). The ZT of $Hf_{0.6}Ti_{0.4}CoSb_{0.83}Sn_{0.17}$ sample remains unaffected after 3 days at 800°C (ZT~1) while the ZT after 10 days of annealing is significantly reduced due to the remarkable increase of thermal conductivity and the notable decrease of Seebeck coefficient and electrical conductivity (ZT~0.34).

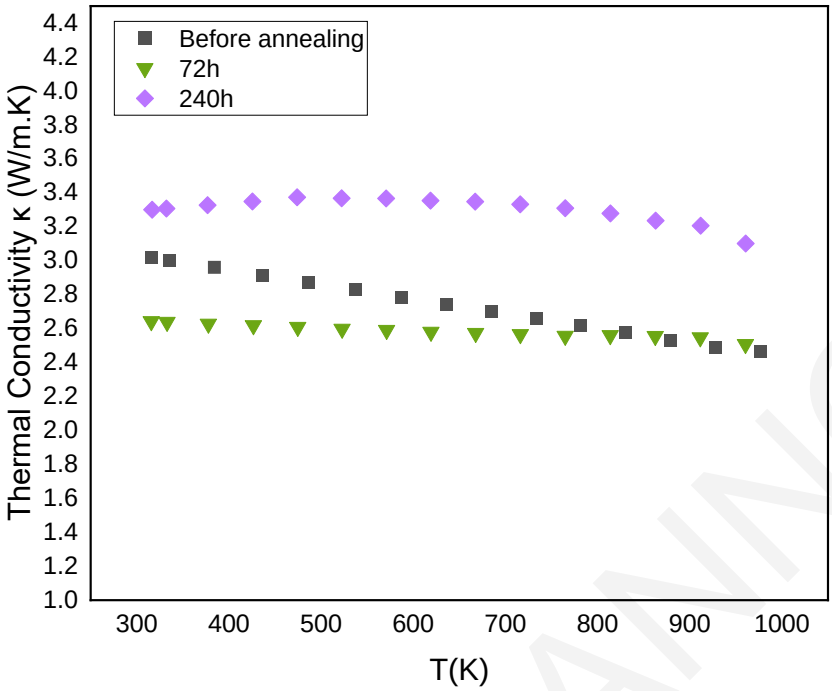

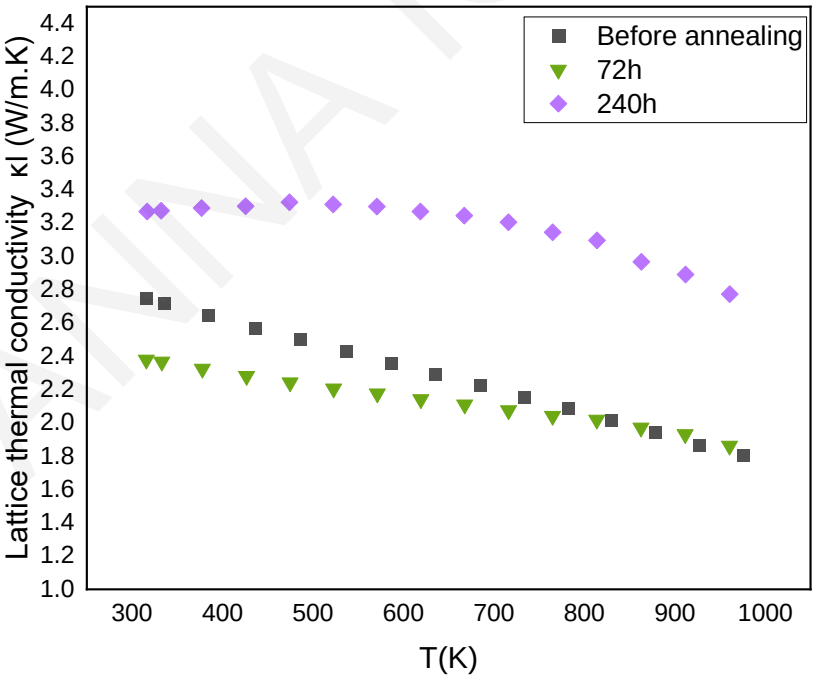

Figure 4.42: Temperature dependent total thermal conductivity and lattice thermal conductivity of $Hf_{0.6}Ti_{0.4}CoSb_{0.83}Sn_{0.17}$ sample before and after 3 and 10 days of annealing at 800°C.

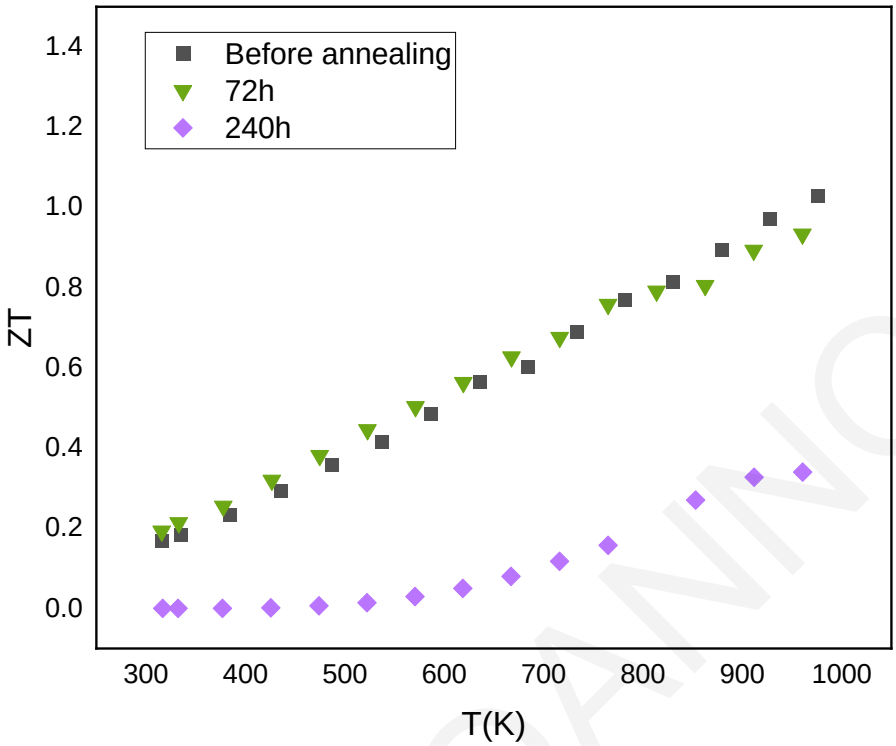

Figure 4.43: Thermoelectric figure-of-merit (ZT) as a function of temperature of $Hf_{0.6}Ti_{0.4}CoSb_{0.83}Sn_{0.17}$ sample before and after 3 and 10 days of annealing at 800°C.

4.5.3 Conclusion

In aim of chapter was the investigation of annealing effect on the promising $Hf_{0.6}Ti_{0.4}CoSb_{0.83}Sn_{0.17}$ composition prepared via MA. The composition was selected due to its outstanding thermoelectric performance (ZT=1.1 at 980K). Hot-pressed samples were annealed at 800^{o}C for 3- and 10-days and their structure, chemical composition and thermoelectric performance were investigated and compared to the sample before annealing. The structure, chemical composition and thermoelectric properties of $Hf_{0.6}Ti_{0.4}CoSb_{0.83}Sn_{0.17}$ remained unaffected after 3 days of annealing (ZT~1.1). On the other hand, there is a significant reduction in the thermoelectric figure-of-merit (ZT~0.34) after 10 days at 800^{o}C, due to the remarkable increase of thermal conductivity and the notable decrease of Seebeck coefficient and electrical conductivity. This change is mainly attributed to the presence of an additional Ti-rich phase in HH matrix, which may indicate an early stage of phase-decomposition.

Since no phase-separation has been detected in mechanically-alloyed single-phase materials after annealing, we conclude that the presence of phase-separation (two or more half-Heusler phases with slightly different lattice parameters) in most arc-melted samples is developed during rapid-solidification and not during the following annealing process.

5. Results of $Bi_xSb_{2-x}Te_3$ solid solutions

5.1 Effect of Bi/Sb ratio in $Bi_xSb_{2-x}Te_3$ solid solutions fabricated via mechanical alloying

The previous chapters suggested that mechanical alloying followed by hot-press sintering is an attractive and easy way to fabricate nanostructured TE materials with reduced lattice thermal conductivity. Mechanical alloying considerably reduces the processing time and cost needed to prepare BiSbTe solid solutions by avoiding vacuum melting, conventional grinding or other high temperature procedures. Further, the ZT of BiSbTe alloys can be improved or shift to higher temperatures via composition modification and doping [141][142]. Bi_2Te_3 has a narrow bandgap of 0.13 eV, and can be easily modified by Sb_2Te_3 doping (bandgap~0.28 eV) [143][144]. Thus, Sb substitution can effectively shift the optimum ZT in higher temperatures by suppressing the onset of intrinsic excitation. An optimization of Bi/Sb ratio cannot only be used to broaden the band gap but also to optimize the hole concentration. The origin of hole concentration in p-type $Bi_xSb_{2-x}Te_3$ materials is mainly associated with Sb'_{Te} and Bi'_{Te} antisite defects, which are created when cations occupy vacant anion sites. The formation energy of antisite defects can be reduced by raising the Sb content in $Bi_xSb_{2-x}Te_3$ compositions due to the smaller difference in electronegativity for Sb–Te compared with Bi–Te. Whilst, the hole concentration may be further tuned through donor-like effects induced during grinding and pressing[145].

In this chapter, p-type $Bi_xSb_{2-x}Te_3$ (x = 0.2,0.3,0.4,0.5) alloy powders were fabricated via mechanical alloying, and consequently consolidated by hot-press sintering. The effect of Sb/Bi ratio on the microstructure and TE properties was investigated.

5.1.1 Synthesis and consolidation conditions

The milling was operated at 300rpm for 20 hours and the ball-to-material ratio was 10:1. The gained powders were loaded in a cylindrical graphite die (inside diameter=10mm) and hot-pressed at 420℃ for one hour under an axial pressure of 80MPa.

5.1.2 Results

Structural characterization:

Figure 5.1a shows the X-ray diffraction patterns of $Bi_xSb_{2-x}Te_3$ (x=0.2-0.5) powders produced by mechanical alloying. The miller indices of all major peaks are indicated and the XRD pattern verifies that the powders are single-phase. The well-known Scherrer formula (see chapter 3), was used to calculate the mean crystallite size generated by MA (Fig. 5.1c). The mean crystallite size linearly increases with increasing Bi(x). The in-pane XRD patterns after hot-pressing are presented in Fig 5.1b. The graph indicates that no other phase or impurity is presented apart from the rhombohedral bismuth-telluride phase. The diffraction peaks of all samples are much sharper after sintering, indicating that sintering has led to better crystallinity and comparatively larger grain size due to the grain growth. The degree of preferred orientation was evaluated by calculating the Lotgering factor (LF) as described in chapter 3[110]. The LF calculations in Table 5.1 reveal randomly oriented samples, as expected.

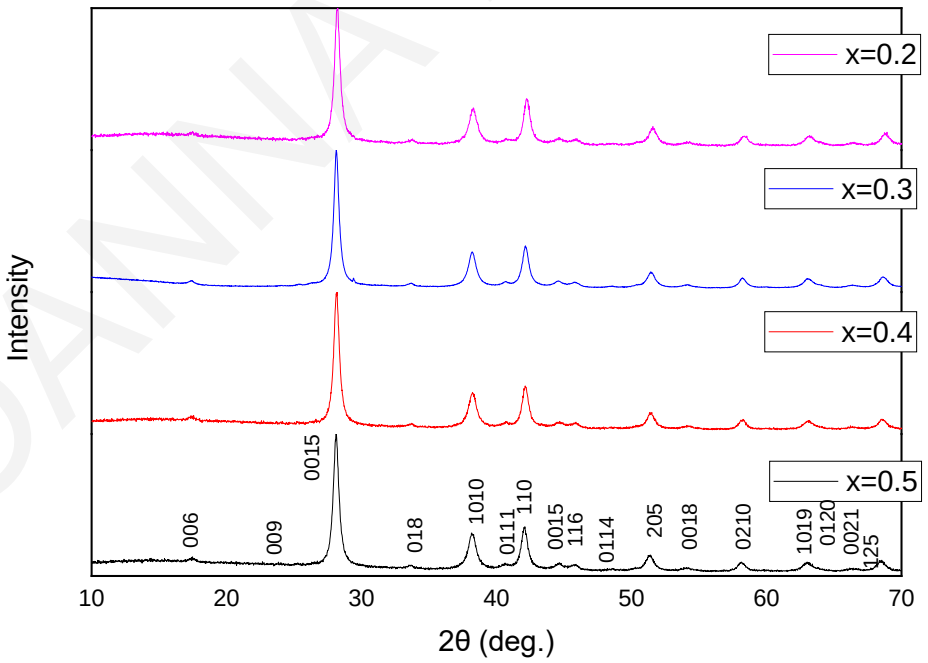

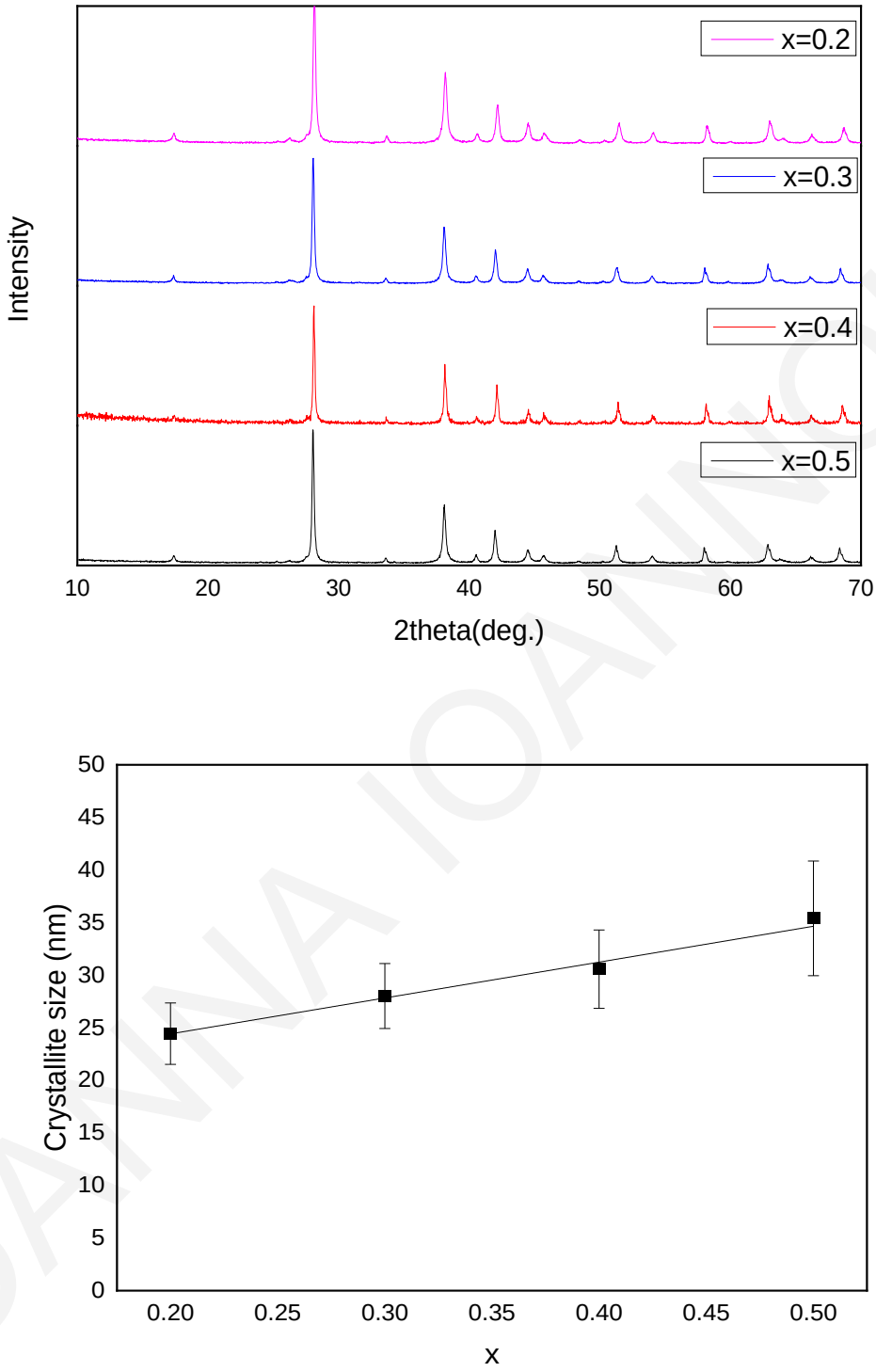

Figure 5.1: XRD patterns of the $Bi_xSb_{2-x}Te_3$ powders after mechanical alloying (a), XRD patterns of hot-pressed pellets (b) and calculated crystallite size of $Bi_xSb_{2-x}Te_3$ powders using Sherrer equation as a function of Bi (x) (c).

Table 5.1: Relative density ρ and Lotgering factor of the hot-pressed $Bi_xSb_{2-x}Te_3$ pellets.

Sample	Relative Density ρ (%)	Lotgering factor (LF)
x=0.5	92	0
x=0.4	91	0
x=0.3	92	0
x=0.2	88	0

Thermoelectric properties:

The carrier concentration (n_H) and carrier mobility (μ) at room temperature and the temperature dependent Seebeck coefficient, electrical conductivity and Power factor of $Bi_xSb_{2-x}Te_3$ samples are presented in Fig 5.2 and Fig 5.3, respectively. The hole concentration decreases with increasing Bi(x), as expected. The substitution of Bi with Sb introduces holes into the system therefore the charge carrier concentration increases with higher Sb content in $Bi_xSb_{2-x}Te_3$ samples. Increasing Sb concentration in $Bi_xSb_{2-x}Te_3$ promotes a reduction in the formation energy of Sb'_{Te} and Bi'_{Te} antisite defects leading to higher carrier density[146]. The carrier concentration values of the mechanically alloyed samples are significantly lower than the values reported for the same compositions synthesized via melting and Hu et al. but closer to the values reported by Symeou et al. [99], [100]. This is attributed to the excess Te (4%) used in this work's samples as well as in Symeou et al. study, which minimizes the presence of Te vacancies and suppresses the Sb'_{Te} antisite defects. The formation of donor-like effects due to lattice defects induced by MA further reduced the carrier concentration[95][147]. The donor-like effects (excess of negative carriers due to the presence of Te vacancies) can partially compensate for the hole concentration in Sb-rich p-type solid solutions [95]. The n_H values of this works samples are also lower than those reported for analogous mechanically alloyed samples by Jang et al. [148]. This is as well attributed to the excess of Te in this work samples that minimize formation of the previously mentioned antisite defects. The carrier mobility (μ) decreases with increasing Bi(x) similarly to n_H. The decrease of μ with increasing x (increased Bi/Sb ratio) is a result of stronger alloy scattering, which is consistent with previous studies [99], [100], [149]. Moreover, the carrier mobility values of this work's investigated

samples are lower than those reported by E. Symeou at al. for materials prepared via melting and hand-grinding due to the absence of preferred orientation and the presence of high-density boundaries in nanostructured materials [100]. However, the μ values of our samples are significantly higher than those reported by Hu et al. and Jang et al. for samples prepared via melting followed by 20 min ball-milling and analogous mechanically alloyed samples, respectively [99][148]. The lower carrier mobility of the aforementioned works is attributed to the higher hole concentration which consequently increase the carrier-carrier scattering.

Accordingly, the Seebeck coefficient increases with increasing Bi(x) due to the decrease of hole concentration. The highest Seebeck coefficient S~268μV/K was recorded for x=0.5 at 330K, and then significantly dropped with rising temperature. The highest S value is achieved at higher temperature with increasing Bi content. In specific, the highest S for x=0.4 was reached at 330K, for x=0.3 at 380K and for x=0.2 at 430K. This effect is attributed to the increase of carrier density as well as to the broadening of the energy bandgab with increasing Sb, which thereafter shifts the onset of bipolar conduction and intrinsic excitation to higher temperatures. Almost identical trends and values have been recorded by Jang et al. and Chen et al. for analogous mechanically-alloyed samples [148][150]. On the other hand, this work's samples exhibit higher S values than those reported by Symeou et al. [100] and Hu et al.[99] for samples prepared via melting, due to the lower carrier concentration.

The electrical conductivity of all the samples decreases with increasing measurement temperature. The temperature dependence of σ samples is typical of a degenerate narrow gap semiconductor and is well described by a power law $\sigma \sim T^{-3/2}$. The carrier concentration of a degenerate semiconductor has a weak dependence on temperature. Therefore, the trend of σ with rising temperature mainly reflects the temperature dependence of carrier mobility, presenting dominant acoustic phonon scattering. The remarkable enhancement in σ with decreasing Bi (x) can be attributed to increases in both n_H and μ because of the presence of antisite defects and reduced alloy scattering, respectively. The σ values of this work's samples are significantly lower than those reported by Symeou et al. [100] for materials prepared via melting and hand grinding and those reported by Hu et al. [99] for materials prepared via melting followed by ball-milling for 20min, mainly due to the lower carrier concentration and mobility. Even though, the electrical conductivity trends and temperature dependence are similar,

the σ values are higher than those reported by Jang et al. for analogous mechanically-alloyed samples, due to the higher hole-mobility of this work's samples[148].

The calculated power factors are presented in Fig. 5.3e. All samples exhibit their highest PF value near room temperature. $Bi_{0.3}Sb_{1.7}Te_3$ achieved the highest value of 39.5μW/cmK^2 at 329K due to its high electrical conductivity and relatively good Seebeck coefficient. This composition ($Bi_{0.3}Sb_{1.7}Te_3$) recorded the highest PF in analogous investigation regarding mechanically-alloyed $Bi_xSb_{2-x}Te_3$ samples[148] [150]. However, the PF of this work's sample is higher than those reported by Jang et al. (PF~30μW/cmK^2) [148] and Chen et al. (PF~32.5μW/cmK^2) [150].

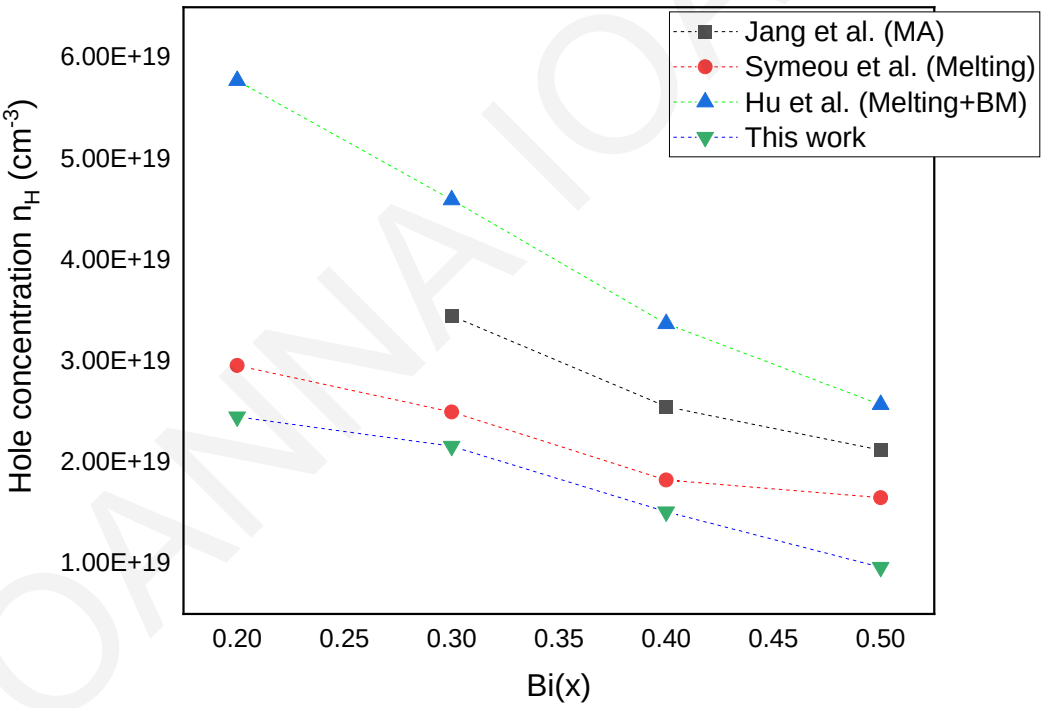

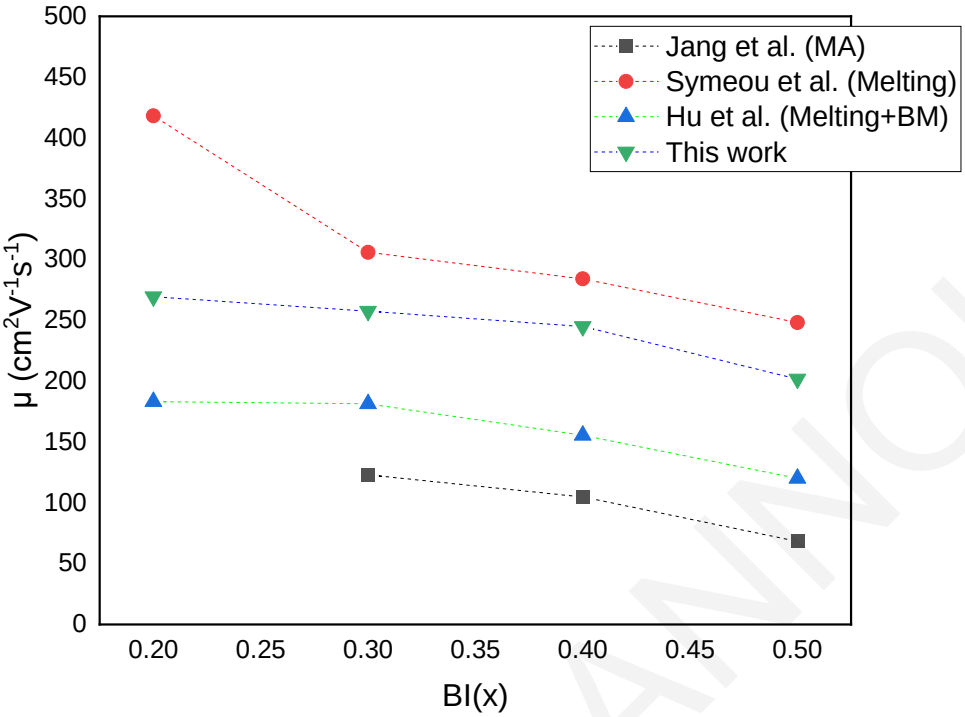

Figure 5.2: : Carrier concentration (n_H) (a) and carrier mobility (b) at room temperature as a function of Bi(x) compared with Hu et al. [99], Symeou et al.[100] and Jang et al.[148]

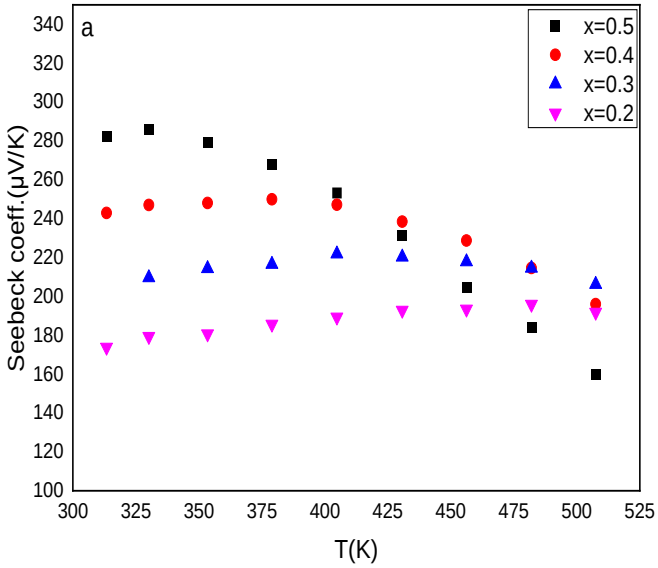

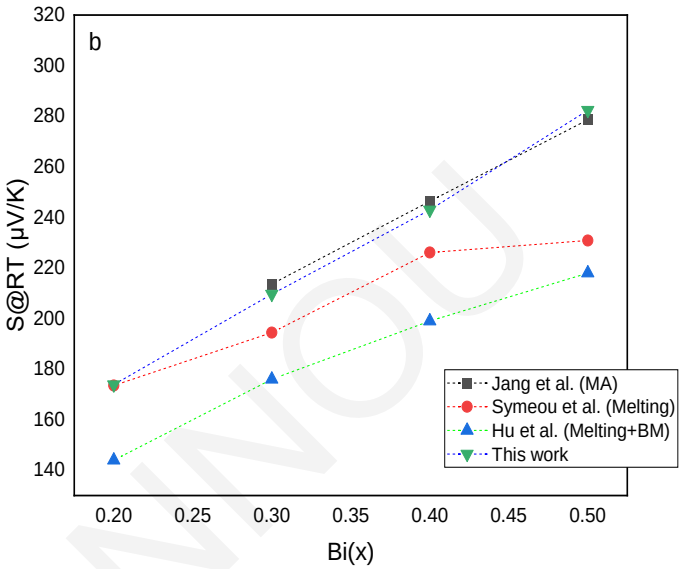

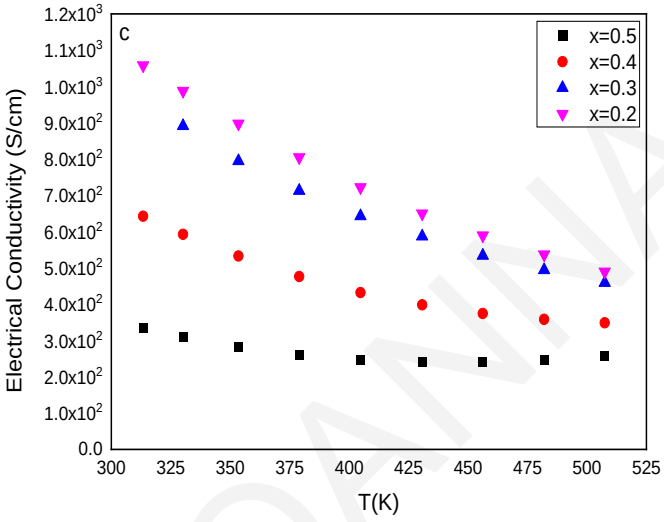

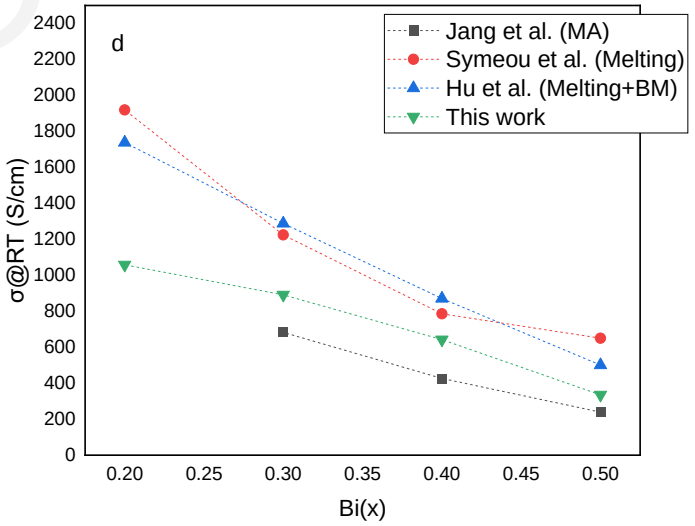

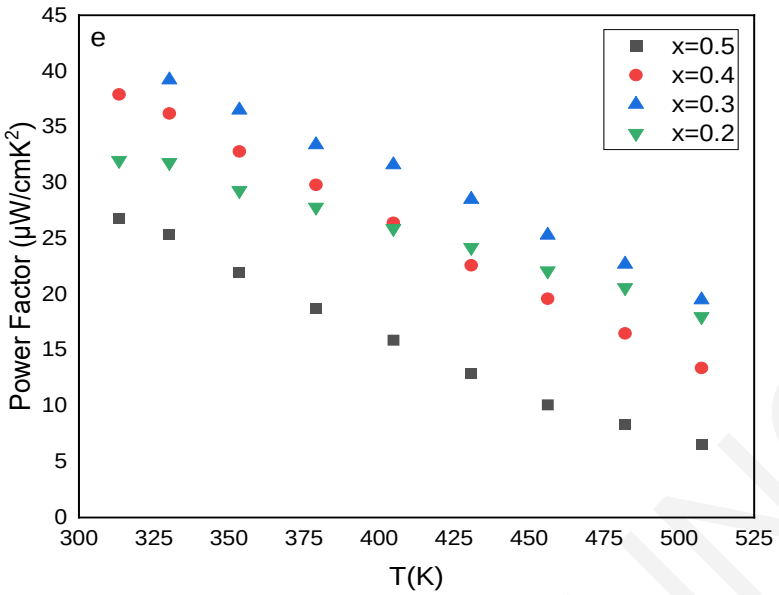

Figure 5.3: Temperature dependence of Seebeck coefficient (a), electrical conductivity (c) and power factor (e) of the hot-pressed $Bi_xSb_{2-x}Te_3$ samples. Seebeck coefficient (b) and electrical conductivity (d) at room temperature as a function of Bi(x) compared with Hu et al. [99], Symeou et al.[100] and Jang et al.[148].

The total thermal conductivity (κ_{total}), electronic thermal conductivity (κ_e) and lattice thermal conductivity ($\kappa_{lattice}$) as function of temperature are shown in Fig. 5.4. The thermal conductivity of samples with x=0.2 and x=0.3 decreases monotonically with increasing temperature up to 425K due to the Umklapp phonon-phonon scattering whereas the κ_{total} for x=0.5 and x=0.4 increases with rising temperature due to bipolar diffusion, which is dominant at low Sb doping levels. As the Sb substitution increased, the temperature at which bipolar conduction occurred shifted to higher temperatures. The increased carrier density in samples with high Sb percentage not only increases the electrical conductivity but also reduces the bipolar thermal conductivity [151]. The decrease of κ_{total} at room temperature with increasing Bi content is attributed to the decreasing fraction of the electronic thermal conductivity (κ_e), which is directly proportional to electrical conductivity σ. Similar trends have been also reported by previous investigations regarding $Bi_xSb_{2-x}Te_3$ as shown in Figure 5.4b. In general, our samples present lower total thermal conductivity than those prepared via melting by Symeou et al.[100] and Hu et al.[99] but slightly higher κ in comparison with analogous mechanically-alloyed solid solutions by Jang et al.[148].

The values of lattice thermal conductivity (κ_{total}-κ_e) are displayed in Fig. 5.4e as a function of temperature for all $Bi_xSb_{2-x}Te_3$ samples. Taking into consideration that the bipolar contribution to thermal conductivity is negligible near 300K, a comparison of the lattice thermal conductivity can be made at low temperatures. The $\kappa_{lattice}$ values range between 0.46-0.76 Wm^{-1} K^{-1} for x=0.2-0.5 at 300K. These $\kappa_{lattice}$ values are significantly lower than those reported for similar compositions prepared via melting and hot-press sintering by Symeou et al.[100] (1-0.77 Wm^{-1} K^{-}) and are closer to the values reported for compositions prepared by Hu et al. [99] (0.6-1 Wm^{-1} K^{-1}) and samples prepared via MA by Jang et al. [148] (0.5-0.8 Wm^{-1} K^{-1}) (Figure 5.4f). The lower room-temperature $\kappa_{lattice}$ values are attributed to the smaller grain size of starting powders, the consequent higher density of grain boundaries and the absence of preferred orientation in nanostructured materials.

The theoretical minimum thermal conductivity κ_{min} for Bi_2Te_3 was calculated using a model proposed by Cahill et al[152]. This model is based on Einstein who considered the atomic vibrations of a solid as harmonic oscillators, all vibrating at the same frequency. If the oscillators are not coupled to one another, the thermal conductivity of this model solid is zero: thermal energy cannot be transmitted from one atom to another. For thermal transport to occur, the oscillators must be coupled, and Einstein did this by supposing that each atom was connected to its neighbours on a simple-cubic lattice by harmonic forces. According to Cahill et al. the minimum thermal conductivity resulting from the random walk between localized quantum mechanical oscillators can be written as the following sum of three Debye integrals:

$$\kappa_{min} = \left(\frac{\pi}{6}\right)^{1/3} k_B n^{2/3} \sum_i Ui \left(\frac{T}{\Theta i}\right)^2 \int_0^{\Theta i/T} \frac{x^3 e^x}{(e^x - 1)^2} dx$$

The sum is taken over the three sound modes (two transverse and one longitudinal) with speeds of sound Ui, Θi is the frequency for each polarization expressed in degrees K ($\Theta i = Ui(\hbar/k_B)(6\pi^2 n)^{1/3}$), and n is the number density of atoms.

According to the calculation, the κ_{min} for Bi_2Te_3 is approximately ~0.31W/mK and agrees with other works [153]. As presented in Figure 5.4f, the lattice thermal conductivity of samples with x=0.3 prepared via MA are approaching the theoretical limit of thermal conductivity, suggesting that nanostructuring and the Bi/Sb ratio optimization is an effective route to approach the minimum possible values of $\kappa_{lattice}$.

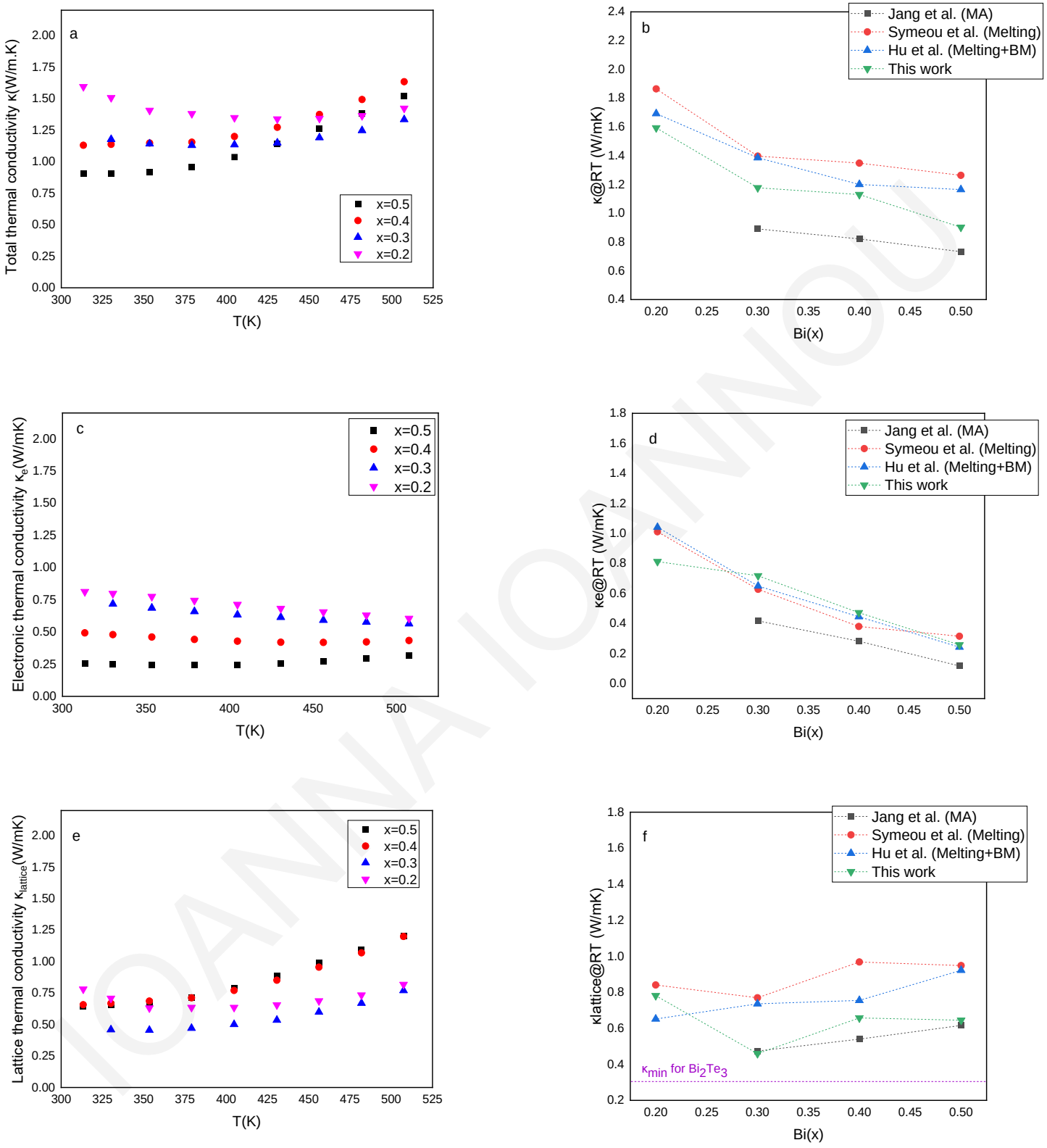

Figure 5.4: Temperature dependence of total thermal conductivity (a), electronic thermal conductivity (c) and lattice thermal conductivity (e) of $Bi_xSb_{2-x}Te_3$. Total thermal conductivity (b), electronic thermal conductivity (d) and lattice thermal conductivity (f) at room temperature as a function of Bi(x) in comparison with Hu et al. [99], Symeou et al.[100] and Jang et al.[148].

In Fig. 5.5 the dimensionless figure-of-merit ZT is presented as function of temperature. Owing to the gradual increases in the energy band-gap and hole concentration with increasing Sb content, the temperature of the maximum ZT shifts gradually to higher temperatures as a result of the suppression of intrinsic conduction. More importantly, there is a significant improvement in the average ZT_{av} value throughout the temperature range studied. The ZT_{av} is 0.60, 0.83, 1.01 and 0.72 for Bi(x)=0.5,0.4,0.3 and 0.2, respectively. The maximum ZT (355K) of 1.13 was achieved for x=0.3 sample which also exhibits the highest average ZT. This result is higher than that (ZT=0.9) reported by Hu et al. [99] for a similar composition prepared via melting followed by 20minutes ball-milling and nearly the same (ZT=1.12) to that reported by Symeou et. al [100] for the same hot-pressed composition prepared via melting and hand grinding. $Bi_{0.3}Sb_{1.17}Te_3$ has also recorded the highest ZT among other $Bi_xSb_{2-x}Te_3$ solid solutions by similar MA investigations. In particular, Jang et al. [148] reported a high ZT(323 K)~1.4, while Chen et al. [150], reported a ZT(423 K) ~ 1.23. The relatively good ZT of $Bi_{0.3}Sb_{1.7}Te_3$ indicates that this composition would be a good selection for further investigation regarding thermoelectric performance.

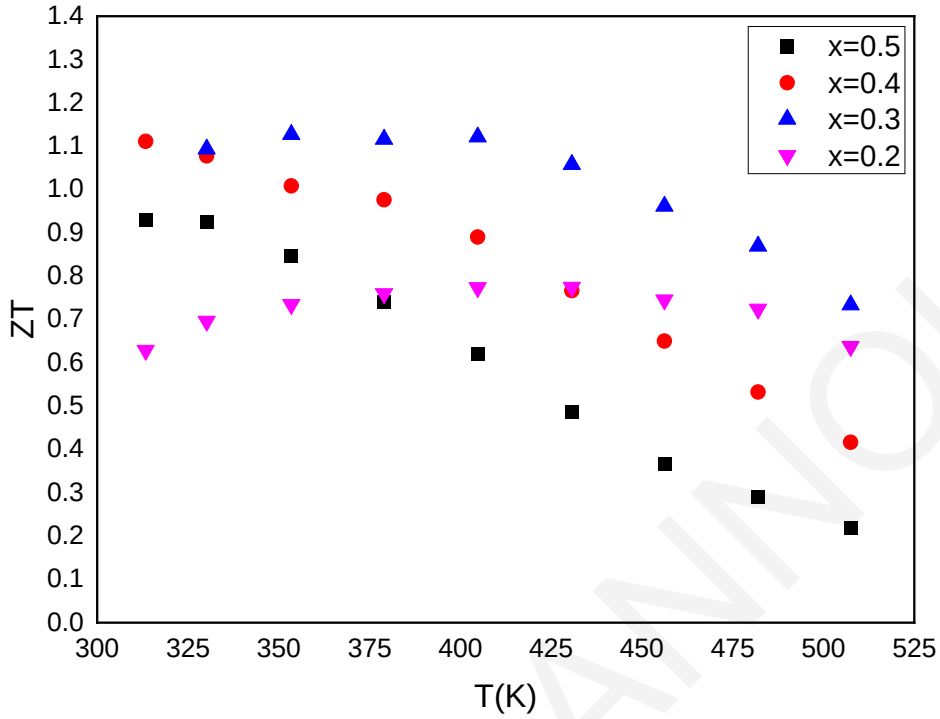

Figure 5.5: Dimensionless figure-of-merit ZT of the hot-pressed $Bi_xSb_{2-x}Te_3$ prepared via mechanical alloying as a function of temperature.

5.1.3 Conclusion

In this chapter, p-type $Bi_xSb_{2-x}Te_3$ alloy powders were fabricated via mechanical alloying, and consequently consolidated by hot-press sintering. The effect of Sb/Bi ratio on the microstructure and TE properties was investigated. The decrease of Bi content resulted in higher hole density and hole mobility which thereafter increased the electrical conductivity and power factor. The absence of preferred orientation and the high density of grain boundaries in nanostructured materials led to impressively low lattice thermal conductivities values. As a result, a high ZT of 1.13 at 355K and an average ZT of 1.01 was achieved for $Bi_{0.3}Sb_{1.7}Te_3$. This result is higher than other results reported for similar compositions prepared via multiple preparation steps (melting followed by hand-grinding or ball milling etc.). This suggests that mechanical alloying can be considered as an advantageous technique for single-step synthesis of highly-efficient $Bi_xSb_{2-x}Te_3$ alloys and that $Bi_{0.3}Sb_{1.7}Te_3$ is the most effective among other $Bi_xSb_{2-x}Te_3$ compositions prepared via MA.

5.2 Effect of powder's particle size on thermoelectric properties of hot-pressed $Bi_{0.3}Sb_{1.7}Te_3$ alloys

During the past decade, nanostructuring and defect engineering have been widely applied to develop efficient thermoelectric materials[154]–[156]. Lattice defects, donor-like effects and microstructural alterations proved to be important tools in order to control carrier and phonon transport properties.

Xie et al. developed a melt-spinning technique to fabricate nanocomposites, in order to reduce thermal conductivity by the presence of multi-scale microstructures and coherent grain boundaries[157]. As a result, a high ZT of 1.5 was achieved at 390K. Another study by Dharmaiah et al., highlights the importance of grain-size and grain boundary scattering for effective phonon scattering[158]. $Bi_{0.5}Sb_{1.5}Te_3$ powders of different sizes were prepared by gas-atomization followed by spark-plasma sintering process. The highest ZT value obtained was 1.23 at 350 K for the 32-75 μm powder bulk samples [158]. Additionally, Fan et al. reported an impressive ZT of 1.80 reached by the nanocomposite $Bi_{0.4}Sb_{1.6}Te_3$ consisting of 40 wt % nanoinclusions [105]. Nanocomposites were obtained via melt spinning and micron-size particles obtained via solid state reaction. The low thermal conductivity due to the effective scattering of phonons and the moderately good power factor played led to a high figure-of-merit. However, Dharmaiah et al. and Fan et al. do not give any information about the orientation of the samples and the direction of measurements, which is very important due to the anisotropic nature of BST material.

In this chapter, p-type $Bi_{0.3}Sb_{1.7}Te_3$ polycrystalline solid solutions were fabricated using different methods: melting and mechanical alloying followed by hot-press sintering. The composition was selected based on the encouraging results of chapter 5.1, which revealed that $Bi_{0.3}Sb_{1.7}Te_3$ prepared via MA followed by hot-press sintering is the most efficient among analogous $Bi_{2-x}Sb_xTe_3$ compositions. In this study, melting followed hand-grinding was used to obtain powders consisting of micro-sized particles. The powders were divided into four groups depending on their particles' size by using sieves. An amount of powder produced by melting was ball-milled in order to produce nano-powders. Mechanical alloying was also used to obtain nano-powders in order to compare the results with the melting-ball milling method. For brevity, samples prepared via **melting and hand grinding** will be noted as **MHG**, samples prepared via **melting and ball-milling** will be noted as **MBM** and samples prepared via **mechanical alloying**

will be noted as **MA**. In summary, six types of powders with different particle sizes were prepared as illustrated in Figure 5.6.

Powders prepared by hand grinding and ball milling were compacted into high density pellets by hot pressing to explore the effect of powder's particle size before consolidation on the thermoelectric properties of $Bi_{0.3}Sb_{1.7}Te_3$ samples. The temperature dependence of all thermoelectric properties (electrical conductivity, thermal conductivity and Seebeck coefficient) was measured along the same in-plane direction and reliable thermoelectric power factor and ZT values were calculated.

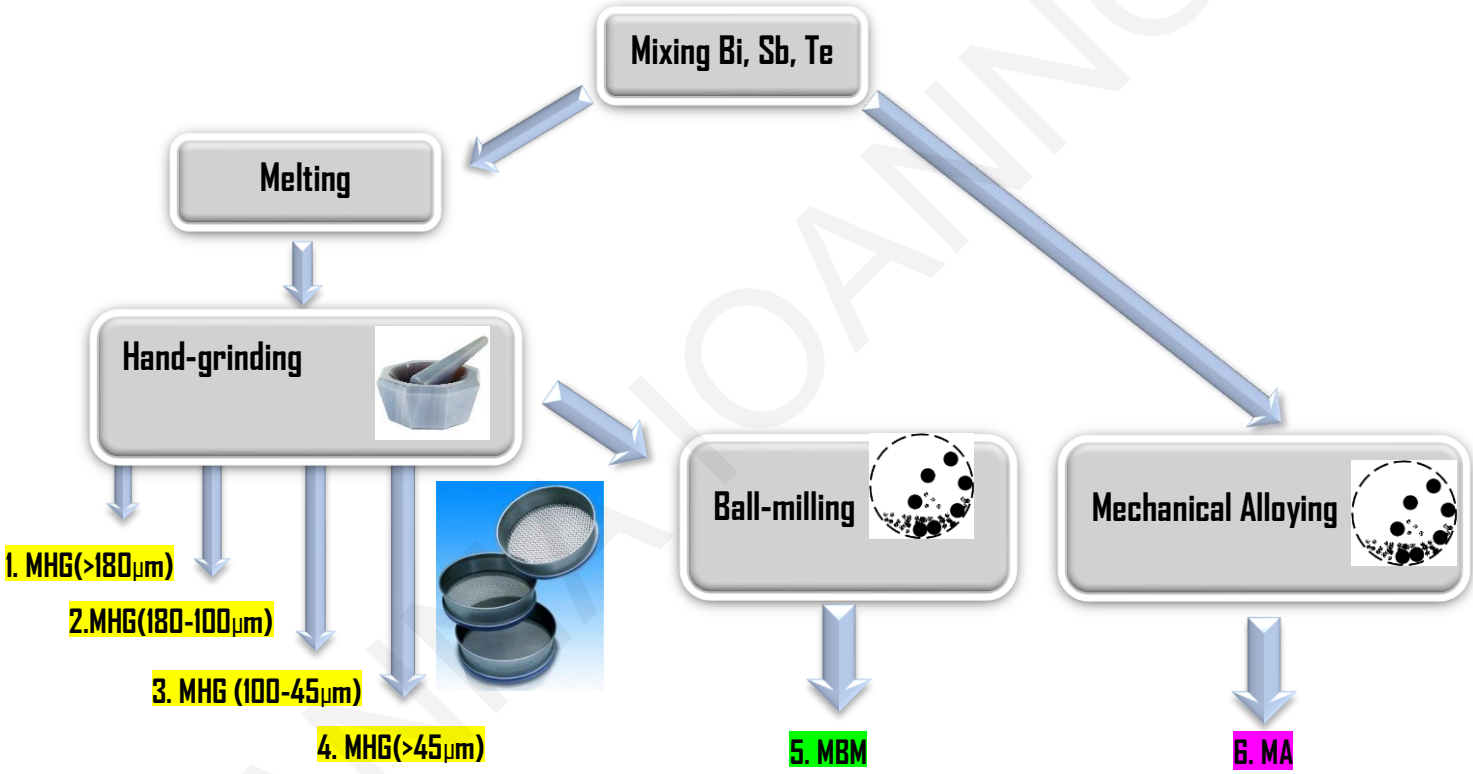

Figure 5.6: Schematic presentation of the preparation of $Bi_{0.3}Sb_{1.7}Te_3$ powders with different particle sizes.

5.2.1 Synthesis and consolidation details

Melting and mechanical alloying was used for the synthesis of the $B_{0.3}Sb_{1.7}Te_3$ solid solution, as described in 3.1.1 and 3.1.2. The ingot obtained from melting was hand grounded to obtain micro-sized particles and an amount of this powder was further ball-milled under Ar atmosphere to obtain powder consisting of crystallites (nano). The milling was operated at 300rpm for 20 hours and the ball-to-material ratio was 10:1.

The obtained powders were loaded in a cylindrical graphite die (inside diameter=10mm) and hot-pressed at 420℃ for one hour under an axial pressure of 80MPa.

5.2.3 Results

Structural Characterization:

Figure 5.7a shows the X-ray diffraction patterns of the powders produced by melting (MHG), mechanical alloying (MA) and ball milling (MBM). The miller indices of all major peaks are indicated and the XRD pattern verifies that the powders are single phase. The well-known Scherrer formula, was again used to calculate the mean crystallite size generated by ball milling (MBM) and mechanical alloying (MA). The mean crystallite size was calculated (28±3) nm and (29±4) nm for the powders produced by MA and MBM respectively.

Figure 5.7b presents a typical XRD diffraction pattern of a $Bi_{0.3}Sb_{1.7}Te_3$ sample in two directions, namely the in-plane direction and the cross-plane direction. The graphs indicate that no other phase or impurity is present apart from the rhombohedral bismuth-telluride phase. The existence of preferred orientation in the in-plane configuration is revealed by the (00l) diffraction intensities which are higher than the ones in the cross-plane pattern. As shown in Table 5.2 and Figure 5.7c the LF increases from zero for MA and MBM to 0.25 for MHG samples, which clearly indicates a microstructural anisotropy. On the other hand, the LFs of samples prepared via MA and MBM were determined to be zero indicating randomly oriented samples. Moreover, samples prepared via melting and especially MHG(>180μm) and MHG(180-100μm) present higher relative density (ρ~94%) than other samples. Specifically, MBM sample consisting of nano-crystallites illustrate the lowest relative density, around 89%, suggesting a possible higher level of porosity which will consequently affect the thermoelectric properties.

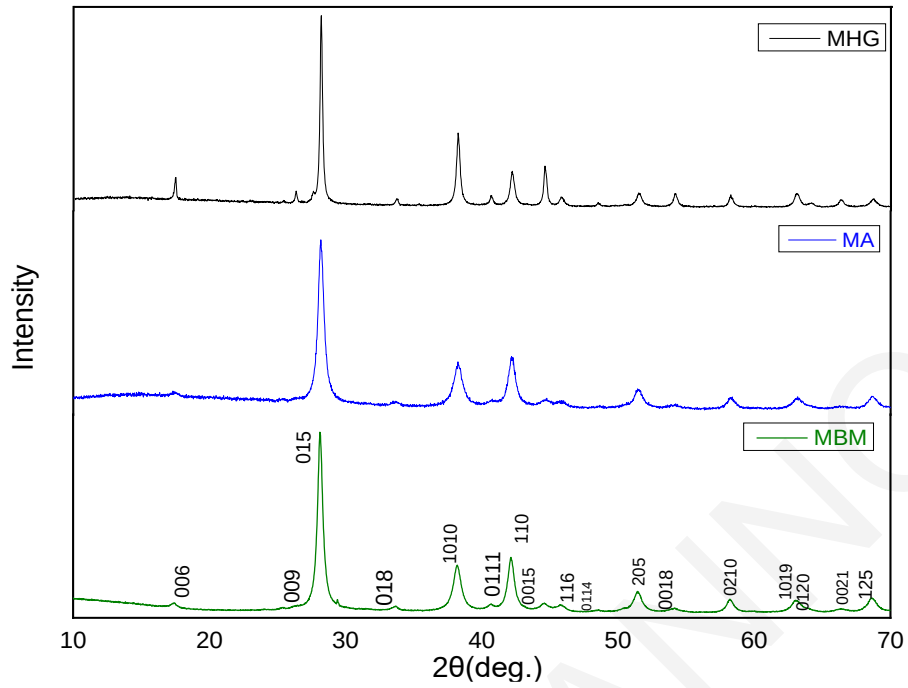

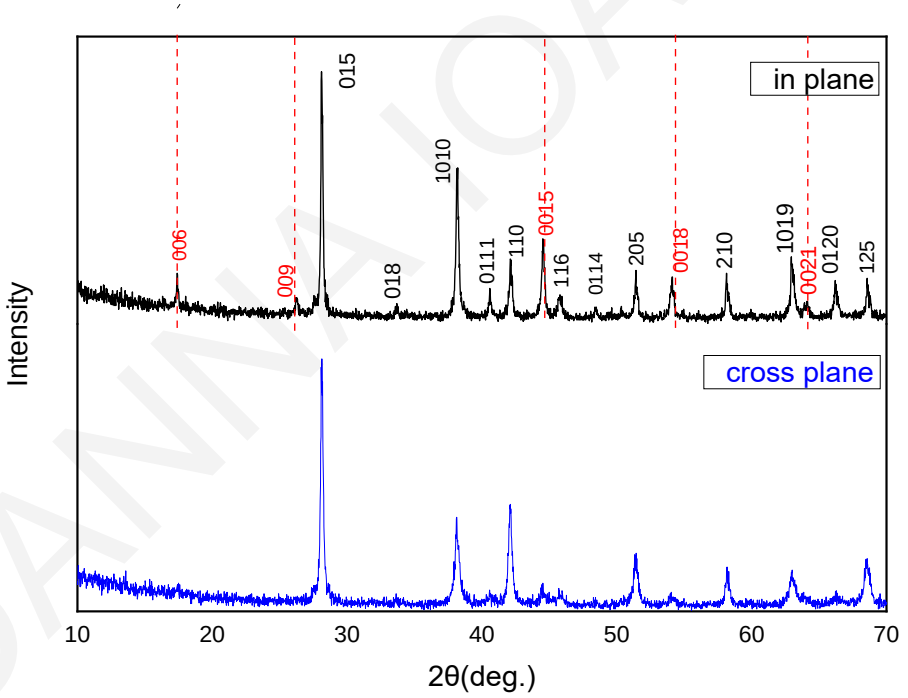

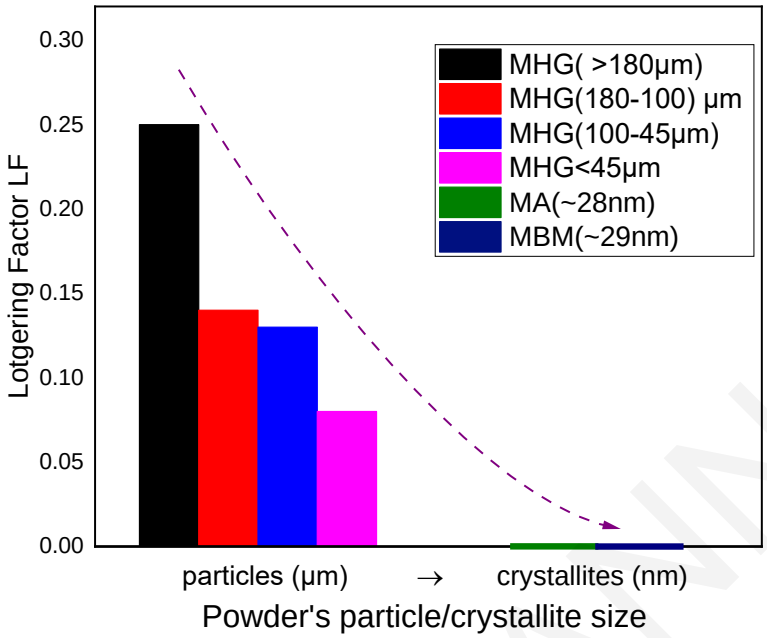

Figure 5.7: (a) XRD diffraction patterns for the powders produced by MGH, MA and MBM, (b) XRD diffraction patterns of the hot-pressed $Bi_{0.3}Sb_{1.7}Te_3$ samples prepared via MGH for both in-plane and cross-plane direction. The dash lines correspond to (00l) peaks and (c) the Lotgering factor (LF) of the $Bi_{0.3}Sb_{1.7}Te_3$ hot-pressed samples prepared via MGH, MBM and MA.

Table 5.2: Lotgering factor (LF), geometrical density and relative density of the hot-pressed $Bi_{0.3}Sb_{1.7}Te_3$ samples.

Powder type	Sample	Lotgering factor (LF)	Pellet Density ρ (g/cm^3)	Relative Density (%)
Powders consisting of μm-particles	MHG(>180μm)	**0.25**	**6.42**	**94**
	MHG(180-100μm)	**0.14**	**6.44**	**94**
	MHG(100-45μm)	**0.13**	**6.11**	**90**
	MHG(<45μm)	**0.08**	**6.12**	**90**
Powders consisting of crystallites	MBM (~29 nm)	**0**	**6.07**	**89**
	MA (~28 nm)	**0**	**6.29**	**92**

Thermoelectric properties:

Figure 5.8 presents the hole concentration (n_H) and carrier mobility (μ) as a fuction of powder's particle size. n_H and μ monotically decrease with decreasing particle size and reach the lowest values for samples prepared from MA and MBM powders. The observed decrease in n_H with decreasing particle size is attributed to the formation of antisite defects. Ionescu et al. proposed a model based on the idea that grinding, sintering and pressing can cause several kinds of defects and vacancies in TE materials [147]. Additionally, Stilbans et al. has showed that the vacancies of Te and Bi atoms produce one acceptor and one donor, respectively, since the ratio $V_{Te}/V_{Bi} \geq 3/2$, the number of acceptors is smaller than that of donors, which explains the trend of changing the conductivity from p- to n-type resulting from mechanical treatment [147]. As described in chapter 2.3, the formation of Te vacancies and the small difference in electronegativity of the atoms forming the compound can lead to the formation of several antisite defects, that not only lead to the donation of electrons to the system but also enhance the vacancy phonon scattering that reduces the lattice thermal conductivity [94]. Navratil et al. analytically described the interaction of vacancies with the antisite defects that are present in $Bi_xSb_{2-x}Te_3$ solid solution which can lead to the decrease of hole carrier concentration [95]. The decrease of μ with decreasing particle size is mainly attributed to the enhanced charge carrier scattering, likely as a result of the absence of preferred orientation and the presence of interfaces, grain boundaries, and high-density lattice defects.

The temperature dependence of Seebeck coefficient and electrical conductivity is illustrated in Fig. 5.9 (a) and (b) respectively. Seebeck coefficient increases with increasing temperature, reaches a maximum value around 400K and then gradually decreases due to the onset of bipolar conduction (minority carriers are excited into the conduction band). The increase of Seebeck coefficient with decreasing particle size is attributed to the carrier concentration variation (see Fig.5.9a). The highest Seebeck coefficient (S~227 μV/K at 400K) was achieved by MBM, while the sample with the largest powder particle size MHG(>180μm) recorded the lowest value (S~188 μV/K at 400K).

Electrical conductivity varies linearly with temperature (in the range of 310-520K) indicating a narrow band degenerate semiconductor behaviour for all studied samples. Electrical conductivity decreases for samples with smaller particle size due to the

decrease of charge carrier concentration caused by the formation of antisite defects, the reduction of hole mobility due to the presence of high-density boundaries and the absence of preferred orientation especially for samples prepared via MA and MBM. Even though, MBM and MA samples were prepared by powders consisting of crystallites of similar size, they present different electrical conductivity values at room temperature (see Figure 5.9a). In specific MA recorded a slightly higher σ than MBM. This discrepancy can be attributed to the relative higher density (ρ) of MA sample, which thereafter increase the carrier mobility as well as to its slightly higher hole concentration.

The temperature dependence of power factor ($PF=S\sigma^2$) is illustrated in Figure 5.9c. A maximum value of PF=48.3 $\mu Wcm^{-1}K^{-2}$ was achieved at room temperature for the MGH(180-100)μm sample due to its high electrical conductivity. Despite the high Seebeck coefficient, the PF of the samples prepared by mechanical alloying and ball milling remained low (PF=40 $\mu Wcm^{-1}K^{-2}$) because of their relatively low electrical conductivity.

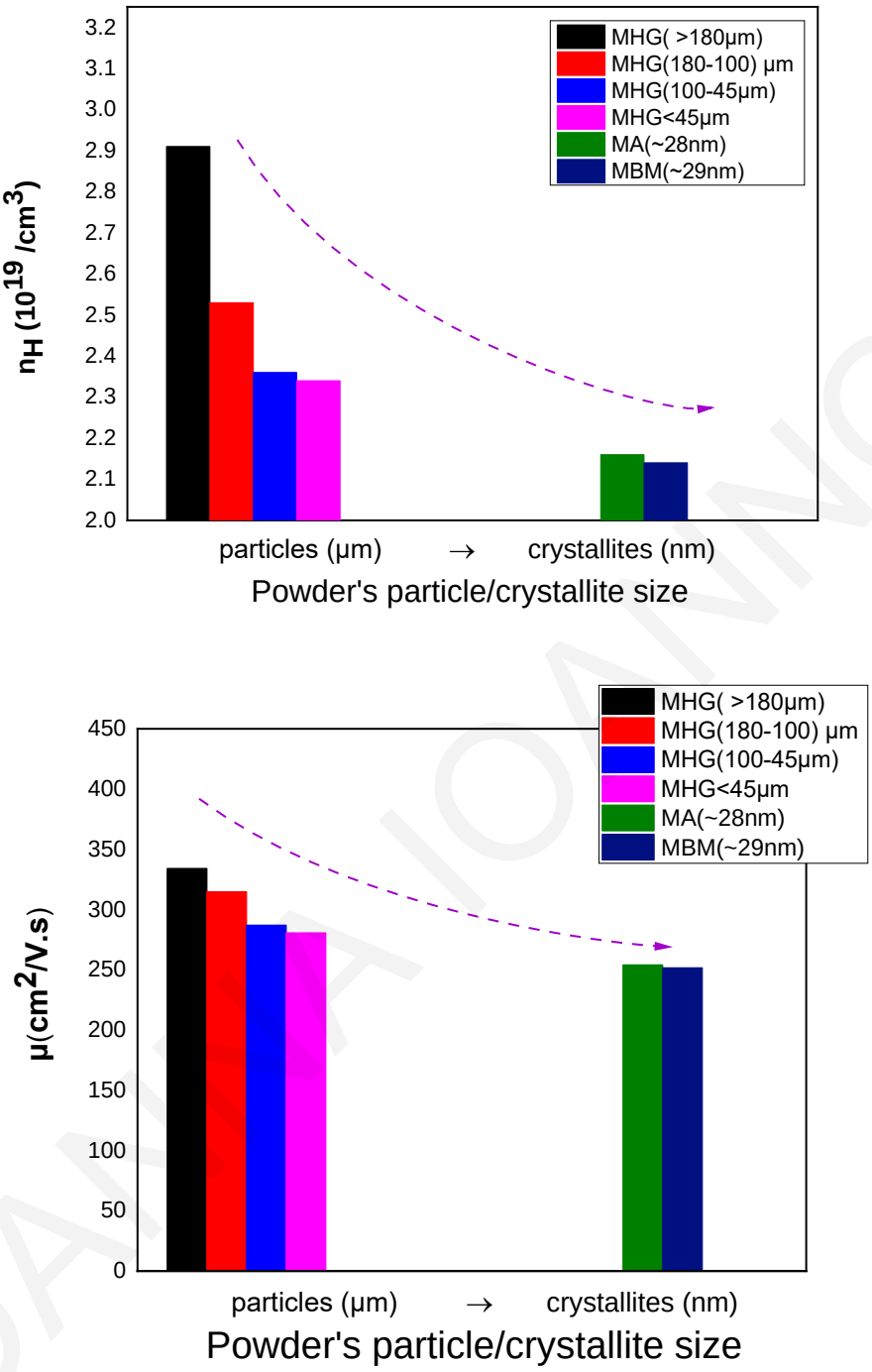

Figure 5.8: Carrier concentration (n_H) (a) and carrier mobility (μ) (b) at room temperature as a function of powder's particle crystallite size of the hot-pressed $Bi_{0.3}Sb_{1.7}Te_3$ samples.

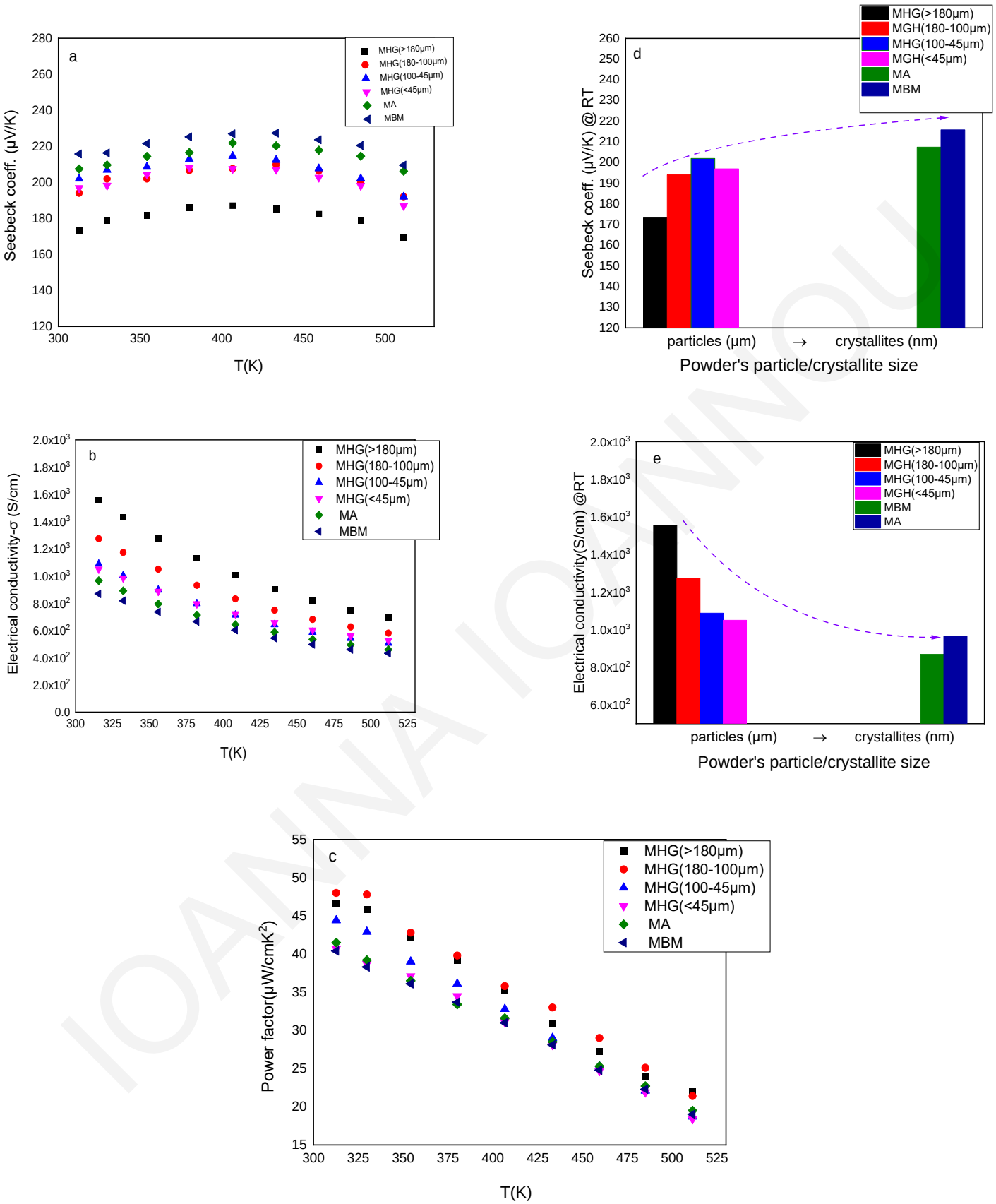

Figure 5.9: Temperature dependence of Seebeck coefficient (a), electrical conductivity (b) and power factor (c) of the hot-pressed $Bi_{0.3}Sb_{1.7}Te_3$ samples. Seebeck coefficient (d) and electrical conductivity (e) at room temperature as a function of powder's particle/crystallite size.

The total thermal conductivity, eletronic thermal conductivity and lattice thermal conductivity as a function temperature are presented in Figure 5.10. The in-plane thermal diffusivity (D) was measured using a method proposed by Xie et al.[159]. According to this method the samples are cut into four bars and then glued together after they had been rotated 90^o counterclockwise. This re-configuration allowed the measurement of D along the in-plane direction (perpendicular to the hot press direction), the same direction Seebeck coefficient and electrical resistivity were measured. The ρ of the samples was calculated using their measured dimensions and masses. The C_p was calculated theoretically based on the temperature dependences of heat capacity of Bi_2Te_3 and Sb_2Te_3 [160], [161].

There is up to 38% decrease in total thermal conductivity (κ_t) of samples prepared via MBM and MA in comparison to the total thermal conductivity of samples prepared via MHG. This is mainly attributed to the formation of several antisite defects during grinding that led to lower carrier concentration and caused a reduction of 44% in electronic thermal conductivity (κ_{el}). The electronic contribution to the total thermal conductivity was estimated by the Wiedeman-Franz relationship ($\kappa_{el}=L\cdot\sigma\cdot T$, $L=2.44\cdot10^{-8}V^2K^{-2}$) and the lattice and ambipolar thermal conductivity was estimated by subtracting the κ_e from κ_{total}. The electronic thermal conductivity decreases with rising temperature, while κ_t-κ_e increases with temperature due to the existence of minority carriers arising with the onset of intrinsic contribution [162]. The lattice and ambipolar contribution (κ_t-κ_e) to the total thermal conductivity is presented in Fig. 5.10b. The presence of interfaces and grain boundaries as well as the abscence of preferred orientation in samples made of nano-powders (MA,MBM), enhanced the scattering of phonons and suppressed the lattice thermal conductivity by 40%. As shown in Figure 5.10e, MHG(≤45μm) recorded the lowest lattice thermal conductivity ($\kappa_{lattice}$~0.4 W/m.K) at room temperature. This value approaches the theoretical limit of thermal conductivity κ_{min}~0.31 W/m.K and suggest that the presence of particles of broad size scale (micron-particles under 45μm and possibly sub-micrometer particles) can effectively reduce the phonon mean free path and reduce the lattice thermal conductivity. According to the theory, structures composed by different size of features, are expected to scatter more effectively different groups of phonon MFPs and potentially reduce the thermal conductivity down to the theoretical limits [38]. The low

lattice thermal conductivity of MHG(≤45μm) suggests that more investigation is needed regarding the influence of the powder's particle size range on the thermoelectric properties.

Due to the significant grain growth during the hot-press, the observed grain sizes, even in the nano-bulk samples can be widely distributed from few nm to ~1 μm, where the averaged grain size can be above 1 μm [163]. In numerous studies, phonon mean free path (MFP) spectra predicted by atomistic simulations suggest that smaller than 100 nm grain sizes are necessary to reduce the lattice thermal conductivity by decreasing phonon MFPs[164][165]. This is in contrast with available experimental data, where a remarkable thermal conductivity reduction is observed even for micro-grained Bi_2Te_3 samples. In this situation, micro-grains should only slightly reduce the $\kappa_{lattice}$ based on classical phonon size effects. According to a theoretical study by Wang et al.[166], the discrepancy between computed phonon MFPs and measured $\kappa_{lattice}$ reduction in polycrystalline materials can be eliminated by considering the interfacial thermal resistance (R_K) [167] at GBs which results from the frequency-dependent phonon transmission or reflection at GBs (see Figure 5.11). It was found that a high R_K at GBs should be the main cause for the observed significant thermal conductivity reduction.

The calculated ZTs are presented in Figure 5.12. The results reveal that the best thermoelectric performance ZT(350K)~1.13 is obtained for the MA sample and the MHG(≤45μm) sample. This value is almost 30% higher than that of MHG(>180μm). In addition, the average ZT_{av} value of MA and MHG(≤45μm) is 1.02 and 0.96 respectively while the average ZT_{av} value of MHG(>180μm) is only 0.74. Even though, the calculated power factors of MA and MHG(≤45μm) samples were significantly lower than those of samples prepared from powders with larger particle sizes due to the lower electrical conductivities, the remarkably reduced thermal conductivity contributed in achieving a high ZT.

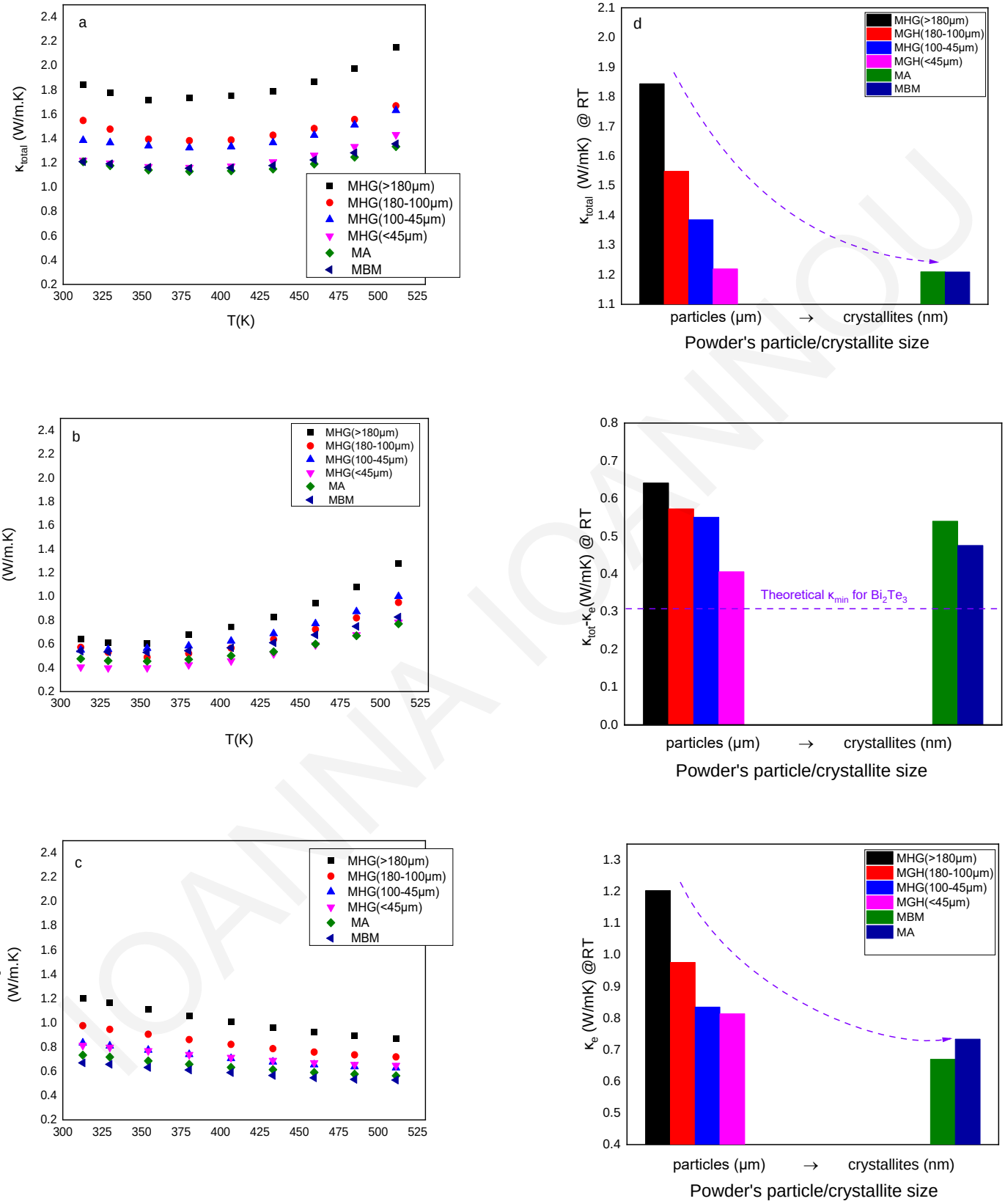

Figure 5.10: Temperature dependence of (a) total thermal conductivity (κ_{total}), (b) lattice and ambipolar thermal conductivity (κ_l-κ_e) and (c) electronic thermal conductivity (κ_e) for the hot-

pressed $Bi_{0.3}Sb_{1.7}Te_3$ samples. κ_{total} (d), κ_l-κ_e (e) and κ_e (f) at room temperature as a function of particle/crystallite size.

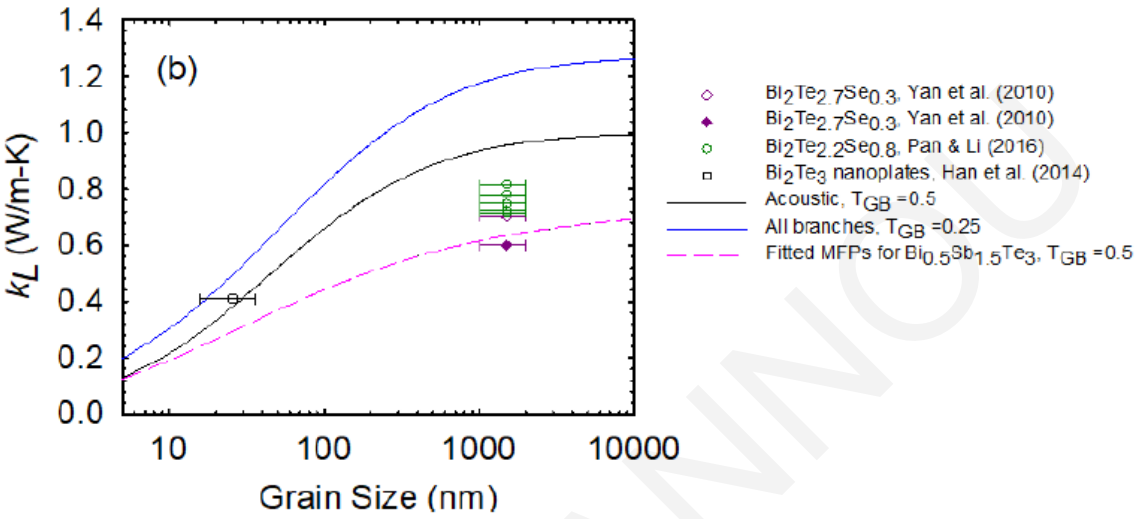

Figure 5.11: Predicted room-temperature $\langle\kappa_{Lattice}\rangle$ values as a function of the averaged grain size, in comparison to representative experimental results on polycrystalline Bi_2Te_3-based samples.Reproduced by Wang et al.[166]. T_{GB} is the grain boundary transmissivity used for the calculations.

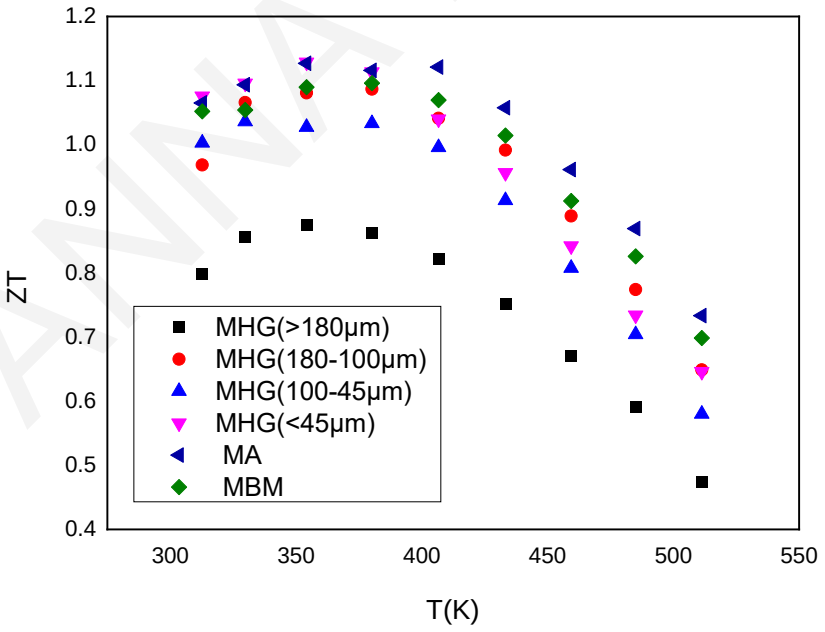

Figure 5.12: Thermoelectric figure of merit-ZT of the hot-pressed $Bi_{0.3}Sb_{1.7}Te_3$ samples as a function of temperature.

5.2.3 Fabrication of nanocomposite bulk $Bi_{0.3}Sb_{1.7}Te_3$ alloys

Theoretical predictions claim that the presence of randomly distributed pores and features of different size scale results in a shortening of the mean free path of thermal phonons, which can cause a substantial reduction of the thermal conductivity[168][169]. Defects in atomic-scale and up to a few nanometres can act as scattering points for short wavelength phonons. Nanoscale defects like dislocations, alloying, nano-precipitates, large quantum dots and second-phase islands can effectively scatter phonons of short and medium wavelength (up to ~100 nm). Long wavelength phonons (up to ~1 mm) can be scattered by micro and mesoscale defects like grain boundariess, especially at elevated temperatures [38][49][50]. Therefore, the combination of the aforementioned defects will theoretically lower the lattice thermal conductivity down to the theoretical limits by achieving broad wavelength scattering of phonons.

The aim of the second part of this work was the fabrication of nano-composite materials with lower thermal conductivity values but relatively unaffected power factors. In order to investigate the thermoelectric properties of nanocomposite bulk $Bi_{0.3}Sb_{1.7}Te_3$ alloys, powders consisting of 50% MHG particles and 50% MBM crystallites were hot-pressed under the same compaction conditions as the previously discussed samples.

Structural Characterization:

Figure 5.13a shows the X-ray diffraction patterns of $Bi_{0.3}Sb_{1.7}Te_3$ solid solutions prepared by mixing MHG and MBM powders. The miller indices of all major peaks are indicated and the XRD pattern verifies that all samples illustrate the desired BST phase without any other secondary phase or impurity presented. The level of preferred orientation (Lotgering factor) was again calculated. In the last section of this work, it was mentioned that samples prepared via MHG have higher LF while samples prepared via MA and MBM are randomly oriented (zero LF). We also shown that the degree of preferred orientation drops as the particle size of MHG samples decreases. As illustrated in Figure 5.13b and Table 5.3, samples prepared after mixing MHG and MBM exhibit lower LF than samples prepared from 100%MHG, as expected. However, the reduction of LF is more obvious for 50%MHG(100-45μm)+50%MBM sample, while the magnitude of LF drop is lower for 50%MHG(180-100μm)+50%MBM and 50%MHG(<45μm)+50%MBM samples.

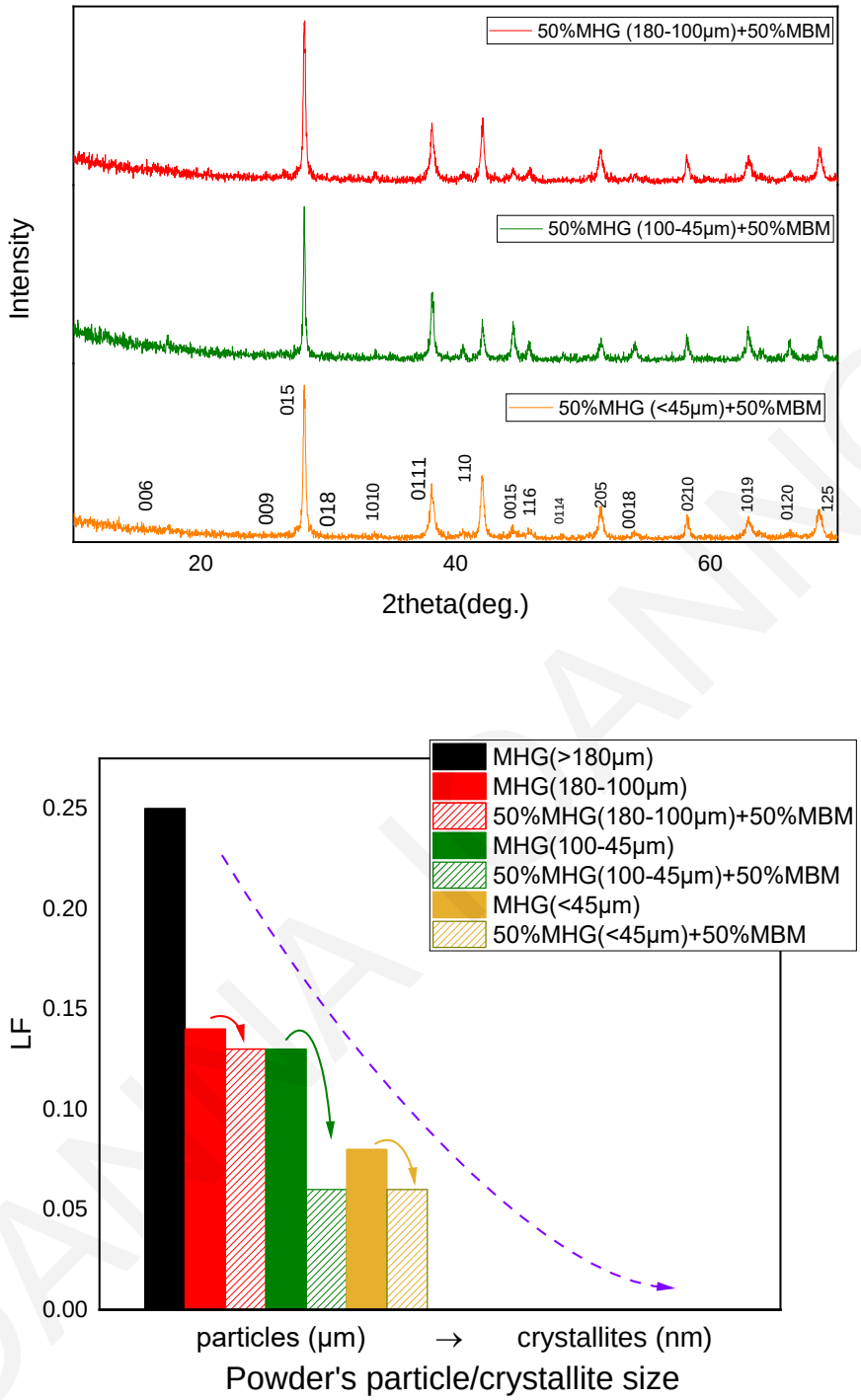

Figure 5.13: In-plane X-ray diffraction patterns of the hot-pressed nanocomposite $Bi_{0.3}Sb_{1.7}Te_3$ samples (a) and Lotgering factor (LF) as a function of powder's particle/crystallite size.

Table 5.3: Lotgering factor (LF), geometrical density and relative density of the hot-pressed $Bi_{0.3}Sb_{1.7}Te_3$ samples prepared using MHG, MBM, MA powders and mixtures of MHG and MBM powders.

Powder type	Sample	Lotgering factor (LF)	Pellet Density ρ (g/cm^3)	Relative Density (%)
Powders consisting of μm-particles	MHG(>180μm)	**0.25**	**6.42**	**94**
	MHG(180-100μm)	**0.14**	**6.44**	**94**
	MHG(100-45μm)	**0.13**	**6.11**	**90**
	MHG(<45μm)	**0.08**	**6.12**	**90**
Powders consisting of both μm-particles and crystallites	50%MHG(180-100μm)+50%MBM	**0.13**	**6.48**	**95**
	50%MHG(100-45μm)+50%MBM	**0.06**	**6.21**	**91**
	50%MHG(<45μm)+50%MBM	**0.06**	**6.00**	**88**
Powders consisting of crystallites	MBM (~29 nm)	**0.00**	**6.07**	**89**
	MA (~28 nm)	**0.00**	**6.29**	**92**

Thermoelectric properties:

Figure 5.14 shows the hole concentration (n_H) and carrier mobility (μ) as a fuction of powder's particle size. As presented in the previous section of this chapter, MHG samples have notably higher carrier concentration than MBM and MA samples. In addition, n_H monotically decrease with decreasing particle size. Thus, the combination of powders consisting of 50% nano-crystallites and 50% micro-particles is expected to decrease the carrier concentration compared to MHG samples. Suprisingly, the difference between MHG(180-100μm) sample and its nanocomposite counterpart (MHG(180-100μm)+50%MBM) is insignificant. On the other hand, 50%MHG(100-45μm)+50%MBM and 50%MHG(<45μm)+50%MBM present slighlty lower n_H than the anologous MHG materials, as expected. Materials prepared from mixing MBM and MHG powders revealed lower hole mobility. Specifically, MHG(180-100μm), MHG(100-45μm) and MHG(<45μm) illustrate 18-20% higher μ in comparison to their nanocomposite counterparts. The decrease of μ is attributed to the increased hole scattering in materials consisting of nm-crystallites, mainly resulting from the lower degree of preferred orientation, the higher density of interfaces and grain boundaries.

The temperature dependence of Seebeck coefficient, electrical conductivity and power factor is illustrated in Fig. 5.15(a-c), while the Seebeck coefficient, electrical conductivity and power factor values at room temperature are presented in Fig.5.15(d-

f) as a function of powder's particle/crystallite size. Despite the slightly lower n_H values, the S of samples prepared from powder mixtures are more or less the same with the analogous MHG materials. Samples prepared via MBM and MA still have the highest S values, while the sample prepared from the powder with the largest particle size has the lowest S. The electrical conductivity (σ) of nanocomposites is significantly lower than that of the analogous MHG samples. In specific, σ at room temperature is reduced by 17%, 21% and 22% for 50%MHG(180-100μm)+50%MBM, 50%MHG(100-45μm)+50%MBM and 50%MHG(<45μm)+50%MBM, respectively, reaching almost similar σ values as the samples prepared exclusively from nano-powders (MBM and MA). As mention before, S and n_H do not significantly change after mixing MHG and MBM powders, leading us to the conclusion that the electrical conductivity reduction is a result of the hole mobility alteration. The mobility of carriers is notably reduced in samples prepared from both MHG and MBM, due to the increased scattering at the grain boundaries and the lower degree of preferred orientation which consequently results in a lower electrical conductivity. The calculated power factors are presented in Figure 5.15(c,f). The PF of 50%MHG+50%MBM samples is severely reduced in comparison to that of their 100%MHG counterparts, reaching even lower values than MBM and MA samples. The intense reduction of PF is mainly attributed to the decrease of carrier mobility which consequently affected the electrical conductivity.

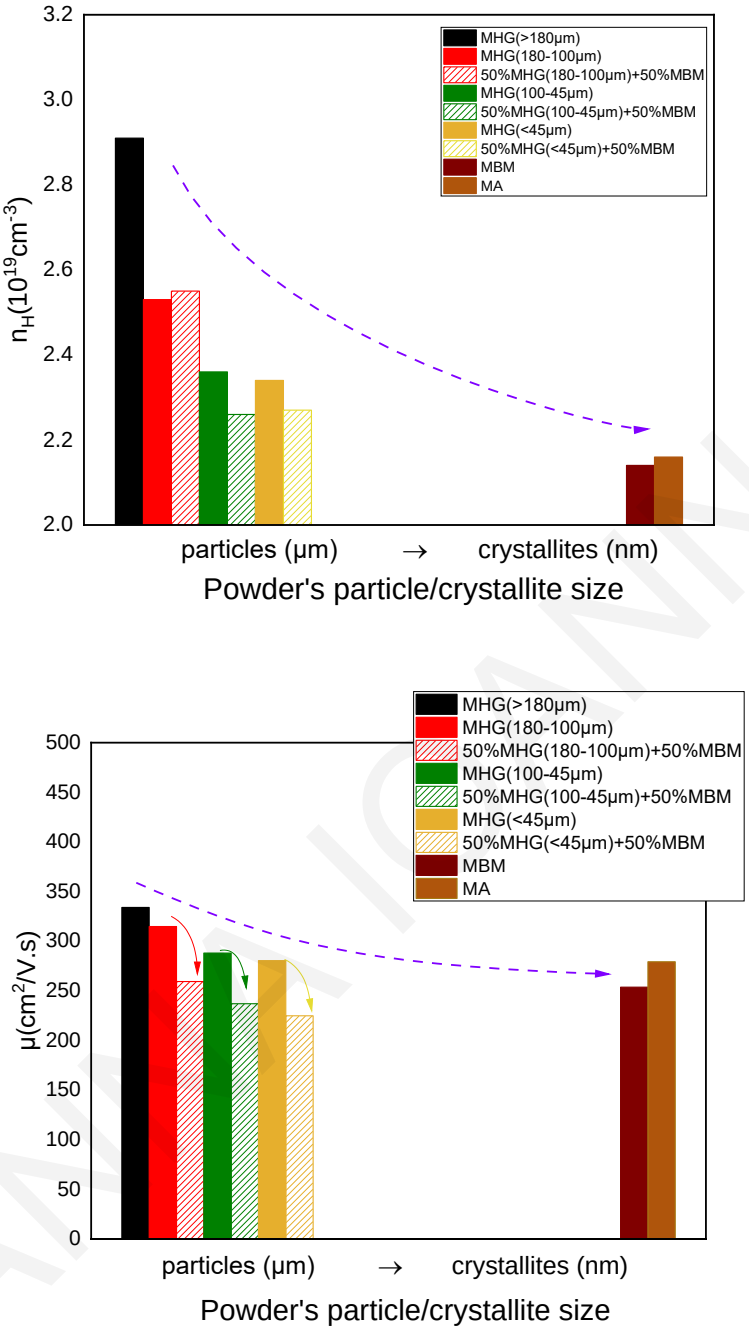

Figure 5.14: Carrier concentration (n_H) (a) and carrier mobility (μ) (b) at room temperature as a function of powder's particle/crystallite size of the hot-pressed $Bi_{0.3}Sb_{1.7}Te_3$ samples.

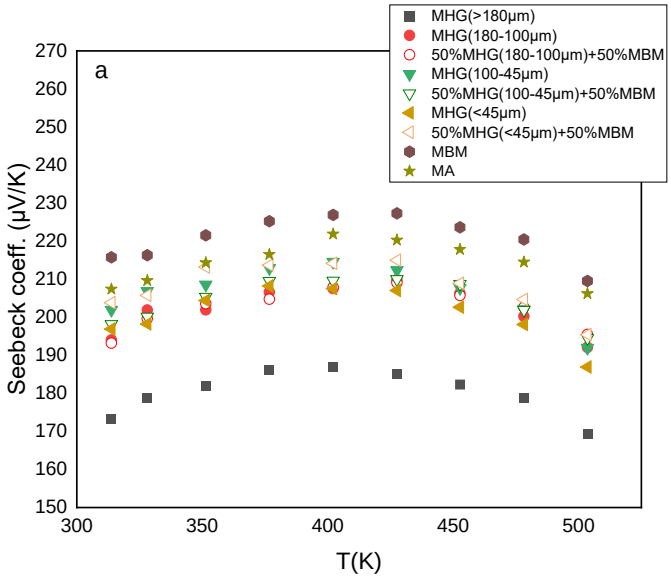

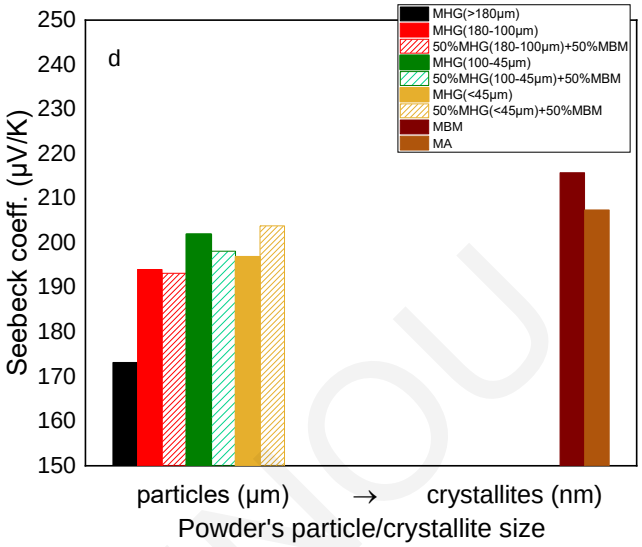

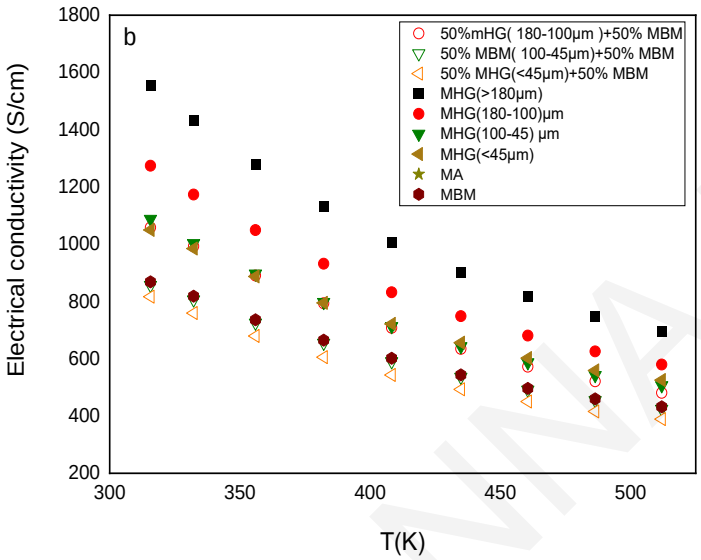

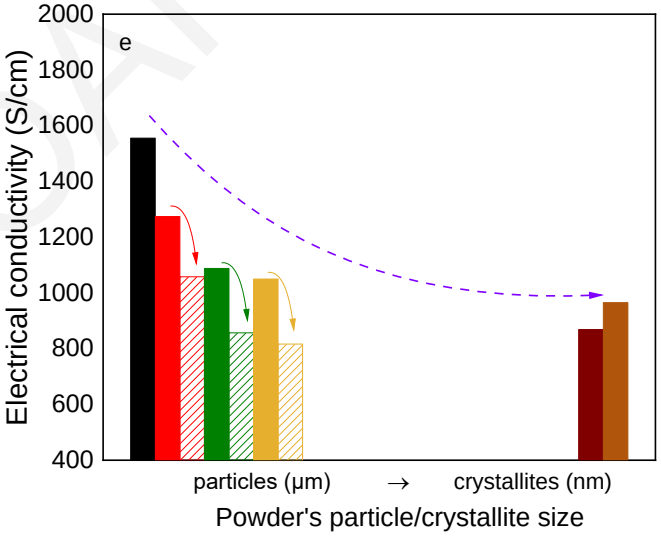

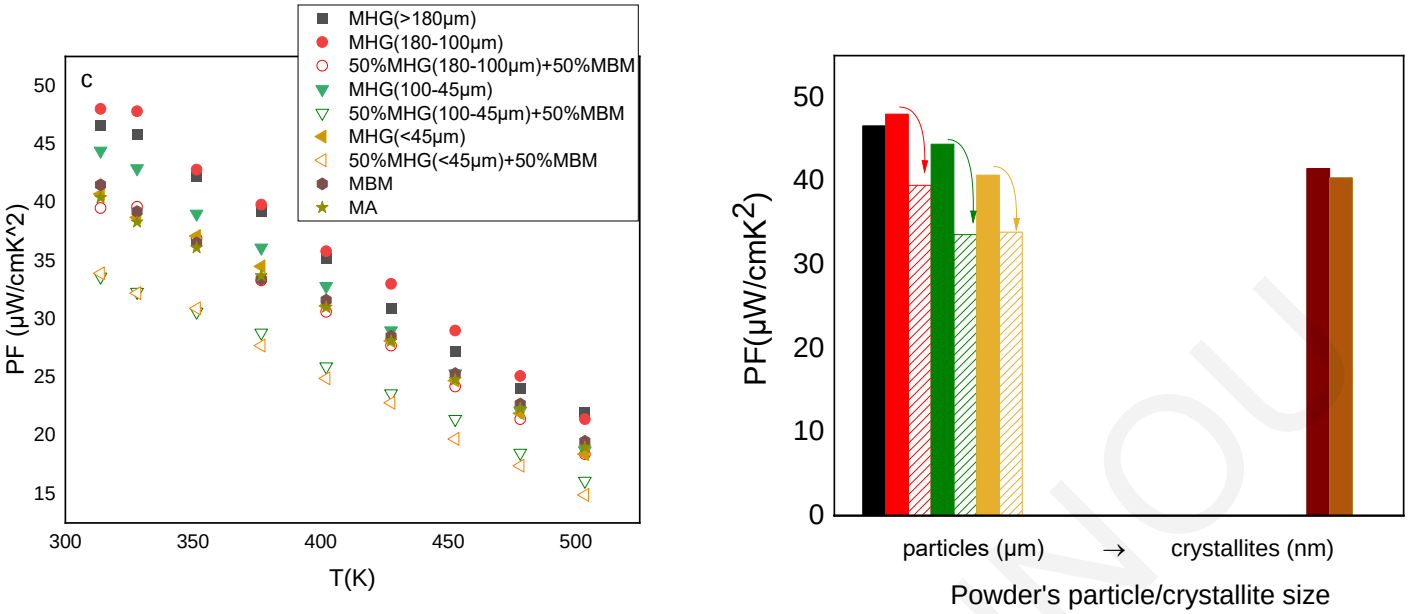

Figure 5.15: Temperature dependence of Seebeck coefficient (a), electrical conductivity (b) and power factor (c) of the hot-pressed $Bi_{0.3}Sb_{1.7}Te_3$ samples. Seebeck coefficient (d) and electrical conductivity (e) and power factor (f) at room temperature as a function of powder's particle/crystallite size.

The results of total thermal conductivity (κ_{total}), eletronic thermal conductivity (κ_e) and lattice thermal conductivity (κ_{total}- κ_e) are presented in Figure 5.16. The in-plane thermal diffusivity (D) was again measured along the in-plane direction using a method proposed by Xie et al.[159]. Even though, the electronic thermal conductivity is remarkably reduced for the 50%MHG+50%MBM samples because of the decrease of electrical conductivity, the total thermal conductivity remains approximately the same due to the increase of lattice thermal conductivity. Normally, the scattering rates of electrons and phonons are expected to both be higher for materials with high density of grain boundaries. Thus, the expected trend is that mobility as well as lattice thermal conductivity will drop as the grain size is reduced. In this case, $\kappa_{lattice}$ shows an unexpected increasing trend with decreasing the average particle size in samples prepared from mixing MHG and MBM powders, which appears contradictory to the standard grain-boundary scattering theory for phonons. This unphysical inverse correlation between $\kappa_{lattice}$ and mobility was also observed in other thermoelectric systems, such as Mg_3Sb_2[170], SnSe[171], (Hf,Zr)CoSb[77] etc. Another example is a study that investigated the effect of ball-milling duration on the grain size and the thermoelectric properties of n-type $Bi_2(Te,Se)_3$ [172] . In this study the lattice thermal

conductivity of the largest grained sample was lower than samples that were ball milled for longer times and had smaller grain sizes. Whereas, the weighted mobility of the small grained samples was lower, leading us to the conclusion that this effect is probably due to electrical grain boundary resistance[172].

The use of the conventional Wiedemann–Franz law assumes homogeneous materials where the scattering probability is uniform everywhere and no net exchange of energy between electrons and phonons is possible at grain boundaries or anywhere else. According to J.Kuo et al.[122], this assumption often leads to an overestimation of the phonon or lattice contribution to the thermal conductivity, especially for inhomogeneous materials, in which the length scale of the heterogeneity is larger than the mean-free-path or the coherence length. In materials with significant grain boundary electrical resistance, the estimated electronic contribution to the total thermal conductivity is low because the measured electrical conductivity is low. However, within the grain electrons may still be transporting more heat than the total conductivity suggests, leading to an overestimation of $\kappa_{lattice}$.

Based on the previously discussed possible overestimation of lattice thermal conductivity, we can conclude that the apparent increase in lattice thermal conductivity with mixing micron- and nano-powders is not a result of a true increase in the phonon contribution to thermal conductivity, but instead an aftereffect of assuming homogeneous electron and phonon transport in nanocomposite materials. J.Kuo et al.[122] suggested that treating grain boundary regions as a second phase with its own unique thermoelectric properties is essential to obtain a correct $\kappa_{lattice}$ of the material. This approximation suggests that the lattice thermal conductivity is dominated by the bulk media of the grain, which can be more precisely calculated via $\kappa_{lattice}=\kappa-L\sigma_G T$, where σ_G is the conductivity of the bulk grain rather than the total conductivity as used in the conventional model.

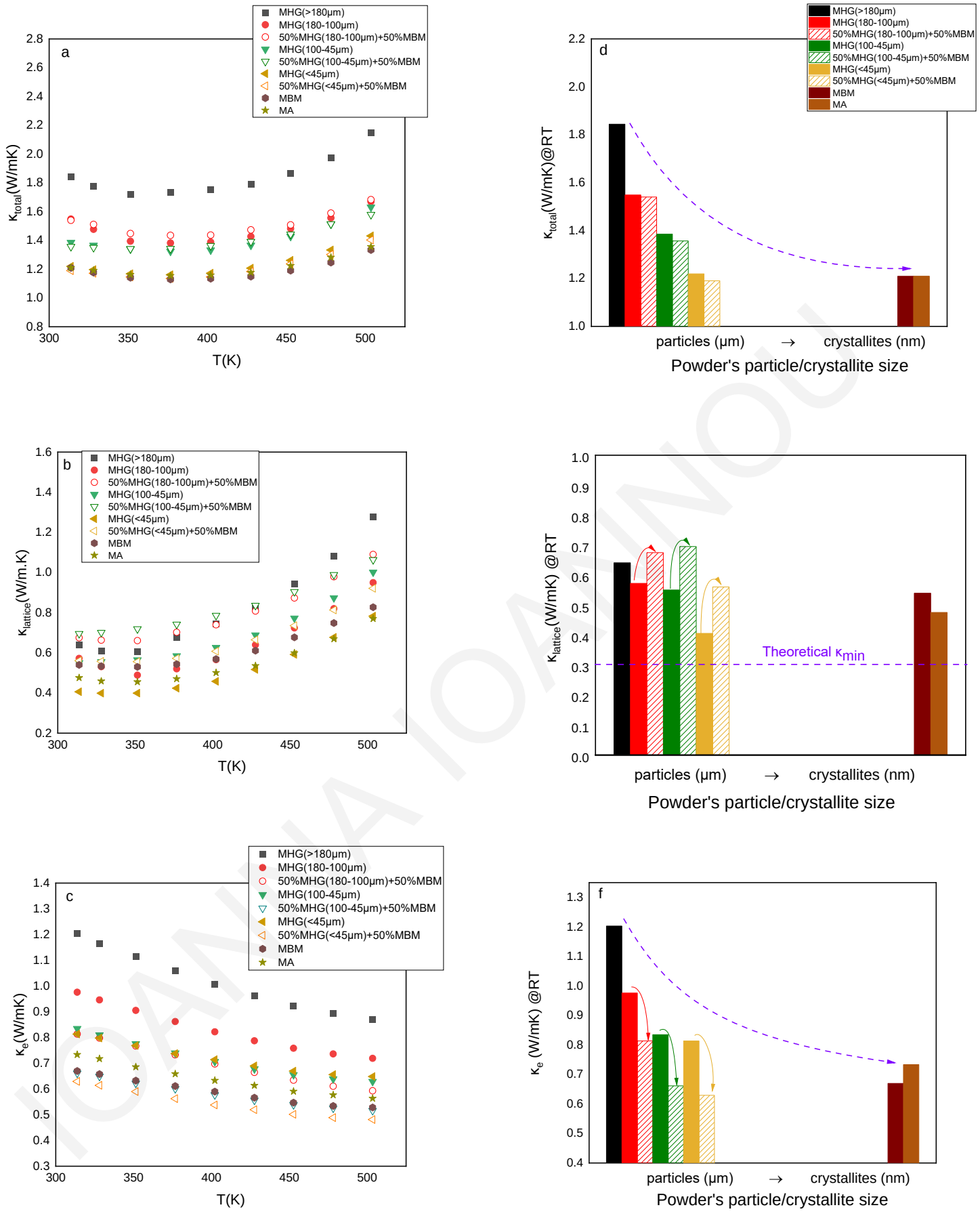

Figure 5.16: Temperature dependence of (a) total thermal conductivity (κ_{total}), (b) lattice and ambipolar thermal conductivity (κ_l-κ_e) and (c) electronic thermal conductivity (κ_e) for the hot-pressed $Bi_{0.3}Sb_{1.7}Te_3$ samples. κ_{total} (d), κ_l-κ_e (e) and κ_e (f) at room temperature as a function of particle/crystallite size.

The calculated ZTs are presented in Figure 5.17 as a function of temperature. The ZT of samples fabricated by mixing 50% MHG and 50% MBM powders is lower than their 100% MHG counterpart, mainly due to the significant decrease of electrical conductivity and power factor. Specifically, 50%MHG(180-100μm)+50%MBM, 50%MHG(100-45μm)+50%MBM and 50%MHG(<45μm)+50%MBM present 17%, 22% and 15% lower ZT_{max} than the analogous 100%MHG samples

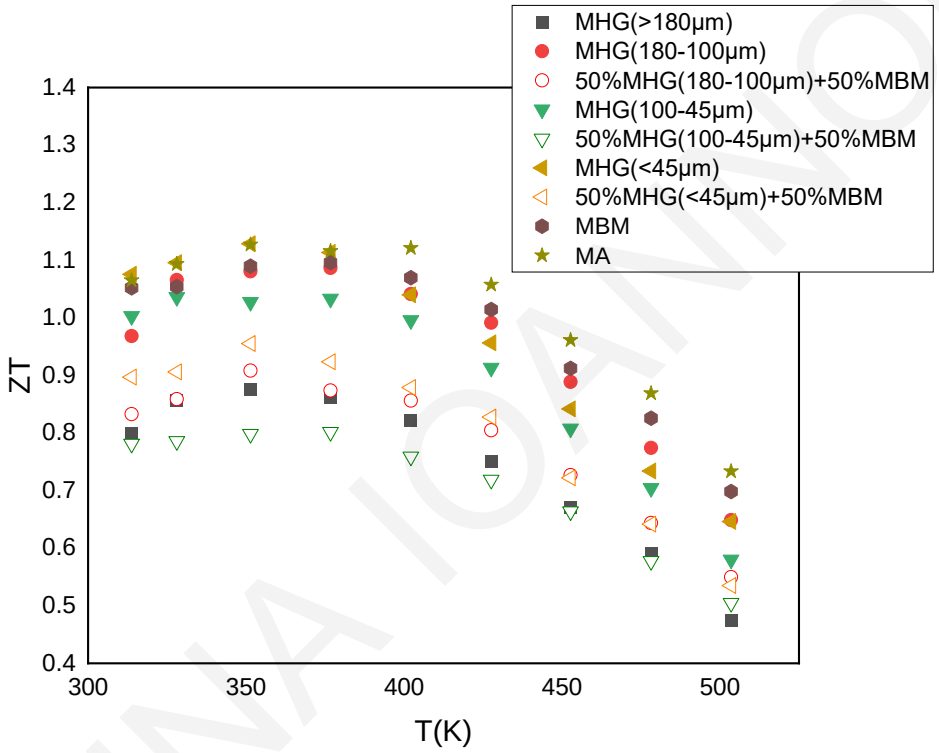

Figure 5.17: Thermoelectric figure of merit-ZT of the hot-pressed $Bi_{0.3}Sb_{1.7}Te_3$ samples as a function of temperature.

5.2.4 Conclusion

P-type $Bi_{0.3}Sb_{1.7}Te_3$ bulk materials were prepared using different methods: melting and mechanical alloying. The temperature dependence of all thermoelectric properties was measured along the same in-plane direction and reliable thermoelectric power factor and dimensionless figure-of-merit values were calculated. The experimental results indicate that the presence of high-density grain boundaries and interfaces in materials prepared using nano-powders and powders consisting of small microsized particles (<45μm) significantly reduced the lattice thermal conductivity while the formation of antisite defects, caused by hand-grinding and ball milling, resulted in lower carrier

concentrations and therefore in higher Seebeck coefficient values. As a result, a ZT(350K)~1.13 at was recorded for MA and MHG(<45μm) samples. In the second part of this work, nanocomposite bulk $Bi_{0.3}Sb_{1.7}Te_3$ alloys were fabricated from powders consisting of 50% MHG particles and 50% MBM crystallites in an attempt to further reduce lattice thermal conductivity without significantly affect the power factor. However, the notable decrease of electrical conductivity due to lower hole mobility resulted in lower PFs. Surprisingly, $\kappa_{lattice}$ showed an unexpected increasing trend in samples prepared by mixing MHG and MBM powders, which was contradictory to the standard grain-boundary scattering theory for phonons. This suggested a possible overestimation of $\kappa_{lattice}$ by using the conventional Wiedemann-Franz law, which is common in nano-composite materials with significant grain boundary electrical resistance.

6 Summary

In this work, mechanical alloying was applied for the synthesis of both p-type half-Heusler and Bismuth-Telluride solid solutions. Mechanical alloying has several advantages such as possibility of scaling up, inexpensive equipment, reduction of processing steps and easy preparation of nanostructured samples with decreased lattice thermal conductivity values.

In the first part of this work, p-type state-of-the-art half-Heusler MCoSb (M=Ti, Hf, Zr) thermoelectric solid solutions were prepared via mechanical alloying followed by hot-press sintering. Different optimization strategies have been applied: isoelectronic substitution and nanostructuring for the lattice thermal conductivity reduction, doping adjustment for the power factor optimization and Hf replacement for the cost reduction.

In the second part of this work, the improvement of the thermoelectric efficiency of bismuth telluride-based materials by tuning both the microstructure and the carrier concentration was attempted. P-type $Bi_xSb_{2-x}Te_3$ alloy powders were fabricated via mechanical alloying to explore the effect of Sb/Bi ratio on the microstructure and thermoelectric properties properties. In a second step, p-type $Bi_{0.3}Sb_{1.7}Te_3$ bulk materials were prepared by different methods (melting followed by hand grinding or ball milling and mechanical alloying) in order to investigate the effect of the powder's particle size on the thermoelectric performance.

In sections 6.1 and 6.2 the main results of these investigations and suggestions for future work regarding half-Heusler and Bismuth-Telluride materials will be provided.

6.1 Half-Heusler

In chapter 4.1, mechanical alloying was successfully applied for the synthesis of half-Heusler (Hf/Ti/Zr)$CoSb_{0.8}Sn_{0.2}$ compositions, suggesting the potential of replacing the time-consuming arc-melting followed by several days of annealing method by an advantageous, single step process. In chapter 4.2, $Hf_xTi_{1-x}CoSb_{0.8}Sn_{0.2}$ samples were prepared to investigate the effect of isoelectronic substitution on the thermoelectric properties and then, the effect of charge carrier concentration was investigated by preparing $Hf_{0.6}Ti_{0.4}CoSb_{1-y}Sn_y$ samples in order to evaluate the effect of Sn/Sb doping on the thermoelectric properties. The isoelectronic replacement of Ti with Hf in combination with nanostructuring approach via mechanical alloying led to an important

reduction in the lattice thermal conductivity. Consequently, a high ZT~0.85 at 980K was recorded by the hot-pressed $Hf_{0.6}Ti_{0.4}CoSb_{0.8}Sn_{0.2}$ sample prepared by 4 hours milling. It also turned out that a substitution level of 17% Sn for Sb is the most effective in $Hf_{0.6}Ti_{0.4}CoSb_{1-y}Sn_y$ materials prepared by mechanical alloying. $Hf_{0.6}Ti_{0.4}CoSb_{0.83}Sn_{0.17}$ sample, reached a maximum ZT~1.1 at 973K, which is among the highest ever reported for p-type MCo(Sb,Sn).

In chapter 4.3, the substitution of Sb with Bi in $Hf_{0.6}Ti_{0.4}Co(Sb,Bi,Sn)$ solid solutions prepared via MA was attempted. Recent published results suggested that a low lattice thermal conductivity and a high ZT (1.42) can be achieved in Bi-based HHs due to the substantial atomic mass difference between Sn and Bi atoms that leads to an intense point defect scattering. $Hf_{0.6}Ti_{0.4}CoSb_{0.8-x}Bi_xSn_{0.2}$ (x=0-0.1) samples were prepared as an attempt to partially replace Sb with Bi. Even though, an extremely low $\kappa_{lattice}$=1.69 W/m.K at 980K was achieved for $Hf_{0.6}Ti_{0.4}CoSb_{0.75}Bi_{0.05}Sn_{0.2}$, the decreased power factor prevented this compound to overcome the ZT of $Hf_{0.6}Ti_{0.4}CoSb_{0.8}Sn_{0.2}$. The highest ZT was reported for the sample without Bi (ZT~0.9) and the second highest for the sample with x=0.075 (ZT~0.73).

In chapter 4.4, we aimed to reduce Hf percentage in (Hf,Zr,Ti)Co(Sb,Sn) solid solutions prepared by MA with the objective to achieve a high thermoelectric performance in a less expensive HH composition. Based on the previously discussed encouraging results of chapter 4.2, $Hf_{0.6-x}Zr_xTi_{0.4}CoSb_{0.8}Sn_{0.2}$ samples were prepared as an attempt to replace Hf with its cheaper homologue Zr and to investigate the effect of isoelectronic substitution on the thermoelectric properties. The isoelectronic substitution of Hf with Zr resulted in lower power factors and ZTs. However, the decreased thermal conductivity of $Hf_{0.4}Zr_{0.2}Ti_{0.4}CoSb_{0.8}Sn_{0.2}$ suggested that this composition would be a good selection for further investigation regarding thermoelectric performance. To this end, the charge carrier concentration was optimized by preparing $Hf_{0.4}Zr_{0.2}Ti_{0.4}CoSb_{1-y}Sn_y$ samples and the effect of Sn/Sb doping was evaluated. As a result, $Hf_{0.4}Zr_{0.2}Ti_{0.4}CoSb_{0.83}Sn_{0.17}$ reached the highest ZT of 0.77 at 960K, a value that corresponds to an improvement of 15% with respect to that of $Hf_{0.4}Zr_{0.2}Ti_{0.4}CoSb_{0.8}Sn_{0.2}$.

Lastly, the effect of annealing under high temperatures and different durations upon thermoelectric performance of p-type HH solid solutions was investigated and

correlated with the impact on the structural properties. For this investigation, the $Hf_{0.6}Ti_{0.4}CoSb_{0.83}Sn_{0.17}$ sample (see chapter 4.2) was selected due to its outstanding thermoelectric performance (ZT=1.1 at 980K). According to the results of chapter 4.5, the structure, chemical composition and thermoelectric properties remained unaffected after 3 days of annealing at 800ºC. On the other hand, there is a significant reduction in the thermoelectric figure of merit after 10 days of annealing, due to the remarkable increase of thermal conductivity and the notable decrease of Seebeck coefficient and electrical conductivity (ZT~0.34). Last but not least, no phase-separation has been detected in the mechanically-alloyed single-phase materials after annealing. It turned out that the presence of phase-separation (two or more half-Heusler phases with slightly different lattice parameters) in most arc-melted samples is developed during rapid-solidification and not during the following annealing process.

6.1.1 Future work

Half-Heuslers are promising thermoelectric materials for future practical medium/high temperature applications. However, much more work is needed to optimize both the n-type and p-type leg. In this work, the p-type $Hf_{0.6}Ti_{0.4}CoSb_{0.83}Sn_{0.17}$ and $Hf_{0.4}Zr_{0.2}Ti_{0.4}CoSb_{0.83}Sn_{0.17}$ compositions prepared via mechanical alloying achieved the highest ZTs. The fabrication of both compositions via arc-melting followed by hot-press sintering, will provide a clear comparison of mechanical alloying and arc-melting methods in terms of thermoelectric performance and long-term stability. Moreover, the low lattice thermal conductivity of $Hf_{0.6}Ti_{0.4}Co(Sb,Bi,Sn)$ solid solutions (see chapter 4.3) suggests that more investigation is needed regarding Bi-based HHs. Different mechanical alloying durations and different hot-press sintering conditions can be tested to eliminate the presence of residual Bi in hot-pressed pellets and further investigate the phase-separation effect. Last but not least, the practical applications of thermoelectric devices involve prolonged and large temperature gradients. Thus, it is really important to investigate the thermal and mechanical stability of a candidate thermoelectric material before its applicability in commercial devices. A heat treatment similar to actual applications in the mid-temperature range can be examined via the effect of thermal cycling. The reliability of the thermoelectric performance of the previously discussed compositions can be easily tested on a laboratory scale by temperature cycling of the thermoelectric material and intermittent measurements of the materials properties.

6.2 Bismuth-Antimony-Telluride

Based on the idea that nano-structuring approaches are ideal for the fabrication of efficient p-type Bi-Sb-Te alloys, mechanical alloying followed by hot-press sintering was considered as an attractive way to make nanostructured TE materials. In chapter 5.1, p-type $Bi_xSb_{2-x}Te_3$ (x = 0.2,0.3,0.4,0.5) alloy powders were fabricated via mechanical alloying, and consequently consolidated by hot-press sintering. The effect of Sb/Bi ratio on the microstructure and TE properties was investigated. The decrease of Bi content resulted in higher hole density and hole mobility which thereafter increased the electrical conductivity and power factor. The absence of preferred orientation and the high density of grain boundaries in nanostructured materials led to impressively low lattice thermal conductivities values. As a result, a high ZT of 1.13 at 355K and an average ZT of 1.01 was achieved for $Bi_{0.3}Sb_{1.7}Te_3$, suggesting that mechanical alloying can be considered as an advantageous technique for single-step synthesis of highly-efficient $Bi_xSb_{2-x}Te_3$ alloys.

In chapter 5.2, p-type $Bi_{0.3}Sb_{1.7}Te_3$ polycrystalline solid solutions were fabricated using different methods: melting and mechanical alloying followed by hot-press sintering. The composition was selected based on the encouraging results of chapter 5.1. The effect of powder's particle size on the thermoelectric properties was investigated in samples prepared by powders of different particle sizes (micro or nano). Experimental results indicate that the presence of high-density grain boundaries in materials prepared using nano-powders and powders consisting of (<45μm) particles reduced the lattice thermal conductivity while the formation of antisite defects resulted in lower carrier concentrations and therefore in higher Seebeck coefficient values. As a result, a ZT(350K)~1.13 at was recorded for MA and MHG(<45μm) samples. In a second step, nanocomposite bulk $Bi_{0.3}Sb_{1.7}Te_3$ alloys were fabricated in an attempt to further reduce lattice thermal conductivity. Surprisingly, $\kappa_{lattice}$ showed an unexpected increasing trend in nanocomposite samples. This suggested a possible overestimation of $\kappa_{lattice}$ by using the conventional Wiedemann-Franz law, which is common in nano-composite materials with significant grain boundary electrical resistance.

6.2.1 Future work

Practical thermoelectric applications require high power and high efficiency while large temperature differences are applied across the device. Studies have shown that, an important obstacle of using a homogenous material in a large temperature gradient, is that a part of the material, does not operate in the optimum temperature range (peak ZT). The efficiency can be improved by creating a functionally graded material (FGM). FGMs operate in a wider temperature range because at any temperature there is a section of the material that is working optimally[173]. For instance, an FGM with a carrier concentration gradient can be made by putting together layers of $Bi_xSb_{2-x}Te_3$ solid solutions in order to optimize the average ZT in a wide temperature range. Moreover, thermal stress-induced cracks and other forms of defects from heating, thermal shock and rapid thermal fatigue lead to limited device lifetime[174]. An FGM with layers of BST materials with different grain sizes could possibly overcome this problem. Large grains provide better stability than small grains at high temperatures, while nanostructured materials have higher ZTs. If large grains are exposed to the heat source and the small grains are placed on the cold side, a higher efficiency can be retained.

References

[1] Y. Matsuo, A. Yanagisawa, and Y. Yamashita, “A global energy outlook to 2035 with strategic considerations for Asia and Middle East energy supply and demand interdependencies,” *Energy Strateg. Rev.*, vol. 2, no. 1, pp. 79–91, Jun. 2013, doi: 10.1016/J.ESR.2013.04.002.

[2] I. Perissi *et al.*, “Potential European Emissions Trajectories within the Global Carbon Budget,” *Sustainability*, vol. 10, no. 11, p. 4225, Nov. 2018, doi: 10.3390/su10114225.

[3] C. Forman, I. K. Muritala, R. Pardemann, and B. Meyer, “Estimating the global waste heat potential,” *Renew. Sustain. Energy Rev.*, vol. 57, pp. 1568–1579, 2016, doi: 10.1016/j.rser.2015.12.192.

[4] D.M.Rowe, “CRC Handbook of Thermoelectrics,” *CRC Handbook of Thermoelectrics*. CRC Press, 1995, doi: 10.1201/9781420049718.

[5] L. D. Zhao, V. P. Dravid, and M. G. Kanatzidis, “The panoscopic approach to high performance thermoelectrics,” *Energy and Environmental Science*, vol. 7, no. 1. Royal Society of Chemistry, pp. 251–268, 2014, doi: 10.1039/c3ee43099e.

[6] N. Jaziri, A. Boughamoura, J. Müller, B. Mezghani, F. Tounsi, and M. Ismail, “A comprehensive review of Thermoelectric Generators: Technologies and common applications,” *Energy Reports*, vol. 6, pp. 264–287, Dec. 2020, doi: 10.1016/J.EGYR.2019.12.011.

[7] R. Ahıska and H. Mamur, “A review : Thermoelectric generators in renewable energy,” vol. 4, no. 1, 2014.

[8] J. R. Sootsman, D. Y. Chung, and M. G. Kanatzidis, “New and old concepts in thermoelectric materials,” *Angew. Chemie - Int. Ed.*, vol. 48, no. 46, pp. 8616–8639, 2009, doi: 10.1002/anie.200900598.

[9] A. J. Minnich, M. S. Dresselhaus, Z. F. Ren, and G. Chen, “Bulk nanostructured thermoelectric materials: Current research and future prospects,” *Energy Environ. Sci.*, vol. 2, no. 5, pp. 466–479, 2009, doi: 10.1039/b822664b.

[10] G. J. Snyder and E. S. Toberer, “Complex thermoelectric materials,” vol. 7, no. February, pp. 105–114, 2008.

[11] T. M. Tritt, *Thermal Conductivity Theory, Properties, and Applications*. Physics of Solids and Liquids, Springer US, 2004.

[12] H. S. Kim, Z. M. Gibbs, Y. Tang, H. Wang, and G. J. Snyder, “Characterization of Lorenz number with Seebeck coefficient measurement,” *APL Mater.*, vol. 3, no. 4, 2015, doi: 10.1063/1.4908244.

[13] F. J. Disalvo, “Thermoelectric Cooling and Power Generation,” vol. 285, no. JULY, pp. 703–707, 1999.

[14] D. Champier, “Thermoelectric generators: A review of applications,” *Energy Convers. Manag.*, vol. 140, pp. 167–181, 2017, doi: 10.1016/j.enconman.2017.02.070.

[15] V. P. Singh, M. Kumar, R. S. Srivastava, and R. Vaish, “Thermoelectric energy harvesting using cement-based composites: a review,” *Mater. Today Energy*, vol. 21, p. 100714, 2021, doi: 10.1016/j.mtener.2021.100714.

[16] S. Patidar, “Applications of Thermoelectric Energy: A Review,” *Int. J. Res. Appl. Sci.*

Eng. Technol., vol. 6, no. 5, pp. 1992–1996, 2018, doi: 10.22214/ijraset.2018.5325.

[17] N. R. Kristiansen, G. J. Snyder, H. K. Nielsen, and L. Rosendahl, "Waste Heat Recovery from a Marine Waste Incinerator Using a Thermoelectric Generator," *J. Electron. Mater. 2012 416*, vol. 41, no. 6, pp. 1024–1029, Mar. 2012, doi: 10.1007/S11664-012-2009-6.

[18] N. R. Kristiansen and H. K. Nielsen, "Potential for Usage of Thermoelectric Generators on Ships," *J. Electron. Mater. 2010 399*, vol. 39, no. 9, pp. 1746–1749, Apr. 2010, doi: 10.1007/S11664-010-1189-1.

[19] J. C. Zheng, "Recent advances on thermoelectric materials," *Front. Phys. China*, vol. 3, no. 3, pp. 269–279, 2008, doi: 10.1007/s11467-008-0028-9.

[20] H. J. Goldsmid and G. S. Nolas, "A review of the new thermoelectric materials," *Int. Conf. Thermoelectr. ICT, Proc.*, pp. 1–6, 2001, doi: 10.1109/ict.2001.979602.

[21] S. K. Bux, J. Fleurial, and R. B. Kaner, "Nanostructured materials for thermoelectric applications," pp. 8311–8324, 2010, doi: 10.1039/c0cc02627a.

[22] M. S. Dresselhaus *et al.*, "New directions for low-dimensional thermoelectric materials," *Adv. Mater.*, vol. 19, no. 8, pp. 1043–1053, 2007, doi: 10.1002/adma.200600527.

[23] G. S. Nolas, D. T. Morelli, and T. M. Tritt, "SKUTTERUDITES: A Phonon-Glass-Electron Crystal Approach to Advanced Thermoelectric Energy Conversion Applications," *http://dx.doi.org/10.1146/annurev.matsci.29.1.89*, vol. 29, pp. 89–116, Nov. 2003, doi: 10.1146/ANNUREV.MATSCI.29.1.89.

[24] J.-P. Fleurial, A. Borshchevsky, T. Caillat, D. T. Morelli, and G. P. Meisner, "High Figure of Merit in Ce-Filled Skutterudites."

[25] H. Kleinke, "New bulk Materials for Thermoelectric Power Generation: Clathrates and Complex Antimonides †," *Chem. Mater*, vol. 22, pp. 604–611, 2010, doi: 10.1021/cm901591d.

[26] Y. Liu, L.-M. Wu, L.-H. Li, S.-W. Du, J. D. Corbett, and L. Chen, "The Antimony-Based Type I Clathrate Compounds Cs8Cd18Sb28 and Cs8Zn18Sb28," *Angew. Chemie Int. Ed.*, vol. 48, no. 29, pp. 5305–5308, Jul. 2009, doi: 10.1002/ANIE.200806158.

[27] K. Fang Hsu *et al.*, "Cubic AgPb m SbTe 2m : Bulk Thermoelectric Materials with High Figure of Merit Downloaded from," Wiley, 1997. [Online]. Available: http://science.sciencemag.org/.

[28] P. Oleynikov, V. Volkov, Q. Jie, Q. Li, and Y. Zhu, "Electron Microscopy Study of Layered Misfit Cobalt Oxide [Ca2CoO3]0.62CoO2," *Microsc. Microanal.*, vol. 13, no. S02, pp. 986–987, Aug. 2007, doi: 10.1017/S1431927607076982.

[29] S. Chen and Z. Ren, "Recent progress of half-Heusler for moderate temperature thermoelectric applications," *Materials Today*, vol. 16, no. 10. pp. 387–395, Oct. 2013, doi: 10.1016/j.mattod.2013.09.015.

[30] T. Graf, C. Felser, and S. S. P. Parkin, "Simple rules for the understanding of Heusler compounds," *Prog. Solid State Chem.*, vol. 39, no. 1, pp. 1–50, May 2011, doi: 10.1016/J.PROGSOLIDSTCHEM.2011.02.001.

[31] C. B. Vining, "An inconvenient truth about thermoelectrics," 2009. [Online]. Available: www.sc.doe.gov/bes/reports/abstracts.html#SEU.

[32] T. C. Harman, M. P. Walsh, B. E. Laforge, and G. W. Turner, “Nanostructured Thermoelectric Materials,” 2005.

[33] R. Venkatasubramanian, E. Siivola, T. Colpitts, and B. O’quinn, “Thin-®lm thermoelectric devices with high room-temperature ®gures of merit,” 2001. [Online]. Available: www.nature.com.

[34] C. B. Vining, “A model for the high-temperature transport properties of heavily doped n-type silicon-germanium alloys ARTICLES YOU MAY BE INTERESTED IN,” *J. Appl. Phys.*, vol. 69, p. 331, 1991, doi: 10.1063/1.347717.

[35] C. B. Vining, W. Laskow, J. O. Hanson, R. R. Van Der Beck, and P. D. Gorsuch, “Thermoelectric properties of pressure-sintered Si0.8Ge 0.2 thermoelectric alloys,” *J. Appl. Phys.*, vol. 69, no. 8, pp. 4333–4340, 1991, doi: 10.1063/1.348408.

[36] T. Zhu, C. Fu, H. Xie, Y. Liu, and X. Zhao, “High Efficiency Half-Heusler Thermoelectric Materials for Energy Harvesting,” *Adv. Energy Mater.*, vol. 5, no. 19, pp. 1–13, 2015, doi: 10.1002/aenm.201500588.

[37] J. A. Perez-Taborda, M. Muñoz Rojo, J. Maiz, N. Neophytou, and M. Martin-Gonzalez, “Ultra-low thermal conductivities in large-area Si-Ge nanomeshes for thermoelectric applications,” *Sci. Rep.*, vol. 6, no. August, pp. 1–10, 2016, doi: 10.1038/srep32778.

[38] N. Neophytou *et al.*, “Hierarchically nanostructured thermoelectric materials: challenges and opportunities for improved power factors,” *Eur. Phys. J. B*, vol. 93, no. 11, 2020, doi: 10.1140/epjb/e2020-10455-0.

[39] Y. Nakamura *et al.*, “Anomalous reduction of thermal conductivity in coherent nanocrystal architecture for silicon thermoelectric material,” *Nano Energy*, vol. 12, pp. 845–851, 2015, doi: 10.1016/j.nanoen.2014.11.029.

[40] B. T. Kearney *et al.*, “From amorphous to nanocrystalline: the effect of nanograins in an amorphous matrix on the thermal conductivity of hot-wire chemical-vapor deposited silicon films,” *J. Phys. Condens. Matter*, vol. 30, no. 8, p. 085301, Feb. 2018, doi: 10.1088/1361-648X/aaa43f.

[41] S. R. Culp, S. J. Poon, N. Hickman, T. M. Tritt, and J. Blumm, “Effect of substitutions on the thermoelectric figure of merit of half-Heusler phases at 800°C,” *Appl. Phys. Lett.*, vol. 88, no. 4, pp. 1–3, 2006, doi: 10.1063/1.2168019.

[42] H. Ghoumari Bouanani, D. Eddike, B. Liautard, and G. Brun, “Solid state demixing in Bi2Se3-Bi2Te3 and Bi2Se3-In2Se3 phase diagrams,” *Mater. Res. Bull.*, vol. 31, no. 2, pp. 177–187, Feb. 1996, doi: 10.1016/0025-5408(95)00185-9.

[43] M. Nambuddee and P. Moontragoon, “Calculation of electronic structure and thermoelectric properties of Ge<inf>(1-x)</inf>Si<inf>x</inf> alloy,” *Chiang Mai J. Sci.*, vol. 40, no. 6 SPEC. IS, pp. 1013–1019, 2013.

[44] M. Zhou, “Disorder scattering effect on the high- temperature lattice thermal conductivity of TiCoSb-based half-Heusler compounds conductivity of TiCoSb-based half-Heusler compounds,” vol. 013708, no. May 2005, 2007, doi: 10.1063/1.1944213.

[45] J. Yang, G. P. Meisner, and L. Chen, “Strain field fluctuation effects on lattice thermal conductivity of ZrNiSn-based thermoelectric compounds,” *Appl. Phys. Lett.*, vol. 85, no. 7, pp. 1140–1142, 2004, doi: 10.1063/1.1783022.

[46] J. A. Phys, “Effects of phase separation on the thermoelectric properties of (Ti , Zr ,

Hf) NiSn half-Heusler alloys," vol. 033708, no. July, 2014, doi: 10.1063/1.4890610.

[47] Q. Shen *et al.*, "Effects of partial substitution of Ni by Pd on the thermoelectric properties of ZrNiSn-based half-Heusler compounds," *Appl. Phys. Lett.*, vol. 79, no. 25, pp. 4165–4167, 2001, doi: 10.1063/1.1425459.

[48] G. Sun, Y. Li, X. Zhao, Y. Mi, and L. Wang, "First-Principles Investigation of the Effect of M-Doped (M = Zr, Hf) TiCoSb Half-Heusler Thermoelectric Material," *J. Mater. Sci. Chem. Eng.*, vol. 03, no. 12, pp. 78–86, 2015, doi: 10.4236/MSCE.2015.312012.

[49] Z. Wang, J. E. Alaniz, W. Jang, J. E. Garay, and C. Dames, "Thermal conductivity of nanocrystalline silicon: Importance of grain size and frequency-dependent mean free paths," *Nano Lett.*, vol. 11, no. 6, pp. 2206–2213, 2011, doi: 10.1021/nl1045395.

[50] D. Chakraborty, L. de Sousa Oliveira, and N. Neophytou, "Enhanced Phonon Boundary Scattering at High Temperatures in Hierarchically Disordered Nanostructures," *J. Electron. Mater.*, vol. 48, no. 4, pp. 1909–1916, 2019, doi: 10.1007/s11664-019-06959-4.

[51] J. He and T. M. Tritt, "Advances in thermoelectric materials research: Looking back and moving forward," *Science (80-.).*, vol. 357, no. 6358, 2017, doi: 10.1126/science.aak9997.

[52] H. J. Goldsmid, *Optimisation and selection of semiconductor thermoelements*, vol. 121. 2016.

[53] Q. Zhang *et al.*, "Environmental Science Deep defect level engineering : a strategy of optimizing the carrier concentration for high thermoelectric performance †," pp. 933–940, 2018, doi: 10.1039/c8ee00112j.

[54] S. J. Poon *et al.*, "Bandgap Features and Thermoelectric Properties of Ti-Based Half-Heusler Alloys," 1999. doi: 10.1109/ICT.1999.843331.

[55] C. Fu, T. Zhu, Y. Liu, H. Xie, and X. Zhao, "Band engineering of high performance p-type FeNbSb based half-Heusler thermoelectric materials for figure of merit zT > 1 † Broader context," 2015, doi: 10.1039/c4ee03042g.

[56] C. Yu, T.-J. Zhu, R.-Z. Shi, Y. Zhang, X.-B. Zhao, and J. He, "High-performance half-Heusler thermoelectric materials Hf 1Àx Zr x NiSn 1Ày Sb y prepared by levitation melting and spark plasma sintering," 2009, doi: 10.1016/j.actamat.2009.02.026.

[57] A. N. Gandi and U. Schwingenschlögl, "Thermoelectric Properties of the XCoSb (X: Ti,Zr,Hf) Half-Heusler alloys," *Phys. Status Solidi Basic Res.*, vol. 254, no. 11, Nov. 2017, doi: 10.1002/pssb.201700419.

[58] S. Ouardi *et al.*, "Electronic transport properties of electron- and hole-doped semiconducting <span class," *Phys. Rev. B*, vol. 82, no. 8, p. 085108, Aug. 2010, doi: 10.1103/PhysRevB.82.085108.

[59] J. E. Douglas *et al.*, "Cite as," *Heusler TiNiSn J. Appl. Phys.*, vol. 115, p. 183902, 2014, doi: 10.1063/1.4862955.

[60] J. Schmitt, Z. M. Gibbs, G. J. Snyder, and C. Felser, "Resolving the true band gap of ZrNiSn half-Heusler thermoelectric materials," 2015, doi: 10.1039/c4mh00142g.

[61] S. R. Culp, J. W. Simonson, S. J. Poon, V. Ponnambalam, J. Edwards, and T. M. Tritt, "(Zr,Hf)Co(Sb,Sn) half-Heusler phases as high-temperature (>700 °c) p -type thermoelectric materials," *Appl. Phys. Lett.*, vol. 93, no. 2, Jul. 2008, doi:

10.1063/1.2959103.

[62] M. Schwall and B. Balke, “On the phase separation in n-type thermoelectric half-Heusler materials,” *Materials (Basel).*, vol. 11, no. 4, pp. 1–17, 2018, doi: 10.3390/MA11040649.

[63] X. Yan *et al.*, “Enhanced thermoelectric figure of merit of p-type half-heuslers,” *Nano Lett.*, vol. 11, no. 2, pp. 556–560, Feb. 2011, doi: 10.1021/nl104138t.

[64] M. Schwall and B. Balke, “Phase separation as a key to a thermoelectric high efficiency,” *Phys. Chem. Chem. Phys.*, vol. 15, no. 6, pp. 1868–1872, Feb. 2013, doi: 10.1039/c2cp43946h.

[65] W. G. Zeier *et al.*, “Engineering half-Heusler thermoelectric materials using Zintl chemistry,” *Nat. Rev. Mater.*, vol. 1, no. 6, 2016, doi: 10.1038/natrevmats.2016.32.

[66] E. Rausch, B. Balke, T. Deschauer, S. Ouardi, and C. Felser, “Charge carrier concentration optimization of thermoelectric p-type half-Heusler compounds,” *APL Mater.*, vol. 3, no. 4, 2015, doi: 10.1063/1.4916526.

[67] J. Krez, J. Schmitt, G. Jeffrey Snyder, C. Felser, W. Hermes, and M. Schwind, “Optimization of the carrier concentration in phase-separated half-Heusler compounds,” *J. Mater. Chem. A*, vol. 2, no. 33, pp. 13513–13518, Sep. 2014, doi: 10.1039/c4ta03000a.

[68] S. Bhattacharya *et al.*, “Effect of Sb doping on the thermoelectric properties of Ti-based half-Heusler compounds, TiNiSn1-xSbx,” *Appl. Phys. Lett.*, vol. 77, no. 16, pp. 2476–2478, Oct. 2000, doi: 10.1063/1.1318237.

[69] S. Sakurada and N. Shutoh, “Effect of Ti substitution on the thermoelectric properties of (Zr,Hf)NiSn half-Heusler compounds,” *Appl. Phys. Lett.*, vol. 86, no. 8, pp. 1–3, 2005, doi: 10.1063/1.1868063.

[70] E. Rausch, M. V. Castegnaro, F. Bernardi, M. C. Martins Alves, J. Morais, and B. Balke, “Short and long range order of Half-Heusler phases in (Ti,Zr,Hf)CoSb thermoelectric compounds,” *Acta Mater.*, vol. 115, pp. 308–313, Aug. 2016, doi: 10.1016/j.actamat.2016.05.041.

[71] E. Rausch, B. Balke, S. Ouardi, and C. Felser, “Enhanced thermoelectric performance in the p-type half-Heusler (Ti/Zr/Hf)CoSb0.8Sn0.2 system via phase separation,” *Phys. Chem. Chem. Phys.*, vol. 16, no. 46, pp. 25258–25262, Nov. 2014, doi: 10.1039/c4cp02561j.

[72] E. Rausch, B. Balke, J. M. Stahlhofen, S. Ouardi, U. Burkhardt, and C. Felser, “Fine tuning of thermoelectric performance in phase-separated half-Heusler compounds,” *J. Mater. Chem. C*, vol. 3, no. 40, pp. 10409–10414, 2015, doi: 10.1039/c5tc01196e.

[73] E. Rausch, B. Balke, S. Ouardi, and C. Felser, “Long-Term Stability of (Ti/Zr/Hf)CoSb1-xSnx Thermoelectric p-Type Half-Heusler Compounds Upon Thermal Cycling,” *Energy Technol.*, vol. 3, no. 12, pp. 1217–1224, Dec. 2015, doi: 10.1002/ente.201500183.

[74] X. Yan *et al.*, “Stronger phonon scattering by larger differences in atomic mass and size in p-type half-Heuslers Hf<inf>1-x</inf>Ti<inf>x</inf>CoSb<inf>0.8</inf>Sn <inf>0.2</inf>,” *Energy Environ. Sci.*, vol. 5, no. 6, pp. 7543–7548, 2012, doi: 10.1039/c2ee21554c.

[75] X. Yan *et al.*, “Thermoelectric property study of nanostructured p-type half-heuslers

(Hf, Zr, Ti)CoSb0.8 Sn0.2," *Adv. Energy Mater.*, vol. 3, no. 9, pp. 1195–1200, 2013, doi: 10.1002/aenm.201200973.

[76] W. Wong-Ng, J. W. Lynn, Q. Huang, C. M. Brown, J. A. Kaduk, and G. Joshi, "Observation of drastic change of generalized phonon density-of-states in nanostructured half-Heusler using inelastic neutron scattering," *Appl. Phys. Lett.*, vol. 107, no. 21, Nov. 2015, doi: 10.1063/1.4936163.

[77] Q. Qiu *et al.*, "Grain Boundary Scattering of Charge Transport in n-Type (Hf,Zr)CoSb Half-Heusler Thermoelectric Materials," *Adv. Energy Mater.*, vol. 9, no. 11, Mar. 2019, doi: 10.1002/aenm.201803447.

[78] C. C. Hsu, Y. N. Liu, and H. K. Ma, "Effect of the Zr0.5Hf0.5CoSb1-xSn x/HfO2 half-Heusler nanocomposites on the ZT value," *J. Alloys Compd.*, vol. 597, pp. 217–222, 2014, doi: 10.1016/j.jallcom.2014.01.208.

[79] J. P. A. Makongo *et al.*, "Simultaneous Large Enhancements in Thermopower and Electrical Conductivity of Bulk Nanostructured Half-Heusler Alloys," pp. 18843–18852, 2011.

[80] W. J. Xie *et al.*, "Simultaneously optimizing the independent thermoelectric properties in (Ti , Zr , Hf)(Co , Ni) Sb alloy by in situ forming InSb nanoinclusions," vol. 58, pp. 4705–4713, 2010, doi: 10.1016/j.actamat.2010.05.005.

[81] S. J. Poon *et al.*, "Half-Heusler phases and nanocomposites as emerging high-ZT thermoelectric materials," *J. Mater. Res.*, vol. 26, no. 22, pp. 2795–2802, 2011, doi: 10.1557/jmr.2011.329.

[82] C. Hu, K. Xia, X. Chen, X. Zhao, and T. Zhu, "Transport mechanisms and property optimization of p-type (Zr, Hf)CoSb half-Heusler thermoelectric materials," *Mater. Today Phys.*, vol. 7, pp. 69–76, Dec. 2018, doi: 10.1016/j.mtphys.2018.11.002.

[83] G. Joshi *et al.*, "Enhancement of thermoelectric figure-of-merit at low temperatures by titanium substitution for hafnium in n-type half-Heuslers Hf0.75-xTixZr0.25NiSn0.99Sb0.01," *Nano Energy*, vol. 2, no. 1, pp. 82–87, Jan. 2013, doi: 10.1016/j.nanoen.2012.07.020.

[84] O. Appel, M. Schwall, D. Mogilyansky, M. Köhne, B. Balke, and Y. Gelbstein, "Effects of microstructural evolution on the thermoelectric properties of spark-plasma-sintered Ti0.3Zr0.35Hf0.35NiSn half-heusler compound," *J. Electron. Mater.*, vol. 42, no. 7, pp. 1340–1345, Jul. 2013, doi: 10.1007/s11664-012-2249-5.

[85] N. S. Chauhan *et al.*, "Facile fabrication of p- and n-type half-Heusler alloys with enhanced thermoelectric performance and low specific contact resistance employing spark plasma sintering," *Mater. Lett.*, vol. 228, pp. 250–253, Oct. 2018, doi: 10.1016/j.matlet.2018.06.019.

[86] Y. Xia, V. Ponnambalam, S. Bhattacharya, A. Pope, S. J. Poon, and T. M. Tritt, "Electrical transport properties of TiCoSb half-Heusler phases that exhibit high resistivity," *J. Phys. Condens. Matter*, vol. 13, no. 1, pp. 77–89, 2001, doi: 10.1088/0953-8984/13/1/308.

[87] S. C. Ur, "Thermoelectric properties of half-heusler TiCoSb synthesized by mechanical alloying process," *Korean J. Mater. Res.*, vol. 21, no. 10, pp. 542–545, Sep. 2011, doi: 10.3740/MRSK.2011.21.10.542.

[88] W.-J. Xie, X.-F. Tang, and Z. Qing-Jie, "Fast preparation and thermal transport

property of TiCoSb-based half-Heusler compounds Fast preparation and thermal transport property of TiCoSb-based half-Heusler compounds *," 2007. [Online]. Available: http://iopscience.iop.org/1009-1963/16/11/065.

[89] P. Maji, J. P. A. Makongo, X. Zhou, H. Chi, C. Uher, and P. F. P. Poudeu, "Thermoelectric performance of nanostructured p-type Zr0.5Hf 0.5Co0.4Rh0.6Sb1-xSnx half-Heusler alloys," *J. Solid State Chem.*, vol. 202, pp. 70–76, Jun. 2013, doi: 10.1016/j.jssc.2013.03.024.

[90] R. He, H. S. Kim, Y. Lan, D. Wang, S. Chen, and Z. Ren, "Investigating the thermoelectric properties of p-type half-Heusler Hfx(ZrTi)1-xCoSb0.8Sn0.2 by reducing Hf concentration for power generation," *RSC Adv.*, vol. 4, no. 110, pp. 64711–64716, 2015, doi: 10.1039/c4ra14343d.

[91] T. M. Tritt and M. A. Subramanian, "T hermoelectric Materials , Phenomena , and Applications : A Bird ' s Eye View," vol. 31, no. March 2006, 2018.

[92] J. Horák, P. Lošťák, and L. Beneš, "Philosophical Magazine B Suppression of antistructural defects in crystals by an increased polarization of bonds," doi: 10.1080/13642818408238891.

[93] J. Horák, K. Čermák, and L. Koudelka, "Energy formation of antisite defects in doped Sb2Te3 and Bi2Te3 crystals," *J. Phys. Chem. Solids*, vol. 47, no. 8, pp. 805–809, Jan. 1986, doi: 10.1016/0022-3697(86)90010-7.

[94] G. Kavei and M. A. Karami, "Formation of anti-site defects and bismuth overstoichiometry in p-type Sb2-xBixTe3 thermoelectric crystals," *EPJ Appl. Phys.*, vol. 42, no. 2, pp. 67–73, May 2008, doi: 10.1051/epjap:2008040.

[95] J. Navrátil, Z. Starý, and T. Plecháček, "Thermoelectric properties of p-type antimony bismuth telluride alloys prepared by cold pressing," *Mater. Res. Bull.*, vol. 31, no. 12, pp. 1559–1566, 1996, doi: https://doi.org/10.1016/S0025-5408(96)00149-3.

[96] Y. Ma *et al.*, "Enhanced Thermoelectric Figure-of-Merit in p-Type Nanostructured Bismuth Antimony Tellurium Alloys Made from Elemental Chunks," *Nano Lett.*, vol. 8, no. 8, pp. 2580–2584, Aug. 2008, doi: 10.1021/NL8009928.

[97] X. B. Zhao, X. H. Ji, Y. H. Zhang, T. J. Zhu, J. P. Tu, and X. B. Zhang, "Bismuth telluride nanotubes and the effects on the thermoelectric properties of nanotube-containing nanocomposites," *Appl. Phys. Lett.*, vol. 86, no. 6, p. 062111, Feb. 2005, doi: 10.1063/1.1863440.

[98] W. Xie, X. Tang, Y. Yan, Q. Zhang, and T. M. Tritt, "Unique nanostructures and enhanced thermoelectric performance of melt-spun BiSbTe alloys," *Appl. Phys. Lett.*, vol. 94, no. 10, p. 102111, Mar. 2009, doi: 10.1063/1.3097026.

[99] L. P. Hu, T. J. Zhu, Y. G. Wang, H. H. Xie, Z. J. Xu, and X. B. Zhao, "Shifting up the optimum figure of merit of p-type bismuth telluride-based thermoelectric materials for power generation by suppressing intrinsic conduction," *NPG Asia Mater.*, vol. 6, no. 2, Feb. 2014, doi: 10.1038/am.2013.86.

[100] E. Symeou, C. Nicolaou, A. Delimitis, J. Androulakis, T. Kyratsi, and J. Giapintzakis, "High thermoelectric performance of Bi2-xSbxTe3 bulk alloys prepared from non-nanostructured starting powders," *J. Solid State Chem.*, vol. 270, pp. 388–397, Feb. 2019, doi: 10.1016/J.JSSC.2018.11.037.

[101] J. J. Shen, Z. Z. Yin, S. H. Yang, C. Yu, T. J. Zhu, and X. B. Zhao, "Improved

Thermoelectric Performance of p-Type Bismuth Antimony Telluride Bulk Alloys Prepared by Hot Forging," *J. Electron. Mater. 2011 405*, vol. 40, no. 5, pp. 1095–1099, Mar. 2011, doi: 10.1007/S11664-011-1549-5.

[102] B. Poudel *et al.*, "High-thermoelectric performance of nanostructured bismuth antimony telluride bulk alloys," *Science (80-.).*, vol. 320, no. 5876, pp. 634–638, 2008, doi: 10.1126/science.1156446.

[103] Q. Jiang *et al.*, "Large ZT enhancement in hot forged nanostructured p-type Bi 0.5Sb1.5Te3 bulk alloys," *J. Mater. Chem. A*, vol. 2, no. 16, pp. 5785–5790, Apr. 2014, doi: 10.1039/c3ta13952b.

[104] L. P. Hu, T. J. Zhu, Y. G. Wang, H. H. Xie, Z. J. Xu, and X. B. Zhao, "Shifting up the optimum figure of merit of p-type bismuth telluride-based thermoelectric materials for power generation by suppressing intrinsic conduction," *NPG Asia Mater.*, 2014, doi: 10.1038/am.2013.86.

[105] S. Fan, J. Zhao, J. Guo, Q. Yan, J. Ma, and H. H. Hng, "P-type Bi0.4 Sb1.6 Te3 nanocomposites with enhanced figure of merit," *Appl. Phys. Lett.*, vol. 96, no. 18, 2010, doi: 10.1063/1.3427427.

[106] S. Il Kim *et al.*, "Dense dislocation arrays embedded in grain boundaries for high-performance bulk thermoelectrics," *Science (80-.).*, vol. 348, no. 6230, pp. 109–114, Apr. 2015, doi: 10.1126/SCIENCE.AAA4166.

[107] C. Suryanarayana, "Mechanical alloying and milling," vol. 46, 2001.

[108] D. Jain, V. Sudarsan, A. K. Tyagi, D. Jain, Á. A. K. Tyagi, and Á. V Sudarsan, "Synthesis of Metallic Materials by Arc Melting Technique," pp. 197–213, 2021, doi: 10.1007/978-981-16-1807-9_7.

[109] "X-ray Powder Diffraction (XRD)." https://serc.carleton.edu/research_education/geochemsheets/techniques/XRD.html (accessed Jan. 11, 2022).

[110] F. K. Lotgering, "TOPOTACTICAL REACTIONS WITH FERRIMAGNETIC OXIDES HAVING HEXAGONAL CRYSTAL STRUCTURES-I," Pergamon Press Ltd, 1959.

[111] K. D. Vernon-Parry, "Scanning Electron Microscopy: an introduction."

[112] "Scanning Electron Microscope - Radiological and Environmental Management - Purdue University." https://www.purdue.edu/ehps/rem/laboratory/equipment safety/Research Equipment/sem.html (accessed Jan. 11, 2022).

[113] J. I. Goldstein, D. E. Newbury, J. R. Michael, N. W. M. Ritchie, J. H. J. Scott, and D. C. Joy, *Scanning electron microscopy and x-ray microanalysis*. 2017.

[114] "SEM Signal - Electron Imaging - Accelerating Microscopy." https://www.thermofisher.com/blog/microscopy/sem-signal-types-electrons-and-the-information-they-provide/ (accessed Jan. 11, 2022).

[115] I. H. Kim, Y. G. Lee, M. K. Choi, and S. C. Ur, "Thermoelectric properties of half-heusler TiCoSb1-xSnx synthesized by mechanical alloying process," in *Advanced Materials Research*, 2013, vol. 660, pp. 61–65, doi: 10.4028/www.scientific.net/AMR.660.61.

[116] S. Martelli and F. Padella, "Mechanical alloying of the Fe−Zr system. Correlation between input energy and end products," doi: 10.1007/BF02452130.

[117] H. Joshi, D. P. Rai, L. Hnamte, A. Laref, and R. K. Thapa, “A theoretical analysis of elastic and optical properties of half Heusler MCoSb (M=Ti, Zr and Hf),” *Heliyon*, vol. 5, no. 3, p. e01155, 2019, doi: 10.1016/j.heliyon.2019.e01155.

[118] H. Joshi, D. P. Rai, A. Laref, and R. K. Thapa, “Electronic, and thermoelectric properties of half-heusler compounds MCoSb (M = Ti, Zr, Hf): a first principles study,” *Mater. Res. Express*, vol. 6, no. 6, p. 066307, Mar. 2019, doi: 10.1088/2053-1591/AB0C68.

[119] M. Wood, J. J. Kuo, K. Imasato, and G. J. Snyder, “Improvement of Low-Temperature zT in a Mg3Sb2–Mg3Bi2 Solid Solution via Mg-Vapor Annealing,” *Adv. Mater.*, vol. 31, no. 35, 2019, doi: 10.1002/adma.201902337.

[120] J. J. Kuo *et al.*, “Grain boundary dominated charge transport in Mg3Sb2-based compounds,” *Energy Environ. Sci.*, vol. 11, no. 2, pp. 429–434, Feb. 2018, doi: 10.1039/c7ee03326e.

[121] T. J. Slade *et al.*, “Understanding the thermally activated charge transport in NaPbMSbQm +2(Q = S, Se, Te) thermoelectrics: Weak dielectric screening leads to grain boundary dominated charge carrier scattering,” *Energy Environ. Sci.*, vol. 13, no. 5, pp. 1509–1518, 2020, doi: 10.1039/d0ee00491j.

[122] J. J. Kuo, M. Wood, T. J. Slade, M. G. Kanatzidis, and G. J. Snyder, “Systematic over-estimation of lattice thermal conductivity in materials with electrically-resistive grain boundaries †,” *1250 | Energy Environ. Sci*, vol. 13, p. 1250, 2020, doi: 10.1039/c9ee03921j.

[123] Y. Nishino, S. Deguchi, and U. Mizutani, “Thermal and transport properties of the Heusler-type Fe2 VAl1-x Gex (0≤x≤0.20) alloys: Effect of doping on lattice thermal conductivity, electrical resistivity, and Seebeck coefficient,” *Phys. Rev. B - Condens. Matter Mater. Phys.*, vol. 74, no. 11, pp. 1–6, 2006, doi: 10.1103/PhysRevB.74.115115.

[124] G. A. Slack, “Effect of isotopes on low-temperature thermal conductivity,” *Phys. Rev.*, vol. 105, no. 3, pp. 829–831, 1957, doi: 10.1103/PhysRev.105.829.

[125] B. Abeles, “Lattice thermal conductivity of disordered semiconductor alloys at high temperatures,” *Phys. Rev.*, vol. 131, no. 5, pp. 1906–1911, 1963, doi: 10.1103/PhysRev.131.1906.

[126] H. Zhu *et al.*, “Discovery of ZrCoBi based half Heuslers with high thermoelectric conversion ef fi ciency,” *Nat. Commun.*, no. 2018, pp. 1–9, doi: 10.1038/s41467-018-04958-3.

[127] N. S. Chauhan, S. Bathula, B. Gahtori, Y. V. Kolen’ko, and A. Dhar, “Enhanced Thermoelectric Performance in Hf-Free p-Type (Ti, Zr)CoSb Half-Heusler Alloys,” *J. Electron. Mater.*, vol. 48, no. 10, pp. 6700–6709, Oct. 2019, doi: 10.1007/s11664-019-07486-y.

[128] S. V Faleev and F. Léonard, “Theory of enhancement of thermoelectric properties of materials with nanoinclusions,” doi: 10.1103/PhysRevB.77.214304.

[129] N. S. Chauhan, A. Bhardwaj, T. D. Senguttuvan, R. P. Pant, R. C. Mallik, and D. K. Misra, “A synergistic combination of atomic scale structural engineering and panoscopic approach in p-type ZrCoSb-based half-Heusler thermoelectric materials for achieving high ZT,” *J. Mater. Chem. C*, vol. 4, no. 24, pp. 5766–5778, 2016, doi:

10.1039/c6tc01115b.

[130] P. Sahoo *et al.*, “Enhancing thermopower and hole mobility in bulk p-type half-Heuslers using full-Heusler nanostructures,” *Nanoscale*, vol. 5, no. 19, pp. 9419–9427, 2013, doi: 10.1039/c3nr03145d.

[131] G.S Nolas, ; J.Sharp,; H.J.Goldsmid, *Thermoelectrics: Basic Principles and New Materials Developments - G.S. Nolas, J. Sharp, J. Goldsmid - Βιβλία Google*. 2001.

[132] U.S. Geological Survey, “Metal Prices in the United States Through 2010,” *Pubs.Usgs.Gov*, pp. 1–204, 2012, [Online]. Available: http://pubs.usgs.gov/sir/2012/5188/.

[133] F. Benzoudji *et al.*, “Insight into the structural, elastic, electronic, thermoelectric, thermodynamic and optical properties of MRhSb (M = Ti, Zr, Hf) half-Heuslers from ab initio calculations,” 2019, doi: 10.1016/j.cjph.2019.04.009.

[134] A. Page, A. Van Der Ven, P. F. P. Poudeu, and C. Uher, “Origins of phase separation in thermoelectric (Ti, Zr, Hf)NiSn half-Heusler alloys from first principles †,” 2016, doi: 10.1039/c6ta04957e.

[135] I. Ioannou, P. S. Ioannou, A. Delimitis, Y. Gelbstein, I. (John) Giapintzakis, and T. Kyratsi, “High thermoelectric performance of p-type half-Heusler (Hf,Ti)Co(Sb,Sn) solid solutions fabricated by mechanical alloying,” *J. Alloys Compd.*, vol. 858, pp. 1–11, 2021, doi: 10.1016/j.jallcom.2020.158330.

[136] M. Schrade *et al.*, “The role of grain boundary scattering in reducing the thermal conductivity of polycrystalline X NiSn (X = Hf , Zr , Ti) half-Heusler alloys,” no. 2007, pp. 1–10, 2017, doi: 10.1038/s41598-017-14013-8.

[137] J. Krez *et al.*, “Cite this,” *Phys. Chem. Chem. Phys*, vol. 17, p. 29854, 2985, doi: 10.1039/c4cp04875j.

[138] T. Sekimoto, K. Kurosaki, H. Muta, and S. Yamanaka, “Annealing effect on thermoelectric properties of TiCoSb half-Heusler compound,” *J. Alloys Compd.*, vol. 394, no. 1–2, pp. 122–125, May 2005, doi: 10.1016/J.JALLCOM.2004.11.017.

[139] T. Katayama, S. W. Kim, Y. Kimura, and Y. Mishima, “The Effects of Quaternary Additions on Thermoelectric Properties of TiNiSn-Based Half-Heusler Alloys,” *J. Electron. Mater.*, vol. 32, no. 11, 2003.

[140] Y. Gelbstein *et al.*, “Thermoelectric properties of spark plasma sintered composites based on TiNiSn half-Heusler alloys,” doi: 10.1557/jmr.2011.107.

[141] B. Madavali, H.-S. Kim, C.-H. Lee, D.-S. Kim, and S.-J. Hong, “High Thermoelectric Figure of Merit in p-Type (Bi 2 Te 3) x À (Sb 2 Te 3) 1Àx Alloys Made from Element-Mechanical Alloying and Spark Plasma Sintering,” vol. 48, no. 3, doi: 10.1007/s11664-018-6706-7.

[142] S. J. Hong and B. S. Chun, “Microstructure and thermoelectric properties of extruded n-type 95%Bi2Te2–5%Bi2Se3 alloy along bar length,” *Mater. Sci. Eng. A*, vol. 356, no. 1–2, pp. 345–351, Sep. 2003, doi: 10.1016/S0921-5093(03)00147-3.

[143] J. Black, E. M. Conwell, L. Seigle, and C. W. Spencer, “Electrical and optical properties of some M2v−bN3vi−b semiconductors,” *J. Phys. Chem. Solids*, vol. 2, no. 3, pp. 240–251, Jan. 1957, doi: 10.1016/0022-3697(57)90090-2.

[144] H. Köhler, “Non-Parabolicity of the Highest Valence Band of Bi2Te3 from Shubnikov-

de Haas Effect," *Phys. status solidi*, vol. 74, no. 2, pp. 591–600, Apr. 1976, doi: 10.1002/PSSB.2220740218.

[145] L.-P. Hu, T.-J. Zhu, Y.-G. Wang, H.-H. Xie, Z.-J. Xu, and X.-B. Zhao, "Shifting up the optimum figure of merit of p-type bismuth telluride-based thermoelectric materials for power generation by suppressing intrinsic conduction," *NPG Asia Mater.*, vol. 6, no. 2, p. e88, 2014, doi: 10.1038/am.2013.86.

[146] Z. Starý, J. Horák, M. Stordeur, and M. Stölzer, "Antisite defects in Sb2−xBixTe3 mixed crystals," *J. Phys. Chem. Solids*, vol. 49, no. 1, pp. 29–34, Jan. 1988, doi: 10.1016/0022-3697(88)90130-8.

[147] R. Ionescu, J. Jaklovszky, N. Nistor, and A. Chiculita, "Grain size effects on thermoelectrical properties of sintered solid solutions based on Bi2Te3," *Phys. status solidi*, vol. 27, no. 1, pp. 27–34, 1975, doi: 10.1002/pssa.2210270103.

[148] K. W. Jang, H. J. Kim, W. J. Jung, and I. H. Kim, "Charge transport and thermoelectric properties of P-type Bi2-xSbxTe3 prepared by mechanical alloying and hot pressing," *J. Korean Inst. Met. Mater.*, vol. 56, no. 1, pp. 66–71, 2018, doi: 10.3365/KJMM.2018.56.1.66.

[149] W. M. Yim, E. V Fitzke, and F. D. Rosi, "Thermoelectric Properties of Bi2Te3-Sb2Te3-Sb2Se3 Pseudo-Ternary Alloys in the Temperature Range 77 to 300 ~ K," *J. Mater. Sci.*, vol. 1, pp. 52–65, 1966.

[150] C. Chen, D.-W. Liu, B.-P. Zhang, and J.-F. Li, "Enhanced Thermoelectric Properties Obtained by Compositional Optimization in p-Type Bi x Sb 2Àx Te 3 Fabricated by Mechanical Alloying and Spark Plasma Sintering," doi: 10.1007/s11664-010-1463-2.

[151] Y. Lan *et al.*, "Structure study of bulk nanograined thermoelectric bismuth antimony telluride," *Nano Lett.*, 2009, doi: 10.1021/nl803235n.

[152] D. G. Cahill, S. K. Watson, and R. O. Pohl, "Lower limit to the thermal conductivity of disordered crystals," *Phys. Rev. B*, vol. 46, no. 10, p. 6131, Sep. 1992, doi: 10.1103/PhysRevB.46.6131.

[153] C. Chiritescu, C. Mortensen, D. G. Cahill, D. Johnson, and P. Zschack, "Lower limit to the lattice thermal conductivity of nanostructured Bi2Te3-based materials," *J. Appl. Phys.*, vol. 106, no. 7, p. 073503, Oct. 2009, doi: 10.1063/1.3226884.

[154] Y. Liu, M. Zhou, and J. He, "Towards higher thermoelectric performance of Bi2Te3 via defect engineering," *Scr. Mater.*, vol. 111, pp. 39–43, Jan. 2016, doi: 10.1016/j.scriptamat.2015.06.031.

[155] W. Liu, X. Yan, G. Chen, and Z. Ren, "Recent advances in thermoelectric nanocomposites," *Nano Energy*, vol. 1, no. 1. pp. 42–56, Jan. 2012, doi: 10.1016/j.nanoen.2011.10.001.

[156] Y. Wu, S. W. Finefrock, and H. Yang, "Nanostructured thermoelectric: Opportunities and challenges," *Nano Energy*, vol. 1, no. 5, pp. 651–653, Sep. 2012, doi: 10.1016/j.nanoen.2012.08.001.

[157] W. Xie *et al.*, "Identifying the specific nanostructures responsible for the high thermoelectric performance of (Bi,Sb)2Te3nanocomposites," *Nano Lett.*, 2010, doi: 10.1021/nl100804a.

[158] P. Dharmaiah, H. S. Kim, C. H. Lee, and S. J. Hong, "Influence of powder size on

thermoelectric properties of p-type 25%Bi2Te3-75%Sb2Te3alloys fabricated using gas-atomization and spark-plasma sintering," *J. Alloys Compd.*, vol. 686, pp. 1–8, 2016, doi: 10.1016/j.jallcom.2016.05.340.

[159] W. Xie *et al.*, "Investigation of the sintering pressure and thermal conductivity anisotropy of melt-spun spark-plasma-sintered (Bi,Sb)2Te3 thermoelectric materials," *J. Mater. Res.*, vol. 26, no. 15, pp. 1791–1799, Aug. 2011, doi: 10.1557/jmr.2011.170.

[160] Y. I. Shtern, A. S. Malkova, A. S. Pashinkin, and V. A. Fedorov, "Heat capacity of the n-Bi 2Te 2.88Se 0.12 and p-Bi 0.52Sb 1.48Te 3 solid solutions," *Inorg. Mater.*, vol. 44, no. 10, pp. 1057–1059, 2008, doi: 10.1134/S0020168508100051.

[161] K. Kusagaya and M. Takashiri, "Investigation of the effects of compressive and tensile strain on n-type bismuth telluride and p-type antimony telluride nanocrystalline thin films for use in flexible thermoelectric generators," *J. Alloys Compd.*, vol. 653, pp. 480–485, Dec. 2015, doi: 10.1016/j.jallcom.2015.09.039.

[162] J. Jiang, L. Chen, S. Bai, Q. Yao, and Q. Wang, "Thermoelectric properties of p-type (Bi2Te3) x(Sb2Te3)1-x crystals prepared via zone melting," *J. Cryst. Growth*, vol. 277, no. 1–4, pp. 258–263, Apr. 2005, doi: 10.1016/j.jcrysgro.2004.12.144.

[163] X. Yan *et al.*, "Experimental studies on anisotropic thermoelectric properties and structures of n-type Bi2Te2.7Se0.3," *Nano Lett.*, vol. 10, no. 9, pp. 3373–3378, Sep. 2010, doi: 10.1021/NL101156V/ASSET/IMAGES/NL101156V.SOCIAL.JPEG_V03.

[164] B. Qiu and X. Ruan, "Molecular dynamics simulations of lattice thermal conductivity of bismuth telluride using two-body interatomic potentials," *Phys. Rev. B - Condens. Matter Mater. Phys.*, vol. 80, no. 16, p. 165203, Oct. 2009, doi: 10.1103/PHYSREVB.80.165203/FIGURES/5/MEDIUM.

[165] O. Hellman and D. A. Broido, "Phonon thermal transport in Bi2 Te3 from first principles," *Phys. Rev. B - Condens. Matter Mater. Phys.*, vol. 90, no. 13, p. 134309, Oct. 2014, doi: 10.1103/PHYSREVB.90.134309/FIGURES/9/MEDIUM.

[166] S. Wang *et al.*, "Revisiting the Reduction of Thermal Conductivity in Nano- to Micro-Grained Bismuth Telluride: The Importance of Grain-Boundary Thermal Resistance," *Eng. Sci.*, vol. 17, pp. 45–55, 2022, doi: 10.30919/es8d513.

[167] C. W. Nan and R. Birringer, "Determining the Kapitza resistance and the thermal conductivity of polycrystals: A simple model," *Phys. Rev. B*, vol. 57, no. 14, p. 8264, Apr. 1998, doi: 10.1103/PhysRevB.57.8264.

[168] R. H. Tarkhanyan and D. G. Niarchos, "Effect of Pore Size on Reduction of the Lattice Thermal Conductivity of Nano to Micro-Scale Porous Materials," *J. Electron. Mater.*, vol. 43, no. 10, pp. 3808–3811, 2014, doi: 10.1007/s11664-014-3168-4.

[169] R. H. Tarkhanyan and D. G. Niarchos, "Reduction in lattice thermal conductivity of porous materials due to inhomogeneous porosity," *Int. J. Therm. Sci.*, vol. 67, pp. 107–112, May 2013, doi: 10.1016/j.ijthermalsci.2012.12.008.

[170] T. Kanno *et al.*, "Enhancement of average thermoelectric figure of merit by increasing the grain-size of Mg3.2Sb1.5Bi0.49Te0.01," *Appl. Phys. Lett.*, vol. 112, no. 3, p. 033903, Jan. 2018, doi: 10.1063/1.5016488.

[171] T. R. Wei *et al.*, "Distinct Impact of Alkali-Ion Doping on Electrical Transport Properties of Thermoelectric p-Type Polycrystalline SnSe," *J. Am. Chem. Soc.*, vol. 138, no. 28, pp. 8875–8882, Jul. 2016, doi:

10.1021/JACS.6B04181/SUPPL_FILE/JA6B04181_SI_001.PDF.

[172] J. H. Son, M. W. Oh, B. S. Kim, and S. D. Park, “Optimization of thermoelectric properties of n-type Bi2(Te,Se)3 with optimizing ball milling time,” *Rare Met.*, vol. 37, no. 4, pp. 351–359, Apr. 2018, doi: 10.1007/S12598-018-1028-8/FIGURES/13.

[173] C. L. Cramer, H. Wang, and K. Ma, “Performance of Functionally Graded Thermoelectric Materials and Devices : A Review,” vol. 47, no. 9, pp. 5122–5132, 2018, doi: 10.1007/s11664-018-6402-7.

[174] C. L. Cramer, W. Li, Z. Jin, J. U. E. Wang, K. Ma, and T. B. Holland, “Techniques for Mitigating Thermal Fatigue Degradation , Controlling Efficiency , and Extending Lifetime in a ZnO Thermoelectric Using Grain Size Gradient FGMs,” *J. Electron. Mater.*, vol. 47, no. 1, pp. 866–872, 2018, doi: 10.1007/s11664-017-5879-9.

[175] C. Wood, “Materials for thermoelectric energy conversion,” *Reports Prog. Phys.*, vol. 51, no. 4, pp. 459–539, Apr. 1988, doi: 10.1088/0034-4885/51/4/001.

[176] N. Bisht, P. More, and K. Khanna, “Materials Advances Progress of hybrid nanocomposite materials for thermoelectric applications,” pp. 1927–1956, 2021, doi: 10.1039/d0ma01030h.

[177] L. Yang, Z. G. Chen, M. S. Dargusch, and J. Zou, “High Performance Thermoelectric Materials: Progress and Their Applications,” *Adv. Energy Mater.*, vol. 8, no. 6, Feb. 2018, doi: 10.1002/AENM.201701797.

[178] C. J. Vineis, A. Shakouri, A. Majumdar, and M. G. Kanatzidis, “Nanostructured thermoelectrics: Big efficiency gains from small features,” *Adv. Mater.*, vol. 22, no. 36, pp. 3970–3980, 2010, doi: 10.1002/adma.201000839.

[179] C. Niu *et al.*, “Realization of tunable Dirac cone and insulating bulk states in topological insulators (Bi1−xSbx)2Te3,” *Sci. Reports 2012 21*, vol. 2, no. 1, pp. 1–7, Dec. 2012, doi: 10.1038/srep00976.